MReadings: Neurology

Contributions from our MAGNETOM users

SIEMENS

Ignacio Vallines, PhD
Global Segment Manager
Neurology

Dear Reader,

Neurology is the largest and one of the more exciting fields of application for MR. Siemens is pushing the boundaries of MR diagnostic imaging in Neurology by closely working with our customers on the optimization and further product implementation of advanced techniques, which go way beyond standard imaging. The result is the most comprehensive catalog of advanced applications, supported by a state-of-the-art system portfolio.

Some of those efforts in the field of neurology are best portrayed by recent contributions from our customers to our customer magazine, MAGNETOM Flash, which we are proud to offer you with this compilation. We would like to thank again the authors of these articles and all those experts who continuously support the development of MR by sharing their experiences and expertise with other MAGENTOM users worldwide.

Enjoy the reading!

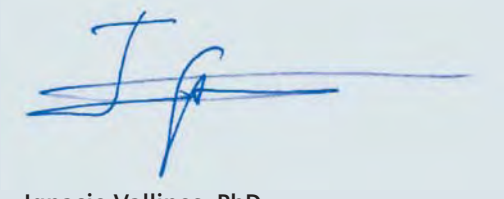

Ignacio Vallines, PhD
Global Segment Manager Neurology

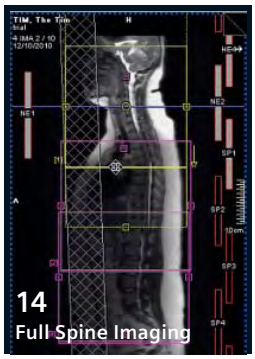

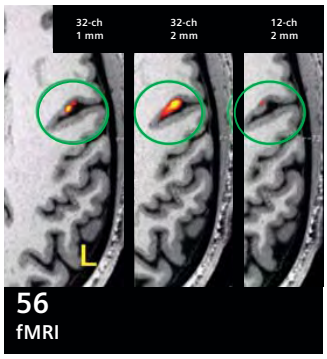

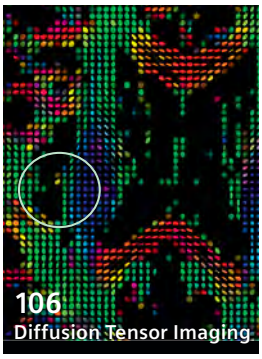

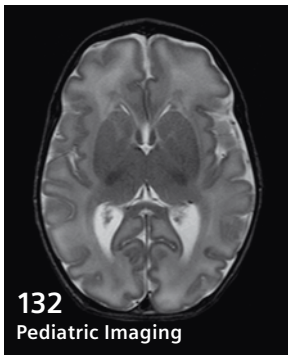

Clinical

How I do it

Clinical

Technology

Clinical

Technology

Clinical

Introduction to Advanced Techniques in MR Neuroimaging

Bernhard Schuknecht, M.D.; Krisztina Baràth, M.D.

Diagnostic, Vascular and Interventional Neuroradiology, Medizinisch Radiologisches Institut MRI Zürich, Bethanien Hospital, Zürich, Switzerland

Functional MRI (fMRI)

Functional magnetic resonance imaging (fMRI) is based on the blood oxygenation level dependent (BOLD) effect. BOLD contrast rises with neural activation and depends on the variables blood flow and oxygenation. Augmentation of regional cerebral blood flow (CBF) is accompanied by a local increase in oxygen extraction due to a rise in the cerebral metabolic rate of oxygen consumption. The ferrous iron in deoxyhemoglobin adopts para-magnetic properties contrary to the

fMRI and DTI of a brain tumor: Function and structure

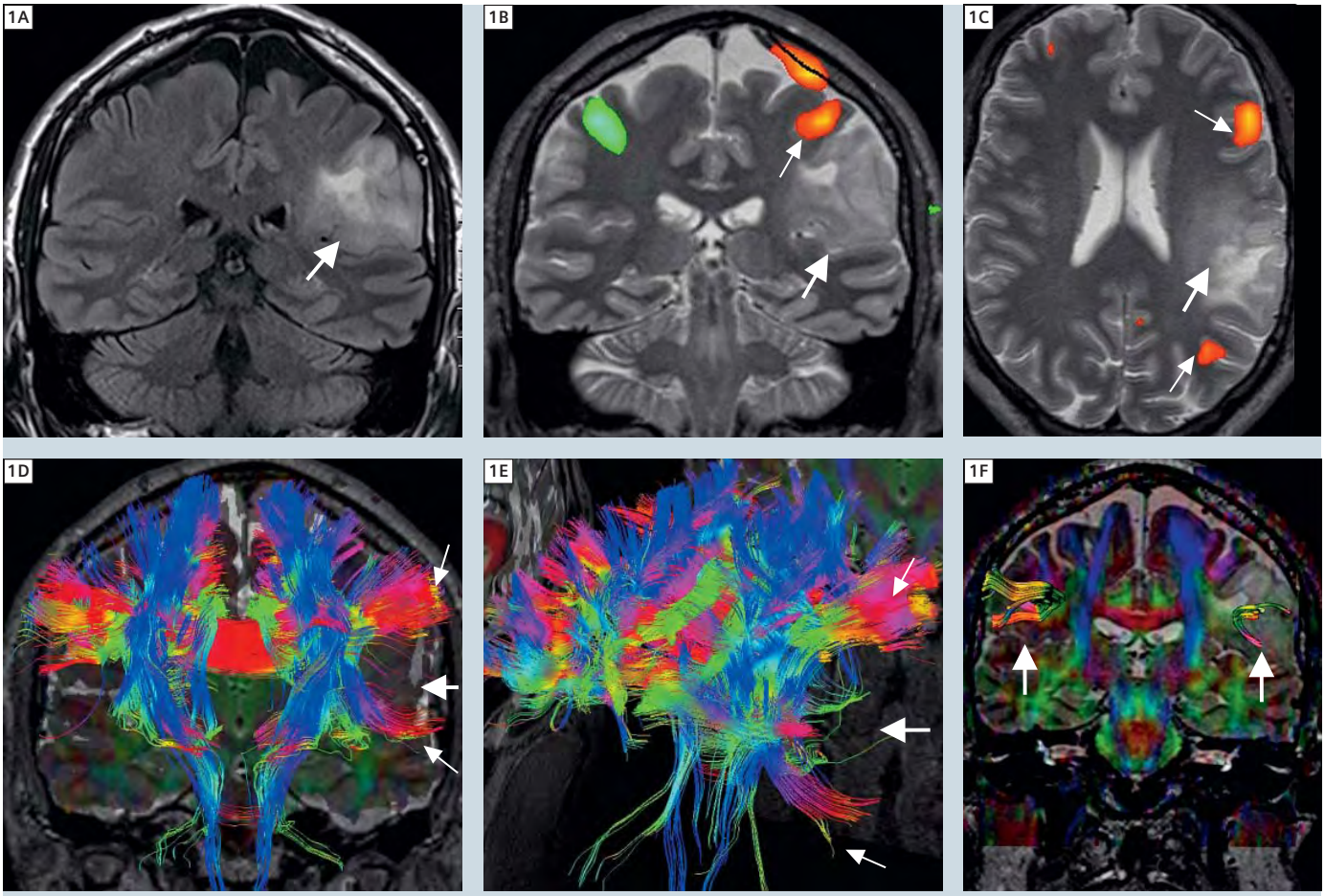

1 **(1A)** Brain tumor (oligodendroglioma) (arrow) in the subcentral gyrus/inferior parietal lobule on the left shown on a FLAIR sequence. **(1B)** Activation of the primary motor cortex (thin arrow) close to the tumor (arrow) during finger tapping. Red = movement on the right, Green = movement on the left. **(1C)** Activation of the motor speech area and the sensory speech area (thin arrows) far away from the tumor (arrow). The DTI sequence **(1D–E)** shows the deviated U-fibers (thin arrow) due to the tumor (arrow).
The Broca- and Wernicke areas are connected through the arcuate fibers, which makes a combination of fMRI and DTI for the preoperative planning necessary. **(1F)** The thinning of the left arcuate fibers indicates an infiltration of the speech-network.

diamagnetic effect in oxyhemoglobin. This results in a susceptibility induced field shift and leads to an increase in T2* value and a signal increase in T2* gradient echo or echo planar imaging (EPI) studies. The high sensitivity of EPI sequences enables real time visualization of activation of different parts of the brain in comparison to a resting state. In a functional MR paradigm the patient is asked to alternatively perform tasks or is stimulated to trigger several processes or emotions. Threshold functional MRI activation maps are spatially addressed (Fig. 1A) and therefore typically overlaid in colour on a high resolution anatomical T1 MPRAGE or SPACE FLAIR MR image (Figs. 1B, C).

fMRI was first employed for mapping of neuronal activation during visual perception tasks and motor activation in the early nineties. Since then fMRI has evolved into an invaluable research tool e.g. in cognitive neuroscience or neuropharmacology as well as a routinely applied clinical MR technique.

Clinical applications comprise mainly neurosurgical planning in order to determine resection margins in relation to functional 'eloquent' areas. With fMRI brain functional plasticity may also be visualized in recovery after stroke or surgery. Furthermore fMRI can be used to evaluate specific brain functions in a range of neuro-degenerative diseases. Despite existing limitations of fMRI, a significant increase in spatial and temporal resolution has been achieved in order to improve localization of specific brain function and individualize treatment.

Diffusion Tensor Tractography (Diffusion Tensor Imaging, DTI)

DTI is a non-invasive MR technique to study brain tissue composition and architecture in vivo. DTI is based on the concept that water diffusion is anisotropic in organized tissues. Cerebral white matter is composed of axons, myelin sheaths and neuroglia which are aligned to form fiber tracts. DTI provides information on water diffusion properties regarding the extent of diffusion anisotropy and its orientation. A pair of magnetic dephasing and rephasing field gradients is successively applied in distinct directions in 3D space. The resulting images exhibit signal attenuation in the direction of the applied gradient which is proportional to water diffusivity. The largest principal axis of the diffusion tensor aligns with the predominant fiber orientation in an MRI voxel. A diffusion tensor or the mean diffusivity may be estimated from as few as 6 diffusion-weighted images acquired along non-collinear directions and 1 minimally = T2-weighted (b_0) image. From the diffusion tensor, the DTI indices derived include the mean diffusion coefficient (ADC), calculated eigenvalues and eigenvectors and an index of diffusion anisotropy, e.g. fractional anisotropy (FA). To achieve a high signal-to-noise ratio DTI employs more than the minimum of 6 diffusion-weighting angulations and/or acquires repeated measurements of diffusion directions. Despite substantial improvement in technique, spatial resolution of DTI in the order of 1–4 mm per dimension, reflects limitations imposed by using a macroscopic technique to visualize microscopic restrictions.

DTI is performed in combination with fMRI for preoperative localization of fiber tracts in proximity to a lesion (Figs. 1D–F), and for preoperative differentiation of white matter tract infiltration from displacement in patients with low grade glioma in particular.

Following hemorrhagic or ischemic stroke and trauma DTI has become an important tool to assess white matter tract involvement beyond findings by morphologic imaging. This holds also true for white matter alterations in patients suffering from neurodegenerative and movement disorders, and to visualize secondary neurodegeneration in inflammatory conditions such as multiple sclerosis.

Diffusion-Weighted Imaging (DWI)

Diffusion-weighted MR imaging renders microscopic molecular motion of water visible within tissues. The anisotropic nature of diffusion in the brain can be visualized by comparing images obtained with DWI gradients applied in three orthogonal directions. DWI consists of an echo planar spin-echo T2w pulse sequence. Alternative DWI sequences are based on a single-shot gradient or single-shot fast spin-echo technique, 'line-scan' and spiral DWI technique. The signal intensity obtained by DWI corresponds to the signal on T2w images decreased by a signal amount that is related to the rate of diffusion in the direction of the applied gradients. Pathology therefore is reflected by high signal on diffusion-weighted images and by decreased signal on apparent diffusion coefficient (ADC) maps.

While DWI is highly sensitive in reflecting the physical properties of diffusion, the observation of restricted water diffusion is relatively non-specific for pathology. Restricted diffusion is the earliest detectable MR sign of ischemia. However diffusion changes are also seen with infection, inflammation and neoplasms. In an abscess restricted diffusion and low ADC values are attributed to increased fluid viscosity and higher cellularity present in pus. Metastases and tumors may have a similar appearance to an abscess on morphologic images but present with normal diffusion and high ADC values in areas of necrosis.

DWI is gaining increasing importance in oncology both for the initial diagnosis and as a sensitive tool to assess tumor response to treatment. Low ADC values in a lesion are an indicator for a malignant compression fracture in the spine as well as for malignant lymphadenopathy in the neck. In cerebral gliomas ADC values inversely correlate with the grading of gliomas, and low values indicate the higher grade component in a 'mixed' glioma. Lower ADC values in the edema of gliomas compared to metastases are an early sign of brain infiltration beyond macroscopic visible margins. Restricted diffusion in the early postoperative phase is more likely to correspond to ischemia and reparative changes, while after 6–8 weeks may indicate true progression or pseudoprogression. Increasing ADC values in a solid lesion like a glioma, lymphoma or metastasis are a more sensitive

parameter to chemo-radiotherapy treatment response than the contrast enhanced T1 images.
Metastases and glial tumors can be differentiated by low ADC due to their high grade cellularity (metastases) and by areas of high ADC due to necrosis (glial tumors) (Figs. 2A–D).

Perfusion-MRI (PWI = Perfusion-weighted imaging)

Perfusion MRI relies on two different techniques: dynamic contrast enhanced (DCE) perfusion MRI consists of a T1w 3D FLASH sequence which is used to depict cerebral microcirculation and is a direct measure of vascular permeability. On the other hand dynamic susceptibility contrast (DSC) MR perfusion is based on a gradient-echo echo planar sequence. DSC provides a measure of vascularity, mircovascular density or relative cerebral blood volume (rCBV) and therefore is complementary to DCE perfusion. Both sequences require a bolus of contrast media injected into a peripheral vein.

Diffusion in glioma and metastasis: Cellularity and tissue ultrastructure

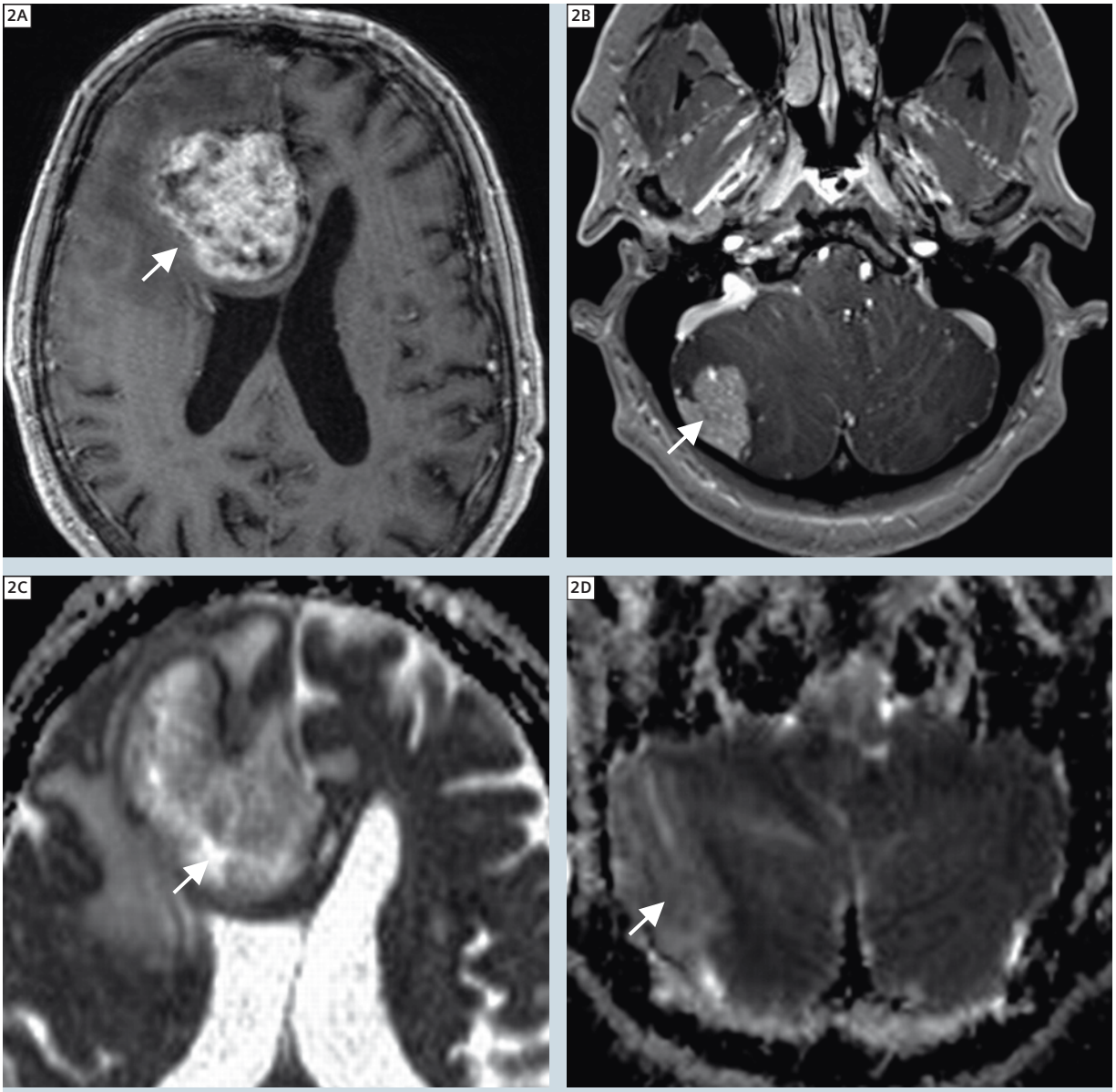

2 Contrast enhanced MRI does not reliably distinguish a glioblastoma multiforme **(2A)** from a metastasis **(2B)**. Focal high ADC values (bright) indicate necrotic components in a glioma (arrow **2C**). Low ADC values represent a solid metastasis **(2B)** as in this case or a lymphoma with dense cellularity **(2D)**. ADC values are lower within the edema of a glioma due to microscopic infiltration which is usually not present within the edema of a metastasis.

Perfusion MR in combination with diffusion-weighted imaging has been routinely applied in the setting of acute stroke. The initial perfusion – diffusion mismatch correlates with the ischemic penumbra, the tissue at risk and the extent of the definite infarct size.
In brain neoplasms vascular proliferation and neoangiogenesis are hallmarks of differentiation to higher grades of malignancy. rCBV values as obtained by DSC show a significant correlation with tumor grade (Figs. 3 A–C), microvascular density and in case of increase predict malignant transformation. Frequently, changes of these parameters during cytostatic, anti-angiogenic and radiation therapy (Figs. 4A–C) precede tumor volume reduction. DCE is applied to assess the degree of tumor angiogenesis and vessel permeability. Dynamic contrast enhanced perfusion (DCE) in combination with dynamic susceptibility contrast (DSC) perfusion (Fig. 5B) and MR spectroscopy (Fig. 6C) is applied to distinguish treatment related effects (pseudoprogression or pseudoresponse) from true progression and true response respectively.

Perfusion and diffusion in brain tumor imaging: Vascularisation, neo-angiogenesis, capillary permeability – cellularity vs. extracellular space

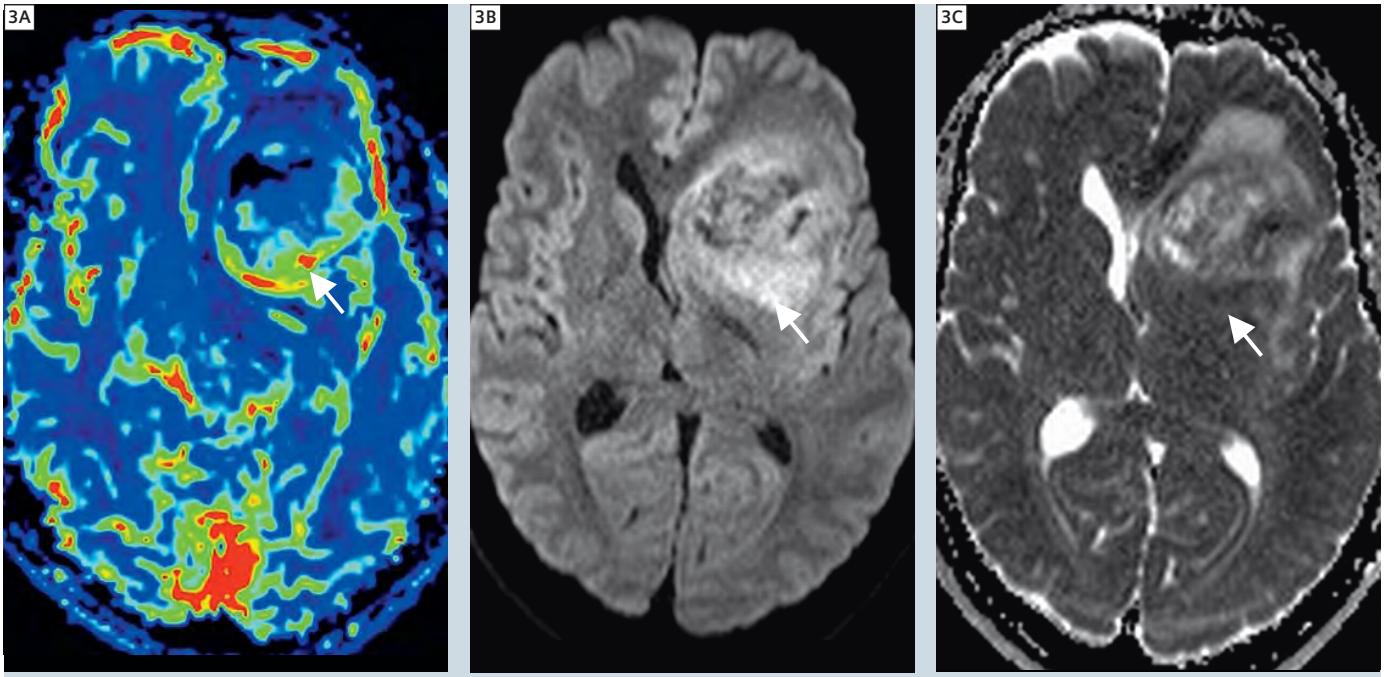

3 Perfusion MRI of a anaplastic glioma with high rCBV within the component of higher maligancy in the posterior part (arrow **3A**) with restricted diffusion **(3B)** and low ADC values **(3C)** as additional signs of a highly cellular anaplastic component.

Treatment monitoring: Decreased vascularity

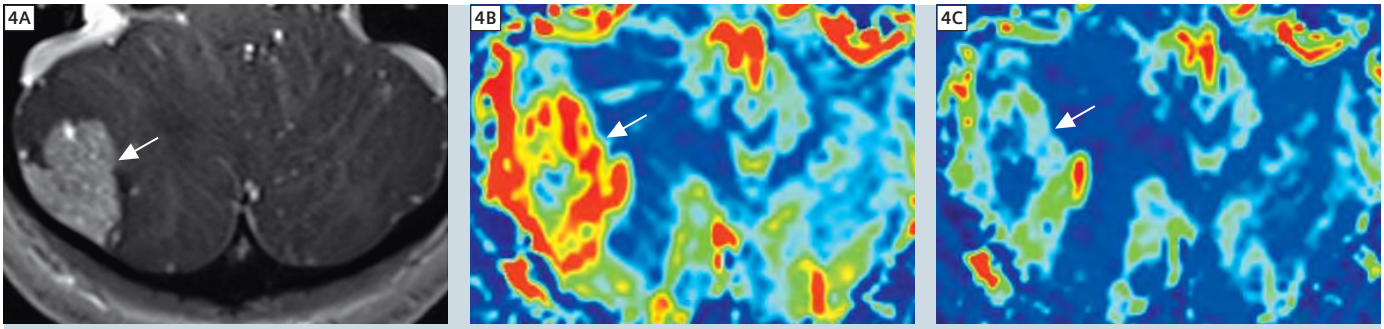

4 **(4A)** Cerebellar metastasis of renal cell carcinoma with subtle peripheral vessels indicated on the contrast enhanced T1w image. DSC perfusion MRI depicts markedly increased vascularity within the entire metastasis with high rCBV values before **(4B)** and with decreased rCBV values under radiotherapy **(4C)**.

Treatment related effects: low perfusion – low cellularity

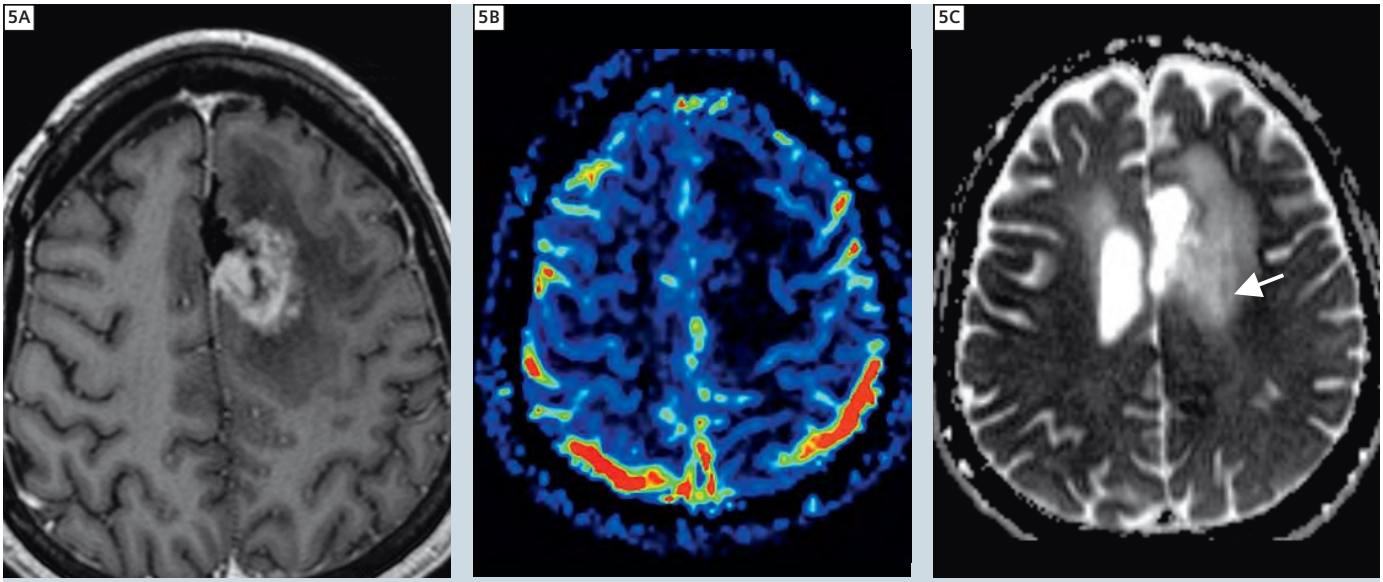

5 T1w contrast enhanced image one year following resection and chemo-radiotherapy of a glioblastoma. Recurrence and treatment related necrosis cannot be reliably differentiated based on morphology **(5A)**. Perfusion MRI depicts low rCBV values **(5B)** contrary to high rCBV values indicating recurrence in a high grade glioma (compare to Fig. 3A). High ADC values **(5C)** denote low cellularity indicative of a necrosis confirmed by subsequent histology.

ASL Arterial Spin labelling

MR imaging with ASL is an alternative method to measure perfusion. Contrary to dynamic contrast enhanced (DCE) and dynamic susceptibility contrast (DSC) perfusion MRI, ASL uses electromagnetically labelled arterial blood water as a freely diffusible intrinsic tracer. In clinical applications, the ASL technique proved reproducible and reliable to assess cerebral blood flow (CBF) despite a relatively low signal intensity-to-noise ratio. ASL has been evaluated in various pathological states including cerebrovascular and neurodegenerative disease and for the assessment of glioma grading and tumor angiogenesis. Quantitative assessment of blood flow in gliomas by ASL yielded results and reproducibility comparable to DSC perfusion MR imaging.

MR Spectroscopy (MRS)

MR Spectroscopy provides a measure of brain metabolic composition or chemistry. Each metabolite appears at a specific ppm (Fig. 6 A–C), and each one reflects specific cellular and biochemical processes. N-Acetyl-Aspartat (NAA) is a neuronal marker and decreases with any disease that adversely affects neuronal integrity. Creatine provides a measure of energy stores. Choline is a measure of increased cellular turnover and is elevated in tumors and inflammatory processes. Lactate is a marker of oxygen deficiency, lipids of tissue necrosis and myoinositol of granulation tissue (gliosis).

Indication of MRS:

- differential diagnosis of low-grade and high-grade tumors
- monitoring under radio-chemotherapy
- differentiation of recurrent tumor from secondary necrosis due to therapy

Susceptibility-Weighted Imaging (SWI)

SWI is a modified 3D gradient-echo technique which exploits the susceptibility differences between tissues and uses the phase image to detect these differences. The magnitude and phase data are combined to produce an enhanced contrast magnitude image which is exquisitely sensitive to products of blood-deterioration (DeoxyHB, MetHB and Hämosiderin) (Fig. 7 A–D).
Iron depositions can be the result of an untreated high blood pressure and accompanied by a gliosis could be a sign of a brain damage. Residual blood after a stroke, amyloid angiopathy or brain injury can be easily detected with gradient-echo sequences, such as SWI or T2*.

Indications of SWI:

- micro-bleedings in hypertension and vascular dementia
- superficial bleedings in amyloid angiopathy
- hemorrhagic contusion and diffuse axonal injury after brain trauma
- iron deposition in neurodegenerativ diseases

MR Spectroscopy: tumor progression vs. pseudoprogression

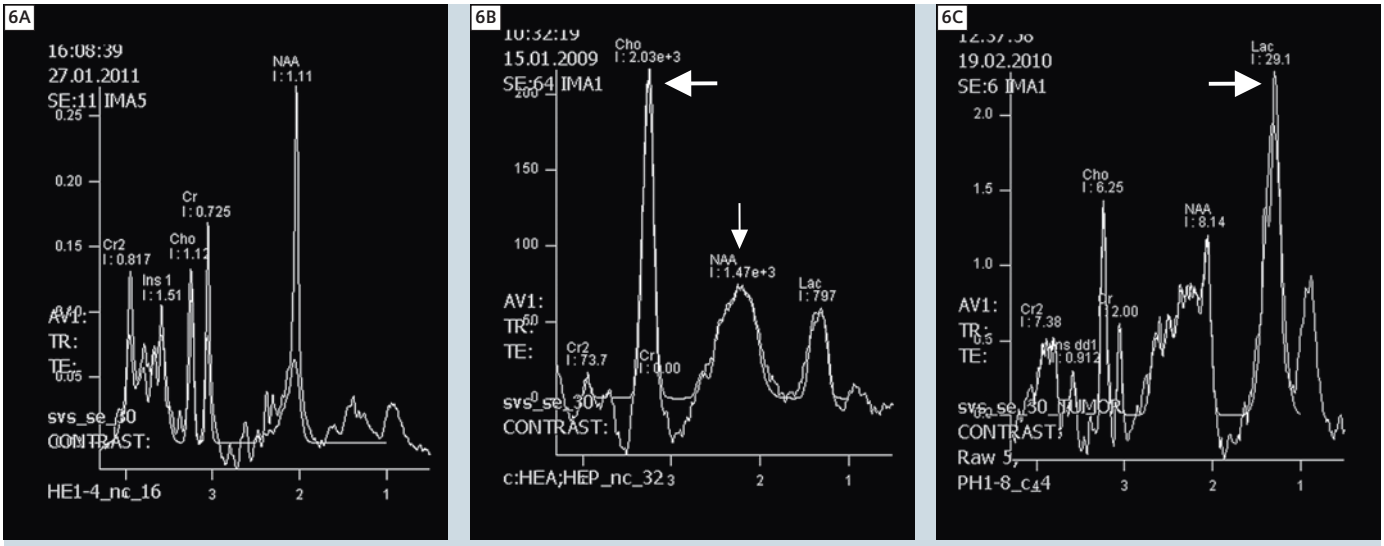

6 **(6A)** Normal spectrum. **(6B)** Spectrum of an Oligodendroglioma with high Cholin as a marker of a high proliferation-rate (thick arrow) and with low NAA as a marker of lost neuronal integrity (thin arrow). **(6C)** Spectrum of a therapy-induced necrosis with low Cholin and NAA and with high Lactate as a sign of oxygen deficiency (thick arrow).

Iron deposition after trauma, in hypertension and in amyloid angiopathy

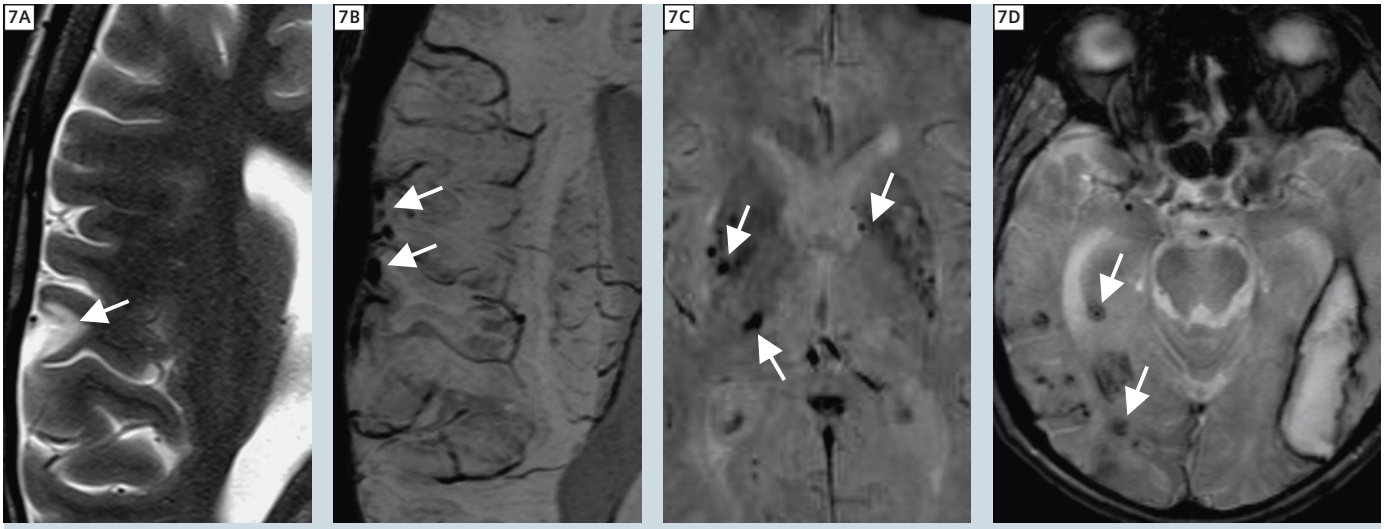

7 **(7A)** Circumscribed cortical gliosis (arrow) after brain injury without visible micro-bleeding on the T2-weighted image. **(7B)** Same patient with the same localization with well visible micro-bleedings (arrows) on SWI. **(7C)** Hypertensive small micro-bleedings in the basal ganglia and in the thalamus. **(7D)** Amyloid angiopathy with a large intraparenchymal bleeding on the left and with multiple superficial micro-bleedings on the right (arrows).

Advanced imaging in cerebrovascular diseases and vascular lesions

Contrast enhanced MR Angiography (MRA) is a well established complementary examination to Doppler sonography and in most cases replacement for digital subtraction angiography by producing high-quality static images.

Time resolved MR Angiography

The latest MRA technique is time resolved or 4D MRA with a time resolution of <0.7 s. This method is capable of capturing the dynamic filling of vessels, thus demonstrating the arterial, capillary and the venous phase of the cerebral circulation, similar to digital subtraction angiography (DSA). Hemodynamic changes caused by arterial stenoses and occlusions can be well

detected and dural arteriovenous fistulas (Figs. 8A, B) or arteriovenous malformations can be easily diagnosed. 4D MRA can contribute to the preoperative evaluation and characterization of a tumor by its degree of vascularization (Figs. 9A–F).

Indication of 4D MR Angiography

- hemodynamic changes due to an arterial stenosis or occlusion
- dural arteriovenous fistulas
- vascular malformations of the brain, face or neck

Advanced MR imaging of inflammatory demyelinating diseases of the central nervous system

Advanced MR techniques have revolutionized the recognition and characterization of white matter disease. MR imaging is required to depict the presence and location of inflammatory lesions within the optic nerve, the brain and spinal cord. The morphology and distribution of lesions along the ventricular lining and perimedullary veins, in juxtacortical and infratentorial location may permit a tentative diagnosis. The acuity of lesions is assessed based on the presence of contrast enhancement or by alterations in the composition of neurometabolites in MR spectroscopy when large and unusual lesions or diffuse white matter changes are present. Follow-up examinations by high resolution MR sequences are of major importance to depict 'dissemination in time'.

3D Fluid-Attenuated Inversion Recovery Sequence (FLAIR SPACE)

provides a higher spatial resolution with 0.8 to 1 mm isotropic slices and inherent contrast resolution in comparison to T2-weighted (Fig. 10A) and proton den-

4D MRA of a dural arteriovenous fistula – high temporal resolution

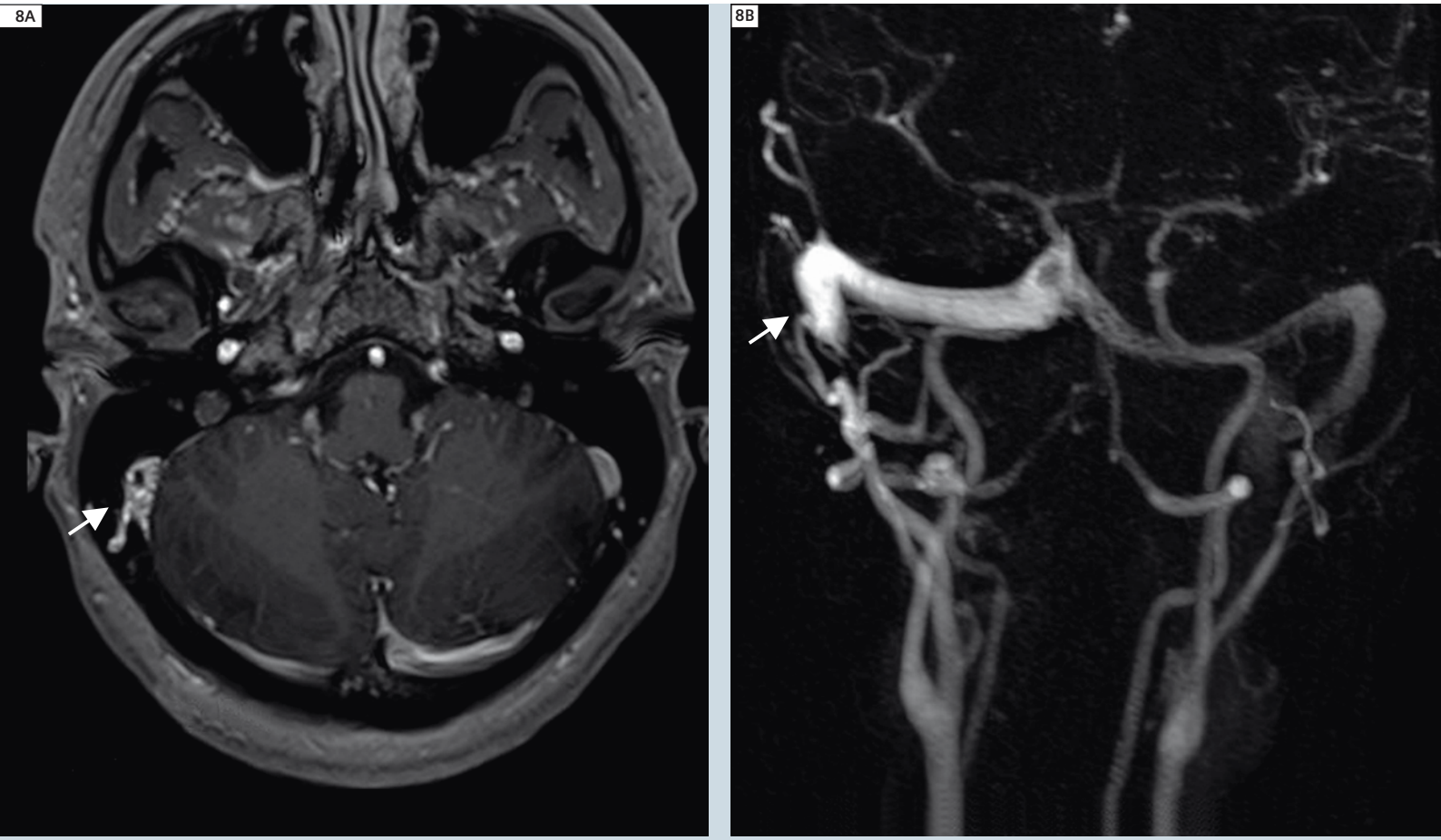

8 **(8A)** Contrast enhanced MRI shows a filling defect of the right sigmoid sinus (arrow). **(8B)** The 4D MRA depicts the arterial filling of the sinus as sign of a dural arteriovenous fistula (arrow) with origin from the branches of the external carotid artery.

sity-weighted images (Fig. 10B) and 2D standard FLAIR sequences. Higher resolution is beneficial due to better recognition of small demyelinating lesions on the initial examination: This holds particularly true in locations such as the brainstem, at the temporal horns, corpus callosum and in juxta- and cortical location. On follow-up examinations, isotropic 3D multiplanar reconstructions facilitate comparison and increase sensitivity to recognize new lesions. High inherent contrast allows to better differentiate cortical and juxta-cortical lesions (Fig. 10C) similar to the 3D DIR sequence. Furthermore 3D FLAIR permits to differentiate acute and old lesions and to distinguish demyelination from perilesional edema and concomitant neurodegenration of white matter tracts.

3D T1 MPRAGE sequence

provides isotropic resolution (0.8 to 1 mm) and thus sensitivity in recognition of small contrast enhancing lesions. High accuracy in detecting focal axonal destruction requires reassessment of the current concept of the frequency and distribution of "dark holes" which are a common finding with this new sequence.

3D Double Inversion-Recovery (DIR) sequence

is characterized by a high sensitivity to depict cortical (Fig. 10D) and deep grey matter involvement due to high signal of the lesions relative to the low white and grey matter signal intensity. 3D SPACE DIR sequence is equivalent to 3D FLAIR SPACE to depict white matter infra- and supratentorial lesions. The sequence appears sligthly superior to recognize focal and generalized cortical grey matter volume loss in the vicinity of subcortical lesions and as a sign of neurodegeneration respectively.

4D MRA for demonstrating tumor perfusion: Diagnostic and preoperative information

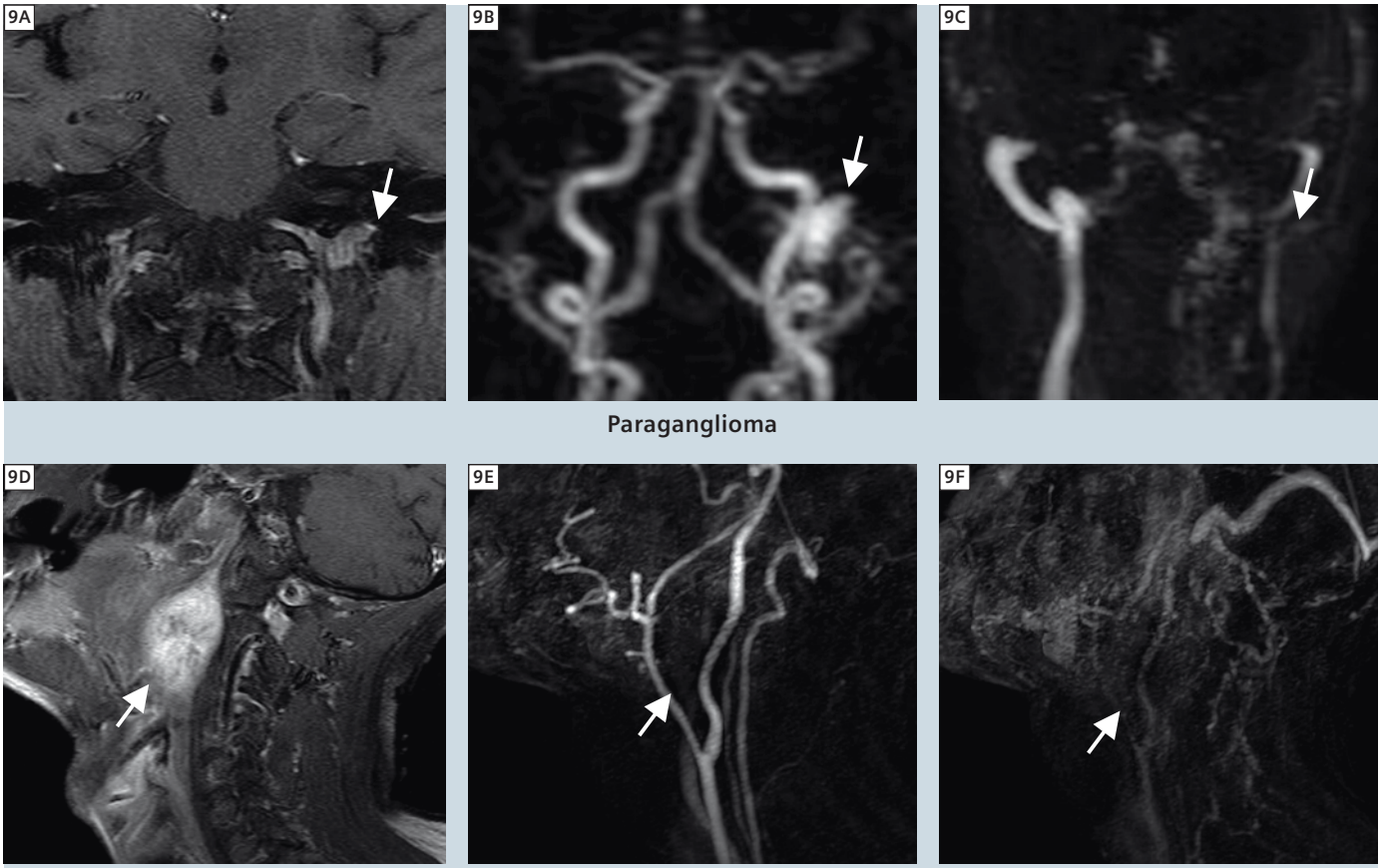

9 The similar location, morphology and signal intensity of a paraganglioma (glomus tumor) and neurinoma (arrows: **9A, C**) makes the differentiation sometimes challenging. The 4D MRA however, demonstrates the difference clearly: a paraganglioma shows an early and strong tumor filling **(9B)**, and early washout in the venous phase **(9C)** whereas a vagal neurinoma **(9D)** exhibits no macrsocopic vascularization in the arterial **(9E)** and venous **(9F)** phase.

New sequences: increased sensitivity to gray and white matter involvement by demyelination

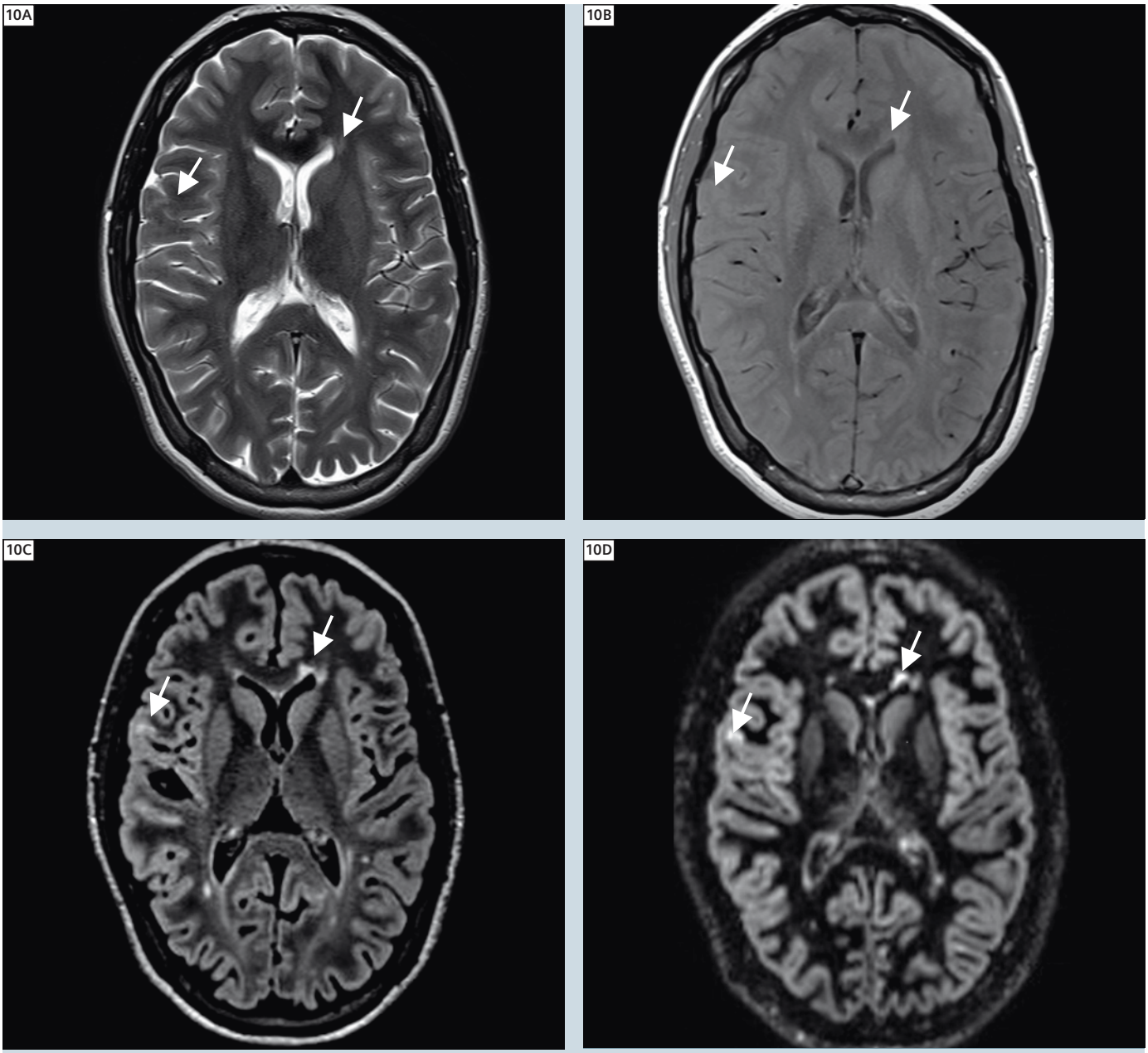

10 Axial T2w **(10A)** and PD images **(10B)** hardly allow recognition of demyelinating lesions indicated by arrows within the forceps minor of the corpus callosum and in intracortical location within the subcentral gyrus. Images are acquired with 3.5 mm contiguous slices. Improved delineation of the corresponding lesions and significant more demyelinating plaques in the 3D FLAIR **(10C)** und 3D SPACE DIR sequence **(10D)** acquired at 1.0 and 1 mm slice thickness respectively.

Inflammatory demyelinating disease: new 3D sequences yield higher diagnostic accuracy, improved clinical and imaging correlation, and more precise follow-up assessment.

Contact
Prof. Bernhard Schuknecht, M.D.
Diagnostic, Vascular and
Interventional Neuroradiology
Medizinisch Radiologisches Institut MRI Zurich
Bahnhofplatz 3
8001 Zürich
Switzerland
image-solution@ggaweb.ch

Siemens Healthcare Publications

Our publications offer the latest information and background for every healthcare field. From the hospital director to the radiological assistant – here, you can quickly find information relevant to your needs.

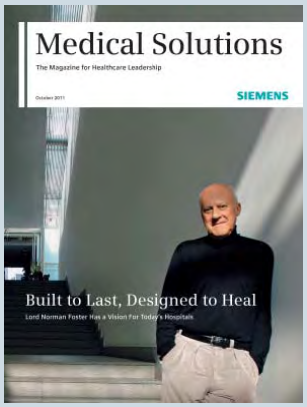

Medical Solutions
Innovations and trends in healthcare. The magazine is designed especially for members of hospital management, administration personnel, and heads of medical departments.

eNews
Register for the global Siemens Healthcare News-letter at www.siemens.com/healthcare-eNews to receive monthly updates on topics that interest you.

AXIOM Innovations
Everything from the worlds of interventional radiology, cardiology, fluoroscopy, and radiography. This semi-annual magazine is primarily designed for physicians, physicists, researchers, and medical technical personnel.

MAGNETOM Flash
Everything from the world of magnetic resonance imaging. The magazine presents case reports, technology, product news, and how-to articles. It is primarily designed for physicians, physicists, and medical technical personnel.

SOMATOM Sessions
Everything from the world of computed tomography. With its innovations, clinical applications, and visions, this semiannual magazine is primarily designed for physicians, physicists, researchers, and medical technical personnel.

Imaging Life
Everything from the world of molecular imaging innovations. This bi-annual magazine presents clinical case reports, customer experiences, and product news and is primarily designed for physicians, hospital management and researches.

For current and past issues and to order the magazines, please visit **www.siemens.com/healthcare-magazine.**

Full Spine Imaging utilizing the Tim User Interface

James Hancock

MRI Radiographer Benson Radiology, Adelaide, South Australia

Planning a full spine with Tim

Positioning technique

- The spine coil is on the table and is plugged in.
- Place the base of the head coil on the table and plug it in.
- Place the base of the C-spine coil on the table and plug it in.
- Position the patient on the examination table with the head comfortably placed in the head coil. Shoulders against the neck coil.
- The triangular leg pad should be placed to reduce back strain.
- Place the top half of the c-spine coil on and clip it into place (this depends on patient size).
- Use the laser to centre on the indicated position on the neck coil.
- Press the isocenter button to move the patient into the magnet bore.

1

1 Patient positioning.

Tim planning

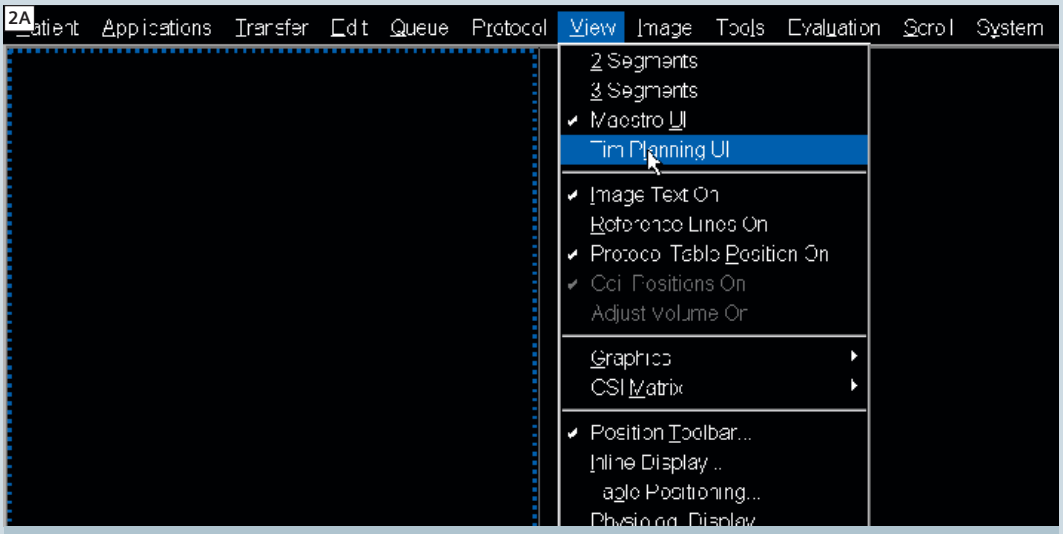

2A Open the Tim Planning Suite from the drop-down menu.

- When performing a full spine examination you need to activate the Tim Planning Suite user interface.

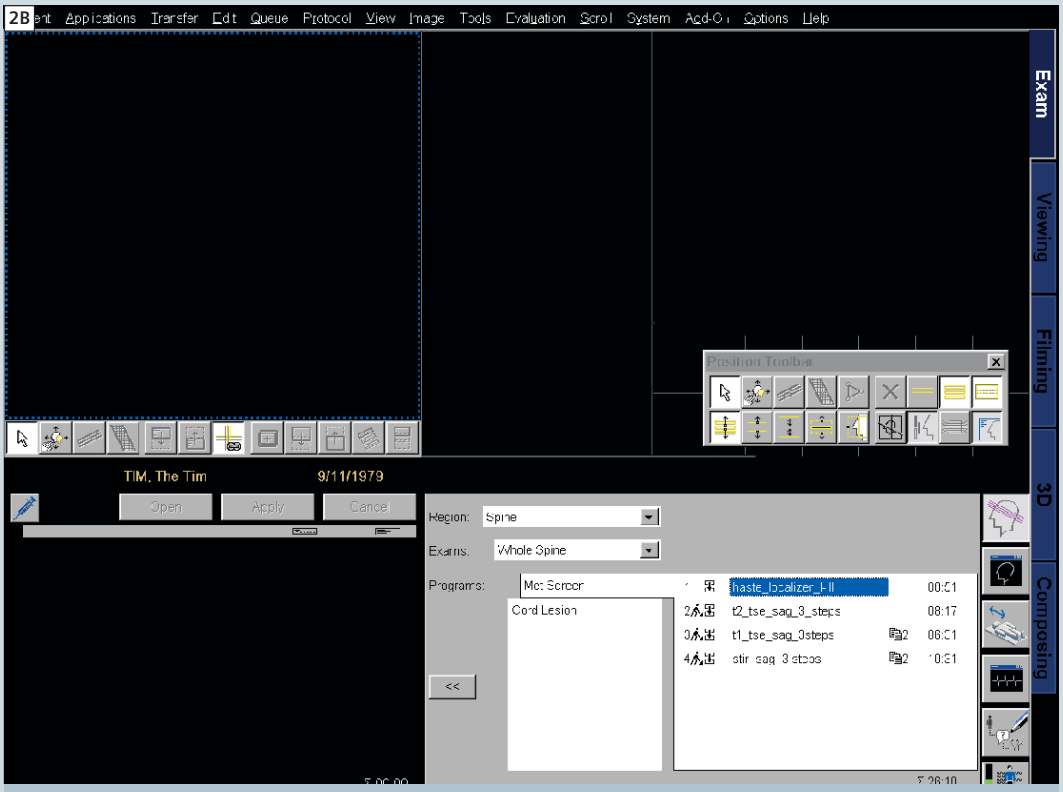

2B The Tim user interface.

- Figure 2B shows the layout for the Tim User Interface. Depending on the clinical indication, at our institution we have two basic protocols saved for full spine imaging: The "Met Screen" protocol can be used for all full spine examinations except in the presence of a potential cord lesion when the "Cord Lesion" protocol should be used instead, as the sagittal slices are thinner and there are more of them.

Running the localizers

- First step to planning is to run the localizers. Drag the appropriate HASTE localizer into the queue for running. This localizer begins in the cervical spine then moves the table before running localizers in the thoracic and lumbar spine. We end up with three localizers in the running queue. Thus it covers three stations. Once complete, Tim composes these three stations into one complete image for the entire spinal cord in both sagittal and coronal planes. These images allow us to plan the setup for the rest of the scans.

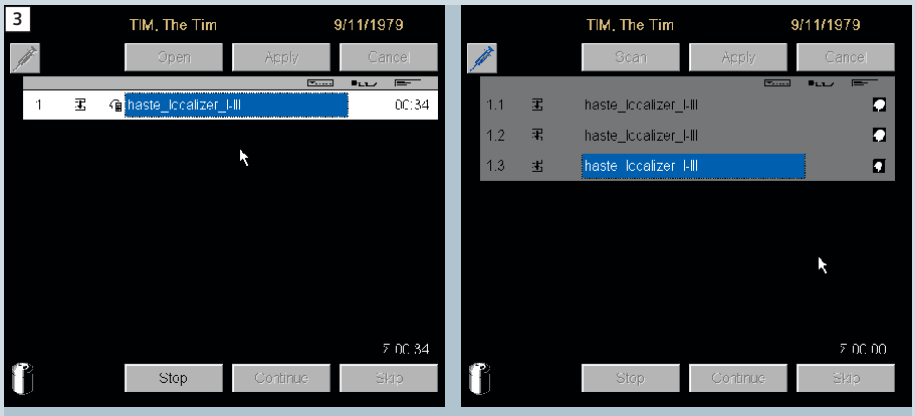

3 The measurement queue with the 3 localizers.

Setting up the correct fields-of-view

- Drag the T2 sagittal sequences across into the queue and open it. This sequence displays three separate sub protocols one for each region of the spine.
- When setting up for a full spine it is best to take a systematic approach.
- Initially set up your FOV to ensure that you are going to cover the entire spine. This involves placing a composed sagittal image of the full spine into the middle rectangular window.
- When setting up your FOV coverage, ensure that "coupled graphics" is on. This can be achieved by right clicking in any of the three boxes and selecting the option.
- With "coupled graphics" on you can then move your FOV and position it appropriately for the correct coverage. See the example in figure 4.

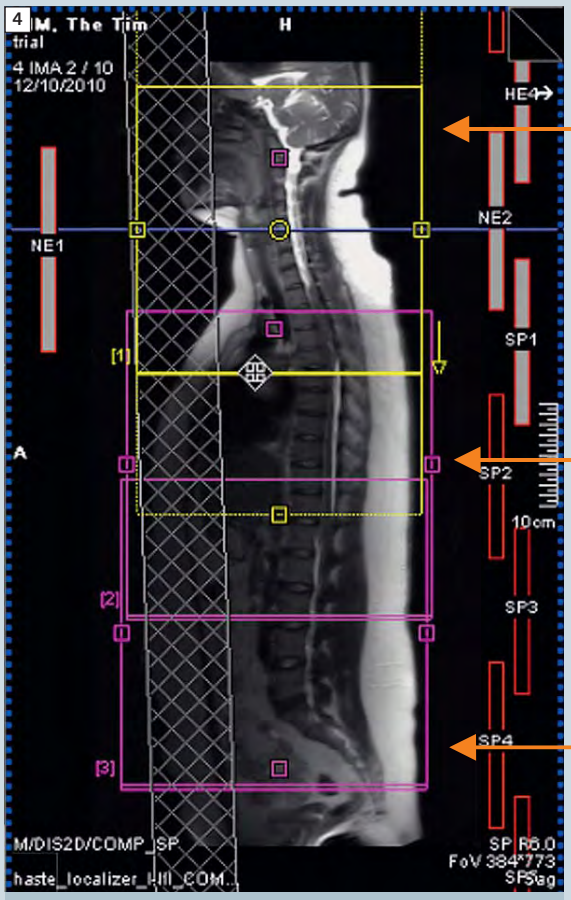

Note the three separate FOV boxes. The upper FOV is yellow, indicating that it is currently active. By utilising "coupled graphics" you can grab and drag all of the three and move them as one. This makes setting up your coverage very easy. Each FOV is also numbered and you can select them by clicking on the little numbers.

4 Easy FOV set up to cover the whole spine.

Setting up the slice positions
C-Spine

- Once the FOV has been set you need to set the slice group locations for each of the subgroups. Applying a systematic approach, begin with the cervical spine.
- The best way to do this is to load your individual C-Spine station localizer and place it into the two square windows. One of these should be a sagittal and the other should be a coronal.
- In the rectangular window place the composed full spine image and choose the coronal orientation.
- Position the C-Spine slice group. Before moving any of the slice groups take "coupled graphics" off. This will allow you to work with and angle an individual group of slices.

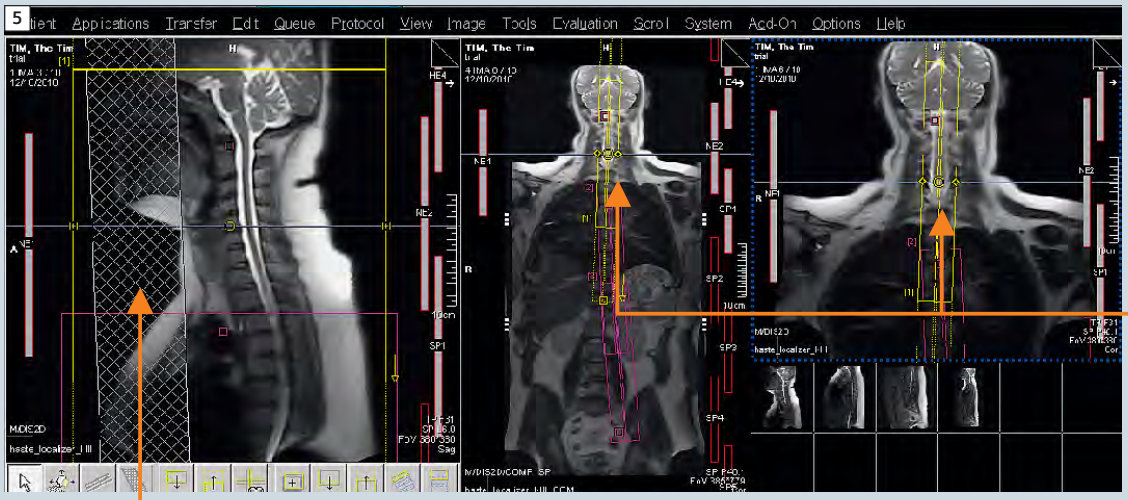

Using the Coronal localizer in these boxes lets you locate your slice group and angle appropriately. With "coupled graphics" off, the changes you make only affect this individual slice group.

By having a sagittal localizer in this box you can keep an eye on your FOV.

T-Spine

- Once you are happy with the C-Spine slice group location you can move on to the T-Spine. Again to set this up follow the same systematic approach.
- Load a sagittal and coronal T-Spine localizer image into the square windows.
- Keep the Full Spine coronal image in the rectangular window.
- To select the thoracic spine subgroup click on the small number 2 displayed next to the second subgroup. You will know you have the group selected as it will turn yellow.
- With "coupled graphics" off you can now proceed to angle the slice group to follow the thoracic spine. You will note that there is some overlap between groups 1 and 2 – this is needed for the composing process later on.

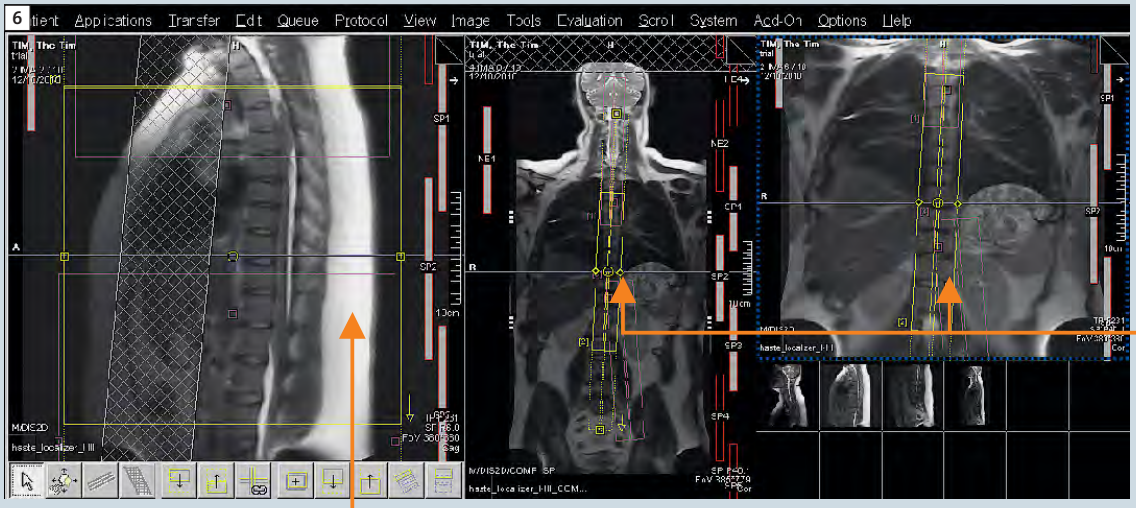

Using the coronal localizer in these boxes lets you locate your slice group and angle appropriately. With "coupled graphics" off, the changes you make only affect this individual slice group.

By having a sagittal localizer in this box you can keep an eye on your FOV.

L-Spine

- Once you are happy with the T-Spine slice group location you can move on to the L-Spine. Again to set this up follow the same systematic approach.
- Load a sagittal and coronal L-Spine localizer image into the square windows.
- Keep the full spine coronal image in the rectangular window.
- To select the lumbar spine subgroup click on the small number 3 displayed next to the third subgroup. You will know you have the group selected as it will turn yellow.
- With "coupled graphics" off you can now proceed to angle the slice group to follow the lumbar spine. You will note that there is some overlap between groups 2 and 3 – this is needed for the composing process later on.

By having a sagittal localizer in this box you can keep an eye on your FOV.

Using the coronal localizer in these boxes lets you locate your slice group and angle appropriately. With "coupled graphics" off, the changes you make only affect this individual slice group.

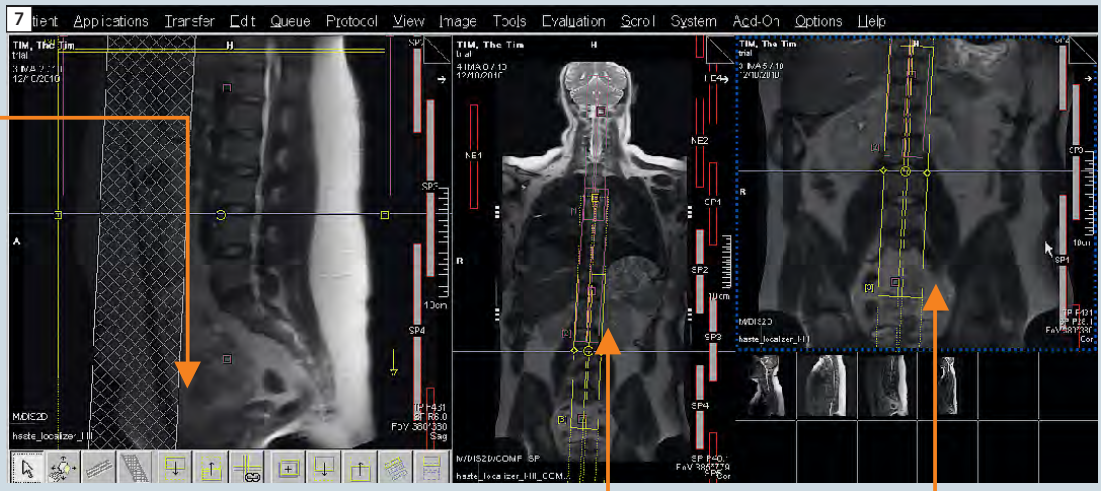

Important notes

- Any presets that you position will affect all three subgroups.
- Changes made to one subgroup will not affect the other groups, so never assume!
- Overlaps are built into the protocols. Be careful when setting up your FOV. Keep these overlaps in place to ensure smooth composing of final images. Thus, when setting up your FOV leave "coupled graphics" on.
- When setting up your slices for the sagittal sequences you will often be angling in the A-P (coronal) plane to follow the spine. Avoid using big differences in angle between one group and another. Too much angle will affect the composing software.
- If the patient is very scoliotic then you can try adding more slices to allow you to cover the region.
- Worst case scenario: Choose your angles for each region of the spine, but you will not be able to compose a full spine image. This may be necessary if the patient is very scoliotic.
- Avoid in-plane rotation as this will cause composing to fail.
- Rotation of subprotocols in the F-H (axial) plane should be avoided. A difference of just 1 degree between subprotocols will cause composing to fail.
- If you need to repeat a region of the spine due to patient movement then you only need to select the region affected by the movement and rerun that particular subgroup. See the example in figure 8.

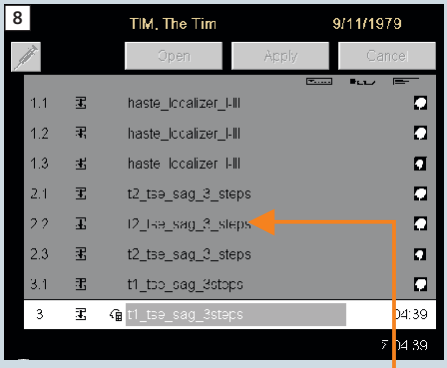

You can see how each subgroup for the T2 sagittals has its own number: 2.1, 2.2, 2.3 etc. Thus if you need to rerun a region simply hold shift and click the one you need to repeat. Drag and drop that region back into the queue. A cross will run through the compose indicator, showing that it is only going to run that one region again.

Performing your axial scanning

- Axial scans can be planned for each individual region as per normal.
- Make use of a nicely composed full spine sagittal image in the rectangular window and an individual region coronal image in one of the square windows to aid in planning.
- With "autocoil select" on wherever you move a slice group, the appropriate coils will be switched on.
- Run the required axial sequences which can be taken from the individual spine protocols as needed.

Using the Compose Task Card

- All full spine sagittal images need to be sent to the composing task card where they are filtered and stitched together. To do this we access the individual sequences from the browser and send them to be composed.

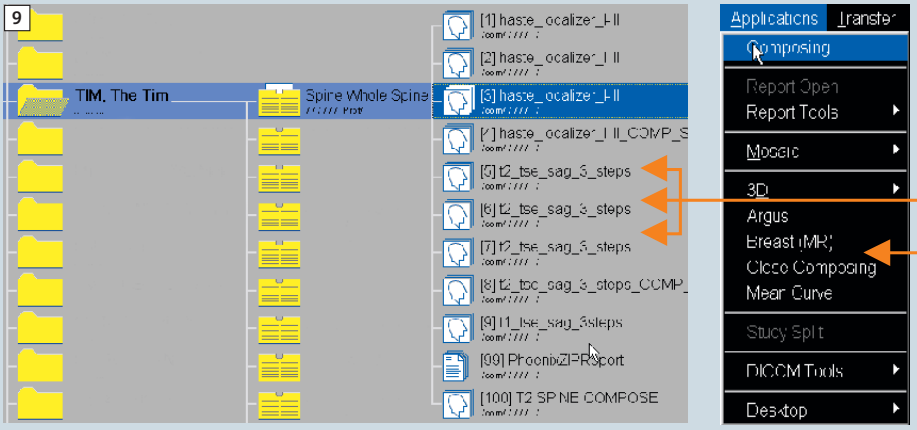

In the browser you select each individual step by holding control and clicking each step with the mouse. This process is performed individually for each type of contrast be it T2, T1 or STIR.

Once you have selected the individual sequences the composing function is found under the Applications menu. Click this and it will open composing.

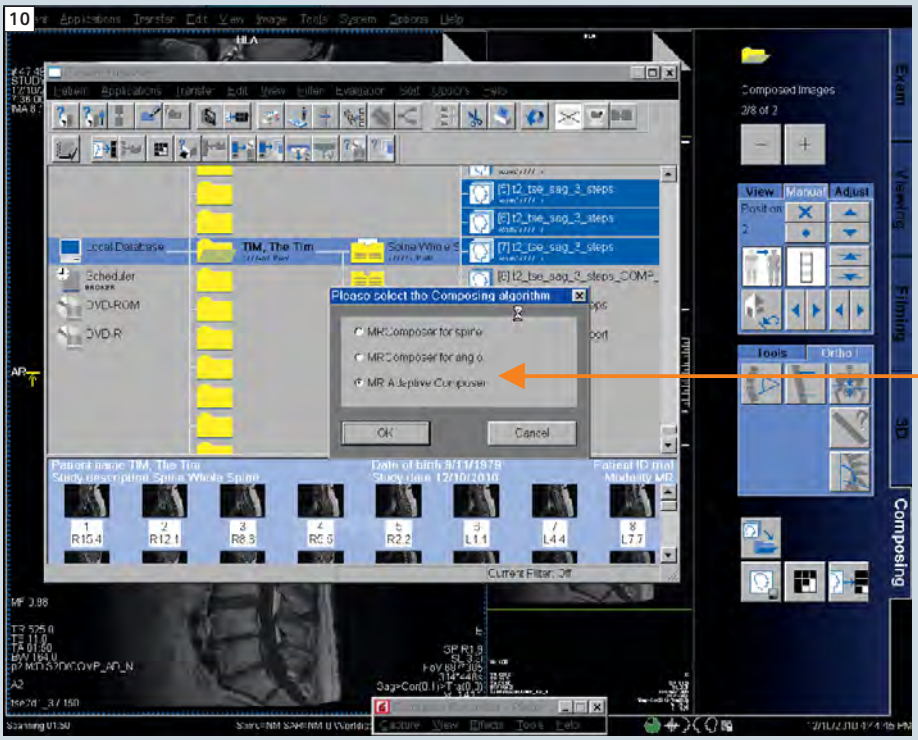

When composing, the software will open and ask you which algorithm you wish to use. Always choose "Adaptive".

Initially your composed images will look like those opposite. We run a normalize filter across the images which helps to smooth out the signal and stitching points.

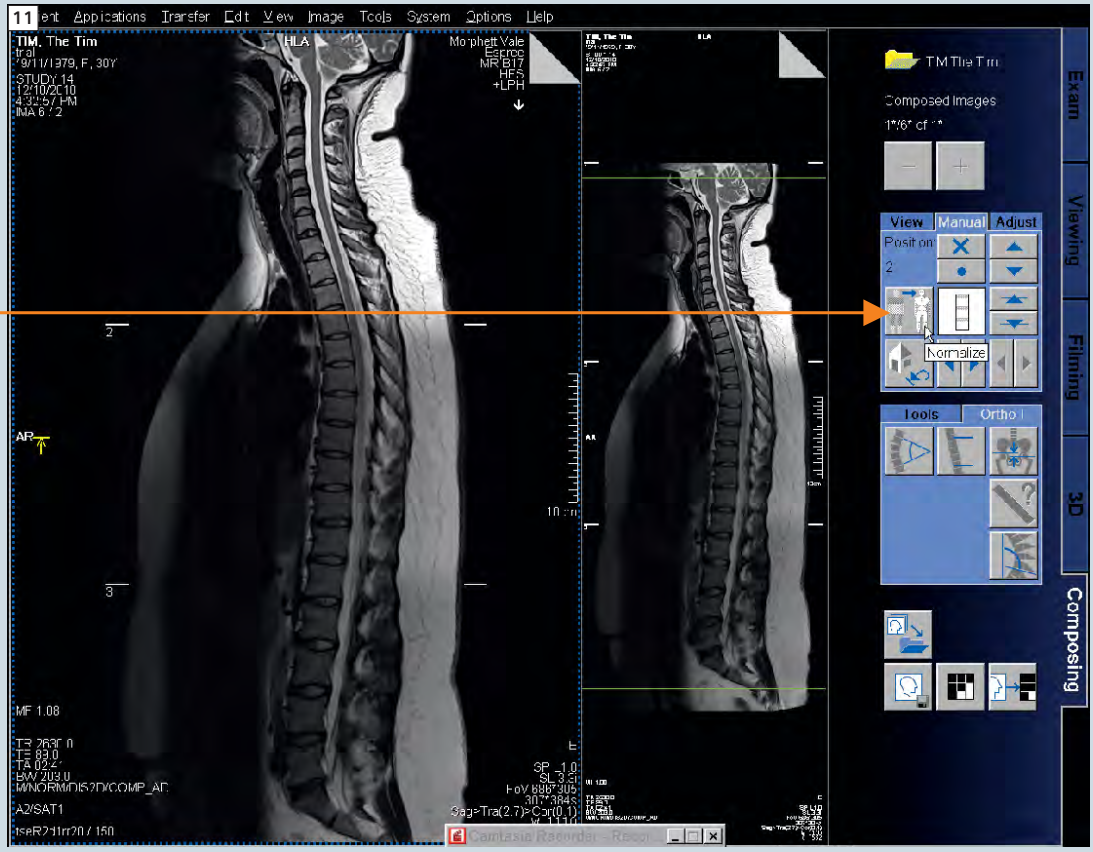

Once the images have been normalized you need to save the entire series, thus select "Save all As" as shown. Give the sequence a name such as T2 SAG Compose, etc. Ensure you save them as a new series. Repeat the process for the other sagittal contrast weightings.

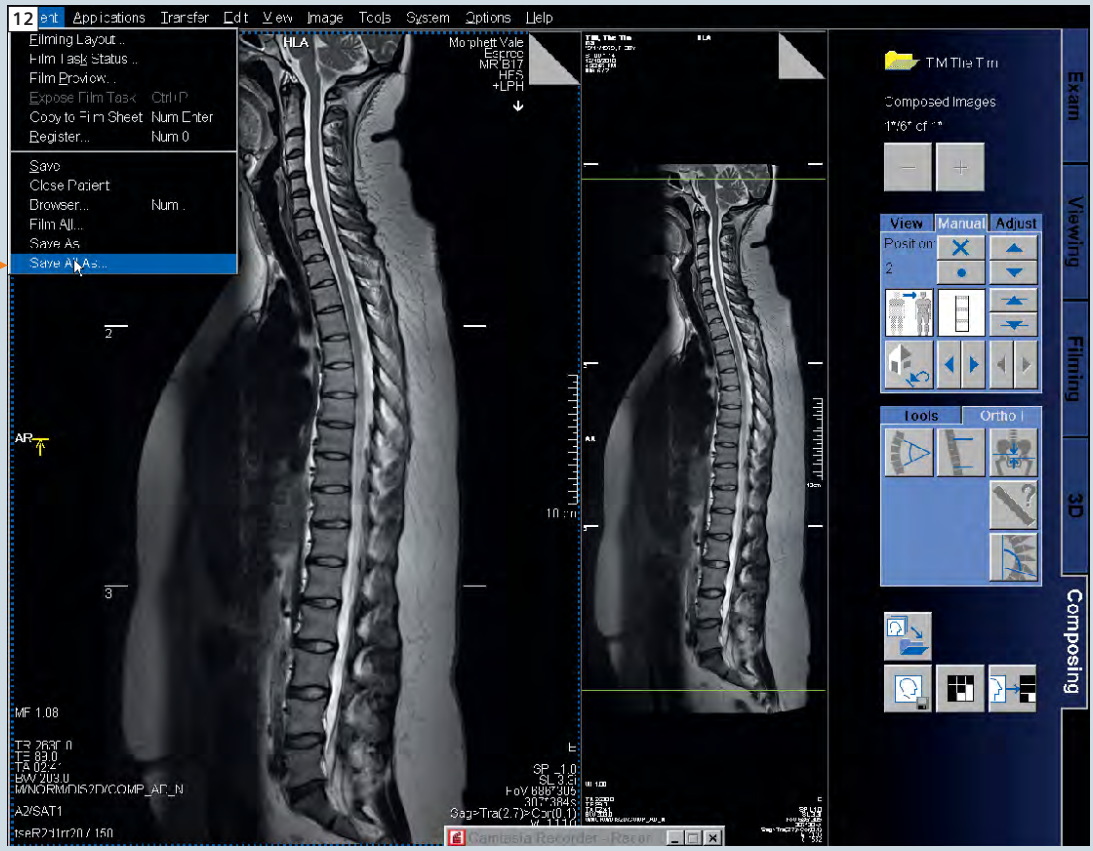

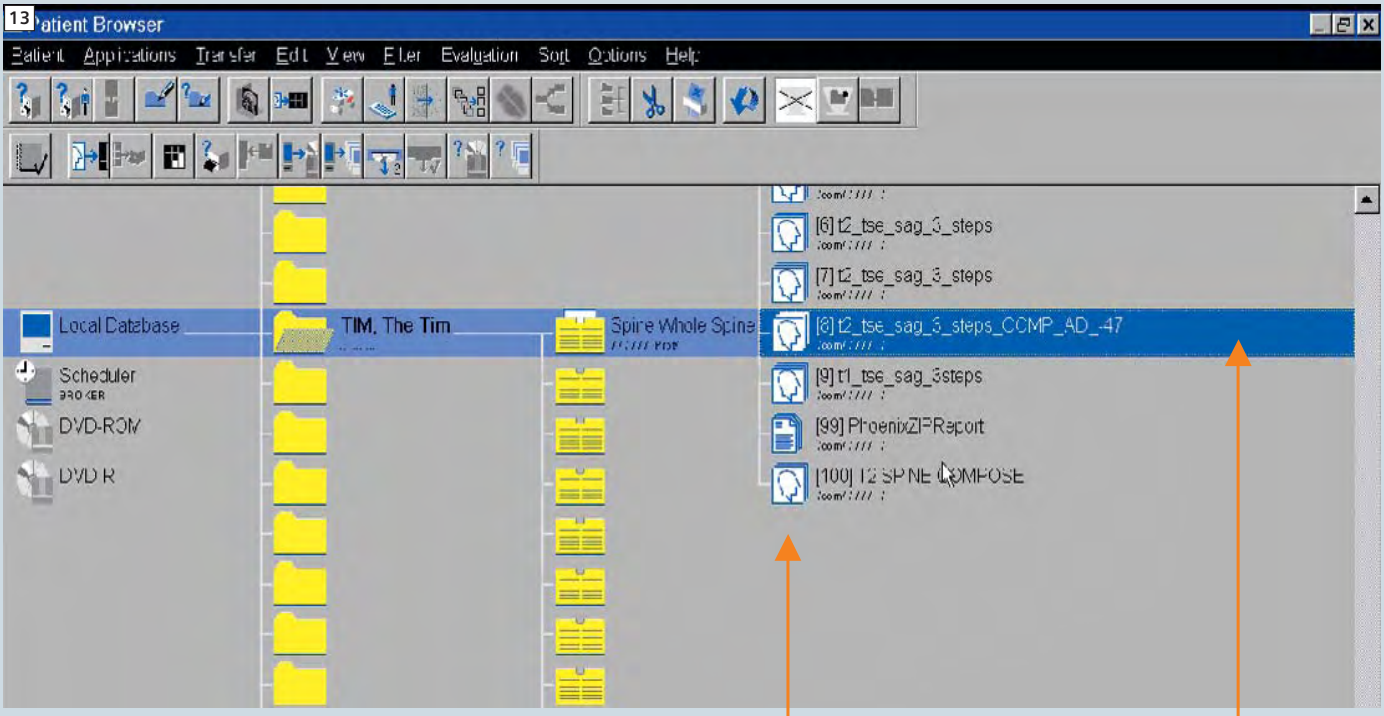

The saved series will appear in the browser and you can then send it to viewing and film it. The initial compose images are highlighted in blue (long red arrow) with our saved series appearing at the bottom of the list (short red arrow). Your composed series can be sent to PACS from here also.

Contact
James Hancock
Benson Radiology
Adelaide
South Australia
James.Hancock@bensonradiology.com.au

Case Report: Traumatic Lesion of the Left Brachial Plexus

Markus Lentschig, M.D.

MR and PET/CT Imaging Center Bremen Mitte, Bremen, Germany

1 MR myelogram.

Patient history

An 18-year-old patient was referred to our institution for evaluation of the integrity of the left brachial plexus 4 weeks after a severe traumatic event. The presented symptoms at the time-point of MR imaging suggested an involvement of the medial and inferior left brachial plexus.

Sequence details

All images were acquired on our 1.5 Tesla MAGNETOM Espree with a combination of the dorsal elements of the head/neck and the spine matrix coils. The imaging protocol comprised a coronal single shot HASTE myelogram, sagittal T1w and T2w TSE, coronal T1w TSE and T2w TIRM, transversal fat saturated T2w TSE and MEDIC and finally 3D T2w TSE (*syngo* SPACE) in coronal orientation. No contrast media was applied in this patient.

Coronal HASTE Myelogram: TR / TE 4500 / 755 ms; FOV 350 x 350 mm; matrix 307 x 384; SL 60 mm; PAT 2; no averages; TA 1.8 s.

Sagittal T2w TSE: TR / TE 4274 / 113 ms; FOV 300 x 300 mm; matrix 314 x 448; SL 3 mm; no iPAT; averages 2; TA 4:13 min.

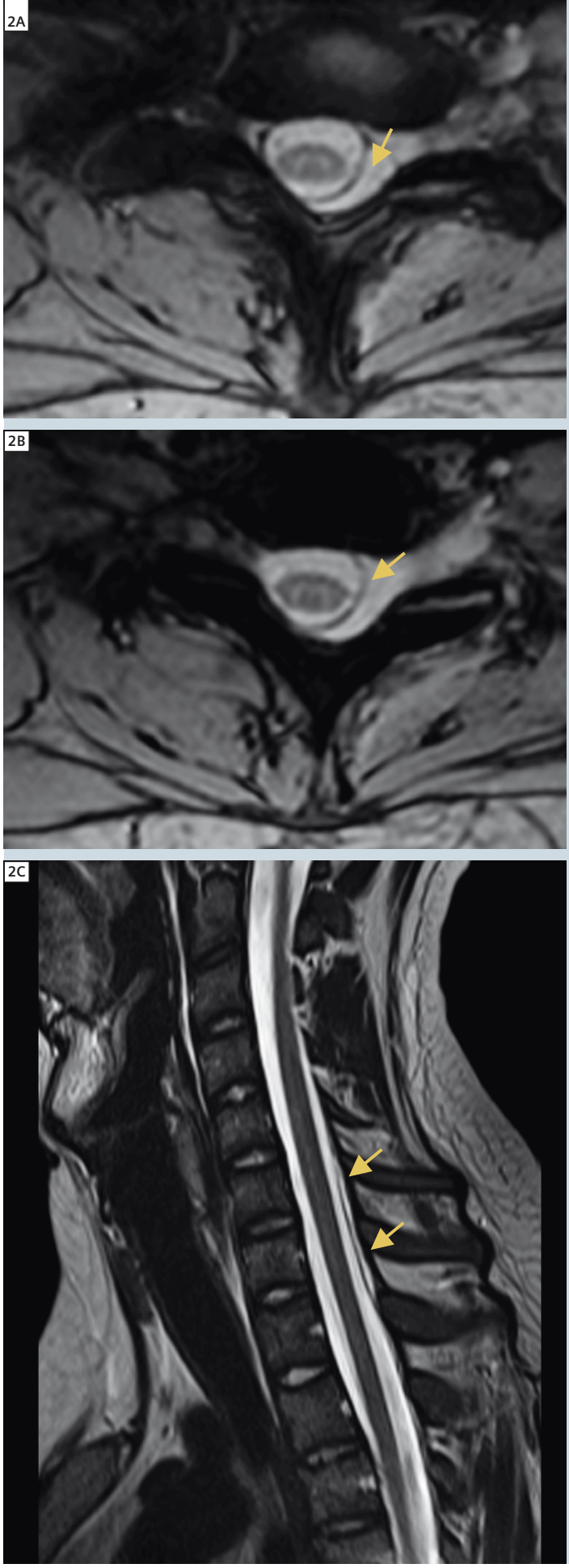

2 A and B transversal MEDIC, C sagittal T2w TSE.

Sagittal T1w TSE (not shown): TR / TE 689 / 11 ms; FOV 241 x 300 mm; matrix 270 x 448; SL 3 mm; no iPAT; averages 3; TA 3:06 min.

Transversal T1w TSE wit spectral fat saturation (not shown): TR / TE 3740 / 93 ms; FOV 303 x 380 mm; matrix 204 x 512; SL 4 mm; no iPAT; averages 2; TA 3:56 min.

Coronal T1w TSE: TR / TE 639 / 20 ms; FOV 309 x 380 mm; matrix 250 x 512; SL 4 mm; no iPAT; no averages; TA 5:20 min.

Coronal T2w TIRM: TR / TE / TI 5940 / 36 / 160 ms; FOV 285 x 380 mm; matrix 192 x 512; SL 4 mm; no iPAT; no averages; TA 5:22 min.

Coronal 3D T2w TSE (*syngo* SPACE): TR / TE 1500 / 173 ms; FOV 280 x 280 mm; matrix 323 x 320; SL 1 mm; PAT 3; no averages; TA 3:56 min.

Imaging findings

A large cystic lesion at the level of the 1st thoracic and 8th cervical nerve root is obvious on the HASTE myelogram (arrowhead in Fig. 1). Accordingly a displacement of the dural border and widening of the subdural space is also obvious (compare transversal T2w MEDIC images in figures 2A, B). A displacement of the spinal dural mater (Fig. 2) can be found on transversal and sagittal T2w images. Edema of the left

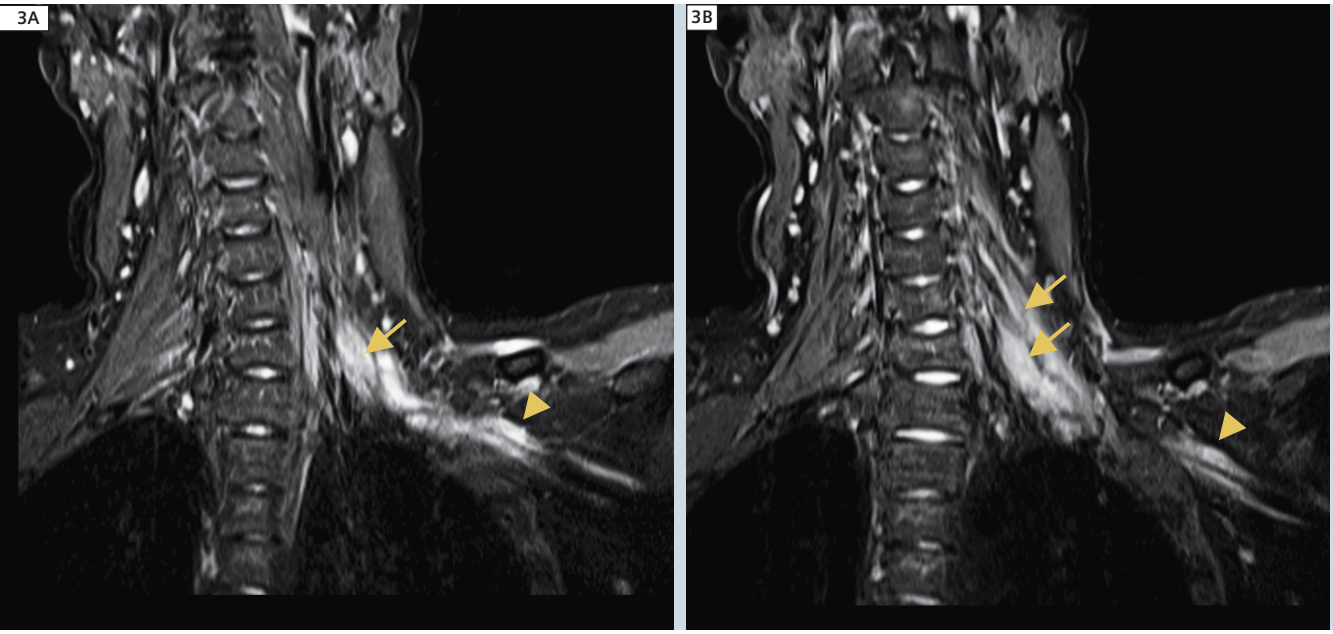

3 Coronal TIRM.

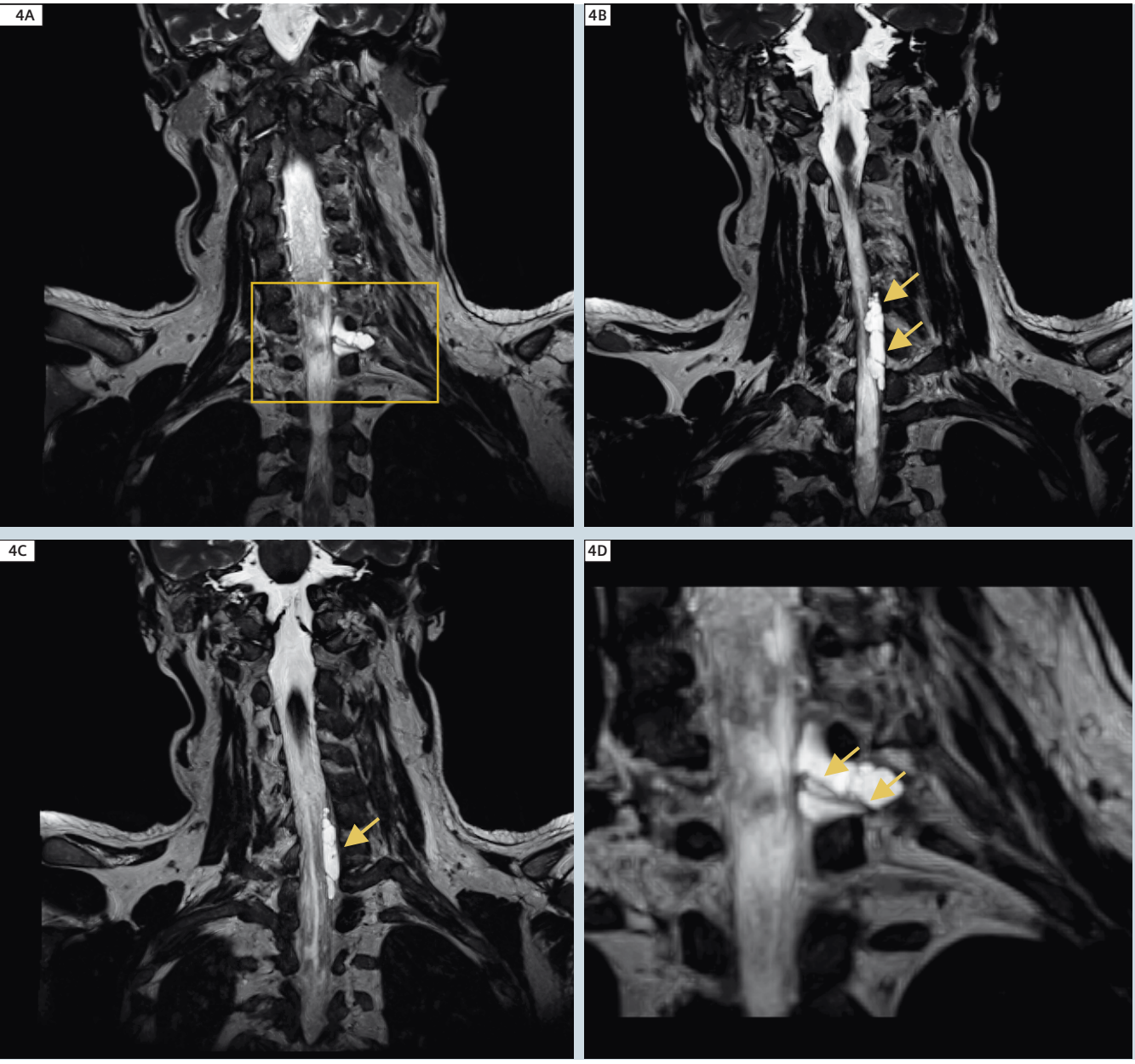

4 A, B, C coronal 3 mm thin-slice MPR based on a 3D T2w TSE scan (*syngo* SPACE).

D: magnified detail of Fig. 3A.

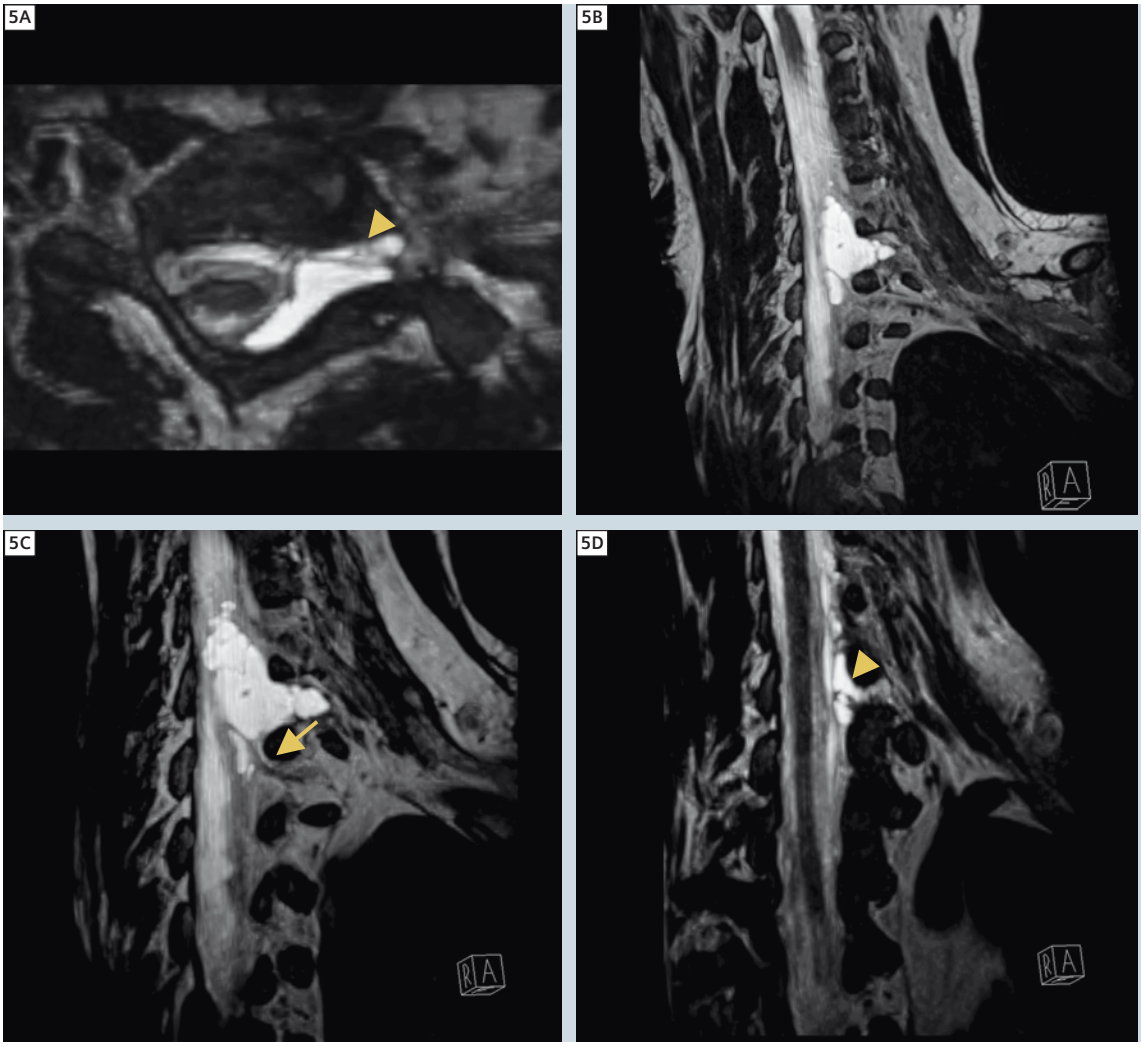

5 Oblique transversal **(A)** and coronal **(B–D)** 3 mm thin-slice MPR based on a 3D T2w TSE scan (*syngo* SPACE) for detailed visualisation of the nerve roots.

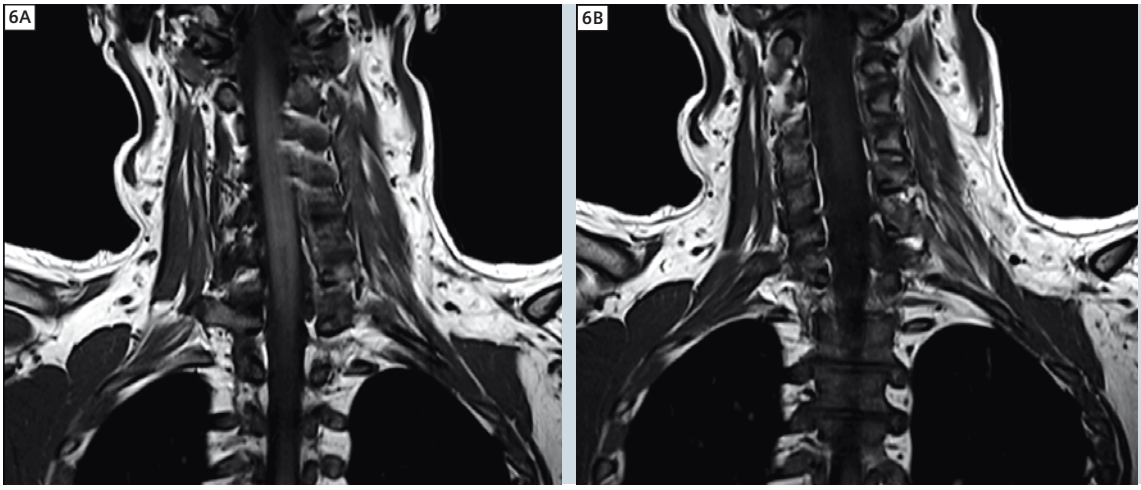

6 Coronal T1w TSE.

cervical muscles (arrows Figs. 3A, B) and of the inferior and medial trunc of the brachial nerve plexus (arrowhead Fig. 3) is clearly delineated on the coronal T2w TIRM images. Best visualized in the 3D T2w TSE (Figs. 4, 5), a nearly complete rupture of the 8th cervical nerve root is the obvious diagnosis, together with an affection and at least partial rupture of the 1st thoracic and 7th cervical nerve root. There is a regular alignment of the vertebra bodies and no evidence of a fracture. There are regular signal intensities of the myelon on the T1w and T2w images; there is no larger hemorrhage within either the myelon or the nerval plexus.

Contact
Markus G. Lentschig, M.D.
MR and PET/CT Imaging Center Bremen Mitte
Sankt-Juergen-Str. 1
28177 Bremen
Germany
www.mr-bremen.de

Parallel Transmit Technology for High Field MRI

Lawrence L. Wald[1, 2, 3]; Elfar Adalsteinsson[1, 3, 4]

[1]Athinoula A. Martinos Center for Biomedical Imaging, Department of Radiology, Massachusetts General Hospital, Boston, MA, USA
[2]Harvard Medical School, Boston, MA, USA
[3]Harvard-MIT Division of Health Sciences and Technology, Boston, MA, USA
[4]Department of Electrical Engineering and Computer Science, Massachusetts Institute of Technology, Boston, MA, USA

Introduction

The success of parallel reconstruction methods and their impact on image encoding has sparked a great deal of interest in using the spatial distribution of transmit coils in an analogous fashion. Namely, by breaking down the transmit field into multiple regions each controlled by a separate transmit channel, spatial degrees of freedom are created that allow the spatial information in the array to be exploited in the excitation process. While a homogeneous birdcage-type body-coil driven by a single RF pulse waveform has served the MR community well, it does not possess spatial degrees of freedom, and subsequently works best for uniform excitations. Parallel excitation arrays and the potential to utilize the spatial information in an array during RF transmission offer the possibility to move beyond the uniform slice-select excitation, and to generate spatially tailored RF pulses; excitation pulses with a carefully controlled spatially varying flip angle or excitation phase that can mitigate artifacts or isolate specific anatomy.
While the concept of spatially tailored excitation pulses has been known for some time, the implementation of such pulses is largely impractical on conventional single-channel excitation systems, and only by introducing the additional spatial degrees of freedom in a transmit array do they achieve practical durations for clinical imaging. An early application of spatially tailored parallel excitation was to mitigate the non-uniform flip angle problem created by RF wavelength effects at high field (Fig. 1). These non-uniformities arise when the wavelength of the RF approaches the dimension of

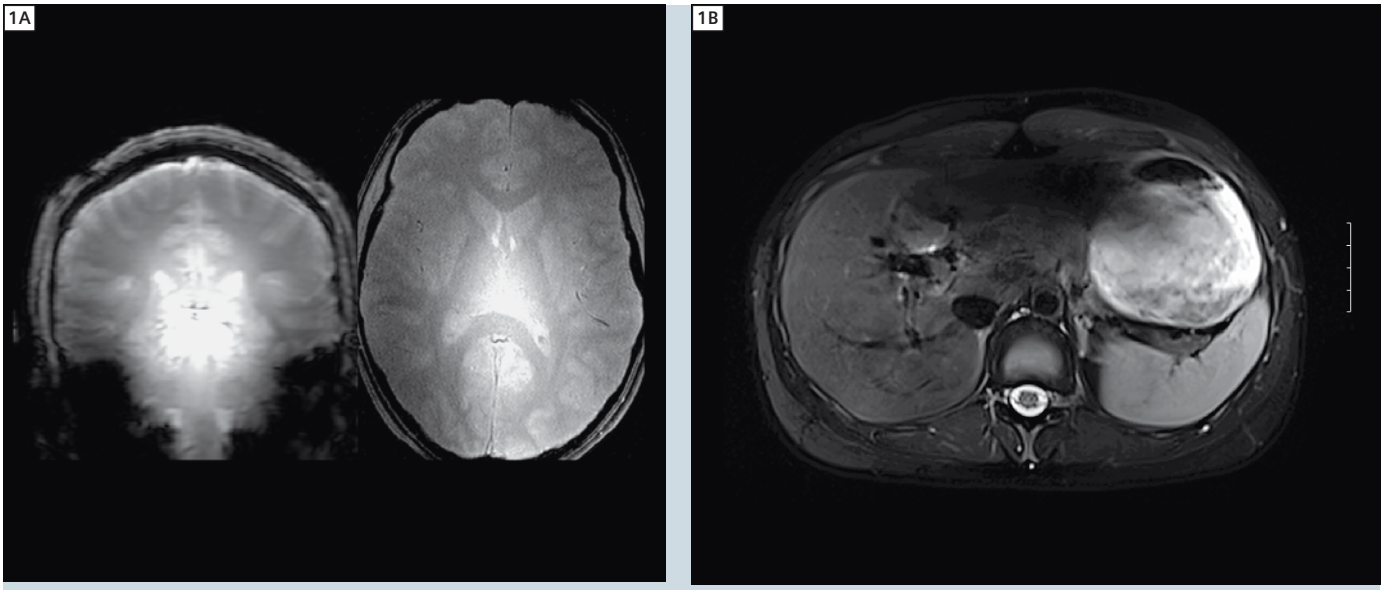

1 Flip angle inhomogeneity resulting from wavelength effects in the brain at 7T (central brightening) and liver at 3T (drop-out). Spatial variations in the transmit efficiency, and therefore the flip angle, are more problematic than the receive inhomogeneities since they lead not only to image shading, but more importantly, image contrast alterations.

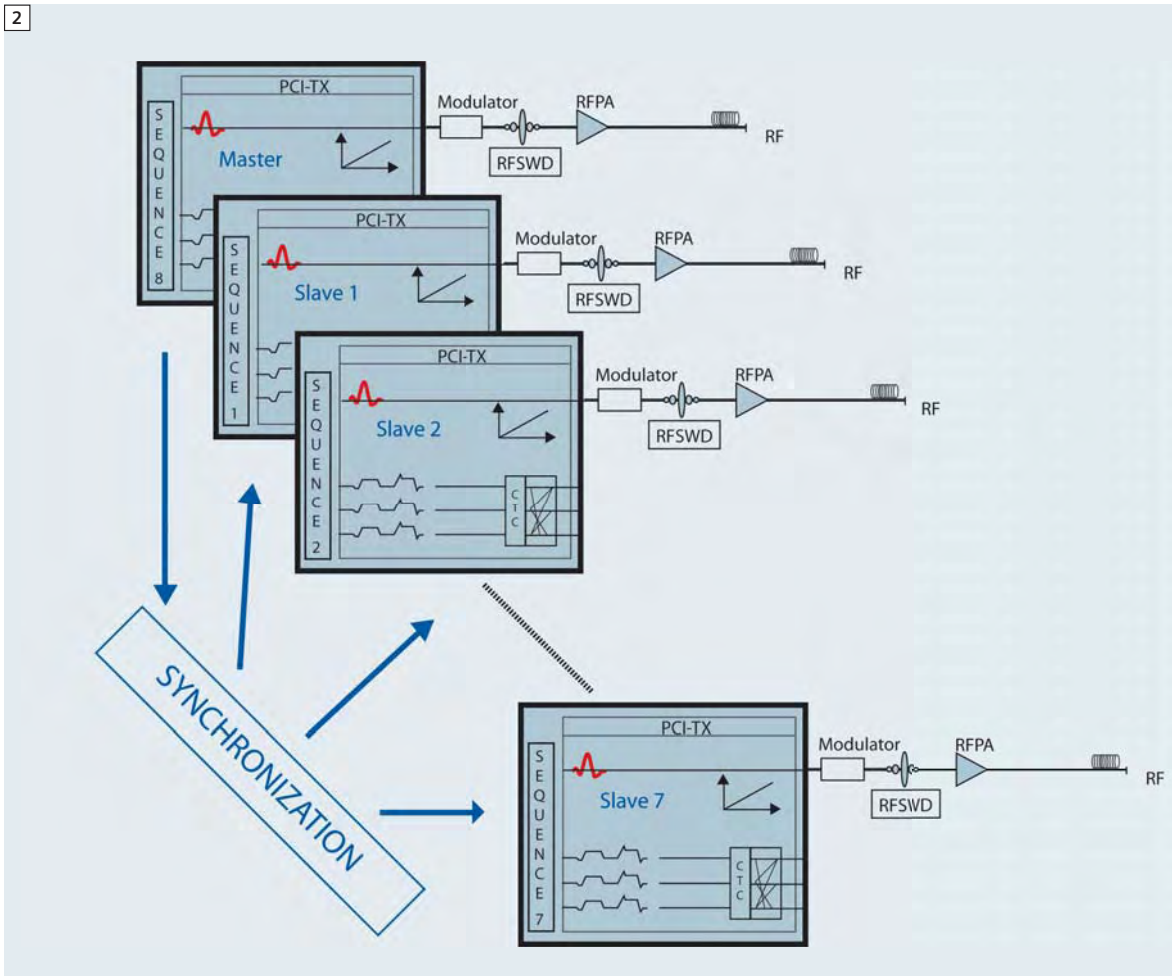

2 System schematic of the 8-channel transmit system. *(Figure courtesy of U. Fontius, Siemens Healthcare.)*

the human head or body and create destructive excitation field interference among sections of a conventional transmit coil. This is most noticeable in the head at 7T where a strong center brightening is a typical feature (perhaps more properly termed peripheral darkening) and in the body at 3T where shading is seen near large regions of non-fatty tissue in the abdomen. Unlike detection inhomogeniety that manifests primarily as image intensity shading, a non-uniform transmit B_1 field results in spatially dependent tissue contrast and therefore reduced diagnostic power, which cannot be recovered with an image normalization scheme. A spatially tailored excitation mitigates this problem by anticipating the flip angle inhomogeniety and compensating for it in the spatial profile of the excitation. Once the technology is in place for spatially tailored RF excitations, the ability to generalize excitation profiles beyond the slice-select pulse offers many exciting opportunities for selective excitations of anatomically tailored volumes. An anatomy-specific excitation could potentially reduce image encoding needs (e.g. for cardiac or shoulder imaging) by reducing the effective field-of-view, it could enable more accurate CSI exams in tissues with many interfaces like in the prostate, and allow selective spin-tagging excitations (potentially allowing vessel territory perfusion imaging), or simply provide clinically useful but non-traditional excitations such as curved saturation bands for the spine or brain.

In this article we review some of the progress which has been made with a prototype 8-channel parallel transmit system integrated into a Siemens MAGNETOM Trio, A Tim System, and a 7 Tesla MAGNETOM system. We discuss some of the recent advances in calculating parallel transmit RF pulses for spatially tailored excitation and show examples of B_1 transmit mitigation at 3T and 7T. Further, we describe some of the recent advances in methodology as well as some of the outstanding issues that must be overcome for routine application.

Experimental Setup

Flexible delivery of independent RF waveforms to each channel of the array is needed to realize the full potential of parallel transmission. Additionally, fast gradient trajectories are required during the RF pulses to modulate the spatial profile of the excitation. Since eddy current compensation is performed during the RF waveform generation using knowledge of the gradient history, each RF channel

needs to be fully integrated into the full waveform generation system of the scanner. To achieve this, a prototype 8-channel transmit system was set up in a master-slave configuration with each channel capable of running an independent pulse sequence, and importantly, independent B_0 eddy current compensation. Finally each channel utilized a separate RF power amplifier (8 kW each in the 3T case and 1 kW each in the 7T case) and fully independent SAR monitoring on each channel.

Which RF transmit array configurations capture the maximum ability to capitalize on the parallel nature of the excitation? This question is central to the optimal design of a flexible parallel excitation system and remains an open research problem. Two principles guide our design of the array configuration:

- obtaining the maximum benefit from the limited (expensive) number of excitation channels, and
- retaining the simplicity of birdcage-like excitation in one channel.

These two goals are elegantly achieved when a so-called "Butler matrix" [1] is inserted in the path from the RF amplifiers to the coil elements to drive a ring of excitation coils on a cylindrical former. In contrast to a direct drive of the coil elements by the RF amplifiers, the Butler matrix transforms the phase relationship of the array elements so that each RF excitation channel drives not just a single RF element but influences all of them in a specific (and familiar) relationship; namely the spatially orthogonal modes of a birdcage coil. The spatial patterns of these modes and the phase relationships needed to generate them are well known from birdcage theory [2], and when achieved, have several benefits. Firstly, it allows the "master" channel of the array to operate as a uniform birdcage-like excitation coil. Although at high field the so-called uniform birdcage mode generates significant field variation (one of the original motivations for parallel TX technology), it is useful in

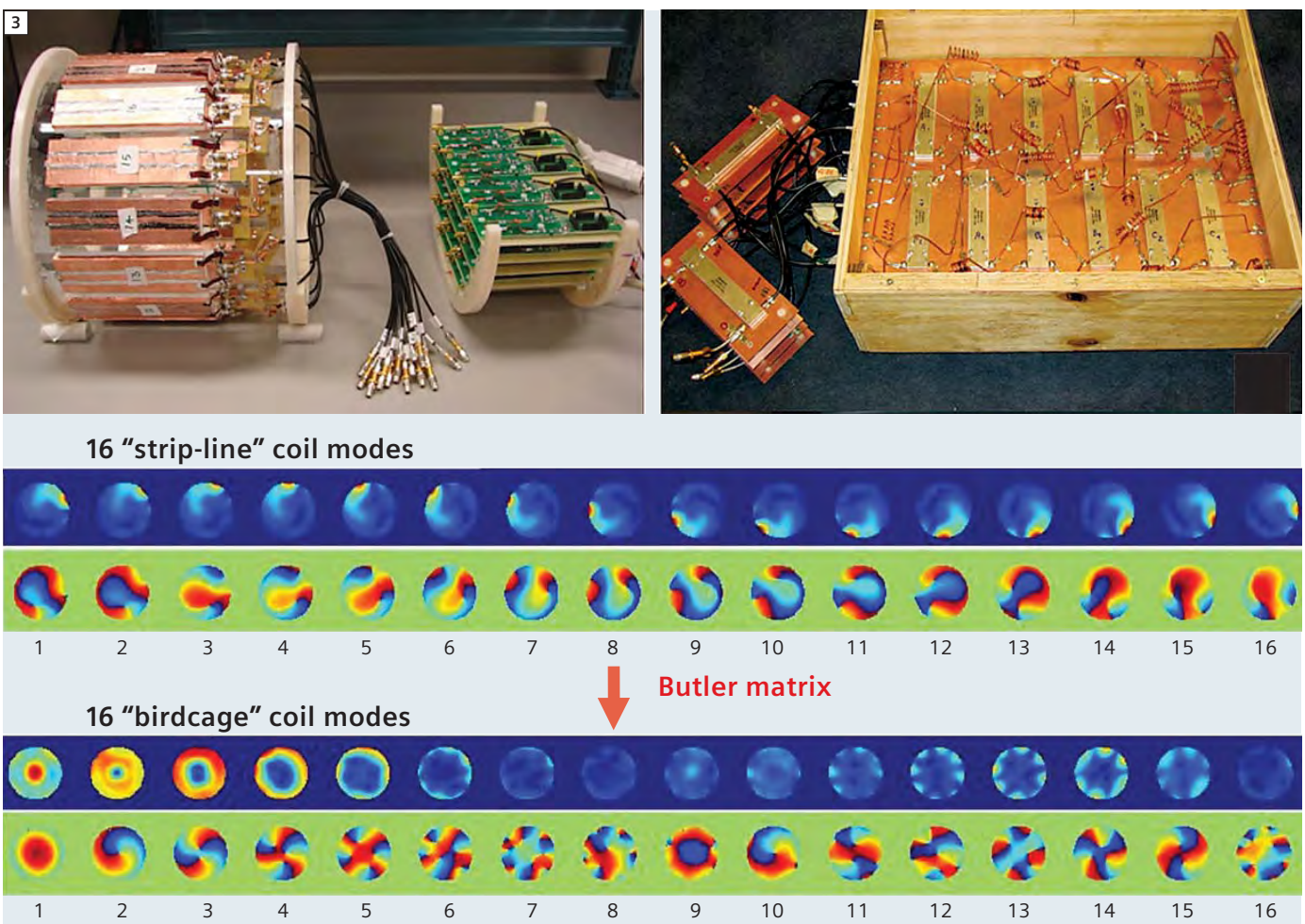

3 A 16-channel 7T strip-line array for the head (upper left) and a 16 x 8 Butler matrix (upper right). Below are the magnitude and phase B_1 maps of each of the 16-channels for both the "strip-line" basis set, and the "birdcage" basis set. While excitation ability is roughly equally divided among the strip-line modes, it is concentrated in a few valuable modes in the birdcage basis set. We can choose which 8 modes to drive based on their performance. *(Figure courtesy of Vijay Alagappan, MGH.)*

practice to have one of the channels operate from this well established and efficient starting point. The other channels then span progressively higher-order modes of the birdcage coils with their spatially specific amplitude and phase variations.
Since the Butler matrix achieves these modes through simple linear combinations, at first blush it would appear that this "basis set" of excitation patterns would be no better or worse for accelerating spatially tailored excitation than simply driving the array of elements one at a time. The superiority of the Butler matrix driven array becomes apparent when only a subset of the array modes is chosen for excitation. In practice this allows the benefit of a larger array to be captured in a system with fewer transmit channels (i.e. lower cost) by capturing a majority of the transmit efficiency and acceleration capabilities in a valuable subset of the channels (and ignoring the less valuable channels). We explored this "array compression" principle by driving a 16-channel stripline array for 7T head transmit with a 16 x 16 Butler matrix connected to the 8-channel transmit system [3], and demonstrated the theoretically predicted tradeoffs. The excitation configuration that integrates a Butler matrix in this manner allowed us to pick and chose among the modes of a 16-channel array and drive only the best subset of the 16 available modes with our 8 transmit channels. The choice of the optimum 8 birdcage modes compared to 8 strip-line elements allowed a flip-angle inhomogeneity mitigating excitation to achieve a 43% more uniform excitation and 17% lower peak pulse power in a water phantom at 7T [3].

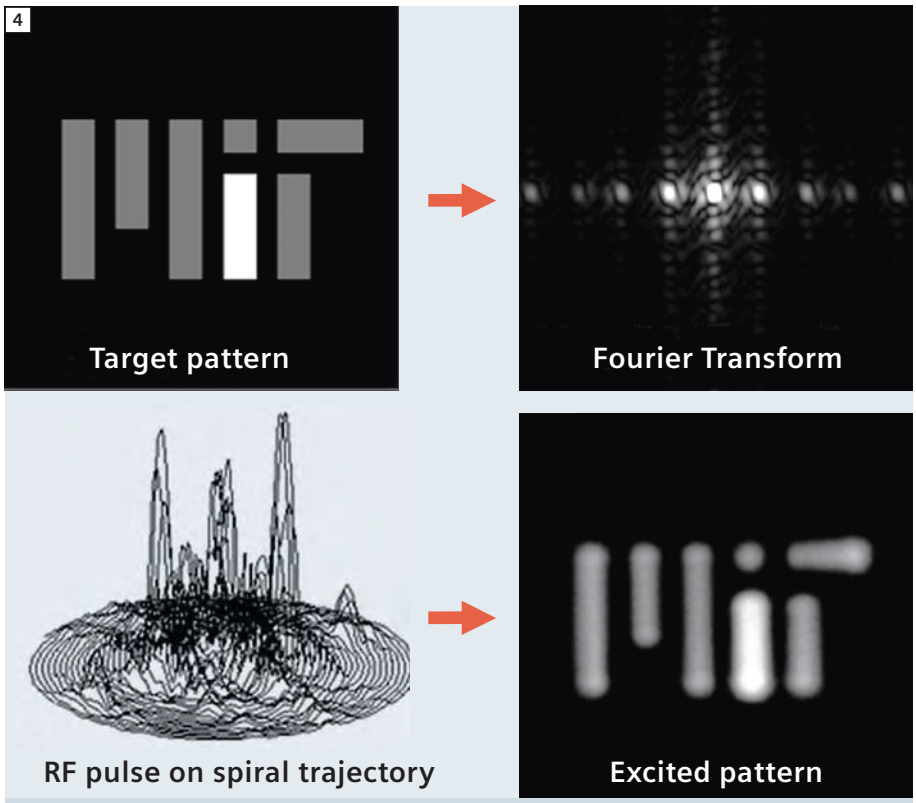

4 RF pulse design for a 2D spatially tailored excitation. Use of parallel transmit allows the spiral gradient trajectory to be accelerated. In this case a 4 x acceleration of the spiral trajectory allowed the excitation pattern to be achieved with a 2.4 ms duration RF pulse.
(Figure courtesy of Kawin Setsompop, MGH, MIT.)

Spatially tailored RF excitation

RF excitations appropriately modulated in amplitude and phase during time-varying gradients offer the potential of spatially tailored RF phase and amplitude in the excitation [4]. Although such pulses have been demonstrated for many years, the lengthy encoding period needed duration of these pulses (as long as 50 ms) has precluded their routine use. Parallel transmission addresses this limitation by accelerating the excitation encoding gradient trajectory analogously to how parallel receive provides unaliased images with an accelerated encoding trajectory [5, 6]. A practical goal is to achieve 3D excitation pulses in less than 5 ms with a spatial profile that can mitigate the observed B_1 pattern in the head or body. This short duration is needed to be useful in common anatomical imaging sequences such as TSE, MPRAGE and FLASH.
Shaping the 2D spatial flip-angle distribution of an RF excitation requires modulated RF amplitude and phase while the gradients trace an excitation k-space trajectory, typically a spiral or echo-planar path. In practice, we first choose a target magnetization map, which is proportional to the flip angle map for small flip angles. For example, the target magnetization map might be a uniform flip-angle distribution or a selected region around the anatomy of interest (for zoomed imaging). The calculation of the corresponding RF waveform is greatly simplified in the low flip angle case where it can be reduced to a k-space or Fourier analysis [4]. The RF excitation during such a gradient traversal is viewed as a series of short, small flip angle excitations. The phase and amplitude of these small RF pulses is altered so that the deposition of RF energy in the "excitation k-space" matrix is the Fourier transform of the desired spatial flip-angle map. In parallel transmit, the pulse duration is significantly reduced since an accelerated, under-sampled excitation k-space trajectory is used. The missing information is provided by incorporation of the spatial profiles of the multiple transmit array elements in the design process so that an unaliased excitation pattern is achieved.

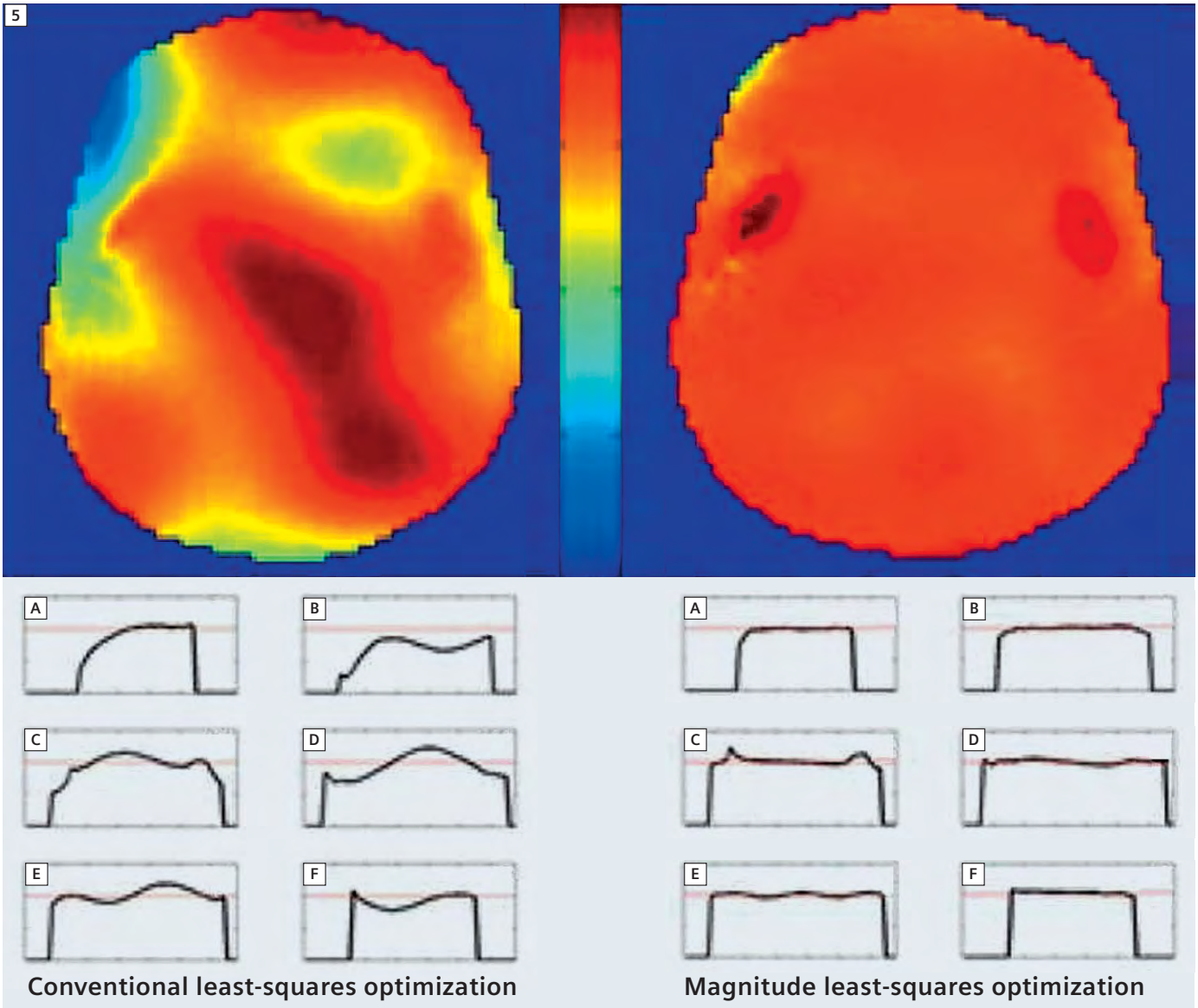

5 Measured flip-angle profiles for a 2.4 ms duration, flip-angle mitigating pulse (uniform target profile) for 7T demonstrated in a head-shaped water phantom. The MLS optimization achieves nearly 4 fold lower error compared to the conventional least-squares optimization. *(Figure courtesy of Kawin Setsompop, MGH, MIT.)*

Regularization of Specific Absorption Rate (SAR) and relaxation of phase constraints

A critical observation about the parallel transmit pulse design problem is that there are many different solutions for the RF pulses that achieve a very similar fidelity to the target excitation pattern. Knowing this, it is beneficial to choose a solution which produces a "close enough" pattern but minimizes SAR. This can be achieved by explicitly penalizing pulse amplitude when solving for the optimal pulse shapes, thus resulting in a significantly lower global SAR with little loss of excitation pattern fidelity [7].

Another important observation that yields significant payoff in the RF design is that the vast majority of MR applications ignore the phase in the final image (only magnitude images are viewed). In this case, the excitation can tolerate a slow phase roll across the FOV with no impact on the final image. We have capitalized on the relaxation of the phase restraint by developing a "Magnitude Least Squares" (MLS) algorithm for solv-

ing the parallel transmit pulse design optimization [8]. In this scheme, the algorithm attempts to achieve the target excitation pattern in magnitude, but allows slow phase variations across the FOV. The relaxed constraint allows a higher fidelity in the magnitude pattern or a lower pulse power (i.e. low global SAR). Figure 5 compares the MLS result for a slice-selective excitation with uniform target flip-angle distribution to the conventional Least Squares optimization. A two-fold improvement in target magnitude fidelity was achieved with similar SAR. Conversely, the same target fidelity could be achieved with a ~2 fold reduction in SAR.

3D shaped excitations

Extending accelerated spatially tailored pulses to general 3D shapes requires covering k-space in 3 directions and is consequently very time consuming. Nonetheless, full 3D excitation is required for many applications, including adding in-plane flip-angle modulation to the traditional slice-selective excitation. We explored the capabilities for these 3D shaped excitations by using a variant of the echo-volume or "spokes" trajectory. This design class of RF excitation pulses can be viewed as multiple slice-selective RF pulses in z that are played out with different amplitude and phase modulations for each (k_x, k_y)-location, providing a conventional slice-selection in z, but with spatial modulations in the image plane, (x, y). Since the conventional axial slice select gradient can be viewed as a line segment in excitation k-space along k_z, multiple such lines look like a collection of spokes orthogonal to (k_x, k_y) when viewed in k-space. The parallel transmit problem then reduces to determining the number and (k_x, k_y) location of such spokes, as well as the calculation of the phase and amplitude of each transmit channel for each spoke to achieve the desired modulation in the x, y plane.

The excitation trajectory design problem is guided by our knowledge of the desired target excitation pattern and B_1 profiles of the transmit array elements, and further augmented by a SAR penalty term in the optimization cost-function. Thus, the k-space trajectory and RF pulse can be jointly optimized to produce a higher fidelity excitation pattern while satisfying constraints on overall SAR. When a mode-mixing strategy is employed in the transmit array, we can additionally choose which modes to connect to the transmit channels based on the excitation trajectory. Since the excitation k-space amplitudes and phases are related to the target pattern by the Fourier transform (for low flip-angle excitations), the k-space trajectory can be limited to regions with the largest magnitude Fourier coefficients. However, this does not take advantage of the "don't care" regions outside the body but within the FOV. A better strategy is to let a sparsity-enforcing algorithm choose the trajectory from among a discrete set of k-space grid points allowing an explicit trade-off between excitation fidelity and pulse length [9]. The simulation in Figure 6 demonstrates the advantage of choosing a subset of circular trajectories

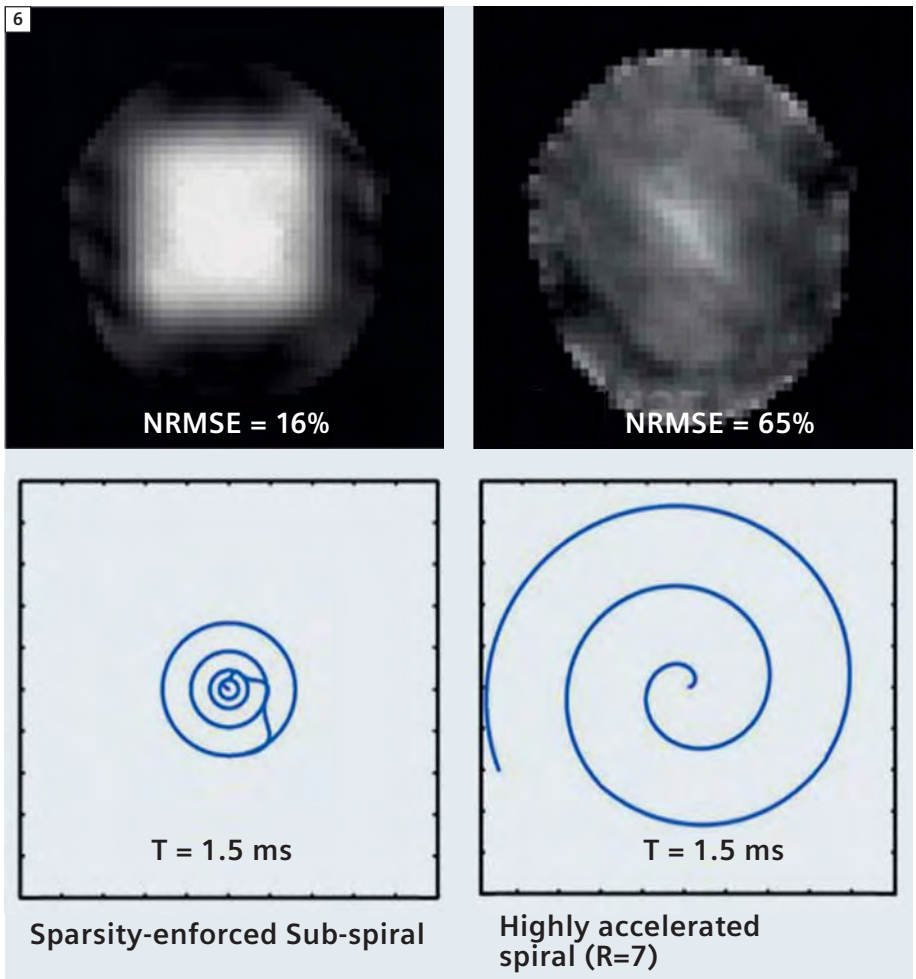

6 Target excitation (box) implemented with a sparsity-enforced choice among a set of concentric circular trajectories and a highly accelerated (R=7) spiral of the same duration. *(Figure courtesy of A. Zelinski, MIT.)*

among a candidate set of circles in the k_x, k_y plane compared to a highly accelerated spiral excitation of the same overall duration. Figure 7 shows a similar optimization from among a grid of possible locations in the k_x, k_y plane of the "spokes" trajectory. The target excitation is slab-selective in z, and selectively excites the two simulated arteries in-plane, such as might be used for a vessel-selective arterial spin labeling experiment. In this case the two crossing vessels are tagged with excitations differing in RF excitation phase by 90°, demonstrating tight RF control in both magnitude and phase for a challenging 3D excitation target.

B_1 mitigation at 7T

Parallel excitations were performed on both head-shape water phantom and in vivo human studies at 7T [10]. Both slice-selective B_1 mitigated excitation and arbitrarily shaped volume excitations were created and validated via a 16-element degenerate strip-line array coil driven with a Butler matrix utilizing the 8 most favorable birdcage modes. RF and gradient excitation waveforms were designed using the MLS optimization, and a spokes' placement optimization algorithm. With this design method, optimized parallel excitation waveforms for human B_1 mitigation were only ~50% longer than conventional single-channel slice-selective excitation while significantly improving flip-angle homogeneity. We compared the B_1 mitigation performance by parallel transmission to "RF shimming," which can be viewed as a simplified form of parallel transmit where the array elements are driven with individual amplitudes and phase shifts but not separate pulse shapes. For the slice-selective excitation, the RF shimming can be viewed as a special case of the "spokes" trajectory where only a single spoke (at the center of (k_x, k_y)-space) is employed. Thus, RF shimming utilizes the spatial patterns of the transmit array, but not the encoding ability of the gradient trajectory. Figure 8 shows the measured B_1 map for the "uniform" birdcage excitation, the RF shimming and pTX with spokes trajectory (all slice selective excitations). The full pTX method clearly demonstrates superior B_1 mitigation performance. The phantom inhomogeniety is similar in shape to that of the head, but exhibits more severe field variations than in the human head; a 3 fold variation in flip angle across the slice. Nevertheless, the

7

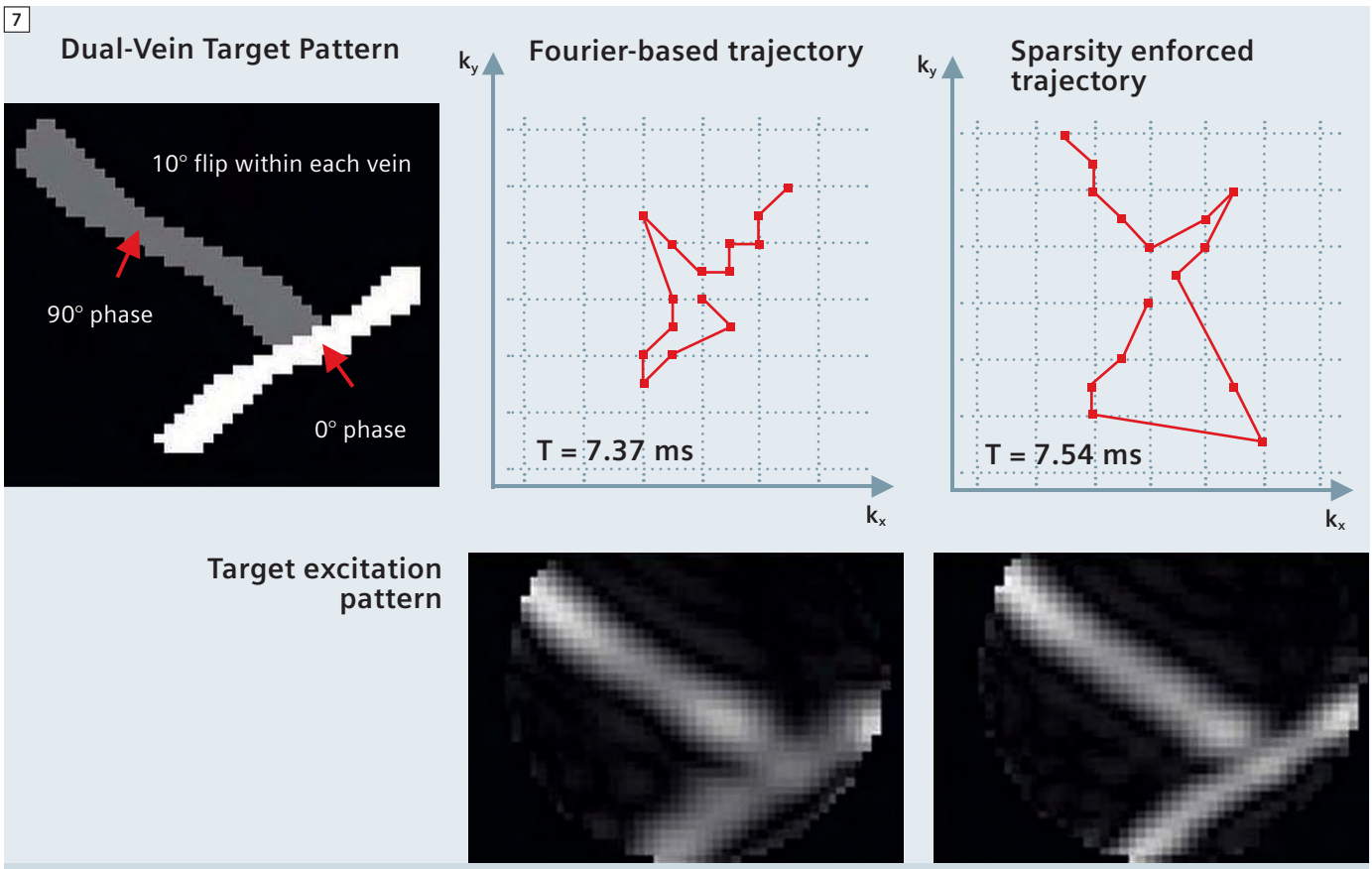

7 Sparsity enforced trajectory generation for a 3D arterial tagging senerio. Slab-selective excitation is performed by 15 "spokes" in the kz direction (each with a weighted excitation amplitude) to create the desired in-plane pattern. The Fourier method utilizes the locations where the transform of the target pattern has highest energy. The sparsity enforced algorithm chooses from a grid of locations and maximizes an L1 norm. *(Figure courtesy of A. Zelinski, MIT.)*

B_1 maps in a head shaped water phantom at 7T.

8A **Birdcage mode**

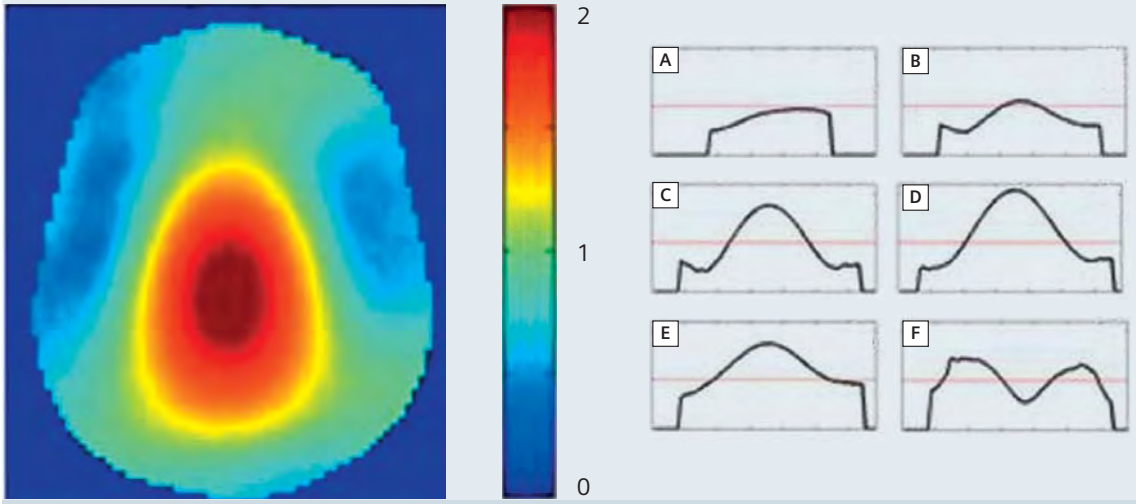

8B **RF shimming**

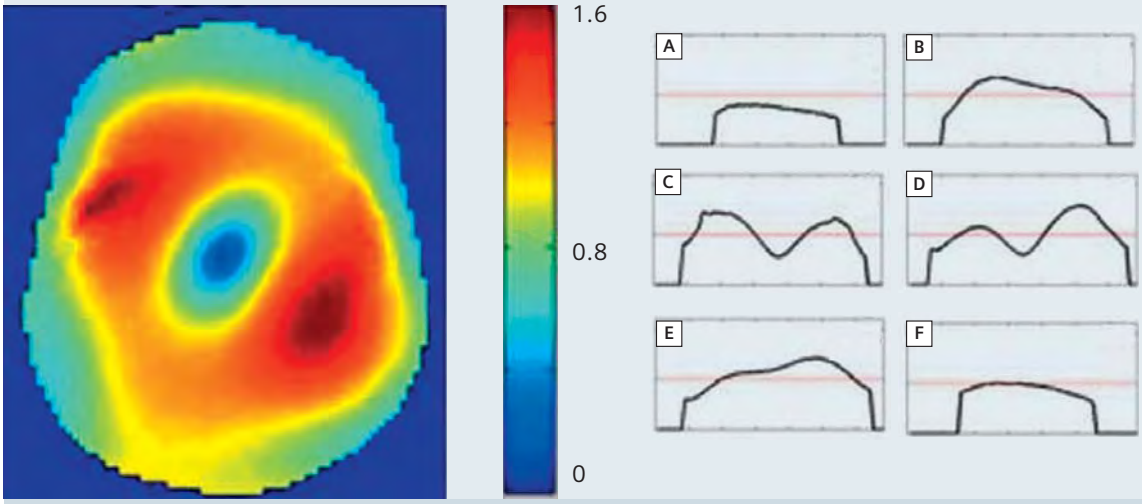

8C **3 spoke pTX**

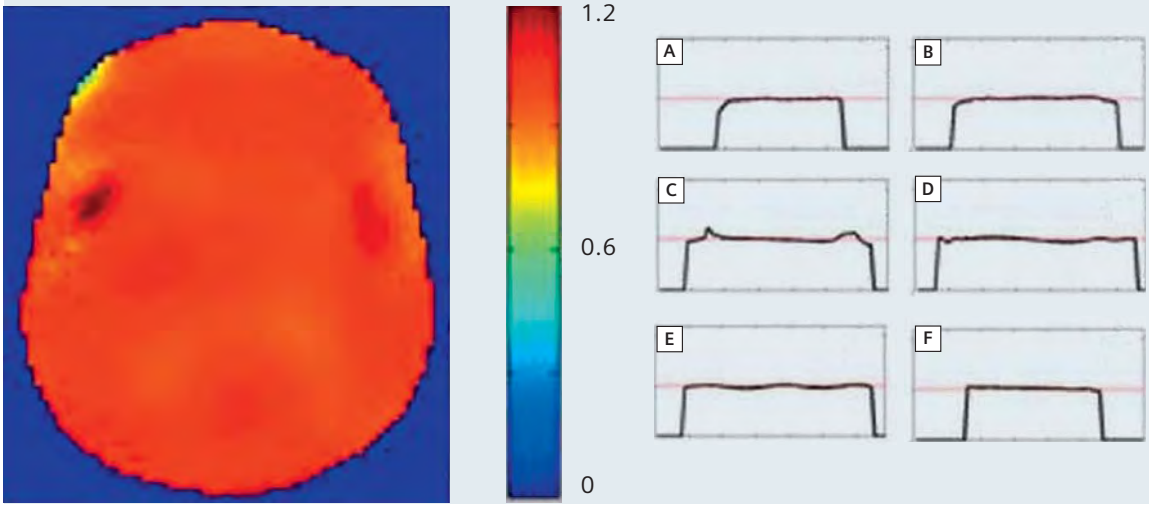

8 Comparison of B_1 inhomogeniety mitigation in slice-selective excitations at 7T (head-shaped phantom) using **A:** conventional birdcage excitation (SD of B_1 across head = 42% of mean), **B:** RF shimming (identification of optimal amplitude and phase excitation settings) with 8-channel transmit array (SD = 29% of mean) and **C:** parallel TX with 3-spoke trajectory (2.4 ms duration) (SD = 5% of mean). *(Figure courtesy of K. Setsompop MGH, MIT.)*

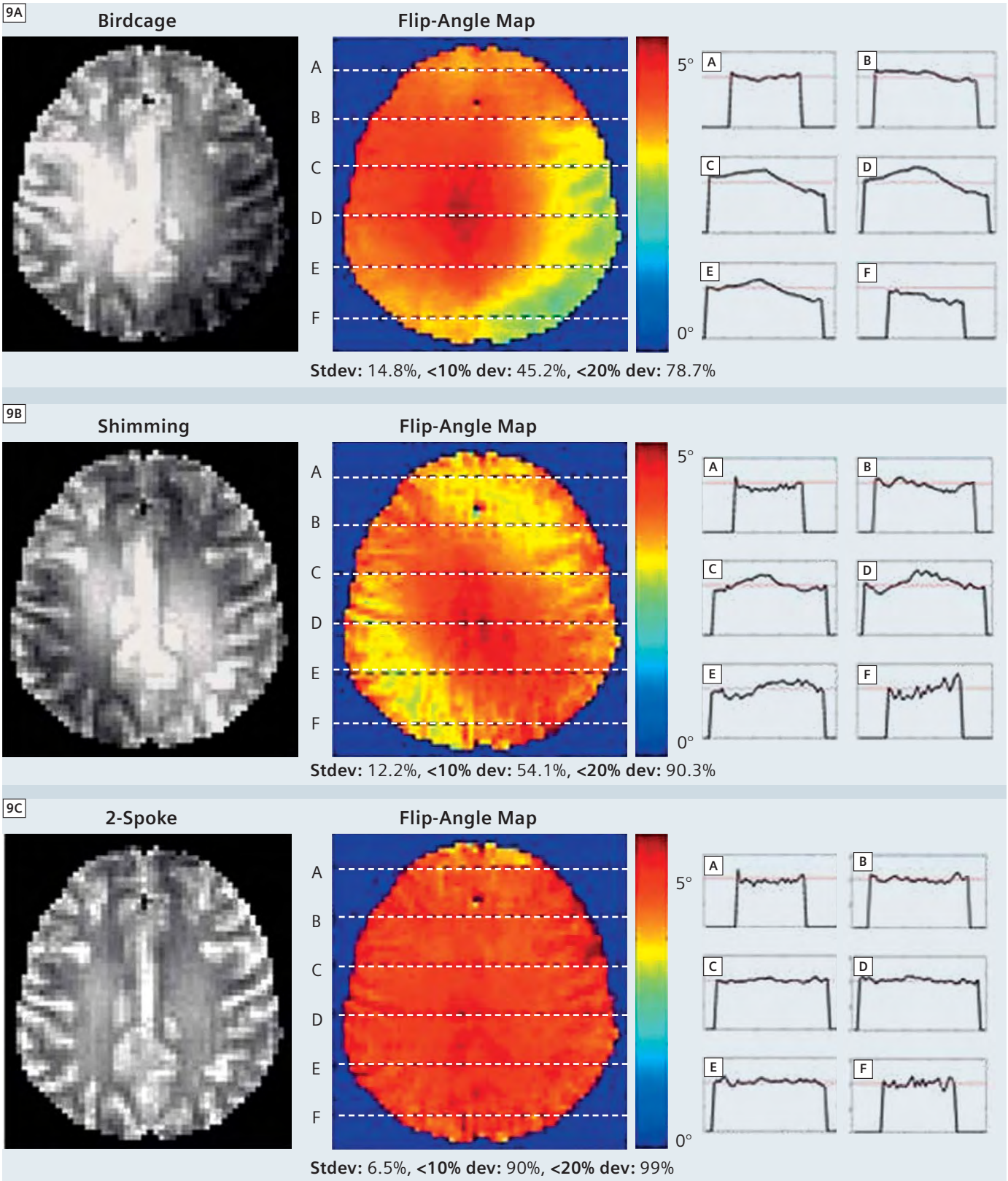

9 Flip-angle inhomogeniety at 7T in the human head using 3 methods (conventional birdcage excitation, RF shimming and pTX with spokes trajectory.) Subject #5 (who displayed the most severe inhomogeniety) is shown. Gray scale images show a proton density-weighted low flip-angle image with the receive profile divided (leaving only variations due to transmit.) Color scale image is a quantitative flip angle map acquired with each of the 3 methods. *(Figure courtesy of K. Setsompop MGH, MIT.)*

10

3T flip angle maps in abdomen

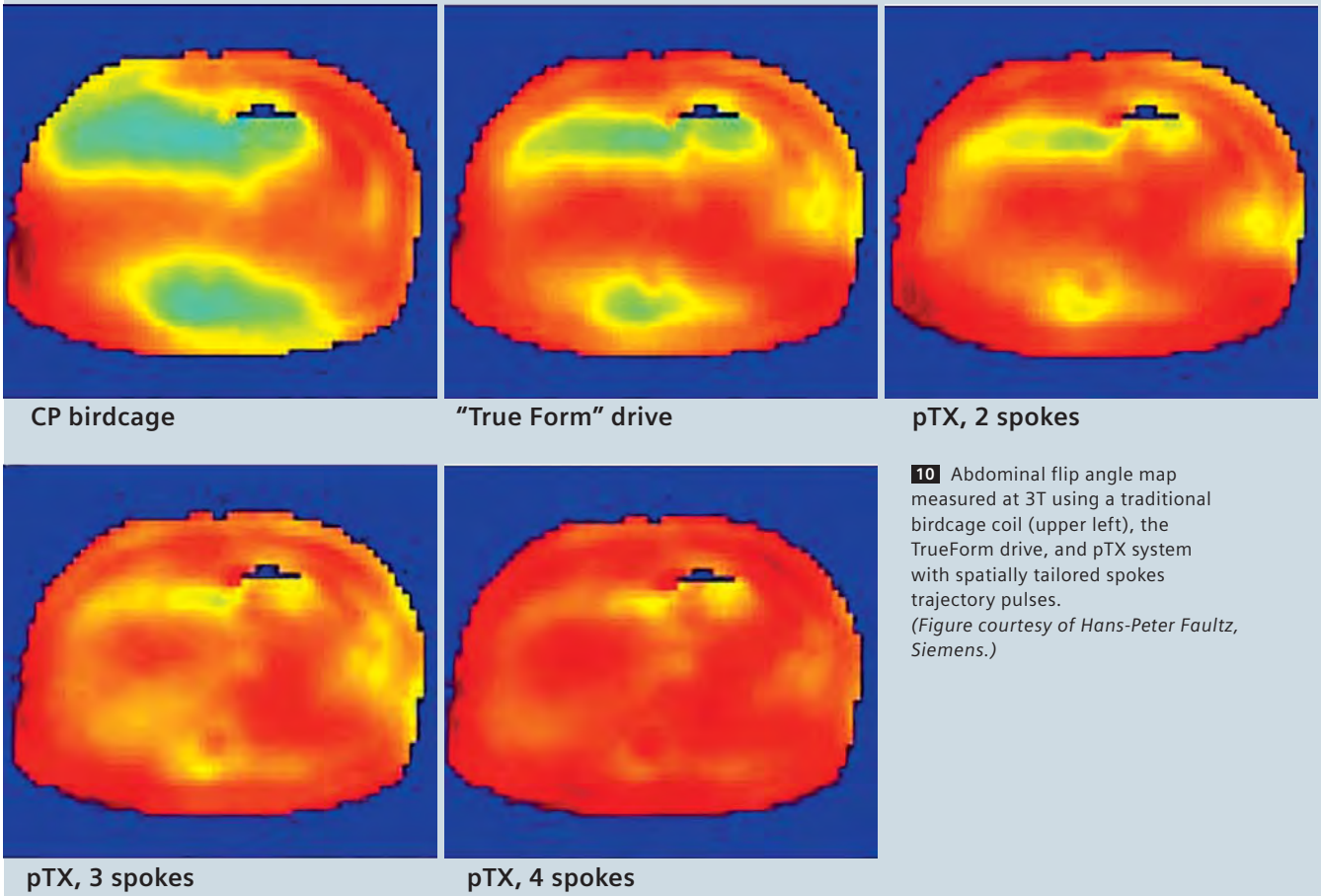

10 Abdominal flip angle map measured at 3T using a traditional birdcage coil (upper left), the TrueForm drive, and pTX system with spatially tailored spokes trajectory pulses.
(Figure courtesy of Hans-Peter Faultz, Siemens.)

3-spoke trajectory and 8-channel array is sufficient to remove the vast majority of the inhomogeneity.
Figure 9 shows B_1 maps obtained from one of 6 healthy subjects (studied with institutional approval and informed consent). In this case a 2.3 ms duration 2-spoke slice-selective trajectory was used with the 8-channel system and the MLS design method. The birdcage and RF shimming acquisition used a 1.4 ms sinc-like excitation. While some contamination from anatomy is seen in the B_1 transmit maps, the pTX method significantly reduced the B_1 inhomogeniety (standard deviation (Stdev.) across slice was 8% of the mean compared to 21% for the birdcage excitation and 14% for the RF shim).

Figure 10 shows the parallel transmit method applied to a similar flip-angle inhomogeneity problem; the abdomen at 3T. Here a similar wave-cancelation occurs in body imaging where the size of the body becomes comparable to the wavelength of the RF. The conventional circularly polarized birdcage can be significantly improved upon by optimizing the phase relationship between the drive ports of the coil to produce a more uniform and efficient elliptical polarization tailored to the body. Further gains in uniformity were realized with parallel transmit and the 3D spokes spatially tailored excitation pulses calculated based on knowledge of the B_1 field profiles of the transmit array elements.

SAR considerations

While the results in Figure 8 demonstrate the ability of the parallel transmit method to mitigate the inhomogeneous flip-angle distribution at high field, the spokes pulses used more RF energy to achieve the desired flip angle than the simple birdcage transmit (but less than the RF shim). The total pulse energy for the birdcage, RF shim, and pTX-spokes methods were 10.7 mJ, 24.8 mJ, and 21.8 mJ respectively. This suggests that the parallel methods achieve uniformity only with some degree of self-cancellation among the fields or excited magnetization. A similar effect is seen in the 2D spiral trajectories, where pulse energy significantly increases with acceleration,

even with an explicit B_1 amplitude penalty in the pulse design cost-function and local SAR levels are difficult to predict [11]. An example is shown in Figure 11 where the local SAR is calculated for a series of box-shaped excitations placed at 5 different positions in the head (left to right). The spatially tailored 2D pulses used an 8-channel array and spiral trajectories with accelerations ranging from R=1 to R=8. The pulse design maintained a constant fidelity to the target pattern by trading off the pulse amplitude constraint and the fidelity constraint. The local SAR was calculated from the E_1 fields in a multi-tissue head model for the array and pulse. The first observation based on these results is the enormous cost in local SAR incurred by keeping the fidelity constant in the face of increasing parallel transmit acceleration (nearly 3 orders of magnitude variation in local SAR!). The second observation is that local SAR varies significantly with the position of the excitation box. For low accelerations the central box positions have the lowest SAR, while the higher accelerations, the peripheral positions have lower SAR.

For evaluation and monitoring of SAR, the main concern for human imaging is the potential for the E_1 fields from the array elements to constructively superimpose locally, creating a local SAR hot spot. A simple estimate demonstrates how serious the "worst-case" superposition can be. If the E_1 fields from the eight elements superimpose and generate an 8 fold increase compared to a single element, then the local SAR at that location will increase 64 fold. Similarly, electric fields can destructively interfere. This means that if one channel stops transmitting due to equipment failure, the local SAR can actually increase. Therefore, in addition to monitoring the average power from each channel, a pTX system must make an estimate of local E_1 fields and how they superimpose so that the local SAR limits are not exceeded. As the pulse design becomes increasingly tailored to the individual patient, the local SAR check must also move in this direction. This will require fast local SAR calculation methods based on the field patterns calculated for the array and the specific pulse designed for that subject. Preliminary work has exploited the ability to penalize high-amplitude RF pulses in the pulse design optimization, but significant future development is needed to explicitly include local SAR regularization in the design of the RF pulses and enable a flexible trade-off between RF excitation properties (due to B_1) and local SAR distribution (due to E_1).

Remaining challenges

In addition to the SAR estimation and monitoring problem, several other outstanding challenges must be solved before accelerated 2D and 3D spatially tailored excitations can be routinely employed. The method relies on a fast but accurate mapping of the B_1 transmit field in the subject, which is an intense and ongoing area of innovation with several promising methods being proposed in the literature. A second area of innovation is the calculation of high flip-angle spatially tailored RF pulses. Most of the work performed to-date has assumed the small flip angle approximation. While this approximation provides

11

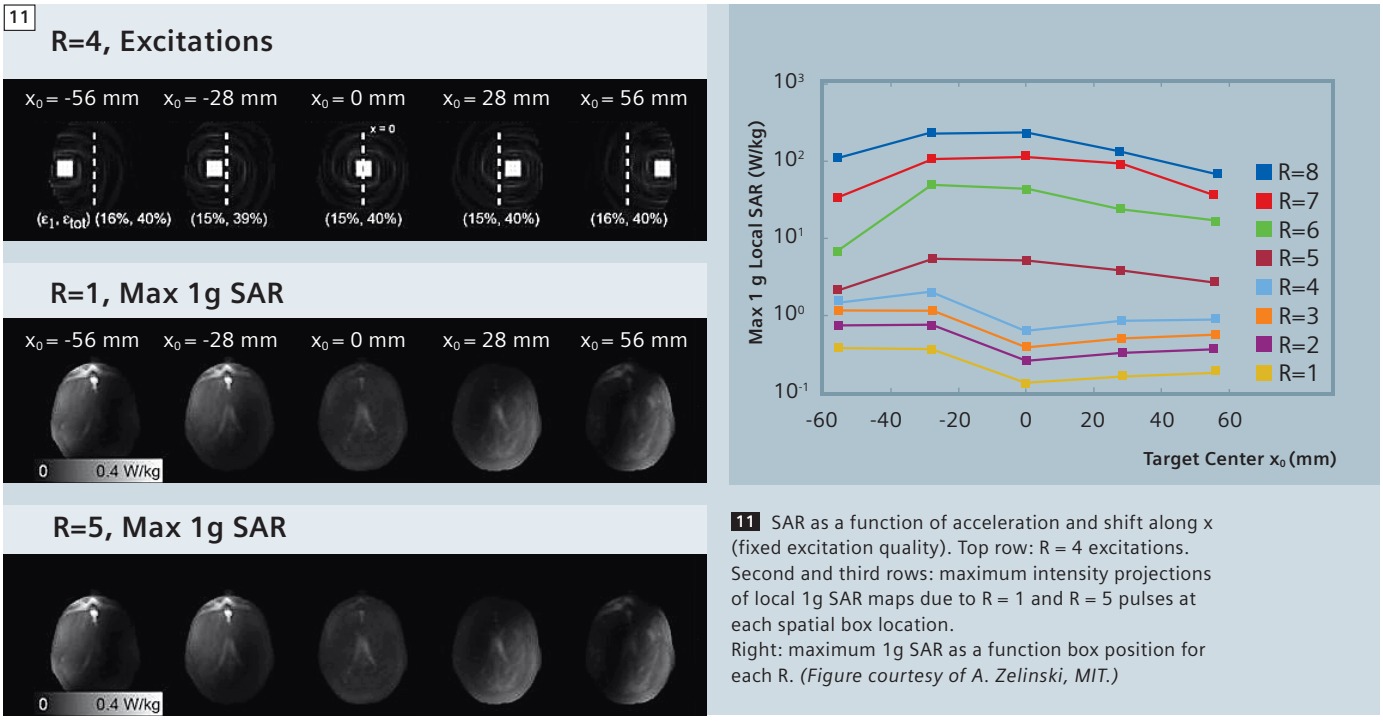

11 SAR as a function of acceleration and shift along x (fixed excitation quality). Top row: R = 4 excitations. Second and third rows: maximum intensity projections of local 1g SAR maps due to R = 1 and R = 5 pulses at each spatial box location.
Right: maximum 1g SAR as a function box position for each R. *(Figure courtesy of A. Zelinski, MIT.)*

for elegant and computationally tractable RF designs with familiar tradeoffs based on well known Fourier transform properties, large flip-angle pulses are central to many clinical pulse sequences and the low flip-angle constraint needs to be addressed for general applicability of pTX. This computational problem is now just starting to be addressed.

Conclusions

Theoretical work on parallel RF transmission and recent experimental validations on 8-channel prototype systems at 3T and 7T indicate that parallel excitation has the potential to overcome critical obstacles to robust and routine human scanning at high field strength. As these developments are extended, high-field human imaging will be possible with essentially constant flip angle, and therefore no compromise in signal strength or clinical contrast, across the human head and body with RF pulse durations comparable to current slice selective pulses. While most work has been concentrated on head-sized transmitters at 7T, the methods are readily translatable to body transmit coils at 3T. Of course, intriguing research questions remain open in several areas, including optimal coil array designs that minimize element couplings and maximize spatial orthogonality of individual channels; the estimation of local SAR from a subject-specific spatially tailored RF pulse; and the development of rapid and robust RF pulse designs that extends the current low-flip angle domain to arbitrary excitation angle, such as spin echoes, saturation, and inversions pulses. However, with continued active research in these areas, progress is likely to accelerate, and logical extensions of the architecture of a current clinical scanner readily accommodates the requirements of a general parallel RF excitation system supported by fast, subject and application tailored RF pulse design software capable of extending MR excitation from the simple slice-select to the more generally tailored anatomy- or application-specific RF excitation pattern.

Acknowledgements

The authors would like to acknowledge the many researchers at Siemens, MGH and MIT whose work is summarized here. We especially acknowledge Kawin Setsompop, Vijay Alagappan, and Adam Zelinski whose thesis work was reviewed here. We also thank Ulrich Fontius and Andreas Potthast for their work setting up the 8-channel 3T and 7T systems and Franz Hebrank and Franz Schmitt for their leadership role in the collaboration and Josef Pfeuffer, Axel vom Endt and Hans-Peter Fautz for their on-going support.
We acknowledge grant support from the NIH (P41RR14075, R01EB007942, and R01EB006847) and a research agreement and research support from Siemens Healthcare. One of us (LLW) acknowledges consulting income from Siemens Healthcare.

WIP – Works in Progress. This information about this product is preliminary. The product is under development and not commercially available in the U.S., and its further availability cannot be ensured.

References

1 Butler, J. and R. Lowe, Beamforming matrix simplifies design of electronically scanned antennas. Electron Design, 1961. 9: p. 170–173.
2 Tropp, J., Mutual Inductance in the Bird-Cage Resonator. J Magn Reson, 1997. 126(1): p. 9–17.
3 Alagappan, V., et al. Mode Compression of Transmit and Receive Arrays for Parallel Imaging at 7T. in International Society for Magnetic Resonance in Medicine. 2008. Toronto, Canada.
4 Pauly, J., D. Nishimura, and A. Macovski, A k-space analysis of small-tip angle excitation. J Magn Reson, 1989. 81: p. 43–56.
5 Katscher, U., et al., Transmit SENSE. Magn Reson Med, 2003. 49(1): p. 144–50.
6 Zhu, Y., Parallel excitation with an array of transmit coils. Magn Reson Med, 2004. 51(4): p. 775–84.
7 Zelinski, A., et al., Comparison of three algorithms for solving linearized systems of parallel excitation RF waveform design equations: Experiments on an eight-channel system at 3 Tesla. Concepts in Magnetic Resonance Part B: Magnetic Resonance Engineering, 2007. 31B: p. 176–190.
8 Setsompop, K., et al., Magnitude least squares optimization for parallel radio frequency excitation design demonstrated at 7 Tesla with eight channels. Magn Reson Med, 2008. 59(4): p. 908–15.
9 Zelinski, A.C., et al., Sparsity-enforced slice-selective MRI RF excitation pulse design. IEEE Trans Med Imaging, 2008. 27(9): p. 1213–29.
10 Setsompop, K., et al., Slice-selective RF pulses for in vivo B1+ inhomogeneity mitigation at 7 tesla using parallel RF excitation with a 16-element coil. Magn Reson Med, 2008. 60(6): p. 1422–32.
11 Zelinski, A.C., et al., Specific absorption rate studies of the parallel transmission of inner-volume excitations at 7T. J Magn Reson Imaging, 2008. 28(4): p. 1005–18.
12 Shinnar, M. and J.S. Leigh, The application of spinors to pulse synthesis and analysis. Magn Reson Med, 1989. 12(1): p. 93–8.
13 Shinnar, M., et al., The synthesis of pulse sequences yielding arbitrary magnetization vectors. Magn Reson Med, 1989. 12(1): p. 74–80.
14 Shinnar, M., L. Bolinger, and J.S. Leigh, The use of finite impulse response filters in pulse design. Magn Reson Med, 1989. 12(1): p. 81–7.
15 Shinnar, M., L. Bolinger, and J.S. Leigh, The synthesis of soft pulses with a specified frequency response. Magn Reson Med, 1989. 12(1): p. 88–92.
16 Pauly, J., et al., Parameter relations for the Shinnar-Le Roux selective excitation pulse design algorithm. IEEE Tr Medical Imaging, 1991. 10(1): p. 53–65.
17 Mao, J.M., TH, K. Scott, and E. Andrew, Selective inversion radiofrequency pulses by optimal control. J Magn Reson, 1986. 70(2): p. 310–318.
18 Conolly, S., D. Nishimura, and A. Macovski, Optimal control solutions to the magnetic resonance selective excitation problem. IEEE T Med Imaging, 1986. MI-5(2): p. 106–115.
19 Geen, H., S. Wimperis, and R. Freeman, Band-selective pulses without phase distortion. A simulated annealing approach. J Magn Reson Med, 1989. 85(3): p. 620–627.

Contact
Lawrence L. Wald
Associate Professor of Radiology
Athinoula A. Martinos Center for Biomedical Imaging
Department of Radiology
Massachusetts General Hospital
Harvard Medical School and
Harvard-MIT Division of Health Sciences and Technology
wald@nmr.mgh.harvard.edu

Elfar Adalsteinsson
Associate Professor
Department of Electrical Engineering and Computer Science
Harvard-MIT Health Sciences and Technology
Massachusetts Institute of Technology
elfar@mit.edu

32-Channel Head Coil Imaging at 3T

Thomas Benner

Athinoula A. Martinos Center for Biomedical Imaging, Department of Radiology, Massachusetts General Hospital and Harvard Medical School, Boston, MA, USA

The new 32-channel head coil for 3T provides considerable benefits over the standard Head Matrix coil. The coil sensitivity and therefore signal-to-noise ratio (SNR) is increased over the whole head [1]. Parallel imaging performance (better g-factor) is increased in any direction, including 2D acceleration for 3D imaging [2]. In practice, these advantages translate into image data with better quality where higher SNR, less distortion in EPI scans, higher resolution or shorter scan times can be traded off. All data in this report were acquired on a 3T MAGNETOM Trio, A Tim System scanner (software version *syngo* MR B15A, SP2). Two scan sessions were performed on a healthy appearing volunteer. In one session the standard 12-channel Head Matrix coil was used. In another session the 32-channel head coil was used.

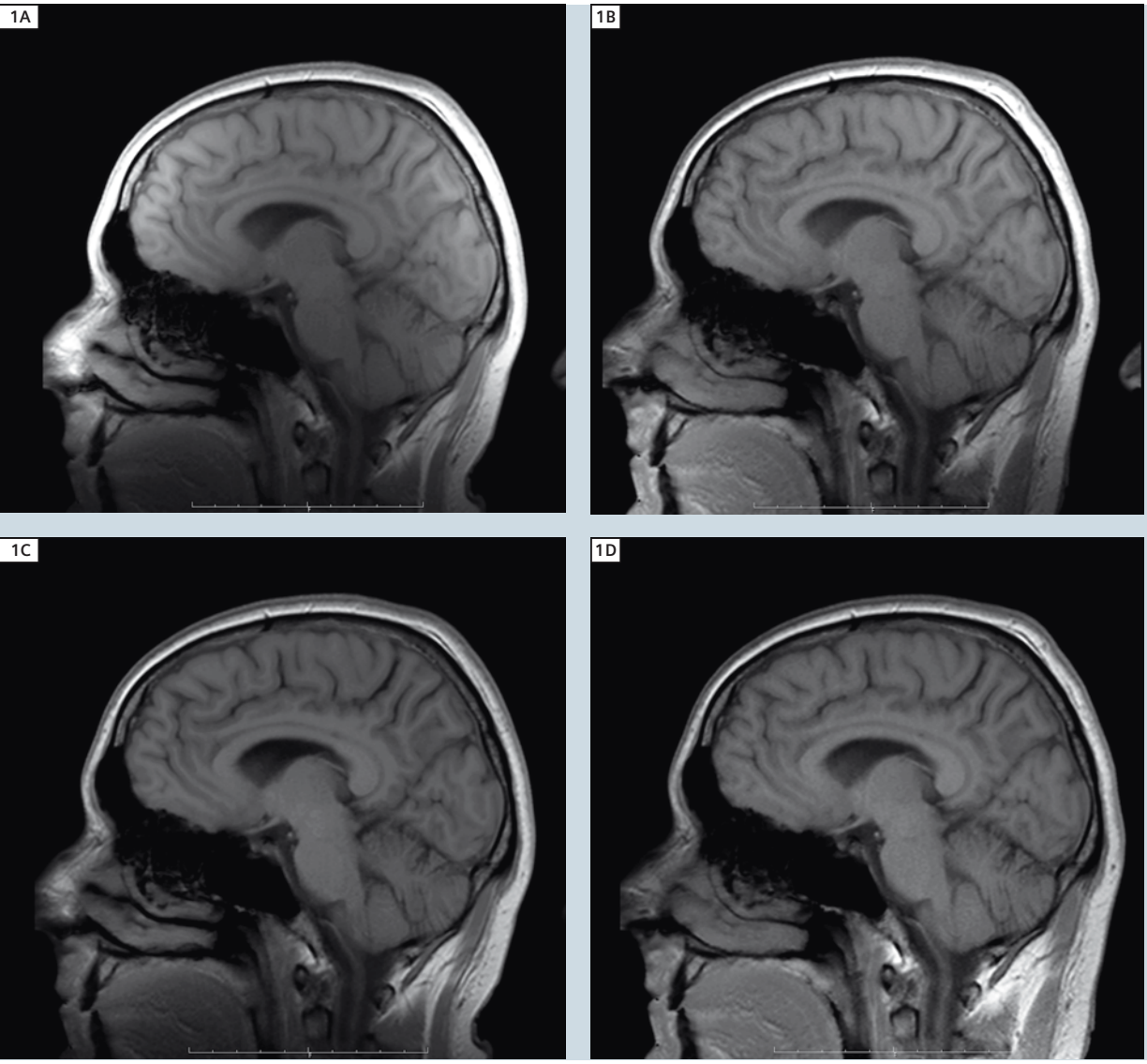

1 T1w 2D FLASH (sagittal orientation, PAT factor 2): top row: unfiltered images; bottom row: pre-scan normalized images; left column: 32-channel head coil; right column: Head Matrix coil. **32, Matrix:** T1w 2D FLASH (sagittal orientation, PAT factor 2), TR 280 ms, TE 2.57 ms, FOV 230 × 230 mm², matrix 256 × 256, 25 slices, slice thickness 5 mm, distance factor 20%, bandwidth 270 Hz/pixel, flip angle 70°, 1 acquisition, PAT mode GRAPPA, acceleration factor PE 2, reference lines PE 24, matrix coil mode auto (triple), reference scan mode integrated, coil combine mode adaptive combine, TA 0:39 min.

To ensure matching slice prescription, AutoAlign was run at the beginning of the session as well as in the middle of the session to adjust for potential subject motion during the study [3–5]. The following examples compare the 32-channel head coil to the Head Matrix coil in terms of image homogeneity, SNR, and parallel imaging performance.

Image homogeneity

The strong gradient of the coil sensitivities of the 32-channel head coil leads to a larger gradient of signal intensities from areas close to the coil elements to areas more distant from the coil elements as compared to the Matrix coil. Therefore, application of the pre-scan normalize filter is essential for homogeneous signal intensities over the whole scan volume. As can be seen from

2

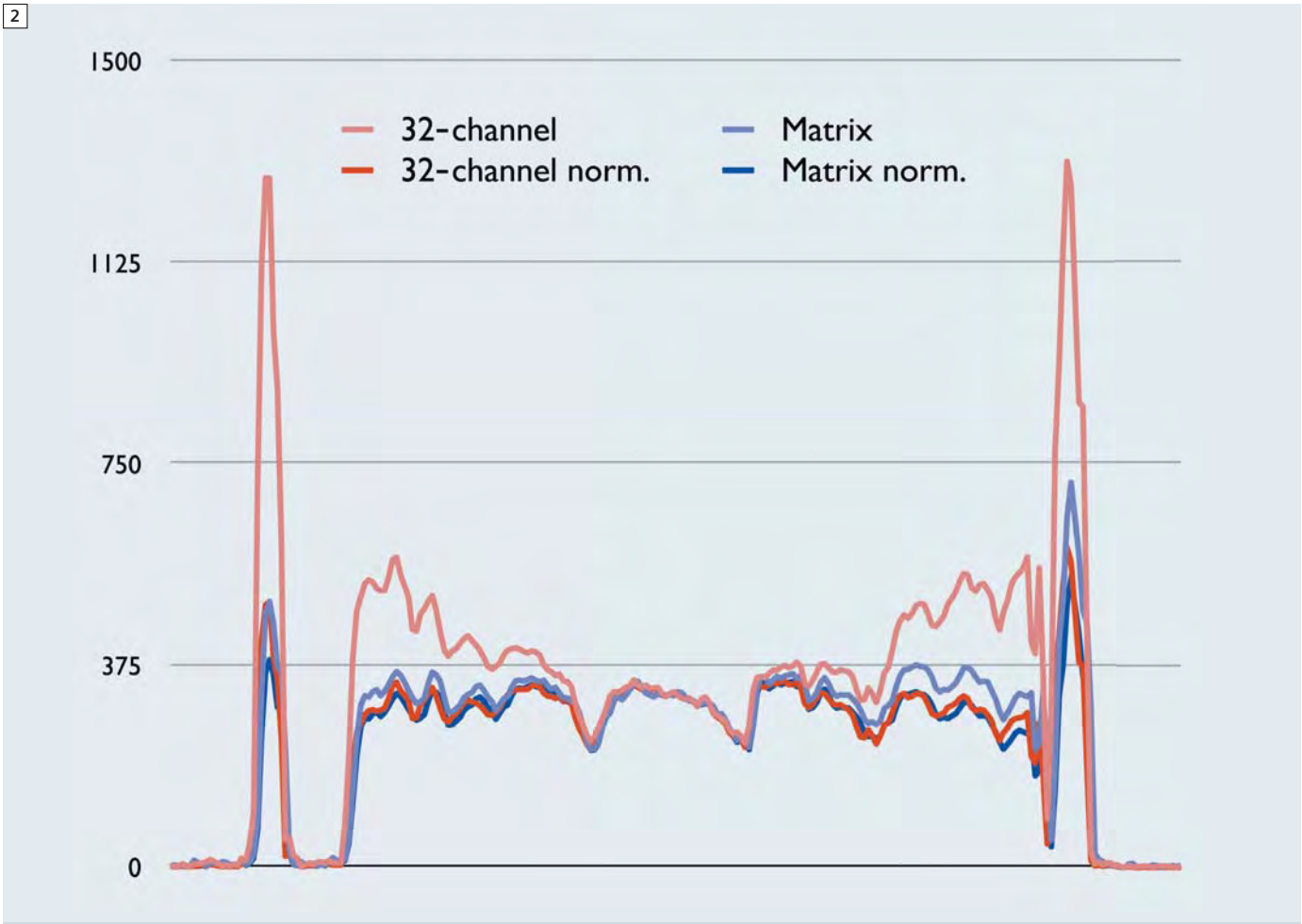

2 T1w 2D FLASH (sagittal orientation, PAT factor 2); horizontal signal intensity profiles for the center row of the images shown in Fig. 1, normalized to the mean signal intensity of the middle 16 pixels. Note the close match of the signal intensity profiles between 32-channel head coil and Head Matrix coil, demonstrating how well pre-scan normalize works. It also shows the very good performance of AutoAlign to align the slice prescription from one session to the other.

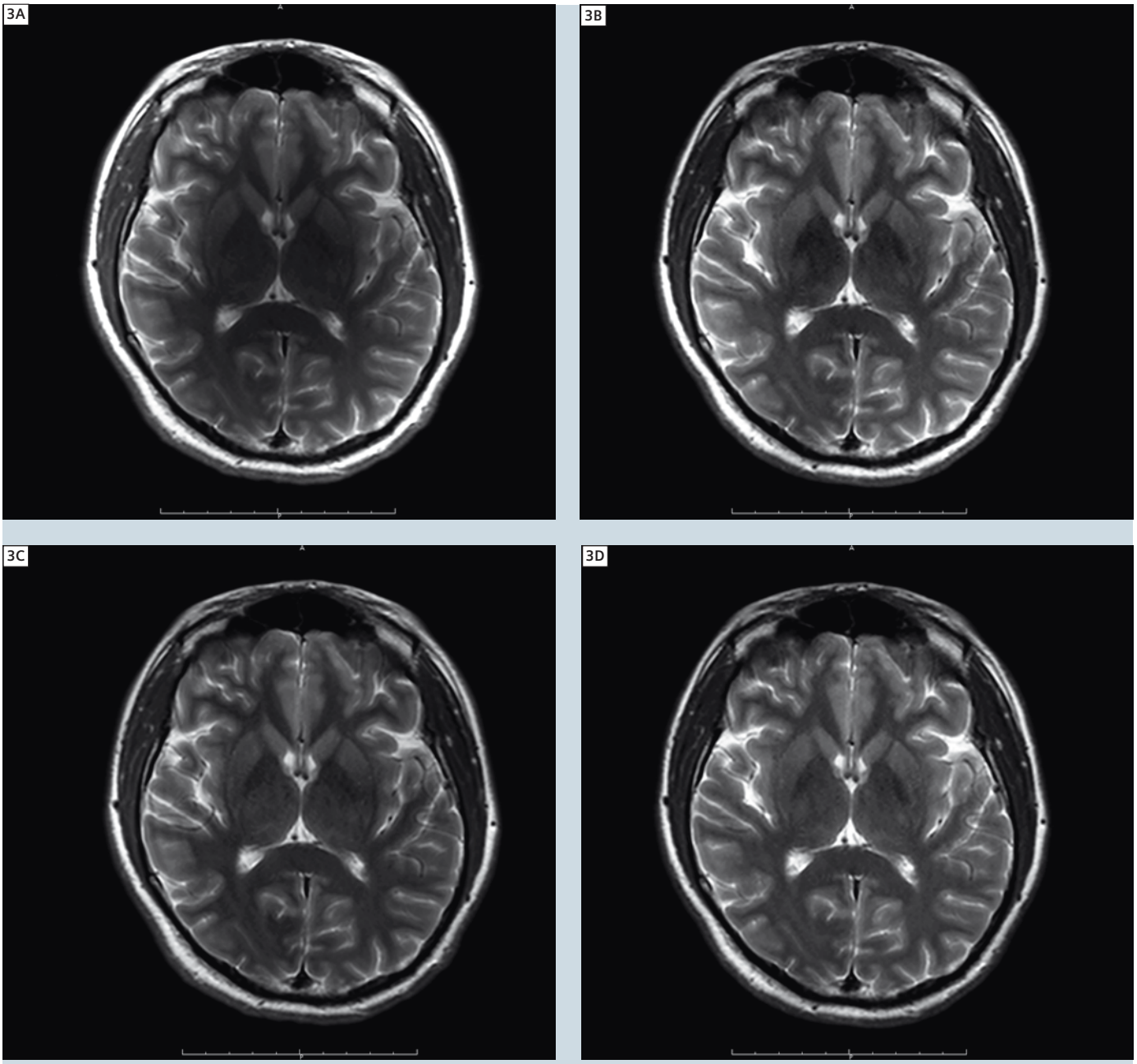

3 T2w TSE (transversal orientation, PAT factor 2); top row: unfiltered images; bottom row: pre-scan normalized images; left column: 32-channel head coil; right column: Head Matrix coil. **32, Matrix:** T2w TSE (transversal orientation, PAT factor 2, TR 6210 ms, TE 84 ms, FOV 220 × 192.5 mm², matrix 256 × 224, 25 slices, slice thickness 5 mm, distance factor 20%, bandwidth 260 Hz/pixel, flip angle 120°, turbo factor 26, 1 acquisition, PAT mode GRAPPA, acceleration factor PE 2, reference lines PE 35, matrix coil mode auto (triple), reference scan mode integrated, coil combine mode adaptive combine, TA 0:39 min.

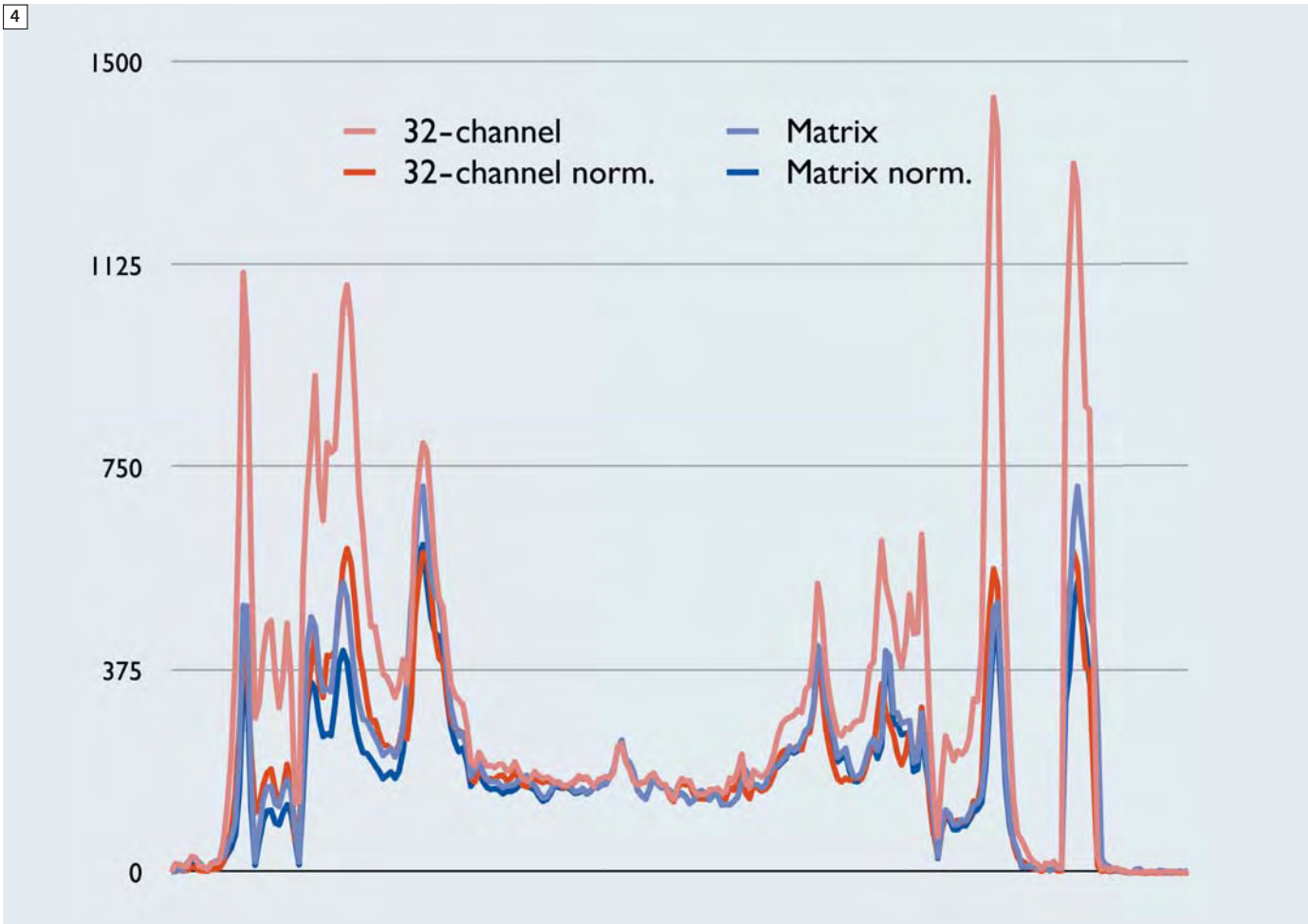

4 T2w TSE (transversal orientation, PAT factor 2; horizontal signal intensity profiles for the center row of the images shown in Fig. 3, normalized to the mean signal intensity of the middle 16 pixels. Note the close match of the signal intensity profiles between 32-channel head coil and Head Matrix coil, demonstrating how well pre-scan normalize works. It also shows the very good performance of auto-align to align the slice prescription from one session to the other.

Figures 1–4, the pre-scan normalize filter works well for both head coils. In case of the 32-channel head coil where the signal intensities become very high towards the periphery of the brain, application of the pre-scan normalize filter results in a flattened signal intensity profile very similar to that of the Head Matrix coil after application of the pre-scan normalize filter. Note, though, that the SNR gain of the 32-channel coil is retained. In comparison, the pre-scan normalize filter has little effect on the images from the Matrix coil.

SNR

Compared to the Head Matrix coil the SNR of the 32-channel head coil is ~20% better at the center of the brain and at least 100% better at the periphery of the brain [1]. The improved SNR can be easily appreciated in Fig. 5. A gradient of SNR from the periphery to the center of the brain can be seen for both coils. Increasing the PAT factor from 2 to 3 causes a drop in SNR that is more noticeable when using the Matrix coil, especially in the center of the brain, demonstrating the better g-factor of the 32-channel head coil.

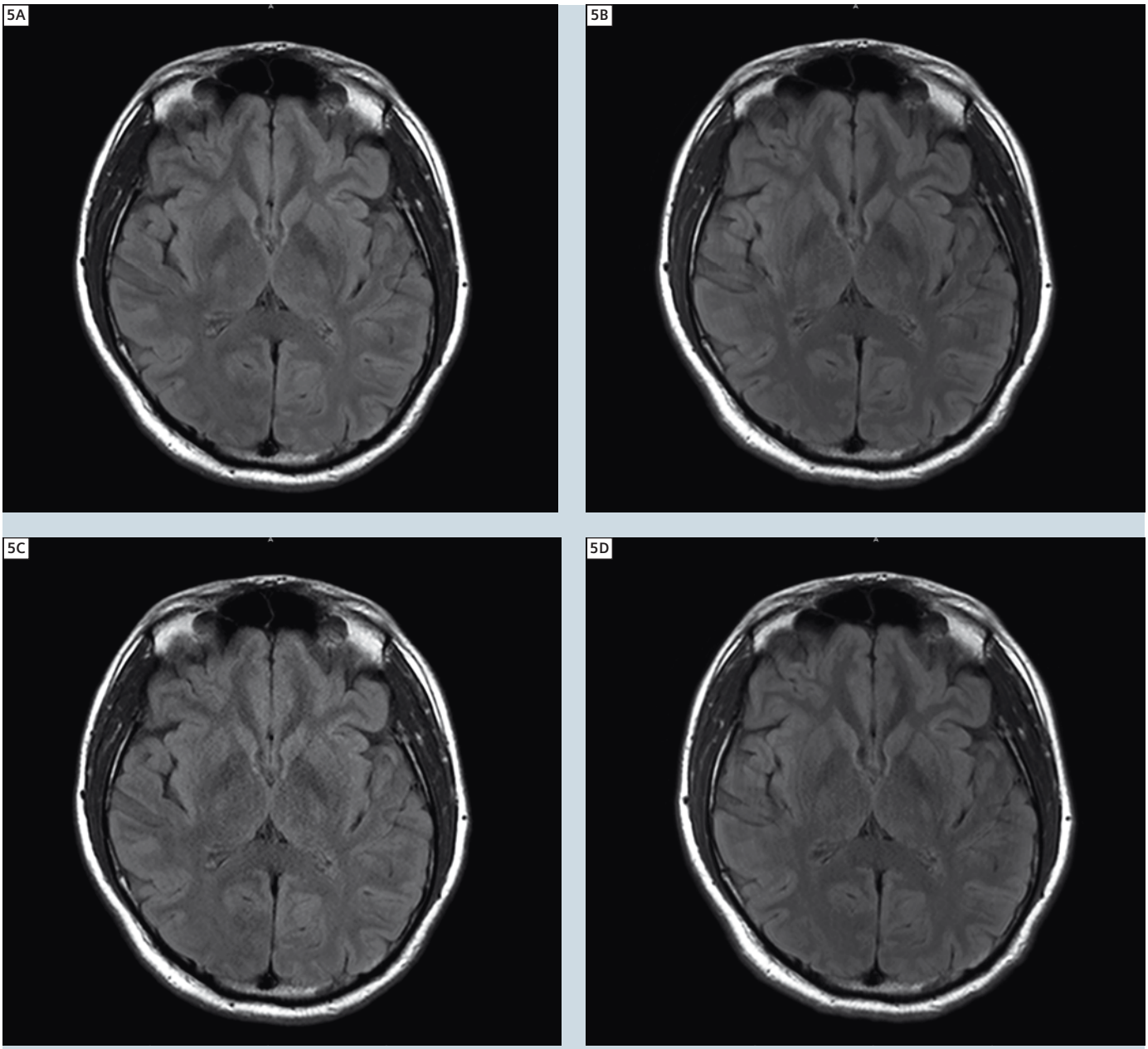

5 T2w TIRM (DarkFluid, transversal orientation, PAT factor 2 / 3); top row: PAT 2; bottom row: PAT 3; left column: 32-channel head coil; right column: Head Matrix coil. **32, Matrix:** T2w TIRM (DarkFluid, transversal orientation, PAT factor 2), TR 7000 ms, TE 81 ms, TI 2500 ms, FOV 220 × 192.5 mm², matrix 256 × 224, 25 slices, slice thickness 5 mm, distance factor 20%, bandwidth 271 Hz/pixel, flip angle 120°, turbo factor 16, 1 acquisition, 2 concatenations, PAT mode GRAPPA, acceleration factor PE 2, reference lines PE 31, matrix coil mode auto (triple), reference scan mode integrated, coil combine mode adaptive combine, pre-scan normalize filter, TA 2:08 min; **32, Matrix:** T2w TIRM (DarkFluid, transversal orientation, PAT factor 3), same as above but for: acceleration factor PE 3, reference lines PE 32, TA 1:40 min.

While image quality (SNR) is better when using the 32-channel head coil compared to Head Matrix coil at an PAT factor of 2, the difference becomes much more obvious when using an PAT factor of 2×2 (Fig. 6). Image quality of the PAT 2×2 scan with the 32-channel head coil (scan time 2:42 min) is comparable to the image quality of the PAT 2 scan with the Head Matrix coil (scan time 4:43 min) i.e. a 43% reduction of scan time can be achieved without image quality loss.

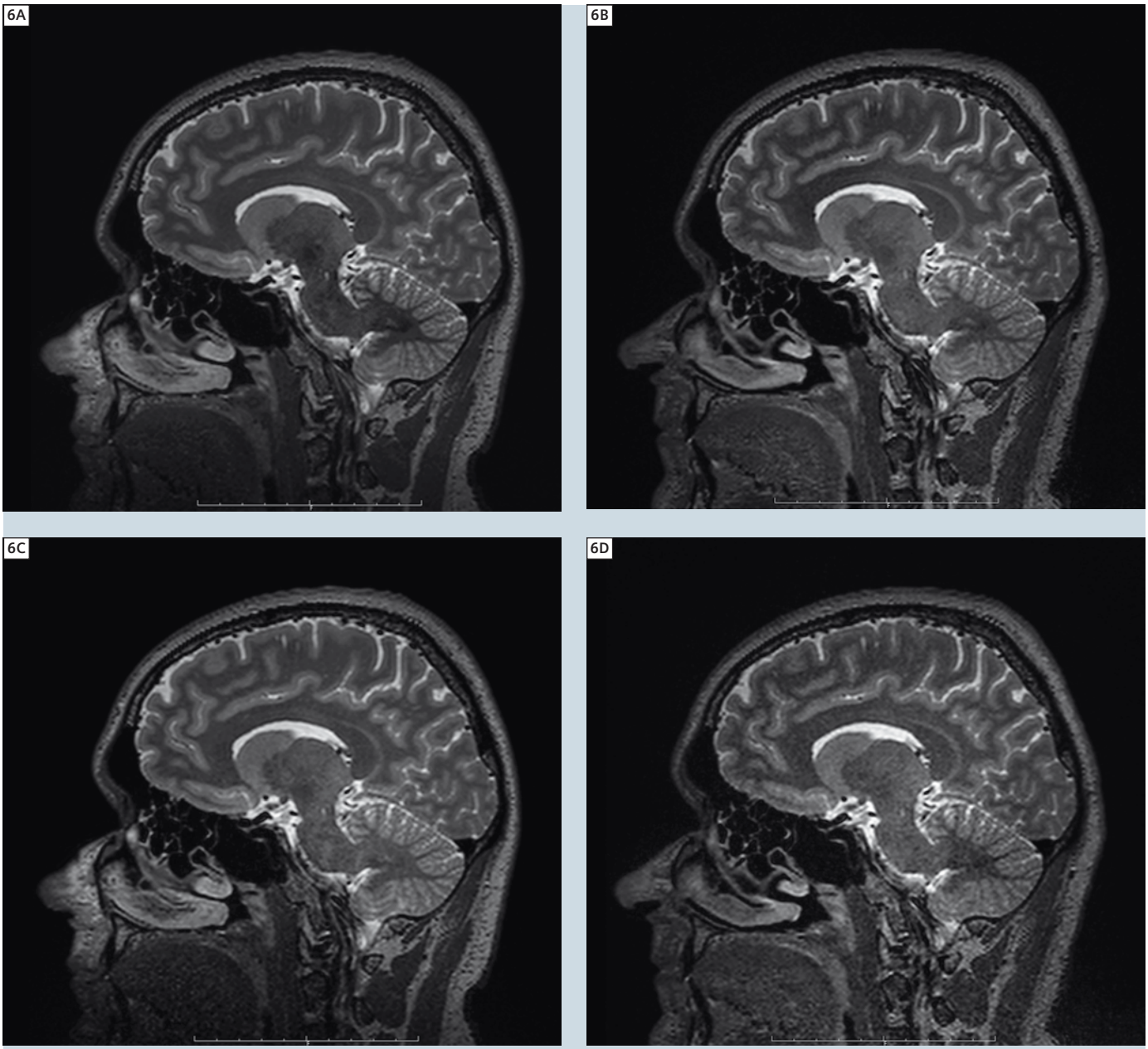

6 Isotropic T2w 3D SPACE (sagittal orientation, PAT factor 2 / 2x2); top row: PAT 2; bottom row: PAT 2×2; left column: 32-channel head coil; right column: Head Matrix coil. **32, Matrix:** Isotropic T2w 3D SPACE (sagittal orientation, PAT factor of 2), TR 3200 ms, TE 403 ms, FOV 250 × 250 mm², matrix 256 × 256, 176 slices per slab, slice thickness 1 mm, bandwidth 751 Hz/pixel, turbo factor 141, 1 acquisition, PAT mode GRAPPA, acceleration factor PE 2, reference lines PE 24, acceleration factor 3D 1, matrix coil mode auto (triple), reference scan mode integrated, coil combine mode adaptive combine, pre-scan normalize filter, TA 4:43 min; **32, Matrix:** Isotropic T2w 3D SPACE (sagittal orientation, PAT factor 2x2), same as above but for: acceleration factor 3D 2, reference lines 3D 24, TA 2:42 min.

Parallel imaging

Figures 7 and 8 demonstrate parallel imaging performance of the two head coils with increasing PAT factor for DTI (Diffusion Tensor Imaging) scans. At a PAT factor of 4 the image data becomes unusable for the Matrix coil while the 32-channel coil still provides reasonable image quality. Image quality of the 32-channel head coil data with PAT factors 3 and 4 compares well with image quality of the Matrix coil at PAT factors 2 and 3, respectively. The figures also

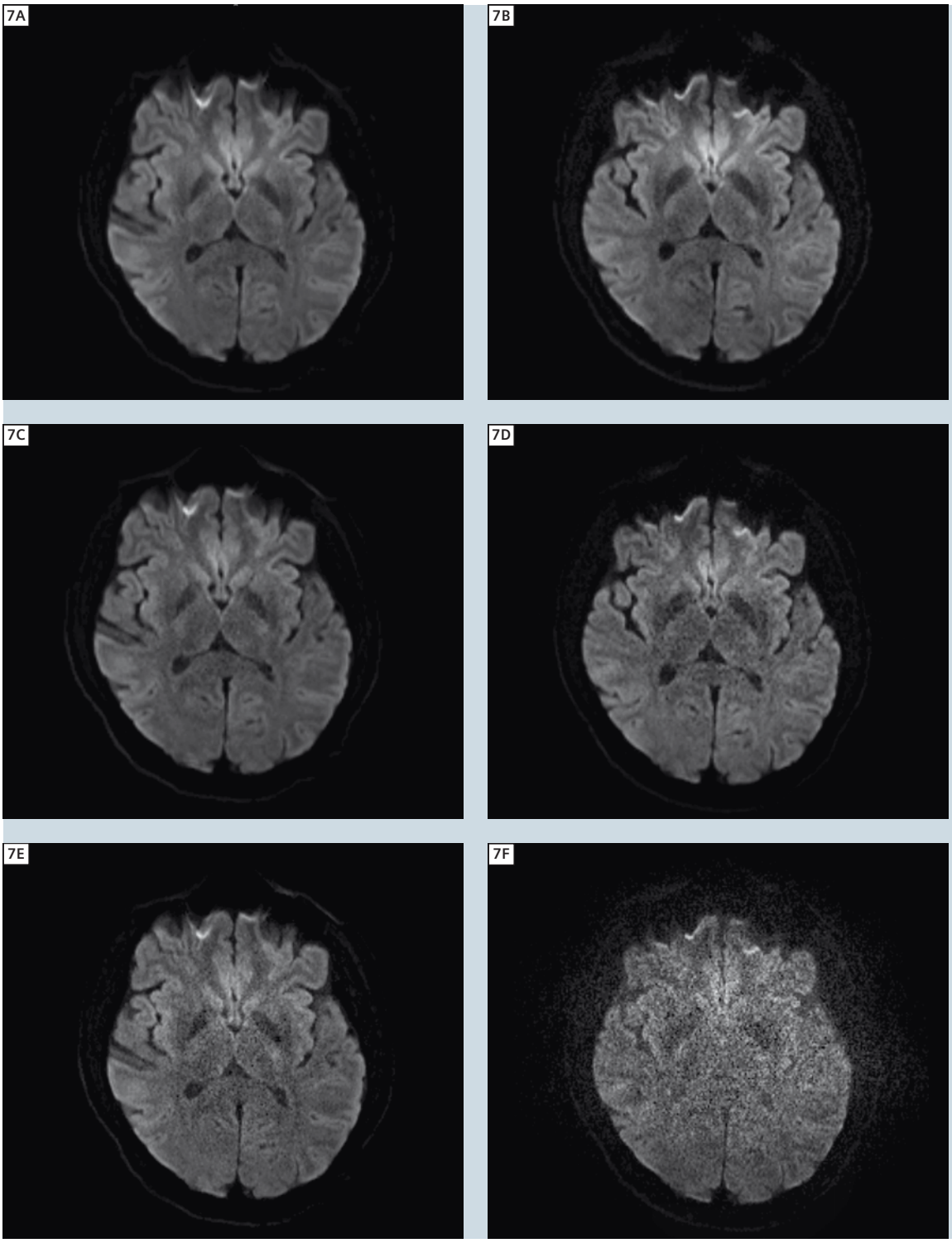

7 Diffusion-weighted imaging (DWI) 2D EPI (transversal orientation, 6 diffusion directions (MDDW), PAT factor 2 / 3 / 4); top row: PAT 2; middle row: PAT 3; bottom row: PAT 4; left column: 32-channel head coil; right column: Head Matrix coil. **32, Matrix:** DWI 2D EPI (transversal orientation, 6 diffusion directions (MDDW), PAT factor 2), TR 3900 ms, TE 94 ms, FOV 220 × 220 mm², matrix 192 × 192, phase partial Fourier 6/8, 25 slices, slice thickness 5 mm, distance factor 20%, bandwidth 1184 Hz/pixel, 1 acquisition, 2 diffusion weightings, b1 0 s/mm², b_2 1000 s/mm², 6 diffusion directions, PAT mode GRAPPA, acceleration factor PE 2, reference lines PE 40, matrix coil mode auto (triple), reference scan mode separate, coil combine mode adaptive combine, pre-scan normalize filter, TA 0:41 min; **32, Matrix:** DWI 2D EPI (transversal orientation, 6 diffusion directions (MDDW), PAT factor 3), same as above but for: acceleration factor PE 3, reference lines PE 48, TA 0:41 min; **32, Matrix:** DWI 2D EPI (transversal orientation, 6 diffusion directions (MDDW), PAT factor 4), same as above but for: acceleration factor PE 4, reference lines PE 128, TA 0:49 min.

show a decrease in distortions with increasing PAT factor because of the shorter EPI readout. Scan times are 0:41 min, 0:41 min and 0:49 min for PAT factors of 2, 3 and 4, respectively. In the case of EPI, scan times are not reduced with increasing PAT factor as is typically the case for non EPI scans. This is due to the increased number of PAT reference scans that are required with higher PAT factors.

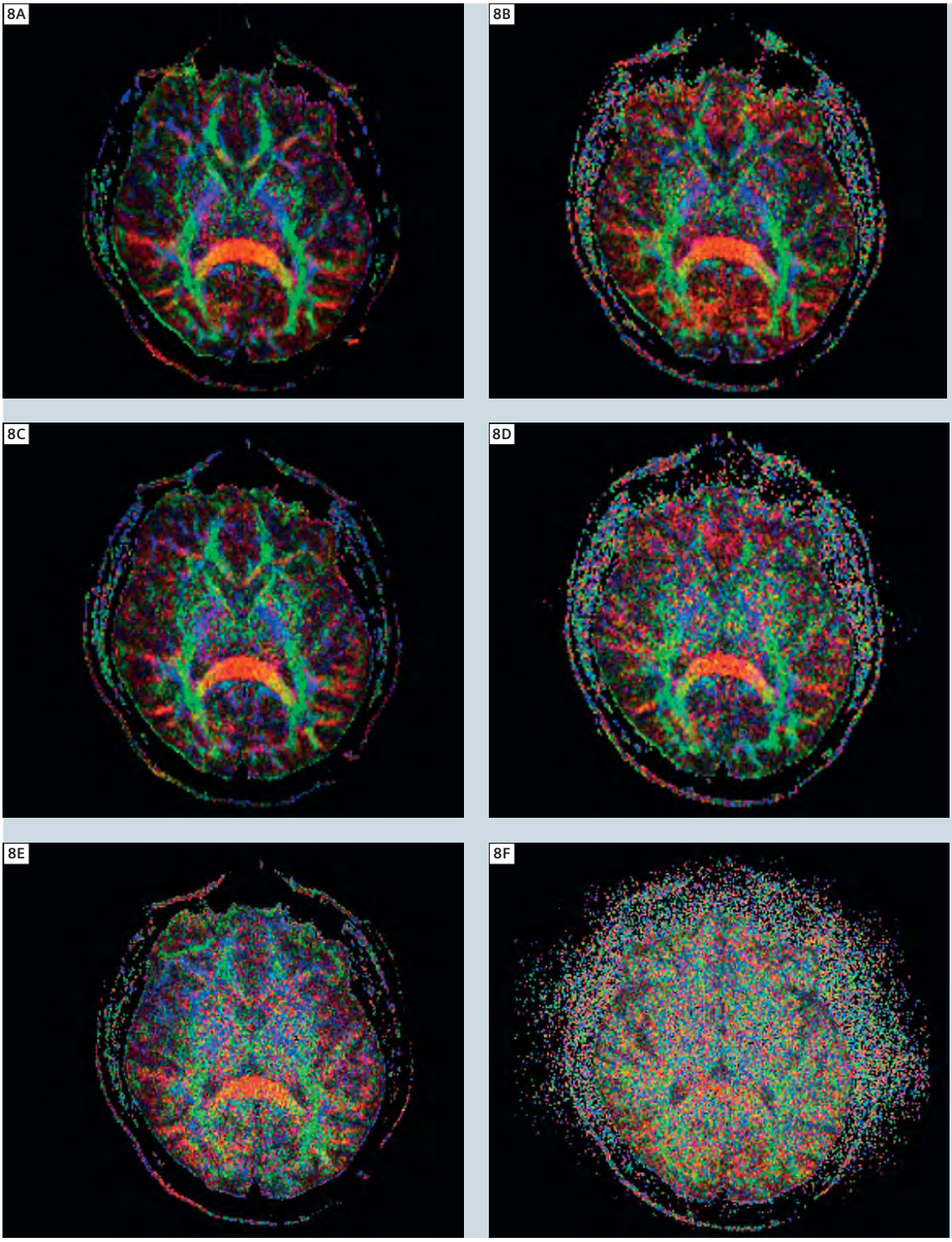

8 Diffusion-weighted imaging (DWI) 2D EPI (transversal orientation, 6 diffusion directions (MDDW), PAT factor 2 / 3 / 4); top row: PAT 2; middle row: PAT 3; bottom row: PAT 4; left column: 32-channel head coil; right column: Head Matrix coil. **32, Matrix:** DWI 2D EPI (transversal orientation, 6 diffusion directions (MDDW), PAT factor 2), TR 3900 ms, TE 94 ms, FOV 220 × 220 mm², matrix 192 × 192, phase partial Fourier 6/8, 25 slices, slice thickness 5 mm, distance factor 20%, bandwidth 1184 Hz/pixel, 1 acquisition, 2 diffusion weightings, b1 0 s/mm², b_2 1000 s/mm², 6 diffusion directions, PAT mode GRAPPA, acceleration factor PE 2, reference lines PE 40, matrix coil mode auto (triple), reference scan mode separate, coil combine mode adaptive combine, pre-scan normalize filter, TA 0:41 min; **32, Matrix:** DWI 2D EPI (transversal orientation, 6 diffusion directions (MDDW), PAT factor 3), same as above but for: acceleration factor PE 3, reference lines PE 48, TA 0:41 min; **32, Matrix:** DWI 2D EPI (transversal orientation, 6 diffusion directions (MDDW), PAT factor 4), same as above but for: acceleration factor PE 4, reference lines PE 128, TA 0:49 min.

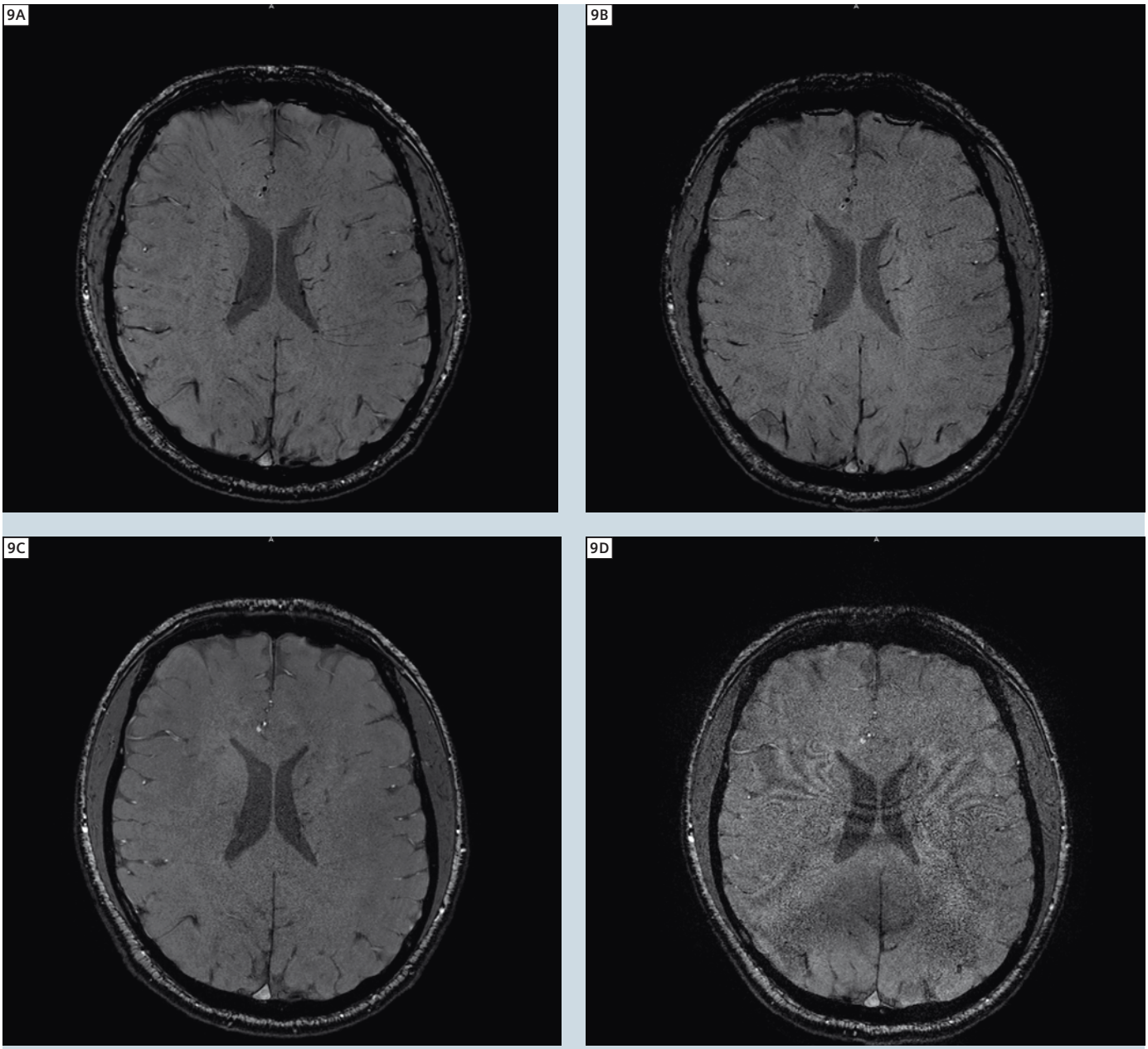

9 Susceptibility-weighted imaging (SWI) 3D FLASH (transversal orientation, PAT factor 2): PAT 2; bottom row: PAT 2x2; left column: 32-channel head coil; right column: Head Matrix coil. **32, Matrix:** SWI 3D FLASH (transversal orientation, PAT factor 2), TR 28 ms, TE 20 ms, FOV 230 × 179.6 mm², matrix 448 × 297, 72 slices per slab, slice thickness 1.2 mm, slice oversampling 22.2%, bandwidth 120 Hz/pixel, flip angle 15°, 1 acquisition, PAT mode GRAPPA, acceleration factor PE 2, reference lines PE 24, acceleration factor 3D 1, matrix coil mode auto (triple), reference scan mode integrated, coil combine mode adaptive combine, pre-scan normalize filter, TA 6:38 min; **32, Matrix:** SWI 3D FLASH (transversal orientation, PAT factor 2x2), same as above but for: acceleration factor 3D 2, reference lines 3D 24, TA 3:17 min.

32-channel head coil.

Figure 9 again demonstrates the better g-factor of the 32-channel head coil compared to the Head Matrix coil. While image quality is acceptable when using the Matrix coil at PAT 2, it becomes unacceptable when using an acceleration factor of 2×2. At this setting, the 32-channel head coil still performs well. At similar image quality, a 50% reduction of scan time from 6:38 min to 3:17 min is achievable with the 32-channel head coil.

Conclusions

The 32-channel head coil provides better performance compared to the Head Matrix coil in terms of SNR and parallel imaging capabilities. The SNR is improved over the whole head with the periphery of the brain benefitting the most. Because of the almost 3x number of coil elements, parallel imaging performance is improved i.e. the acceleration factor can be increased without imaging artifacts and with an SNR that is comparable to that of the Matrix coil at a lower PAT factor. It should also be noted that acceleration is possible in any direction with the 32-channel head coil since the coil elements are distributed on a helmet shaped geometry, thereby allowing arbitrary slice prescriptions without having to consider the direction of the acceleration.

Because of the helmet shaped form that conforms closely to the head, the 32-channel head coil has the disadvantage that some subjects with large head circumference will not be able to fit into the coil and will have to be scanned using the Matrix coil instead. Image reconstruction times can be slightly increased as well when using the 32-channel head coil since about 3 times the data volume has to be processed. However, this is not a problem in routine imaging when using the high-end image reconstruction computer.

References

1 Stapf J. 32-Channel Phased-Array Head Coil for 1.5T and 3T. MAGNETOM Flash 1/2008, 45.

2 Wald LL; Wiggins G. Highly Parallel Detection for MRI. MAGNETOM Flash 1/2008, 34–44.

3 van der Kouwe AJ, Benner T, Fischl B, Schmitt F, Salat DH, Harder M, Sorensen AG, Dale AM. On-line automatic slice positioning for brain MR imaging. Neuroimage. 2005 Aug 1;27(1):222–230.

4 Benner T, Wisco JJ, van der Kouwe AJ, Fischl B, Vangel MG, Hochberg FH, Sorensen AG. Comparison of manual and automatic section positioning of brain MR images. Radiology. 2006 Apr;239(1):246–254.

5 Scott KT. Software Compensation for Patient Position Enabling Reproducible Slice Positioning – AutoAlign. MAGNETOM Flash 1/2006, 98–103.

Contact
Thomas Benner
Athinoula A. Martinos Center
for Biomedical Imaging
Dept. of Radiology
Massachusetts General Hospital
and Harvard Medical School
Boston, MA
USA
benner@nmr.mgh.harvard.edu

Fast Clinical Protocols at 1.5T and 3T with Matrix and 32-Channel Head Coils

Thomas Benner

Athinoula A. Martinos Center for Biomedical Imaging, Department of Radiology, Massachusetts General Hospital and Harvard Medical School, Boston, MA, USA

In routine clinical MR imaging, short scan times are advantageous for patient compliance, patient throughput and image quality (images are less likely to be affected by motion) but can usually only be achieved at the cost of spatial resolution, coverage or image quality i.e. lower signal-to-noise ratio (SNR). The new 32-channel head coils for 1.5T and 3T provide better SNR and better parallel imaging performance compared to the standard 12-channel Head Matrix Coil [1, 2]. The use of these new coils should therefore allow very short acquisition times at higher acceleration factors at comparable image quality i.e. without loss of SNR and without increase in iPAT (integrated Parallel Acquisition Technique) related image artifacts. For this report, T1-weighted, T2-weighted, FLAIR, and diffusion tensor imaging (DTI) scans were performed at 1.5T (MAGNETOM Avanto, software version *syngo* MR B 15A SP2) and 3T (MAGNETOM Trio, A Tim System, software version *syngo* MR B15A SP2) with the Head Matrix coil and the 32-channel head coil, respectively. While not necessarily achieving optimal contrast at each field strength, the same imaging parameters were used at both field strengths and both head coils for ease of comparison. Echo-planar imaging (EPI) allows ultra-fast image acquisition and may therefore present an alternative to conventional imaging. For comparison, T1-weighted EPI, T2-weighted EPI and FLAIR EPI scans were acquired in addition to the conventional imaging scans.

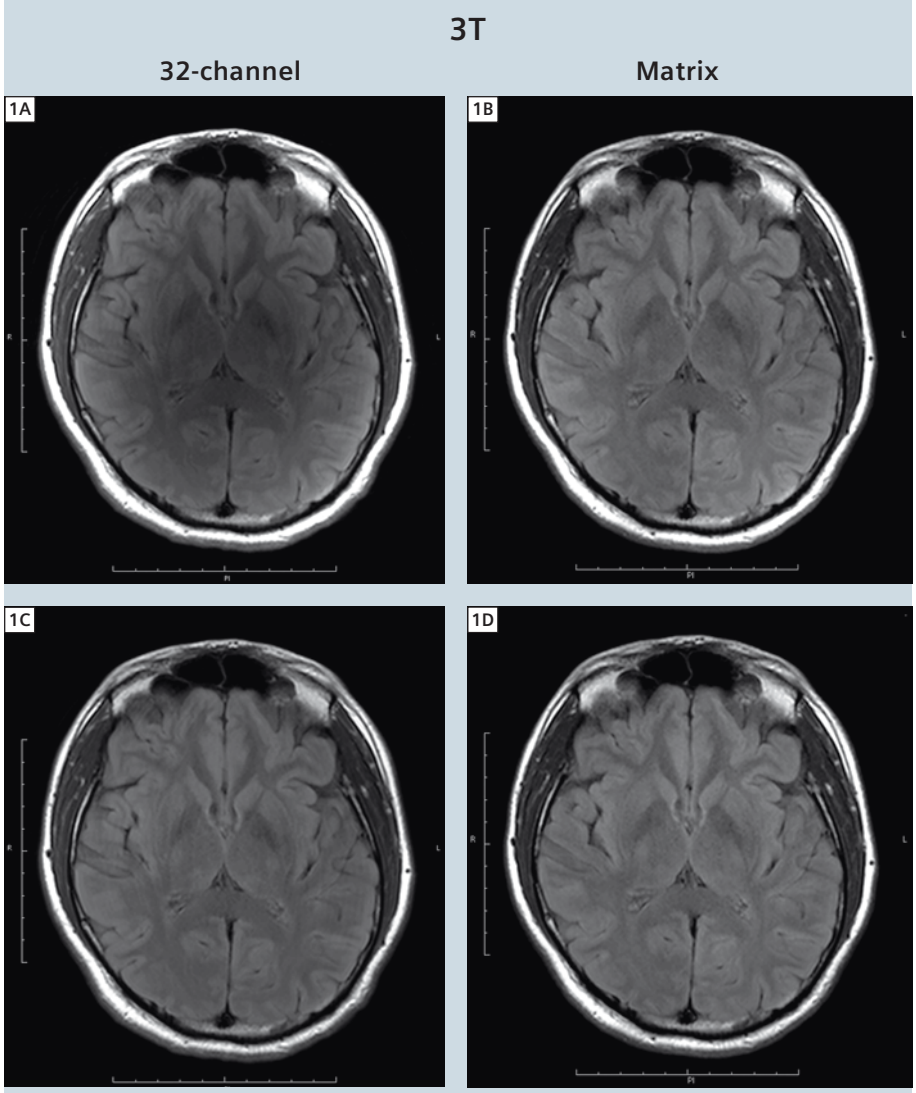

1A–D t2_tirm_tra_dark-fluid_p2; top row: unfiltered; bottom row: pre-scan normalize filter. 3T 32-channel head coil, 3T Head Matrix coil, t2_tirm_tra_dark-fluid_p2, tse, TR 7000 ms, TE 81/79 ms (3T/1.5T), TI 2500 ms, FOV 220 × 192.5 mm², matrix 256 ×224, 25 slices, slice thickness 5 mm, distance factor 20%, bandwidth 271 Hz/pixel, flip angle 120°, turbo factor 16, 1 average, 2 concatenations, iPAT mode GRAPPA, acceleration factor 2, 31 reference lines, matrix coil mode auto (triple), reference scan mode integrated, coil combine mode adaptive combine, unfiltered (top row only), pre-scan normalize filter (bottom row only), TA 2:08 min.

Altogether, four studies were performed: one study using the Head Matrix coil and one using the 32-channel head coils on each of the two MR scanners. The same healthy appearing volunteer was scanned. AutoAlign was used to ensure closely matching slice positioning between the studies [3–5]. Each study lasted about 25 minutes.
The resulting image data was compared according to

- scan type being used i.e. conventional scans vs. EPI scans,
- acceleration factor being used i.e. PAT 2 vs. PAT 3 vs. PAT 4,
- head coil being used i.e. 32-channel head coil vs. Head Matrix coil, and
- field strength being used i.e. 3T vs. 1.5T.

The performance of the image normalization filter was examined as well.

Signal intensity normalization

Smaller coil elements coupled with closer proximity of the head to these coil elements causes a more pronounced signal intensity as well as SNR gradient. To reduce the large signal intensity variations from periphery to the center of the brain a signal intensity normalization filter should be used. As expected, the signal intensity variations are larger on images from the 32-channel head coil compared to the more subtle effect on images from the Head Matrix coil (Fig. 1, top row). The signal intensity normalization (pre-scan normalize filter) works well at 1.5T and 3T (Fig. 1, bottom row). This not only applies to the conventional FLAIR scans but also to the T1-weighted, T2-weighted and EPI scans performed.

EPI vs. conventional imaging

Echo-planar imaging allows very fast image acquisition in the order of 10–100's of milliseconds per slice and should therefore allow shorter scan times than conventional imaging. However, at high spatial resolutions acceleration is essential to achieve short echo times and to reduce susceptibility induced artifacts in EPI. Parallel imaging requires the acquisition of reference lines at the beginning of the scan, lengthening the scan times by multiple times the repetition time. Thus EPI scans become comparable in duration or even exceed the duration of conventional

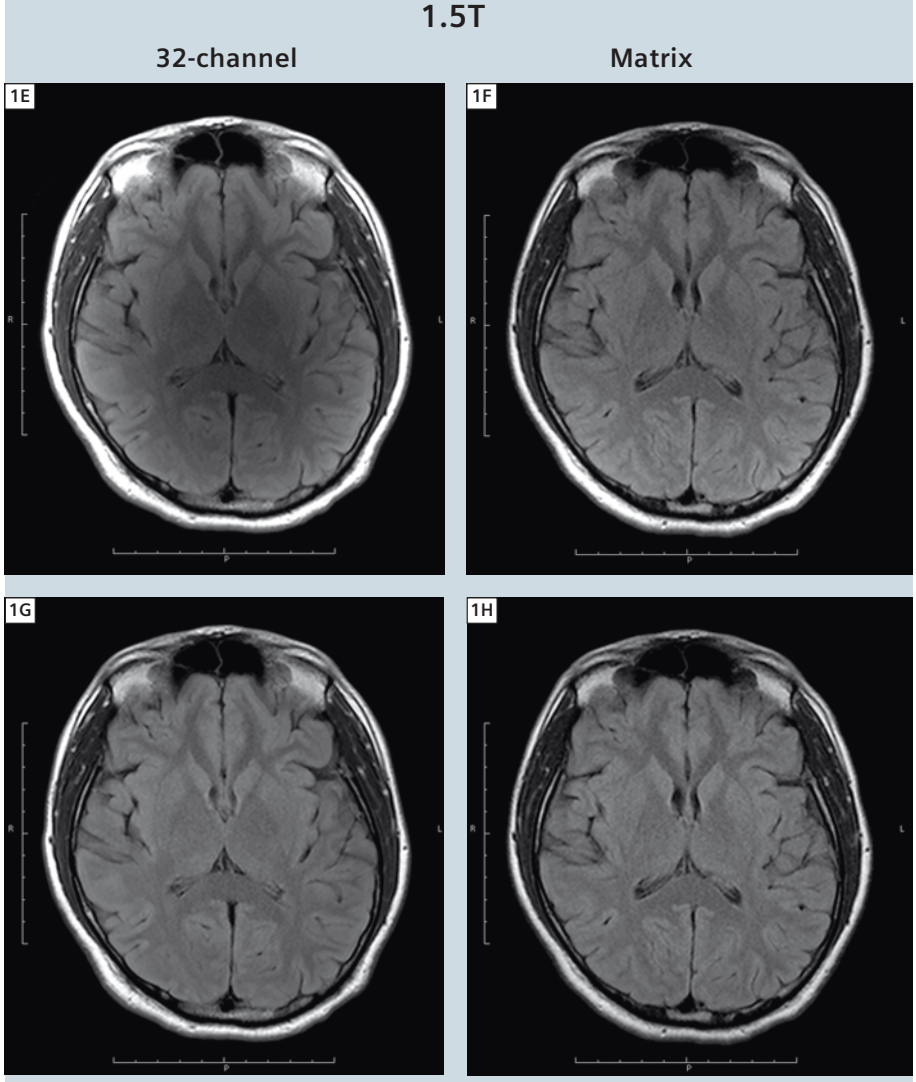

1E–H t2_tirm_tra_dark-fluid_p2; top row: unfiltered; bottom row: pre-scan normalize filter. 1.5T 32-channel head coil, 1.5T Head Matrix coil, t2_tirm_tra_dark-fluid_p2, tse, TR 7000 ms, TE 81/79 ms (3T/1.5T), TI 2500 ms, FOV 220 × 192.5 mm², matrix 256 ×224, 25 slices, slice thickness 5 mm, distance factor 20%, bandwidth 271 Hz/pixel, flip angle 120°, turbo factor 16, 1 average, 2 concatenations, iPAT mode GRAPPA, acceleration factor 2, 31 reference lines, matrix coil mode auto (triple), reference scan mode integrated, coil combine mode adaptive combine, unfiltered (top row only), pre-scan normalize filter (bottom row only), TA 2:08 min.

scans. This is also the case if multiple averages or measurements need to be acquired e.g. for increased SNR.
Figure 2 shows T2-weighted images acquired with a conventional TSE scan and an EPI scan. At similar scan times (t2_tse_tra_p2, 0:39 min vs. t2_ep2d_tra_p3, 0:24 min) the image quality of the TSE data is superior in terms of SNR, contrast, distortions and susceptibility artifacts. The same effect is shown in Figure 3 where images from conventional FLAIR scans are compared to EPI based FLAIR scans (t2_tirm_tra_dark-fluid_p3, 1:40 min vs. t2_ep2d_tra_p3, 1:47 min). At comparable scan time, the image quality of the conventional scans is superior. The same was found for the T1-weighted scans (images not shown).

Parallel imaging

A larger number of coil elements usually translates into better acceleration performance (improved g-factor) [2]. This is demonstrated in Figures 4 and 5. Increasing the PAT factor from 3 to 4 for an EPI FLAIR scan (ep2d_tra_dark_fluid_p3 to ep2d_tra_dark_fluid_p4) causes little image degradation when using the 32-channel coil at 3T (Fig. 4 A, C). A more pronounced degradation can be found at 3T when using the Head Matrix coil and at 1.5T when using the 32-channel coil (Fig. 4B, D and E, G). An already noisy image at 1.5T with PAT factor 3 is rendered unusable when increasing PAT to a factor of 4 (Fig. 4F, H). The same effect is demonstrated for PAT factor 2 vs. 3 for a conventional T1-weighted scan (t1_fl2d_tra_p2 vs. t1_fl2d_tra_p3) (Fig. 5). While there is little effect at high field with the 32-channel head coil (Fig. 5A, C), a noticeable increase in noise appears at 3T with the Head Matrix coil and at 1.5T with the 32-channel head coil (Fig. 5B, D and E, G). At 1.5T with the Head Matrix coil, an iPAT related image artifact and noise dominate the picture at a PAT factor of 3 (Fig. 5F, H).
For DTI, increasing the PAT factor from 2 to 3 and to 4 leads to a reduction of distortion artifacts. However, the additional gain is diminishing beyond a PAT factor

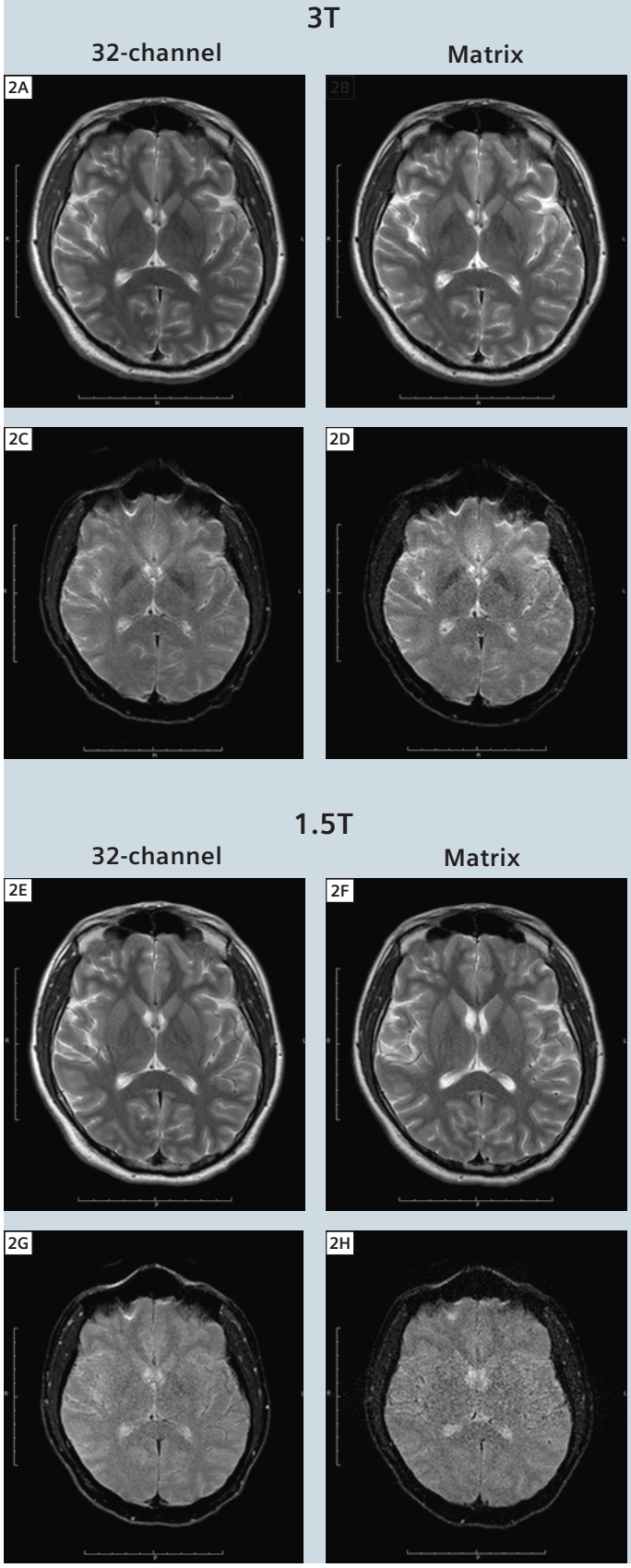

2A–H top rows: t2_tse_tra_p2; bottom rows: t2_ep2d_tra_p3; 3T 32-channel head coil, 3T Head Matrix coil, 1.5T 32-channel head coil, 1.5T Head Matrix coil.
t2_tse_tra_p2, tse, TR 6210/ 6220 ms (3T/1.5T), TE 84 ms, FOV 220 × 192.5 mm², matrix 256 × 224, 25 slices, slice thickness 5 mm, distance factor 20%, bandwidth 260 Hz/pixel, flip angle 120°, turbo factor 26, 1 average, iPAT mode GRAPPA, acceleration factor 2, reference lines 35, matrix coil mode auto (triple), reference scan mode integrated, coil combine mode adaptive combine, pre-scan normalize filter, TA 0:39 min.
t2_ep2d_tra_p3, ep2d_se, TR 2000 ms, TE 70 ms, FOV 220 × 220 mm², matrix 192 ×192, phase partial Fourier off, 25 slices, slice thickness 5 mm, distance factor 20%, fat saturation, bandwidth 1302 Hz/pixel, 1 average, iPAT mode GRAPPA, acceleration factor 3, reference lines 40, matrix coil mode auto (triple), reference scan mode separate, coil combine mode adaptive combine, pre-scan normalize filter, raw filter weak, TA 0:24 min.

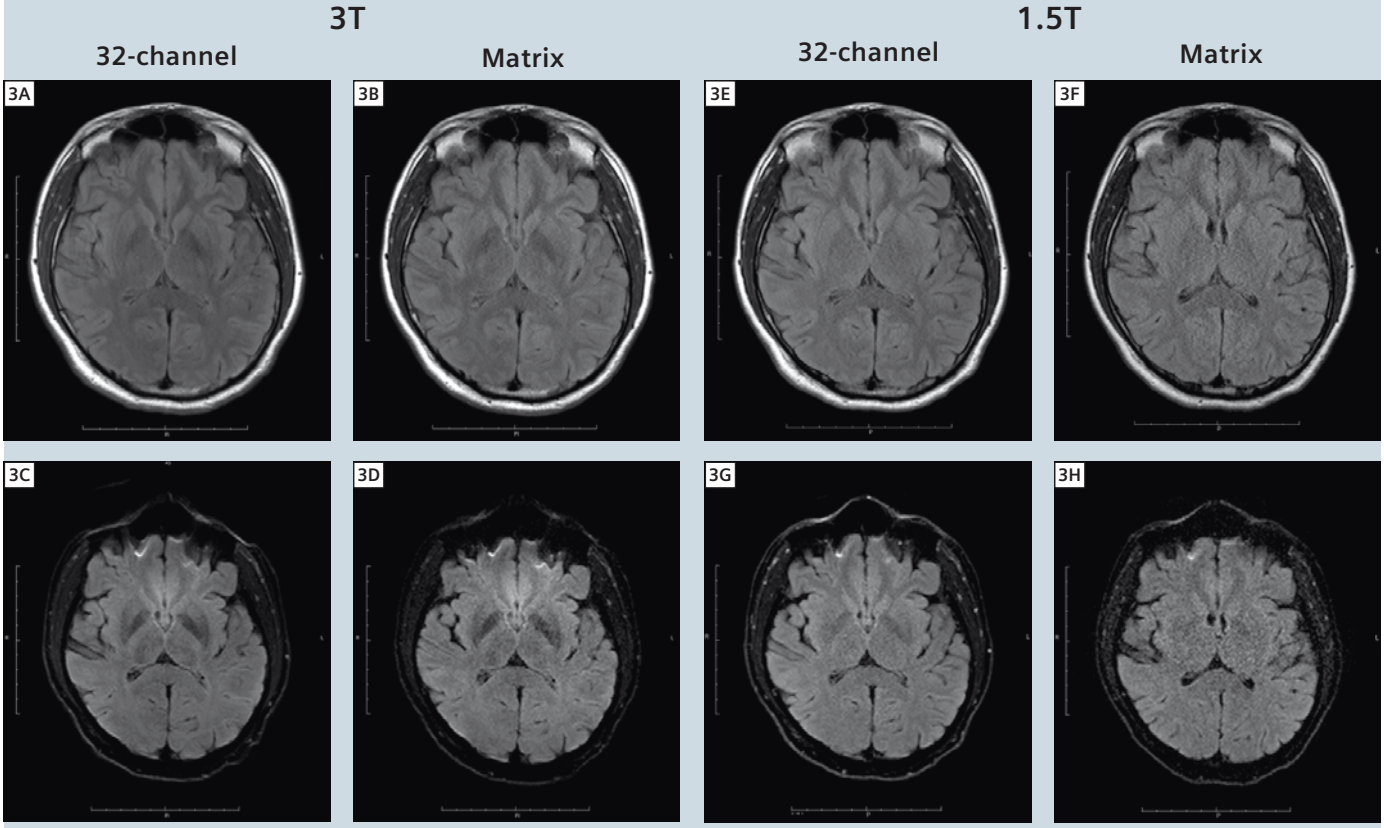

3A–H top row: t2_tirm_tra_dark-fluid_p3; bottom row: ep2d_tra_dark_fluid_p3; from left to right: 3T 32-channel head coil, 3T Head Matrix coil, 1.5T 32-channel head coil, 1.5T Head Matrix coil. t2_tirm_tra_dark-fluid_p3, tse, TR 7000 ms, TE 81 ms, TI 2500 ms, FOV 220 × 192.5 mm², matrix 256 × 224, 25 slices, slice thickness 5 mm, distance factor 20%, bandwidth 271 Hz/pixel, flip angle 120°, turbo factor 16, 1 average, 2 concatenations, iPAT mode GRAPPA, acceleration factor PE 3, reference lines PE 32, matrix coil mode auto (triple), reference scan mode integrated, coil combine mode adaptive combine, pre-scan normalize filter, elliptical filter, TA 1:40 min. ep2d_tra_dark_fluid_p3, ep2d_se, TR 15000 ms, TE 83 ms, FOV 220 × 220 mm², matrix 192 × 192, phase partial Fourier off, 25 slices, slice thickness 5 mm, distance factor 20%, fat saturation, bandwidth 1240 Hz/pixel, 2 averages, iPAT mode GRAPPA, acceleration factor 3, reference lines 40, matrix coil mode auto (triple), reference scan mode separate, coil combine mode adaptive combine, pre-scan normalize filter, raw filter weak, TA 1:47 min.

of 2. SNR is decreasing as well as making the images unusable at 1.5T with the Head Matrix coil at a PAT factor of 3. At a PAT factor of 4 only the 32-channel head coil at 3T provides sufficient SNR for interpretable images.

32-channel head coil vs. Head Matrix coil

At both field strengths, 1.5T and 3T, the 32-channel head coil shows improved image quality i.e. higher SNR and better acceleration performance for all scan types performed (Fig. 6). The increased SNR is more dominant at the periphery and less at the center of the brain, which is attributable to the gradient in coil sensitivity with distance from each coil element [1]. Because of the better g-factor of the 32-channel head coil fewer PAT related artifacts are visible even at higher PAT factors.

1.5T vs. 3T

A higher field strength (3T vs. 1.5T) translates into increased SNR when using the same head coil i.e. Head Matrix coil at 3T vs. 1.5 (Fig. 6, columns 2 vs. 4) or 32-channel head coil at 3T vs. 1.5T (Fig. 6, columns 1 vs. 3). Interestingly, the image quality (SNR) at 1.5T when using the 32-channel head coil is very comparable to the SNR when using the Head Matrix coil at 3T (Fig. 6, middle two columns). The most dramatic differences in image quality can be seen between images acquired with the Head Matrix coil at 1.5T compared to those acquired with the 32-channel head coil at 3T (Fig. 6, columns 1 vs. 4).

Conclusions

At both field strengths i.e. 1.5T and 3T, the 32-channel head coils provide image quality that is superior to that from the standard Head Matrix coil. This is mostly due to the increased SNR of the 32-channel head coil compared to the 12-channel Head Matrix coil [1]. Note, though, that the 32-channel head coils exhibit a much larger gradient in SNR

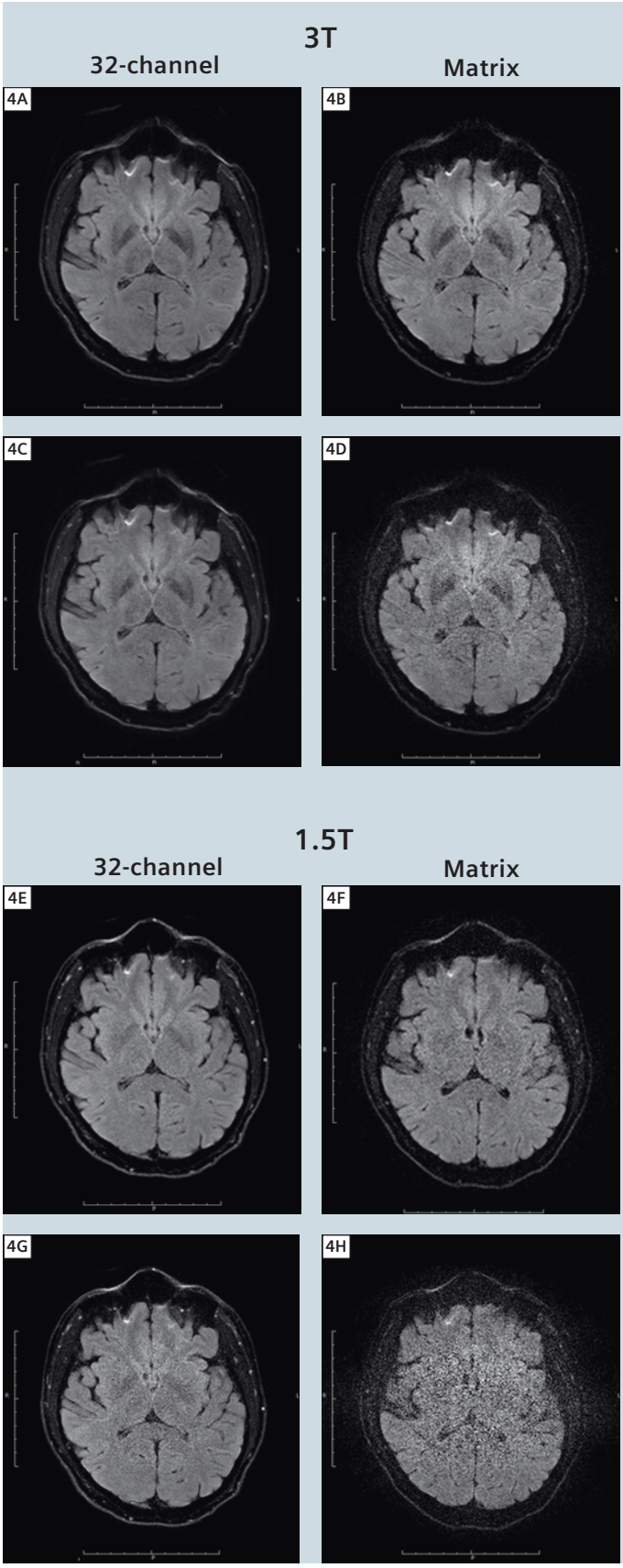

4A–H top rows: ep2d_tra_dark_fluid_p3; bottom rows: ep2d_tra_dark_fluid_p4; 3T 32-channel head coil, 3T Head Matrix coil, 1.5T 32-channel head coil, 1.5T Head Matrix coil. ep2d_tra_dark_fluid_p3, ep2d_se, TR 15000 ms, TE 83 ms, FOV 220 × 220 mm², matrix 192 × 192, phase partial Fourier off, 25 slices, slice thickness 5 mm, distance factor 20%, fat saturation, bandwidth 1240 Hz/pixel, 2 averages, iPAT mode GRAPPA, acceleration factor 3, reference lines 40, matrix coil mode auto (triple), reference scan mode separate, coil combine mode adaptive combine, pre-scan normalize filter, raw filter weak, TA 1:47 min:s. ep2d_tra_dark_fluid_p4, same as above but for: matrix 256 × 256, bandwidth 930 Hz/pixel, acceleration factor 4, reference lines 128, TA 2:02 min.

from the periphery to the center of the brain as compared to the Matrix coil, even when the latter is set to triple mode. At the center of the brain, the SNR gain was estimated at 20% compared to >100% at the cortex [1].

It was also shown that the larger number of coil elements allows higher acceleration factors to be used without significantly deteriorating image quality i.e. without causing increase in noise level and PAT related image artifacts. The prescan normalize filter works well for all coils at both field strengths to level the signal intensity gradient caused by close proximity to small local coils. No artifacts were seen in any of the scans that may have been caused by the application of this filter.

For fast T1-weighted, T2-weighted and FLAIR clinical protocols, echo-planar imaging is no alternative to conventional imaging with respect to scan times and image quality. However, EPI is unmatched in terms of SNR and acquisition speed for DTI.

Higher field strength provides the expected boost in SNR as can be appreciated in all scans performed for this study. It must be mentioned that the image quality in terms of SNR of scans performed at 1.5T with the 32-channel head coil are very comparable to the image quality of scans performed at 3T with the Head Matrix coil. In other words: for clinical head imaging the 32-channel head coil may be a worthwhile upgrade to an existing 1.5T MRI scanner. Of course, differences in image contrast between different field strengths e.g. for susceptibility-weighted imaging (SWI) [6] cannot be achieved by using the 32-channel head coil.

Table 1 lists a set of recommended protocols that allows the acquisition of T1-weighted, T2-weighted, FLAIR and DTI data in less than 5 minutes while preserving good image quality when using a 32-channel head coil. These protocols apply to both, 1.5T and 3T. However, the image quality (SNR) can be

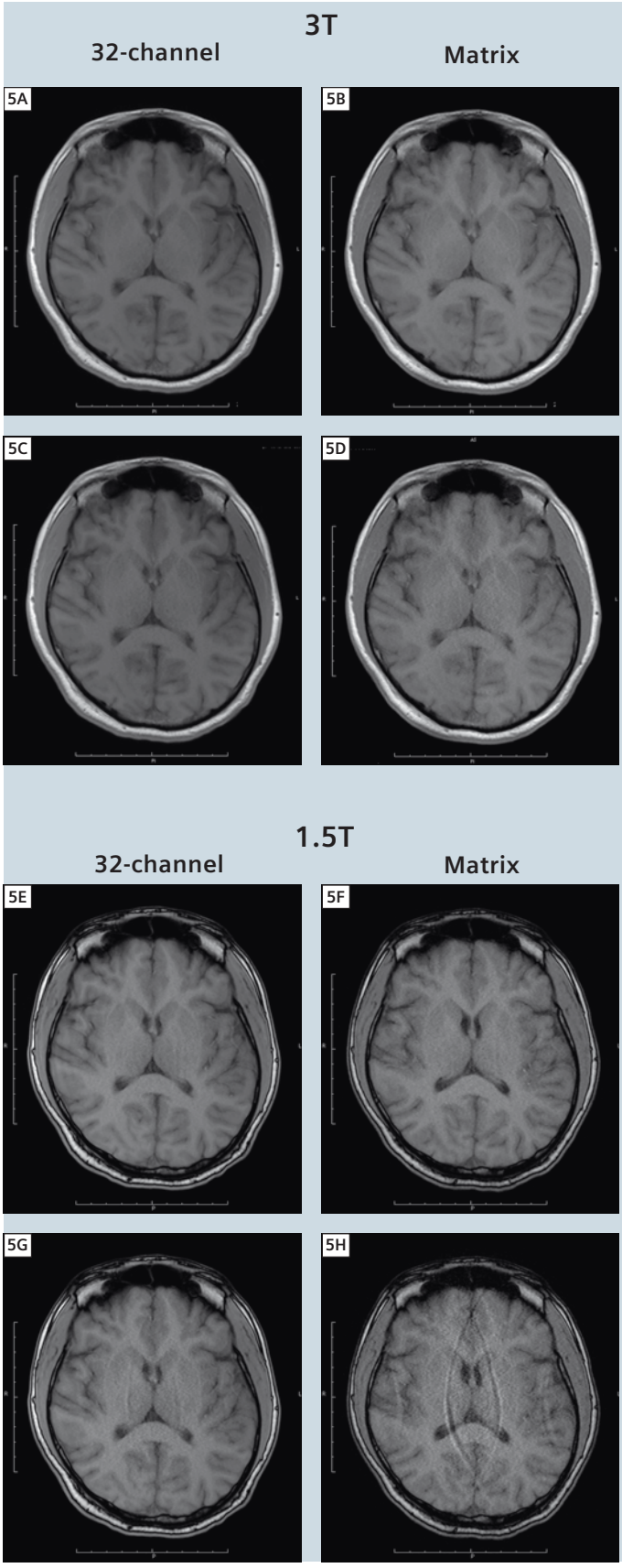

5A–H top rows: t1_fl2d_tra_p2; bottom rows: t1_fl2d_tra_p3; 3T 32-channel head coil, 3T Head Matrix coil, 1.5T 32-channel head coil, 1.5T Head Matrix coil. t1_fl2d_tra_p2, gre, TR 220 ms, TE 2.46 ms, FOV 220 × 192.5 mm², matrix 256 × 224, 25 slices, slice thickness 5 mm, distance factor 20%, bandwidth 320 Hz/pixel, flip angle 70°, 1 average, 1 concatenation, iPAT mode GRAPPA, acceleration factor PE 2, reference lines PE 24, matrix coil mode auto (triple), reference scan mode integrated, coil combine mode adaptive combine, pre-scan normalize filter, elliptical filter, TA 0:27 min. t1_fl2d_tra_p3, same as above but for: acceleration factor 3, TA 0:20 min.

improved by switching the conventional protocols from a PAT factor of 3 to 2 at the cost of slightly increased scan times. With the use of AutoAlign, these protocols can be set up to allow a "one-click" scan session i.e. after the landmarking of the patient, a single click will load the protocols into the scan queue, perform an automatic slice prescription and acquire the scans. No further user interaction is necessary. As can be seen from the figures, the automatic slice prescription with AutoAlign results in very reproducible slice locations over the course of multiple studies even at different field strength and scanner types. Due to the large number of receive channels, image reconstruction times can be slightly increased when using the 32-channel head coil although this is barely noticeable for the scans performed in this study. A minor disadvantage is the fact that the close fitting 32-channel head coils may not be large enough for some subjects. Finally, the neck array can currently not be used in combination with the 32-channel head coils thereby requiring a coil change when head and neck scans are required. In summary, the 32-channel head coils for 1.5T and 3T provide improved image quality and allow faster image acquisition at comparable image quality when using the Head Matrix coil without significant disadvantages.

Acknowledgements

I would like to thank Michael Hamm for help with data acquisition and acknowledge support from the National Center for Research Resources (P41RR14075).

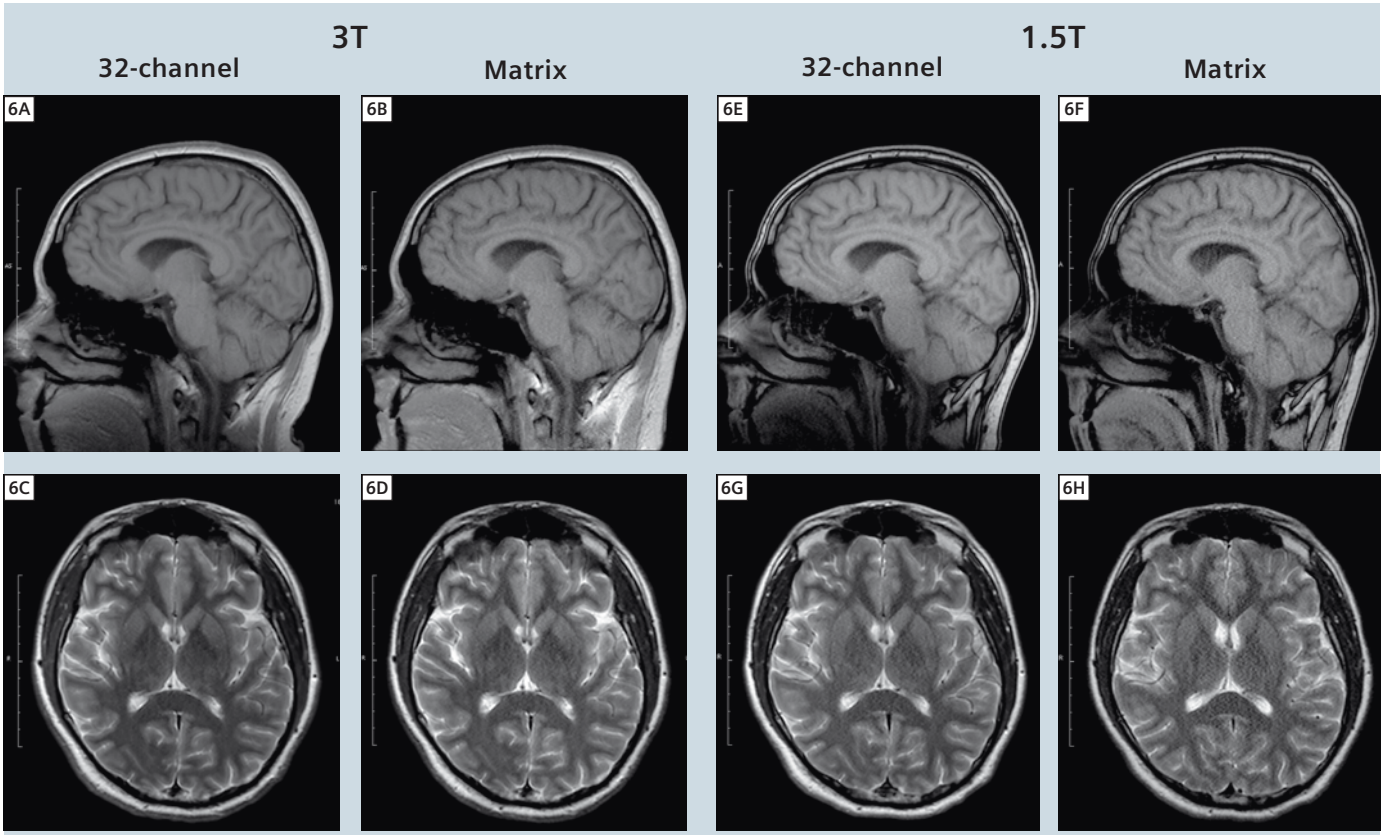

6A–T **6A-F:** t1_fl2d_sag_p3, **6C-H:** t2_tse_tra_p3, **6I-P:** t2_tirm_tra_dark-fluid_p3, **6K-R:** ep2d_diff_MDDW_6_p2 trace-weighted, **6M-T:** ep2d_diff_MDDW_6_p2 FA; t1_fl2d_sag_p3, gre, TR 280 ms, TE 2.57 ms, FOV 230 × 230 mm², matrix 256 × 256, 25 slices, SL 5 mm, distance factor 20%, BW 270 Hz/pixel, flip angle 70°, 1 average, iPAT mode GRAPPA, acceleration factor 3, reference lines 24, matrix coil mode auto (triple), reference scan mode integrated, coil combine mode adaptive combine, pre-scan normalize filter, elliptical filter, TA 0:28 min.
t2_tse_tra_p3, tse, TR 6210/6220 ms (3T/1.5T), TE 84 ms, FOV 220 × 192.5 mm², matrix 256 × 224, 25 slices, SL 5 mm, distance factor 20%, BW 260 Hz/pixel, flip angle 120°, turbo factor 26, 1 average, iPAT mode GRAPPA, acceleration factor 3, reference lines 44, matrix coil mode auto (triple), reference scan mode integrated, coil combine mode adaptive combine, pre-scan normalize filter, TA 0:33 min.

Table 1: Listing of selected short clinical protocols with scan duration. Protocols correspond to data shown in Figure 6.

Protocol	TR [ms]	TE [ms]	FoV [mm × mm]	Matrix	Bandwidth [Hz/pixel]
localizer					
AAScout					
t1_fl2d_sag_p3	280	2.57	230 × 230	256 × 256	270
t2_tse_tra_p3	6210/6220*	84	220 × 192.5	256 × 224	260
t2_tirm_tra_dark-fluid_p3	7000	81/79*	220 × 192.5	256 × 224	271
ep2d_diff_MDDW_6_p2	3900/4000*	94	220 × 220	192 × 192	1184

Note: total scan duration does not include time needed for scanner adjustments e.g. shimming. (*3T/1.5T)

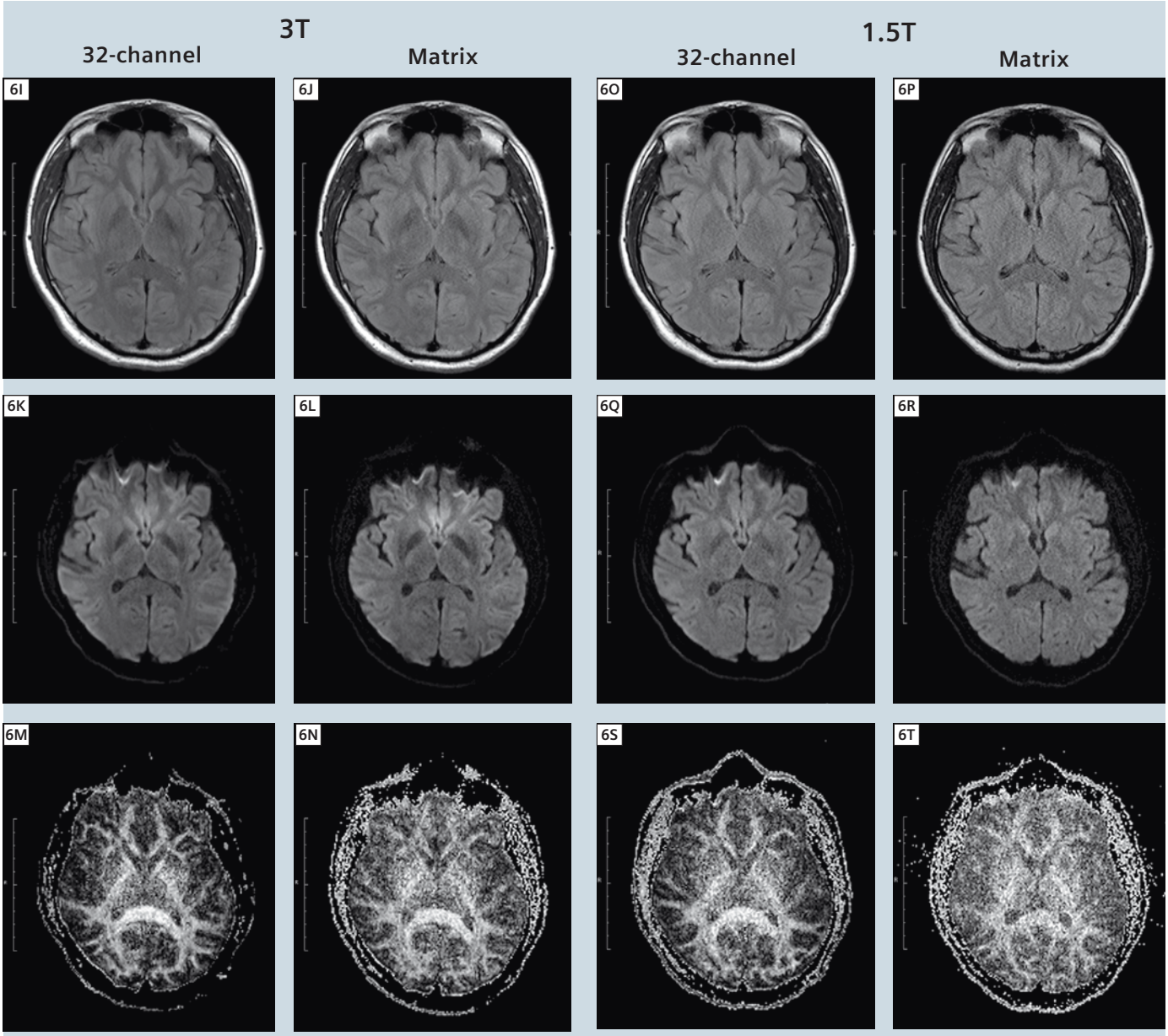

6A–T t2_tirm_tra_dark-fluid_p3, tse, TR 7000 ms, TE 81/79 ms (3T/1.5T), TI 2500 ms, FOV 220 × 192.5 mm², matrix 256 × 224, 25 slices, SL 5 mm, distance factor 20%, BW 271 Hz/pixel, flip angle 120°, turbo factor 16, 1 average, 2 concatenations, iPAT mode GRAPPA, acceleration factor 3, reference lines 32, matrix coil mode auto (triple), reference scan mode integrated, coil combine mode adaptive combine, pre-scan normalize filter, elliptical filter, TA 1:40 min. ep2d_diff_MDDW_6_p2, ep2d_diff, TR 3900/4000 ms (3T/1.5T), TE 94 ms, FOV 220 × 220 mm², matrix 192 × 192, phase partial Fourier 6/8, 25 slices, SL 5 mm, distance factor 20%, fat sat, BW 1184 Hz/pixel, 1 average, 2 diffusion weightings, b1 0 s/mm², b2 1000 s/mm², 6 diffusion directions, iPAT mode GRAPPA, acceleration factor 2, reference lines 40, matrix coil mode auto (triple), reference scan mode separate, coil combine mode adaptive combine, pre-scan normalize filter, raw filter, TA 0:41 min.

References

1 Stapf J. 32-Channel Phased-Array Head Coil for 1.5T and 3T. MAGNETOM Flash 1/2008, 45.
2 Wald LL; Wiggins G. Highly Parallel Detection for MRI. MAGNETOM Flash 1/2008, 34–44.
3 van der Kouwe AJ, Benner T, Fischl B, Schmitt F, Salat DH, Harder M, Sorensen AG, Dale AM. Online automatic slice positioning for brain MR imaging. Neuroimage. 2005 Aug 1;27(1):222–230.
4 Benner T, Wisco JJ, van der Kouwe AJ, Fischl B, Vangel MG, Hochberg FH, Sorensen AG. Comparison of manual and automatic section positioning of brain MR images. Radiology. 2006 Apr;239(1):246–254.
5 Scott KT. Software Compensation for Patient Position Enabling Reproducible Slice Positioning – AutoAlign. MAGNETOM Flash 1/2006, 98–103.
6 Haacke EM, Xu Y, Cheng YC, Reichenbach JR. Susceptibility weighted imaging (SWI). Magn Reson Med. 2004 Sep;52(3):612–618.

Contact
Thomas Benner
Athinoula A. Martinos Center
for Biomedical Imaging
Dept. of Radiology
Massachusetts General Hospital
and Harvard Medical School
Boston, MA
USA
benner@nmr.mgh.harvard.edu

Improving High Resolution fMRI at 3T with the 32-Channel Head Array

Christina Triantafyllou[1,2]; Lawrence L. Wald[2,3]

[1]Athinoula A. Martinos Imaging Center, McGovern Institute for Brain Research, Massachusetts Institute of Technology, Cambridge, MA, USA
[2]Athinoula A. Martinos Center for Biomedical Imaging, Department of Radiology, Massachusetts General Hospital, Boston, MA, USA
[3]Harvard-MIT Division of Health Sciences and Technology, Massachusetts Institute of Technology, Cambridge, MA, USA

Introduction

It is well known that BOLD (Blood Oxygenation Level Dependent) effects increase in amplitude at higher field strength, due to the general enhancement of susceptibility contrast resulting in improvements in BOLD sensitivity and specificity. Nevertheless, identifying additive methods of improving BOLD imaging are also worth pursuing. In particular, the new generation of highly parallel brain arrays offers a potential adjuvant approach to high field functional MRI (fMRI). These close-fitting, highly parallel detection arrays allow impressive increases in image signal-to-noise ratio (SNR) in cortical areas and increases in iPAT (integrated Parallel Acquisition Technique) acceleration, helpful for mitigating image distortion in EPI (Fig.1) [1, 2]. It is nonetheless important to closely examine their benefits for fMRI, since the fMRI experiment is limited by physiological fluctuations in the time-series SNR (tSNR) rather than in the image SNR (SNR_0).

In this paper, we review our findings on the benefits of 32-channel receive arrays for the time-series SNR in the fMRI experiment and validate the sensitivity gains in two illustrative fMRI examples; retinotopy of the primary visual system and speech motor region activation. We show that highly parallel detection offers a powerful adjuvant method to high field fMRI, especially when high resolution brain mapping is desired. The article is organized in two parts. First we characterize the fMRI time-series fluctuations (noise) for different coils and image resolution combinations as a metric for potential improvements in fMRI sensitivity. Second we show results from two real world fMRI experiments.

Physiological noise in fMRI time-series SNR using array coils

Our ability to detect small changes in image intensity associated with subtle brain activation in the fMRI time-series is limited by physiologically induced image intensity modulations (physiological noise). Thus, the noise in fMRI is not the traditional image noise important for anatomical imaging, but arises from the interplay between the imaging and physiological processes which occur during the time-series. The time-series SNR (tSNR) is the most important metric for determining the smallest activation effect which can be seen in a given fMRI experiment. It is defined as a pixel's mean intensity divided by the standard deviation of this intensity over time. In contrast, the image SNR (SNR_0) is defined as the image intensity divided by the noise in that image (traditionally taken as the standard deviation in the image background area, although this definition is problematic for arrays).

Previous studies of the physiological noise in fMRI time-series have shown that it acts as a modulation of the image intensity with time [3, 4]. Thus, as the signal gets stronger (from higher field scanners or an improved head coil), then the physiological noise grows proportionally, since the noise level is a fixed percentage of the signal level. This is problematic in that at first glance it appears that improving detection sensitivity with array coils will not translate to improved tSNR for fMRI. Namely, gains in image sensitivity are offset by proportional gains in physiological noise. Defining σ_p as the physiological noise standard deviation, and S as the image signal intensity, Krüger and colleagues showed this scaling relationship; $\sigma_p = \lambda S$, where λ is a constant. But, the total time-series noise is the statistical sum of the physiological noise, σ_p, and the conventional image noise, σ_o, thus the potential benefit of improvements in array technology (which improves image SNR) will depend on the relative importance of these two noise sources. For example, as the voxel size is decreased, we expect thermal image noise to dominate and improvements in array technology will translate

to improved fMRI time-series SNR (tSNR). Thus, we sought to examine the benefits of high-N arrays on the tSNR in fMRI experiments of different image resolutions and using a range of head coils. At different image resolutions the time series noise can be expected to derive from varying ratios of physiological to image noise. Furthermore, since many fMRI studies now use iPAT to reduce the image distortion associated with single shot EPI, and since iPAT alters the image noise, we examine the effect of iPAT on fMRI time-series SNR by varying the degree of acceleration for a number of image resolutions commonly used in fMRI.

Methods

To evaluate the physiological noise in fMRI, resting state EPI time-series were collected at 3T on a MAGNETOM Trio, A Tim System, using a single-shot gradient echo EPI sequence and three different receive RF coils; a transmit/receive volume head coil (Birdcage), the 12-channel Matrix receive-only head coil, and the 32-channel receive-only phased array head coil. All subjects were asked to relax while in the scanner; no specific stimulus was applied. Written consent was obtained from all the subjects under protocols approved by institutional review. To achieve accurate comparison between the coils, the same four healthy volunteers were scanned.

Data were collected parallel to the AC-PC line at six different in-plane resolutions (1 x 1 mm^2, 1.5 x 1.5 mm^2, 2 x 2 mm^2, 3 x 3 mm^2, 4 x 4 mm^2 and 5 x 5 mm^2). Other imaging parameters were: slice thickness = 3 mm, TR = 5400 ms, TE = 30 ms, 60 time points, flip angle = 90°. Figure 2 shows example images from the 1 x 1 mm^2 data set acquired with the 32-channel array.

The use of array data requires a more complex analysis to generate SNR_0 in a way that renders it directly comparable to time-series measurements [5]. After

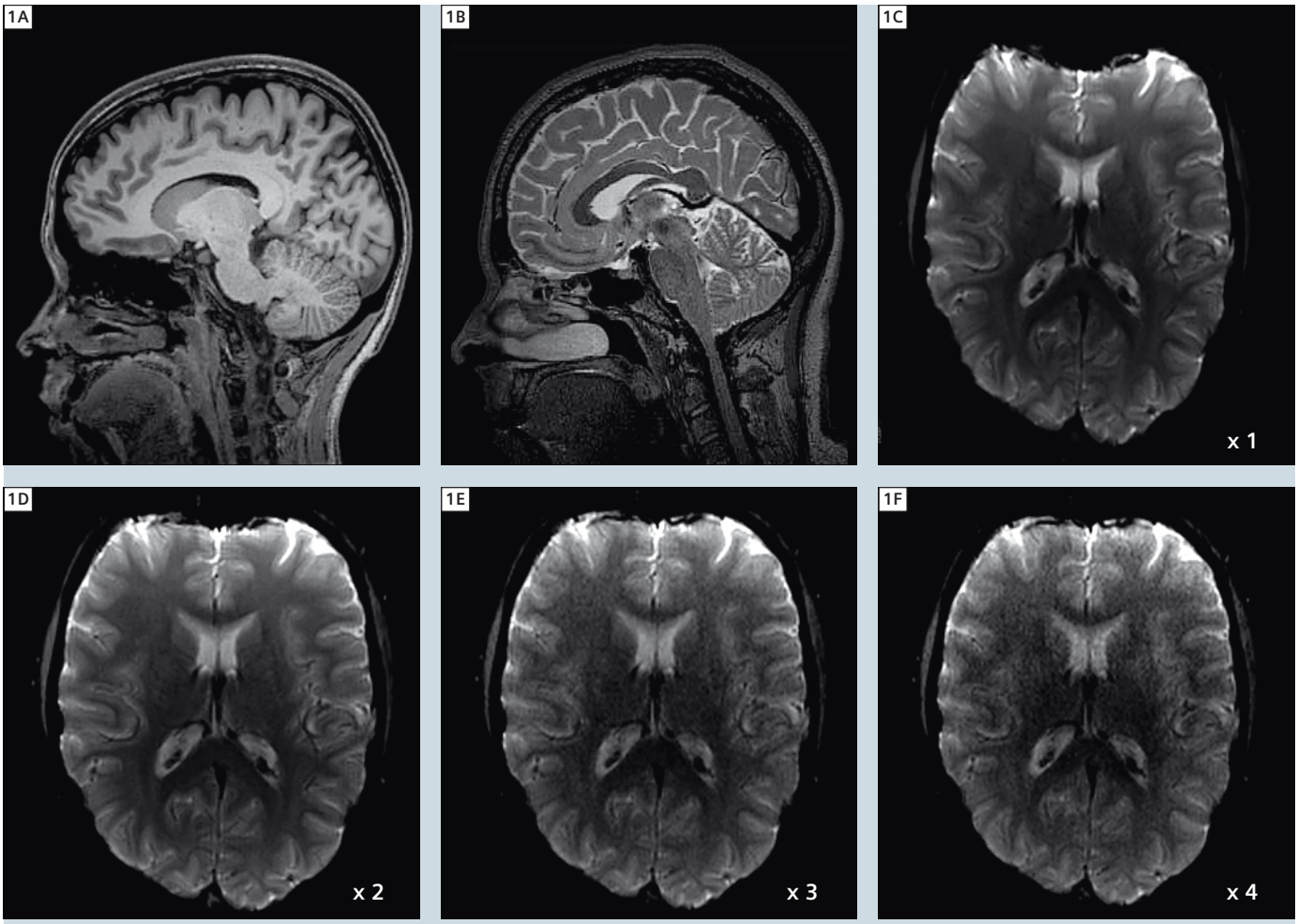

1 High resolution images acquired with the 32-channel coil. **A:** T1-weighted 3D MPRAGE (1 mm isotropic). **B:** T2-weighted 3D-SPACE (0.6 mm isotropic). **C–F:** Single-shot gradient echo EPI images acquired at 1 x 1 x 3 mm^3, TE = 30 ms, with GRAPPA acceleration factors of 1–4, respectively (1 = no acceleration).

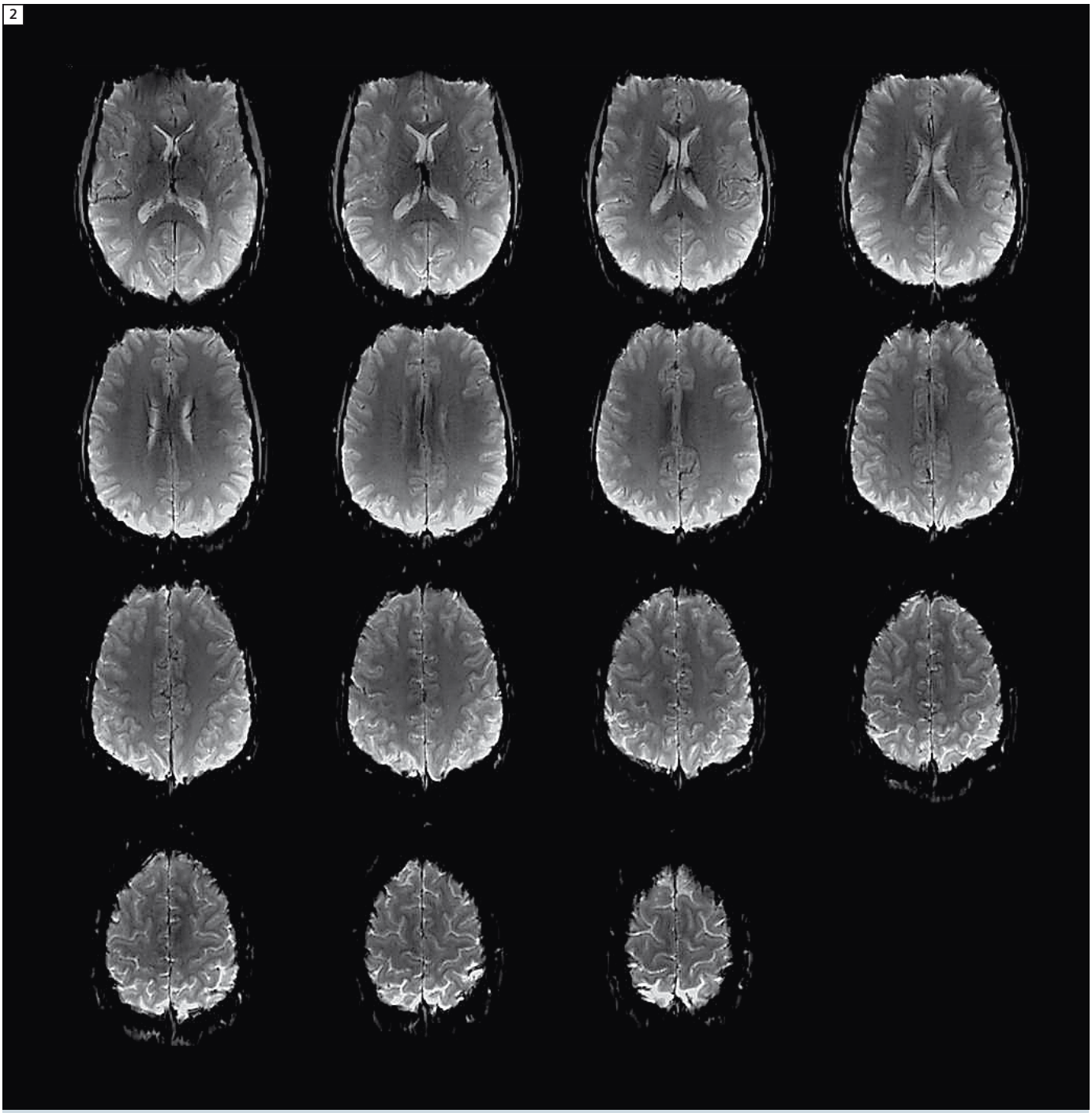

2 Resting state gradient echo 32-channel EPI images acquired at 1 x 1 x 3 mm^3 with TE = 30 ms.

motion correction, time-series SNR maps (tSNR) were estimated as the ratio of the mean pixel intensity across time points to the temporal standard deviation. Measurements of tSNR and SNR_0 were evaluated in a cortical gray matter region-of-interest (ROI) and tSNR was plotted as a function of SNR_0 for the different in-plane resolutions and receive coils. The data were fit to the model of Krüger et al. [3]. EPI time-series were also collected at three resolutions (2 x 2 x 2 mm^3, 3 x 3 x 3 mm^3, 3 x 3 x 5 mm^3) using iPAT (*syngo* GRAPPA) with acceleration factors of 1, 2, 3 and 4 at each resolution.

Results

Figure 3 shows SNR_0 as a function of voxel volume for the 3 different coils. As expected, the SNR_0 is nearly linear in

voxel volume and at each resolution the sensitivity is substantially improved in the cortex when the 32-channel array is used. For example, for the isotropic 3 mm voxel, the 32-channel SNR_0 was 1.2 fold higher than that of the 12-channel array. The results shown in Figure 4 suggest that the relationship between tSNR and SNR_0 can be well parameterized by the Krüger model at different resolutions and for array data. Namely, when SNR_0 is modulated by coil performance and image resolution, the physiological noise is well modeled as proportional to the signal. At low values of SNR_0 (small voxels or lower coil performance), the tSNR is dominated by thermal image noise and grows linearly with SNR_0. As the image SNR increases (above approximately 200), then the curve approaches an asymptote and additional improvement in SNR_0 does not translate to substantial gains in tSNR. Since the highly parallel array coils chiefly increase image SNR, this suggests that their biggest benefits for fMRI (tSNR) will be for higher image resolutions where SNR_0 is below 200. For example, the 32-channel coil increased the tSNR of the 1.5 x 1.5 x 3 mm^3 acquisition by 57% compared to the 12-channel coil. At lower resolutions however, (e.g. 5 x 5 x 3 mm^3) the increase was only 13%.

Figure 5 shows the tSNR as a function of resolution at acceleration rates R=1, 2, 3, 4. The tSNR decreases at higher resolutions as expected, but is also reduced as R increases in all cases.

For example, at the lowest resolution used (3 x 3 x 5 mm^3), tSNR decreased by 34% between the R = 1 and R = 4 acquisition showing that the improvement in susceptibility distortion afforded by iPAT comes at a cost in time-series SNR. For the higher resolution (2 x 2 x 2 mm^3) the percentage decrease in tSNR between R = 1 to R = 4 is the greatest; 43%.

3

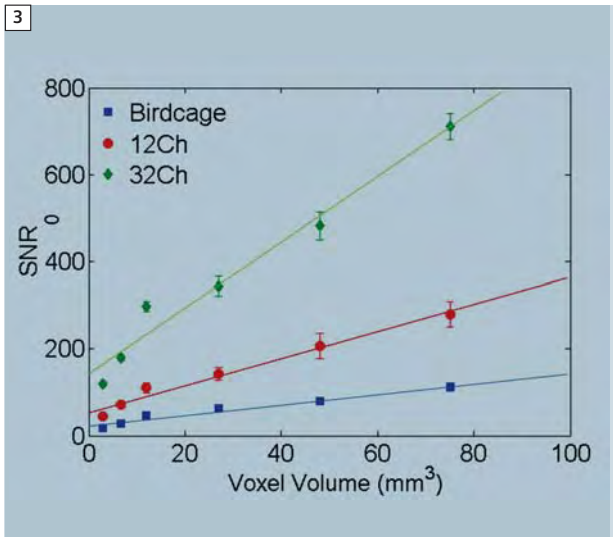

3 Image SNR (SNR_0) as a function of voxel volume. Lines are linear least-squares fit to the data.

4

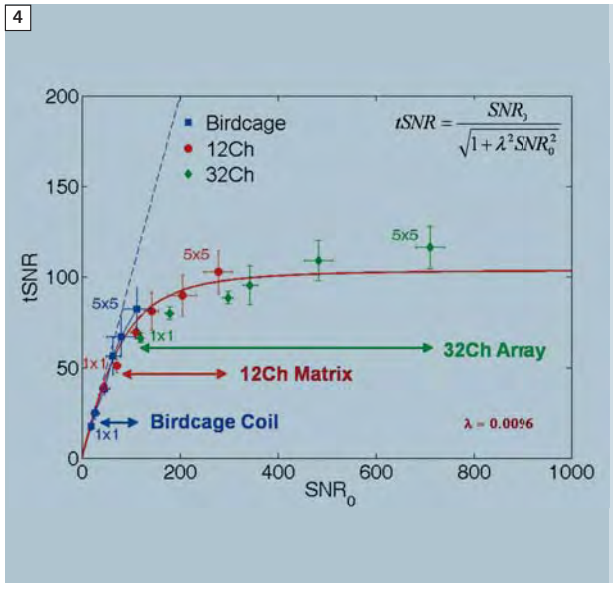

4 SNR in fMRI time-series (tSNR) as a function of image SNR (SNR_0) for different spatial resolutions. Changes in image SNR were produced by varying the voxel volume and coils. Squares, circles and diamonds represent the 3T data for birdcage coil, 12-channel and the 32-channel array coil respectively. Measurements derived from areas of cortical gray matter and are averages over four subjects. The dotted line represents the line of identity (tSNR = SNR_0) which should parameterize the data in the absence of physiological noise, and the solid line shows the Krüger noise model fit to all the data points.

5

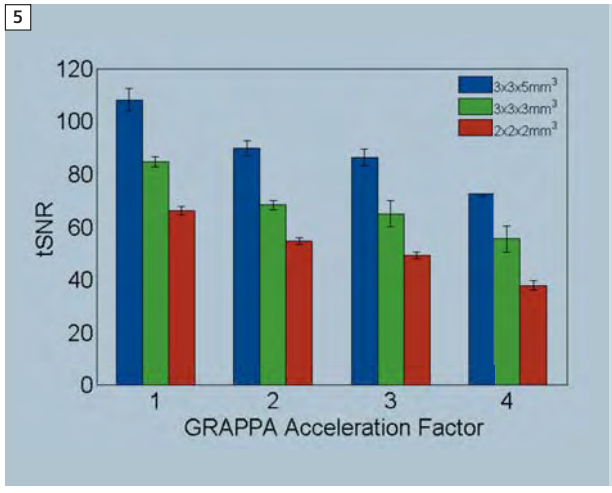

5 SNR in fMRI time-series (tSNR) as a function of acceleration factor at different spatial resolutions using the 32-channel coil. Measurements derived from areas of cortical gray matter and are averages over four subjects.

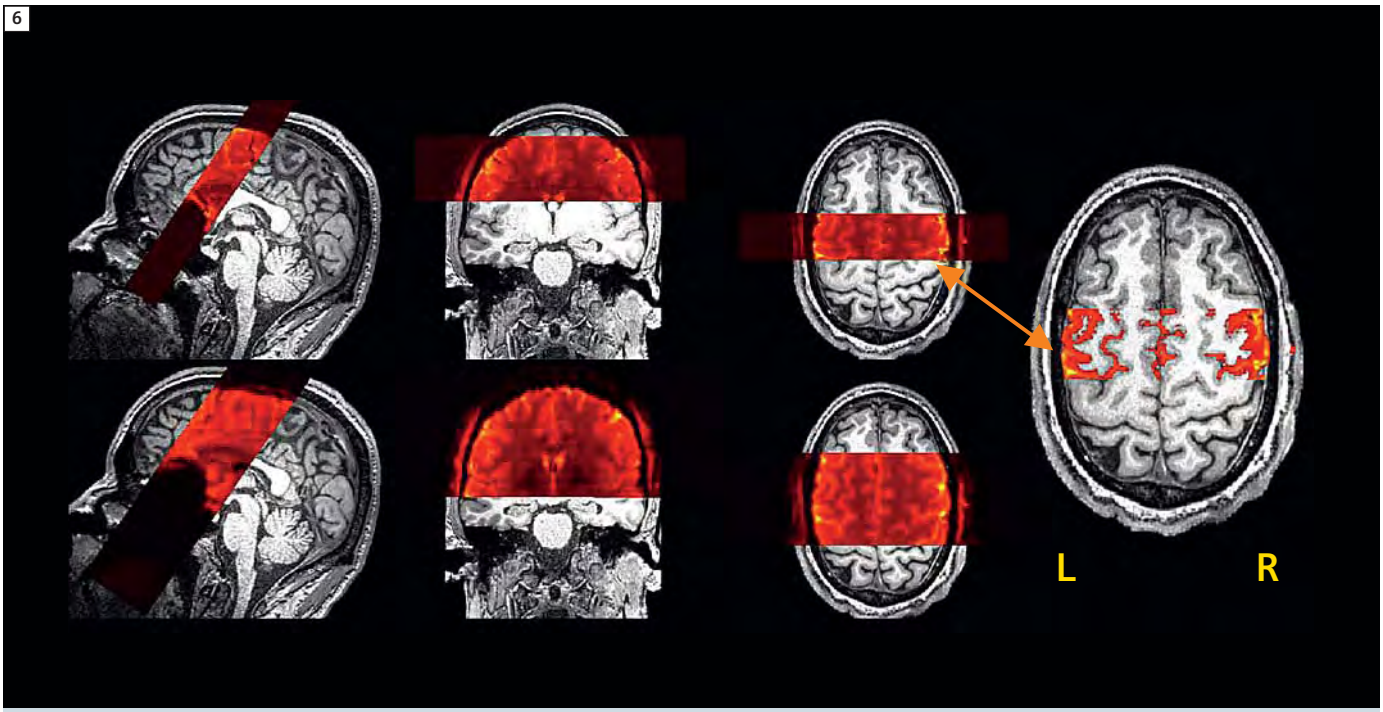

6 EPI slice prescription superimposed onto the high resolution 0.6 mm isotropic T1-weighted MPRAGE; top row 1 mm isotropic EPI data, bottom row 2 mm isotropic data, both acquired with 32-channel coil. Image on the right shows a thresholded EPI image and its correspondence to the T1-weighted anatomy. *(Figure courtesy of S. Ghosh, MIT.)*

Functional MRI applications

a) High-resolution fMRI using a 32-channel coil to identify individual-specific speech motor regions

Previous studies of overt speech sequencing [6] have reported activity in several brain regions such as ventral motor and pre-motor cortex, frontal operculum, posterior inferior frontal gyrus, supplementary motor area (SMA) and the pre-SMA. However, it has been difficult to reliably identify precise locations of activity in individuals because high spatial resolution is needed to resolve the ventral motor regions of the frontal lobe and the activation is weak for experiments limited to an individual. The spatial resolution problem is especially problematic for conventional resolutions (3 mm^2 x 3 mm^2) and when spatial smoothing is needed in the statistical analysis. In this study, we will utilize the added sensitivity of the 32-channel coil to allow higher spatial resolution at acquisition in conjunction with reduced spatial smoothing in the analysis, to allow the identification of the ventral motor regions in individual subjects and dissociate the clusters of activity around the frontal operculum and the supplementary motor area.

Methods

High-resolution single-shot gradient echo EPI time-series were acquired using the 32-channel phased array head coil. Written consent was obtained from all the subjects under protocols approved by institutional review. The imaging parameters were: TE = 30 ms, flip angle = 90°, TR = 12 s, TA = 2.5 s, TR delay = 9.5 s, *syngo* GRAPPA reconstruction with acceleration factor of 2. Twenty five 1 mm thick slices were acquired with a inter-slice gap of 0.1 mm, and in-plane resolutions of 1 x 1 mm^2, FOV = 192 x 192 and matrix size = 192 x 192. Slices were positioned so that they cover the SMA passing through the ventral pre-motor cortex (Fig. 6, top row). A second set of images with FOV = 256 x 256 and matrix size = 128 x 128 also acquired with in-plane resolution 2 x 2 mm^2, and slice thickness of 2 mm, (Fig. 6, bottom row). For comparison, 2 mm isotropic data was also acquired using the 12-channel Head Matrix coil. High resolution T1-weighted structural data was collected using an MPRAGE pulse sequence with isotropic voxel dimensions of 0.6 mm. Participants were asked to perform a speech task consisting of 3 conditions:

a) speaking complex sequences of complex syllables (e.g., stra-spli-stru),
b) speaking simple sequences of simple syllables (e.g., ba-ba-ba), and
c) passively viewing the letter string (e.g., xxx-xxx-xxx) (baseline).

Statistical analysis was performed using SPM5 (Wellcome Department of Cognitive Neurology, London, UK), including motion correction, smoothing and General Linear Model (GLM) fitting. The 1 mm and 2 mm data were smoothed with 2 mm and 4 mm FWHM Gaussian kernels respectively. Two contrasts were evaluated:

A) speaking trials compared to baseline trials; and
B) complex trials compared to simple trials.

Results

Data from a single subject are shown in Figure 7 illustrating the t-statistics derived from contrast B; complex sequences compared to simple syllables. Activity in the anterior bank of the precentral sulcus is found in all three acquisitions (1 mm isotropic 32-channels, 2 mm isotropic 32-channels and 2 mm isotropic 12-channels), however the 32-channel coil showed significantly greater sensitivity to the task than the 12-channel Head Matrix coil. Figure 8 demonstrates data from a different individual where activation with 12-channel coil was not detected compared to the 32-channel coil that exhibited activation patterns even at higher resolution (1 mm isotropic).

In this functional MRI study we show that the higher sensitivity of the 32-channel array translates directly into improved detection capability for detecting speech motor activation in individual subjects. Using a high-resolution EPI protocol with the 32-channel coil, we were able to demonstrate sulcal bank specific localization of speech motor activity related to the production of complex sequences of syllables. The amount of required smoothing was limited to the minimum, thus preventing extensive smearing of activity across sulcal banks, bringing the location of the significant voxels to an accurate correspondence with the brain gray matter as identified in the high resolution MPRAGE. This was a significant improvement in localization compared to conventional 3 mm isotropic resolution scans coupled with 6 mm smoothing. In conclusion, our findings demonstrate that employing high-resolution acquisition and highly parallel detection, it is possible to achieve accurate individual-specific mapping of cognitive task related brain networks and enables the examination of individual variability of the structure-function relationship.

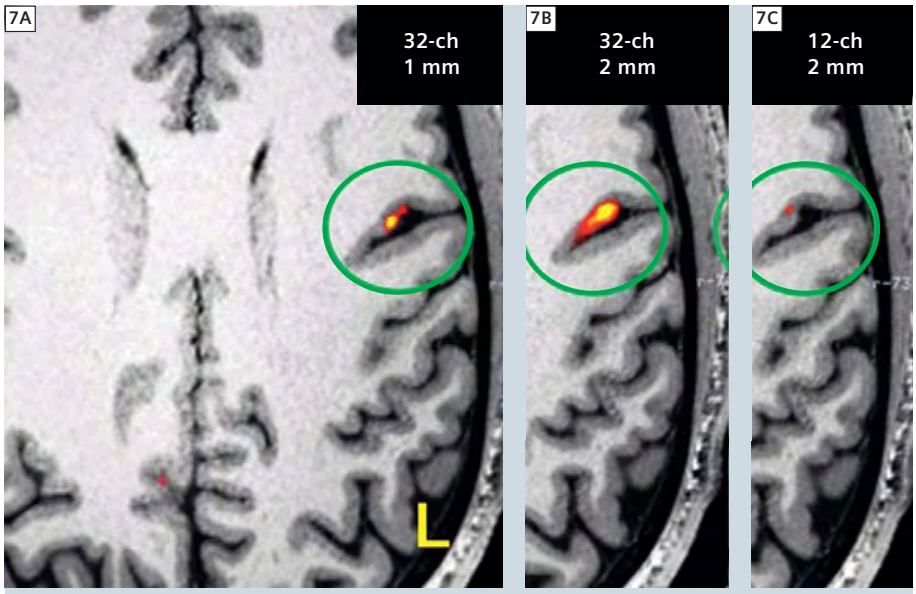

7 Activation map (t-statistics) of a single subject overlaid on the 0.6 mm isotropic T1-weighted structural scan. Data acquired with the 12-channel coil are shown at the far right (2 mm isotropic), while 32-channel data are shown at the center (2 mm isotropic) and on the left (1 mm isotropic). Direct comparison of the BOLD activity exhibits higher significance with the 32-channel compared to 12-channel data. Red and yellow indicate lower and higher significance, respectively (FDR = 0.05). *(Figure courtesy of S. Ghosh, MIT.)*

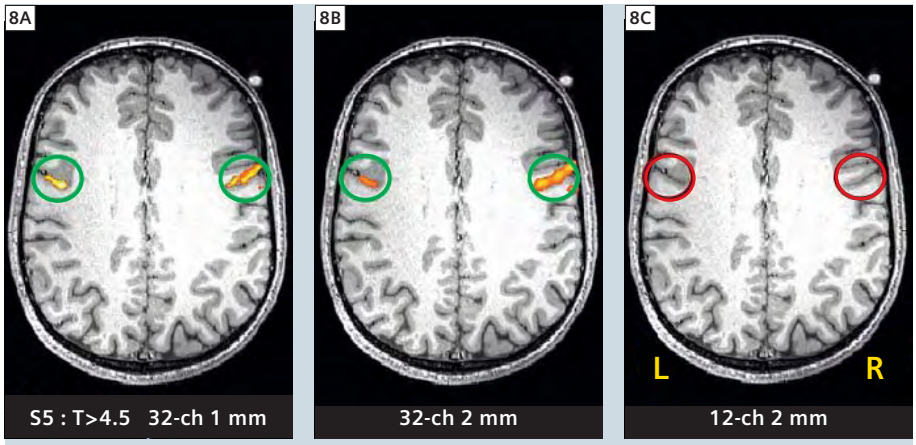

8 Activation map (t-statistics) from another subject, overlaid on the 0.6 mm isotropic T1-weighted structural scan. Activation is present on the 32-channel data, **(A)** and **(B)** green circles, while no activation was detected when using the 12-channel coil **(C)**, red circles. *(Figure courtesy of S. Ghosh, MIT.)*

b) High-resolution fMRI using a 32-channel coil to improve the accuracy of visual field mapping

The visual cortex consists of distinct histologically and functionally defined areas arranged topographically based on visual space. Thus, there is a direct topographic mapping of the visual field onto the cortical surface which can be used to identify the boundaries of these areas. This orderly representation is likely to play a critical role in how people process visual information, but it is also often used as a functional marker to locate primary and secondary visual areas in individual subjects as a first step in an fMRI experiment. The mapping of functional boundaries allows a better understanding of the relationships between activation in more complex visual processing experiments. It is important that this initial survey of occipital cortex is robustly and quickly accomplished in each individual subject, so that the bulk of the examination can be devoted to further studies of the workings of the visual system.

In this study we evaluate the potential benefit of highly parallel detectors on the accuracy of fMRI-based mapping of the visual cortex. The visual field mapping benchmark was chosen because the neural organization of primary visual cortex is well understood yet its exact mapping is routinely needed. Furthermore, this benchmark assesses the effect of the array on a more complex fMRI analysis; the quality of boundary estimation is even further dissociated from a simple metric such as image SNR than the more direct measure of activation statistics explored above. Our findings demonstrate that using the 32-channel array provides almost a four-fold decrease in acquisition time needed for a robust estimate of the boundary between visual cortical areas V1 and V2 compared to the 12-channel coil.

Methods

Data from the two healthy subjects were acquired using the product 12-channel and 32-channel head coils (i.e. each subject was scanned twice). Written consent was obtained from all the subjects under protocols approved by institutional review. Functional MRI data acquired using a single-shot gradient echo EPI sequence. Imaging parameters were: TR = 2000 ms, TE = 30 ms, flip angle = 90°, twenty-eight 2 mm thick slices with inter-slice gap of 0.2 mm and an in-plane resolution of 2 x 2 mm^2 with FOV = 192 x 192 and matrix = 96 x 96. A high resolution T1- weighted structural scan was acquired using an MPRAGE pulse sequence (voxel size of 1 x 1 x 1 mm^3, TR/TI/TE/flip angle = 2530 ms / 1100 ms / 3.48 ms / 7°) and used for slice prescription and to generate the cortical surface for flattened representation of the visual activation. The visual field was mapped using a standard fMRI-based phase-encoded retinotopy paradigm consisting of flickering expanding and contracting rings and clockwise and counterclockwise rotating wedges presented in runs lasting 8 minutes each. A single functional run performed with the 32-channel coil was compared to the average of up to five runs acquired with the 12-channel Head Matrix coil.
The visual field representation for each

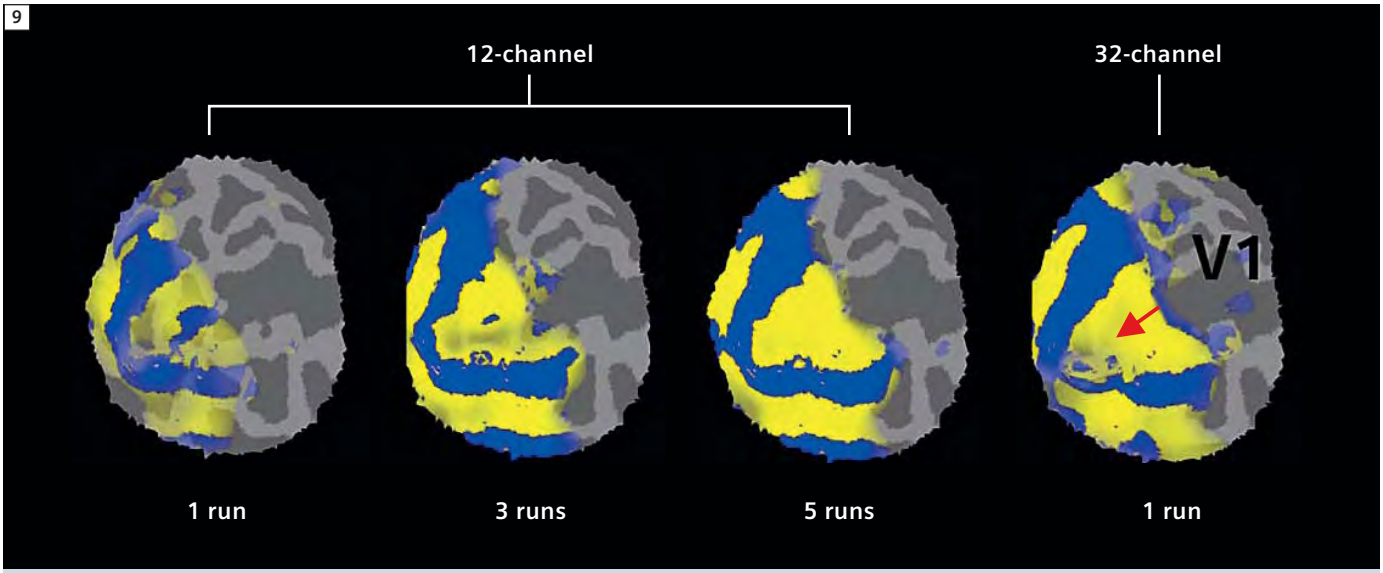

9 Qualitative comparison in the accuracy of visual field mapping for both 32-channel and 12-channel coils. The same flattened patch of the occipital lobe (left hemisphere in an individual subject) is shown with the field-sign computed from different number of scans and different coils. The color (yellow or blue) indicates the handedness of the local coordinate system of the visual field mapping, while the opacity of the color indicates significance of the fit of the measured BOLD signal to the expected response to the visual stimulus. The single acquisition cycle acquired with the 32-channel coil qualitatively shows a similar V1 detection quality to between 3 and 5 acquisitions with the 12-channel Head Matrix coil. *(Figure courtesy of O. Hinds, MIT.)*

10

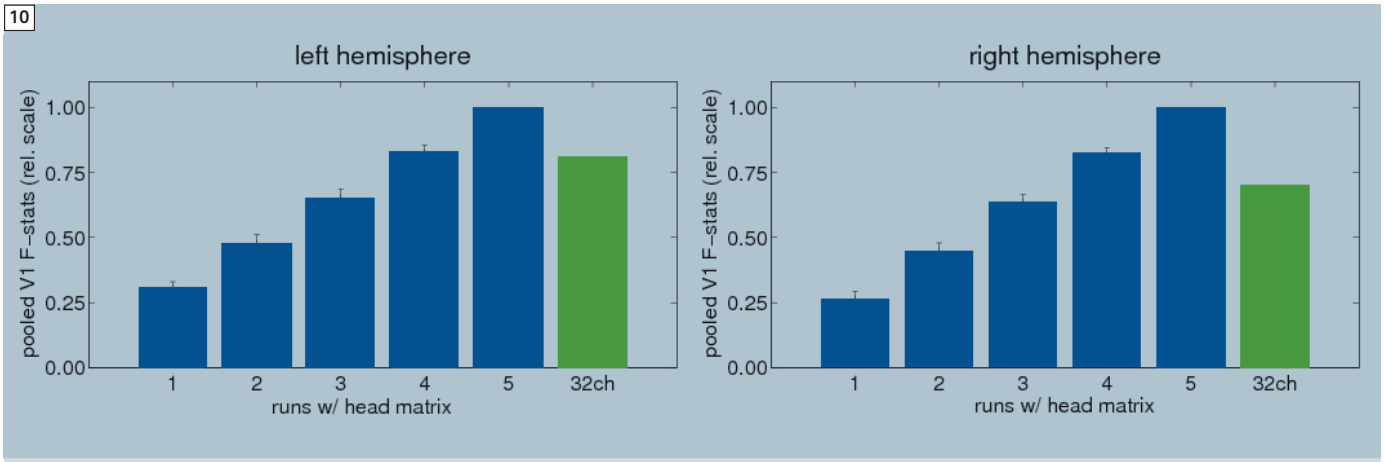

10 Comparison of the accuracy of V1 identification in both hemispheres, using different numbers of runs with the 2 coils (blue = 12-channels, green = 32-channels). The boundary of V1 was traced on the cortical surface based on the field-sign estimate computed from all data. The total number of correct and incorrect field-sign surface vertices within this region was counted to compute the fraction of V1 depicting the correct field-sign (y axis) for all combinations of a given number of runs (x axis) and for the single run collected with the 32-channel coil. *(Figure courtesy of O. Hinds, MIT.)*

11

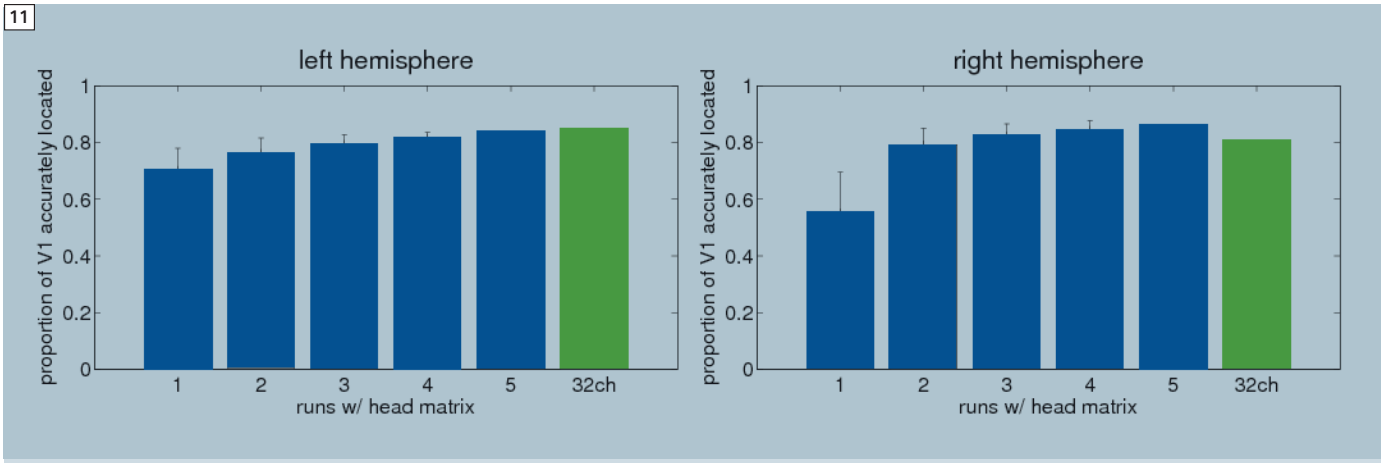

11 Comparison of the significance (F statisitic) of the estimate of the visual field mapping experiment within V1 over different numbers of runs with the 2 coils (blue = 12-channels, green = 32-channels). *(Figure courtesy of O. Hinds, MIT.)*

functional voxel was determined from the preferred phase of the periodic visual stimulus as estimated using the FSFAST software package.
The visual field coordinates were then projected onto the cortical surface generated using the FREESURFER software package [8]. The functional areas, such as primary visual cortex (V1) and secondary visual cortex (V2), are determined by the handedness of the coordinate system required for the mapping between the visual field and the cortex. Because this handedness is opposite in V1 and V2, it can be used to determine the V1/V2 boundary. Thus, mathematically, the boundary is determined by a change in the sign of the determinant of the Jacobian of the visual field mapping transformation (a measure of the handedness of its coordinate system referred to as a field-sign reversal).

Results

Figure 9 shows representative field-sign estimates derived from different numbers of runs with the 12-channel coil compared with a single run acquired with the 32-channel coil. V1 is the large yellow region in the center and V2 surrounds V1 in blue. The opacity of the color overlay codes the statistical significance of the result. Qualitatively, a single run with the 32-channel coil has similar accuracy and significance to three runs with the 12-channel array. Figures 10 and 11 show more quantitative results for the accuracy of V1 identification. Figure 10 shows the proportion of cortical surface locations within V1 for which the field-sign was estimated correctly, where "correct" was determined from the average of all the data. The total number of correct and incorrect field-sign locations within this region was counted to compute the fraction of correct assignments for all combinations of runs and coils. Figure 11 shows statistical significance (F-statistic) of the V1 activation for the 2 coils and number of runs. The mean significance of all locations within V1 was computed as a measure of the effective contrast-to-noise ratio of the activation for each coil and given number of runs. This analysis suggests that for retinotopic mapping, a single run with the 32-channel array has the F-statistic significance (proportional to BOLD contrast-to-noise ratio) of between 3 and 4 runs with the 12-channel array.

In this study we compared the 32-channel phased array head coil with the 12-channel Head Matrix coil based on qualitative inspection of the visual field map and quantitative measures of the V1 accuracy and significance of the visual coordinate mapping. Our findings demonstrate that images acquired in a single run using the 32-channel coil provide the same quality retinotopy maps and boundary estimation of V1/V2 areas as three to four acquisitions with the 12-channel coil. A single 8 min stimuli cycle with the 32-channel coil has similar contrast-to-noise ratio within primary visual cortex (V1) as three to four cycles with the 12-channel Head Matrix coil. This is a greater difference than expected based on the time-series SNR studies above where the tSNR difference at a similar image resolution was about 30%. The greater benefit might result from the difficulty of averaging runs in fMRI; a further inducement to develop technology to achieve the desired activation mapping in as few runs as possible.

Conclusion

Highly parallel detection of functional imaging time-series provides the potential for higher image signal-to-noise ratio (SNR_0) as well as decreased susceptibility distortions in echo-planar imaging. When the time-series is thermal (image) noise dominated, we expect the same general increases in functional contrast-to-noise ratio as seen in imaging comparisons. However, for all but the highest fMRI resolutions, physiological noise becomes increasingly important as SNR_0 is improved, and improvements in image sensitivity from more advanced RF detectors are expected to play a smaller role. Nonetheless, switching to the 32-channel coil improved the tSNR for all of the resolutions and provided clear benefits in the functional experiments.

Acknowledgements

The authors would like to acknowledge Satrajit Ghosh (MIT) and Oliver Hinds (MIT) whose work is included in this manuscript. We thank Steven Shannon and Sheeba Arnold at the A.A. Martinos Imaging Center at MIT, for technical support. We also thank Franz Hebrank, Karsten Jahns, Josef Pfeuffer from Siemens. Special thanks to Michael Hamm for his ongoing support in this collaboration with Siemens.
We acknowledge grant support from the NIDCD (R01 DC01925), NIH (P41RR140 75, R01EB007942), and funding from A.A. Martinos Imaging Center at MIT, the McGovern Institute for Brain Research, and Harvard-MIT Health Science and Technology (HST), and a research agreement and research support from Siemens Healthcare. One of us (LLW) acknowledges consulting income from Siemens Healthcare.

References

1 Wald LL; Wiggins G. Highly Parallel Detection for MRI. MAGNETOM Flash 1/2008, 34–44.
2 Wiggins GC, Triantafyllou C, Potthast A, Reykowski A, Nittka M, Wald LL., 32-channel 3 Tesla receive-only phased-array head coil with soccerball element geometry (2006). Magn Reson Med., Vol. 56(1):216–23.
3 Krüger G, Glover GH., Physiological noise in oxygenation-sensitive magnetic resonance imaging (2001). Magn Reson Med., Vol. 46(4):631-7.
4 Triantafyllou C, Hoge RD, Krüger G, Wiggins CJ, Potthast A, Wiggins GC, Wald LL., Comparison of physiological noise at 1.5 T, 3 T and 7 T and optimization of fMRI acquisition parameters (2005). NeuroImage, Vol. 26(1):243–50.
5 Kellman P, McVeigh ER., Image reconstruction in SNR units: a general method for SNR measurement (2005). Magn Reson Med., Vol. 54(6): 1439–47.
6 Bohland, J.W., and Guenther F.H., An fMRI investigation of syllable sequence production (2006). NeuroImage, Vol. 32(2):821-41.
7 Sereno MI, Dale AM, Reppas JB, Kwong KK, Belliveau JW, Brady TJ, Rosen BR, Tootell RB, Borders of multiple visual areas in humans revealed by functional magnetic resonance imaging (1995). Science, Vol. 12;268(5212): 889–93.
8 Dale AM, Fischl B, and Sereno MI, Cortical surface-based analysis. I. Segmentation and surface reconstruction (1999). NeuroImage, Vol. 9(2):179–194.

Contact
Christina Triantafyllou, Ph. D.
Massachusetts Institute of Technology
77 Massachusetts Avenue
Cambridge, MA 02139-4307
USA
ctrianta@mit.edu

Tim 4G

Head/Neck 20

- Combined Head/Neck design for largest anatomy coverage
- No cables thanks to DirectConnect technology
- One-hand easy removal of the upper part of the coil
- Homogeneous high SNR across the field-of-view
- Excellent iPAT performance
- Seamless combination with the built-in Spine32 and/or Body16 for whole CNS imaging with up to 44 independent channels

Available for 3T MAGNETOM Skyra and 1.5T MAGNETOM Aera.

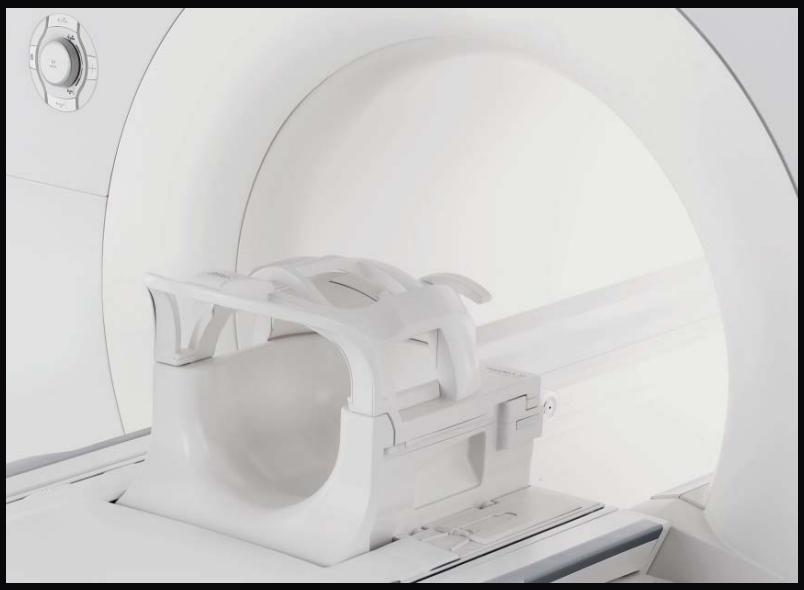

Case Reports: Susceptibility-Weighted Imaging (*syngo* SWI) at 3T

Kate Negus; Peter Brotchie, MBBS, Ph.D.

Barwon Medical Imaging, The Geelong Hospital, Geelong, Victoria, Australia

Introduction

This is a pictorial review of susceptibility-weighted imaging (*syngo* SWI) using a MAGNETOM Trio system with software version *syngo* MR B15 and a 32-channel head coil at The Geelong Hospital, Victoria, Australia.

syngo SWI is a 3D FLASH sequence that is flow compensated in slice, read and phase directions. The data received contains a combination of phase and magnitude information. The susceptibility-weighted images are produced by first filtering the phase images of unwanted field inhomogeneities and then weighting the magnitude images with this phase mask. Two maps are automatically calculated; phase mask multiplied magnitude images and SWI minIP (minimum intensity projection of 8 images on a sliding scale). In addition, the phase and magnitude images can also be produced by modifying the reconstruction tab card.

The SWI images are T2*-weighted and are enhanced by flow compensation and phase masking, so there is exquisite detail of areas of susceptibility due to venous blood, haemorrhage and iron storage.

The phase images can be windowed to see contrast between iron deposition and normal tissue and also to visualize gyral pattern to anatomically orientate lesions more accurately. The SWI sliding minIP is useful to visualize change in tissue susceptibility caused by structures such as veins that cross many slices.

SWI sequence details for all case studies: swi3d1r, transverse plane, TR 28 ms, TE 20 ms, flip angle 15, bandwidth 120 Hx/px, FOV 220 (FOV phase 84.4%), resolution 199 x 256, slice thickness 3 mm, 48 slices, voxel size 0.9 x 0.9 x 3 mm, 1 average, acquisition time 2:19 min.

Since SWI is more sensitive to haemorrhage than conventional T2* gradient echo imaging, we replaced the T2* gradient echo sequence with *syngo* SWI in all of our brain protocols. In order to do this without increasing scan time, the SWI sequence as provided by the standard protocol tree with the software version *syngo* MR B15 was modified by increasing the voxel size from 0.8 mm x 0.7 mm x 1.2 mm (resolution 256 x 384 and 1.2 mm slice thickness) to 0.9 mm x 0.9 mm x 3 mm (resolution 199 x 256 and slice thickness 3 mm), giving us lower resolution but allowing us to image the whole brain rather than only a section of it, in half the time of the standard sequence. The 3 mm slice thickness also correlates to our other brain sequences allowing direct comparison to be made.

The resolution is high enough to diagnose clinically relevant lesions and the sequence short enough to include in all protocols that would benefit from this new technique, without a time penalty. Whole brain coverage of our sequence means that lesions in unexpected locations would not be missed due to lack of coverage.

Case 1: Thrombosis and Associated Venous Infarct

Patient history

A 65-year-old male presented to our emergency department with dysphagia, word-finding difficulty and right sided weakness.

Imaging findings

Non-contrast CT identified a hypodense mass lesion in the left thalamus with a hyperdense border. Contrast CT and CT venogram demonstrated a segment of non-filling likely due to thrombosis in the left internal cerebral vein with associated venous infarct in the left thalamus. MRI was obtained to confirm the vein thrombosis and extent of infarction. Initial MRI on our Philips Edge 1.5T system confirmed a non-filling section of the left internal cerebral vein in keeping with thrombosis, extending to the vein of Galen. There was an area of susceptibility artefact in the gradient echo images in the left thalamus representing haemorrhage. There were 2 small

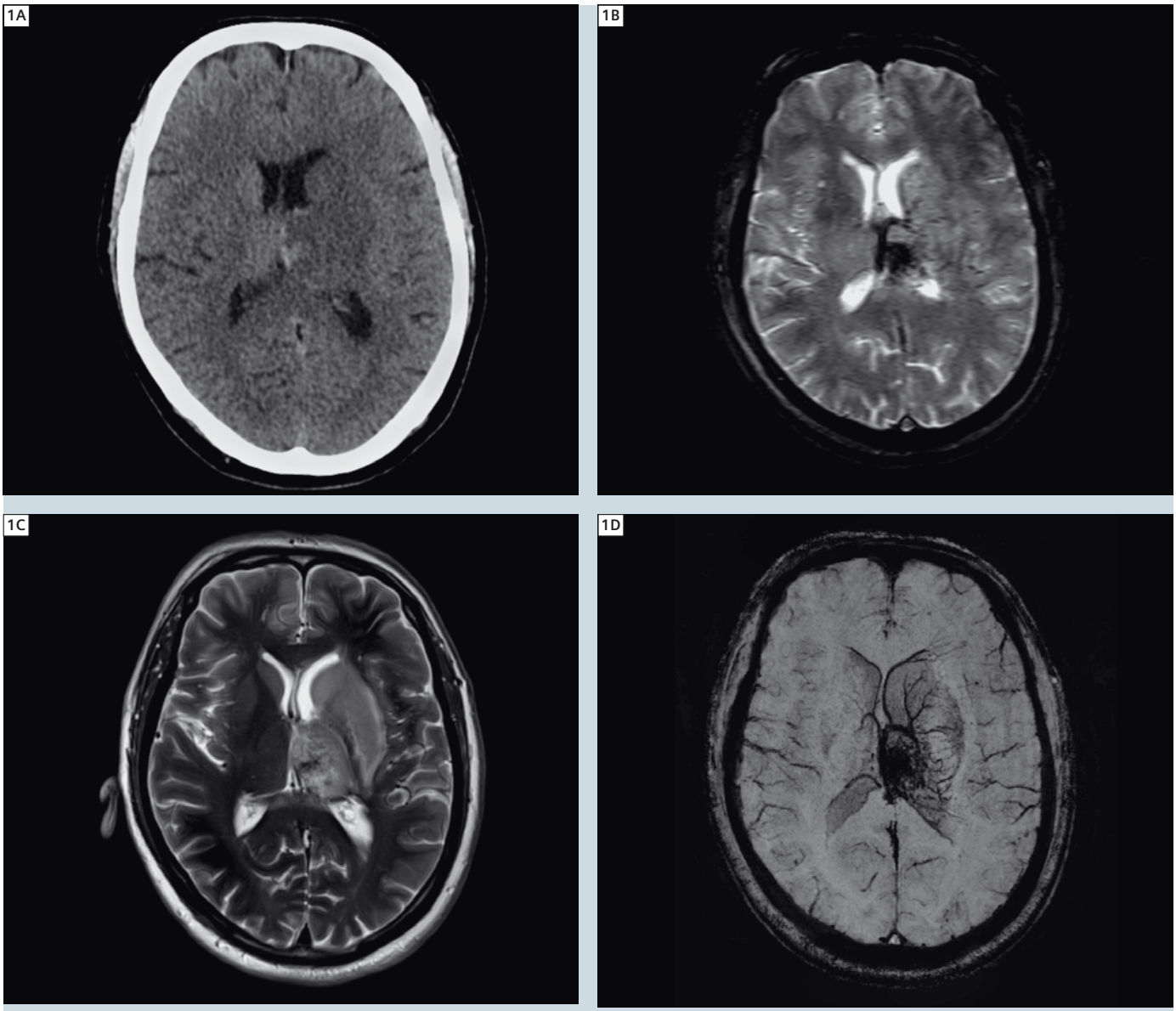

1 **A)** Native CT scan. **B)** T2* GRE at 1.5 Tesla. **C)** T2w TSE with *syngo* BLADE at 3 Tesla. **D)** Corresponding *syngo* SWI at 3 Tesla.

foci of restricted diffusion in the left centrum semiovale likely related to the venous infarction, but no definite restricted diffusion involving the left thalamus or the left basal ganglia. MR spectroscopy of the basal ganglia region showed an increased lactate peak suggestive of ischaemia.

The patient was recalled to our Siemens 3T MAGNETOM Trio scanner the following day. The sequences performed included axial T2w, T1w, Diffusion-Weighted Imaging (DWI), Susceptibility-Weighted Imaging (*syngo* SWI) and MR venography. This imaging confirmed the left internal cerebral vein thrombosis and associated venous infarct.

Discussion

SWI nicely demonstrated the venous tributaries of the left internal cerebral vein with signal dropout due to the presence of deoxyhaemoglobin in the vessels. Signal dropout is also seen in the thrombosed internal cerebral vein and within the thalamic haemorrhage, demonstrating the high sensitivity but low specificity of this sequence.

Case 2: Amyloid Angiopathy

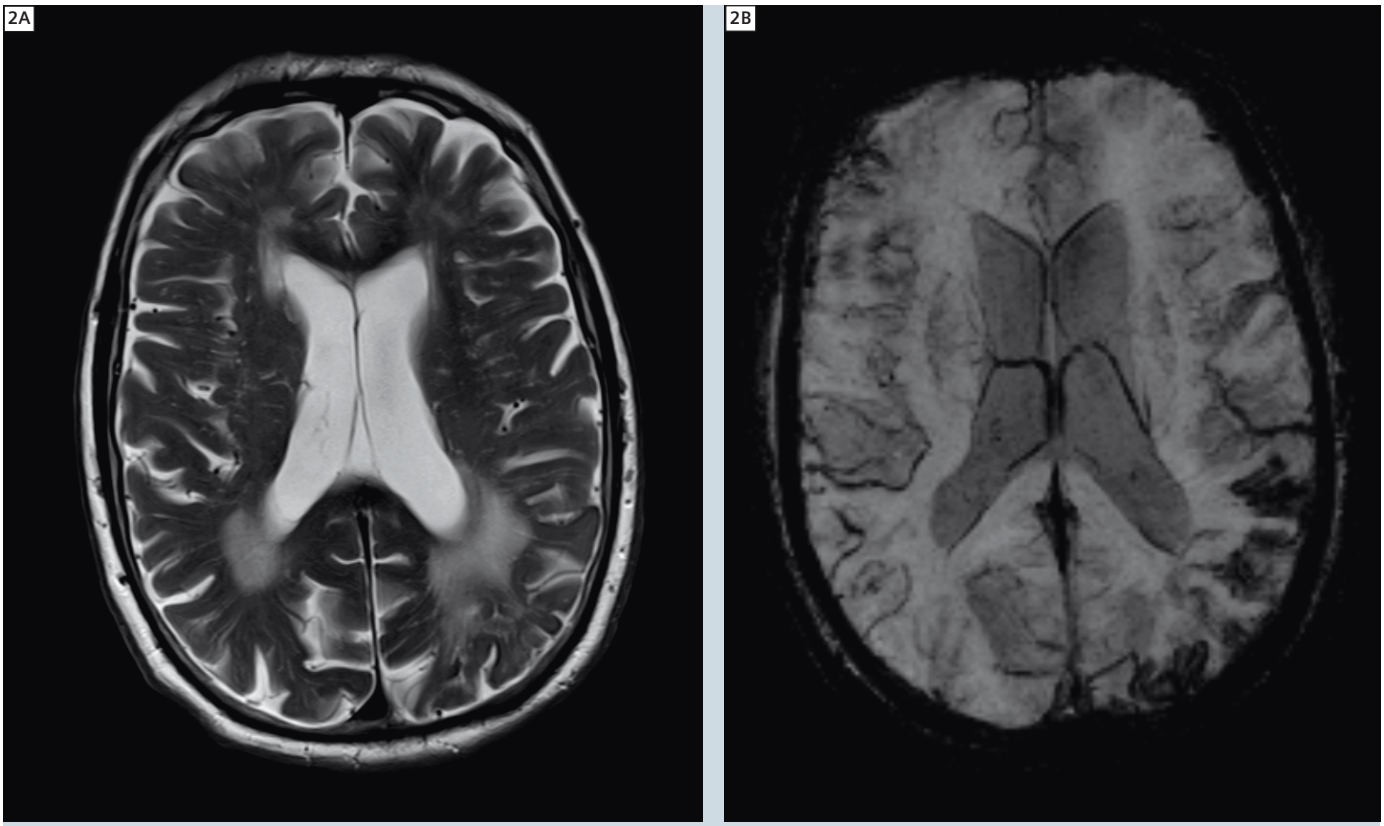

2 All images acquired at 3 Tesla. **A)** T2w TSE. **B)** *syngo* SWI.

Patient history

An 83-year-old male presented for MRI from the memory clinic query fronto-temporal dementia versus Alzheimers Disease with frontal features.

Sequence details

The standard dementia protocol was performed: T1 volume, axial T2, FLAIR, *syngo* SWI, DWI whole brain images with PRESS 30 MR spectroscopy of the parietal grey matter.

Imaging findings

Haemosiderin staining over the cortical surface of the frontal and parietal lobes was evident on the SWI, consistent with previous subarachnoid haemorrhage, most likely secondary to amyloid angiopathy.

Discussion

The SWI demonstrated signal loss due to haemorrhage which was not appreciable on the routine imaging. Micro haemorrhages in the arterioles of the grey matter may lead to vascular dementia associated with amyloid angiopathy. *syngo* SWI may provide useful information in the imaging of dementia.

Case 3: Cerebral haemorrhage in case of AVM

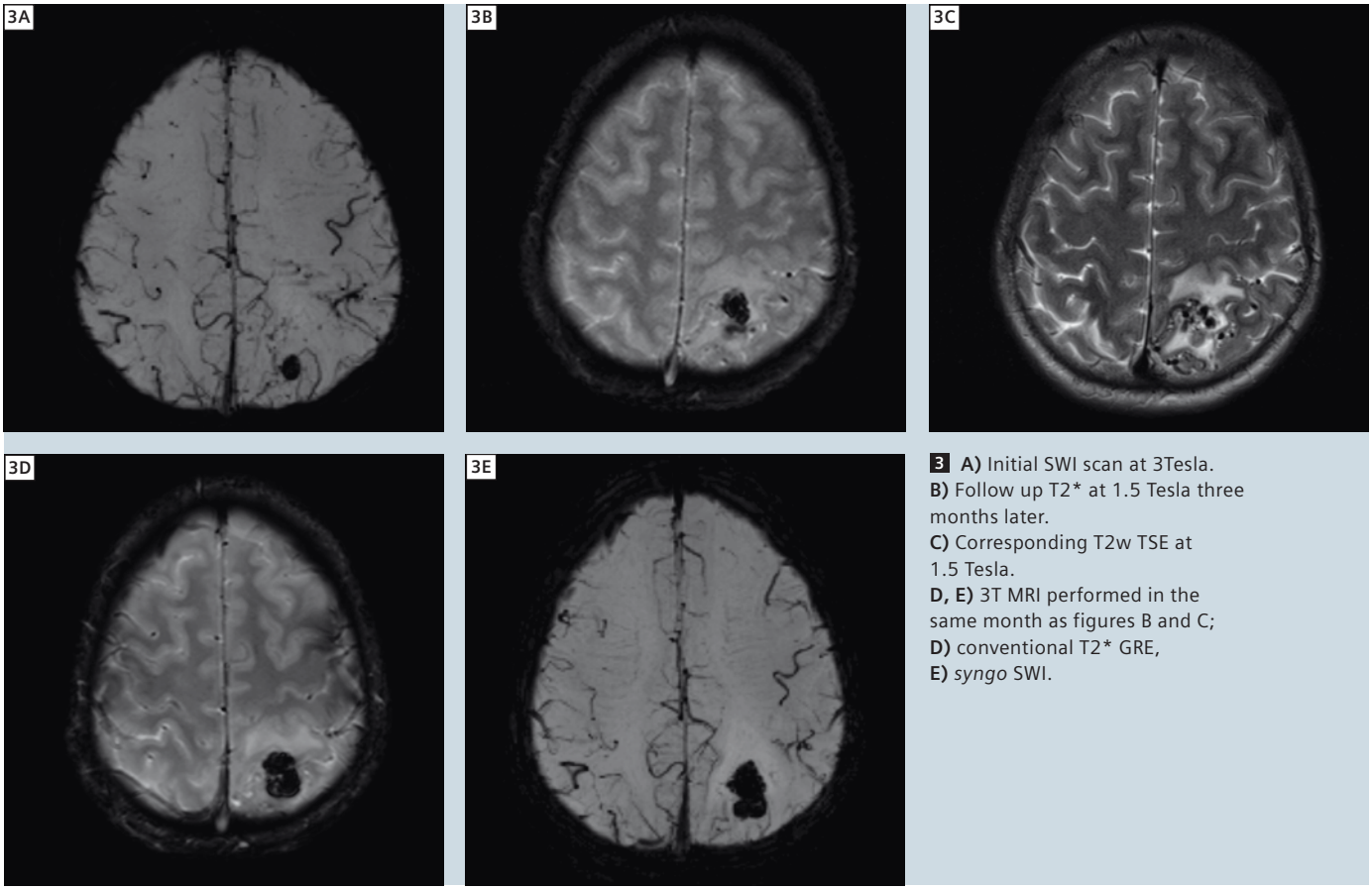

3 **A)** Initial SWI scan at 3Tesla.
B) Follow up T2* at 1.5 Tesla three months later.
C) Corresponding T2w TSE at 1.5 Tesla.
D, E) 3T MRI performed in the same month as figures B and C;
D) conventional T2* GRE,
E) *syngo* SWI.

Patient history

A 33-year-old male with a known brain arterio-venous malformation (AVM) presented to our emergency department with a history of 5 minutes of motor problems in his right hand. MRI was performed to rule out cerebral haemorrhage.

Sequence details

T1 volume, axial T2, FLAIR, field-echo whole brain images, 3D Time-of-Flight (TOF) and contrast-enhanced MR angiography and MR venography sequences were performed on our Siemens 1.5T MAGNETOM Avanto system.

Imaging findings

A collection of serpiginous flow-voids was evident within the left superior parietal lobule, similar in appearance to the patient's previous study. However there was a region of hypointense signal present within the region of the vascular malformation that was not visible on the SWI from a previous study performed on the patient 3 months prior. This was suspicious for acute haemorrhage.
The patient was recalled for SWI at 3 Tesla, so we could have a direct comparison with the previous imaging that was also performed on our 3T scanner. This demonstrated the development of a region of hypointensity situated centrally within the vascular malformation within the left parietal lobe, measuring 2.0 x 1.5 x 3.0 cm in size. On the previous imaging from 3 months prior, a small focus of hypointensity at this site was evident measuring 1 x 1 x 1 cm in diameter.

Discussion

The SWI appearance indicated the development of haemorrhage into the vascular malformation within the left parietal lobe, which had occurred since the previous study. The signal dropout on the SWI shows the margin of the haemorrhage and the associated anomalous vessels more accurately than other routine sequences.

Case 4: Traumatic haemorrhage

Patient history

48-year-old female presented to our emergency department with vomiting and headache after previously discharging herself following a diagnosis of cortical vein thrombosis.

Sequence details

Pre and post contrast T1 whole brain images, axial T2, DWI, *syngo* SWI whole brain images with MR venogram.

Imaging findings

syngo SWI demonstrated a number of hypointense foci within the sulci of the frontal lobes bilaterally and a number of extra-axial locations. These were associated with a number of small foci of restricted diffusion within the cerebral cortex. The history of recent head trauma, subsequently elicited from the patient, indicated that the appearance was most likely due to regions of extra-axial haemorrhage and small cortical contusions.

Discussion

SWI is more sensitive to very small areas of traumatic haemorrhage because of its higher resolution and better sensitivity to blood products than the routine sequences.

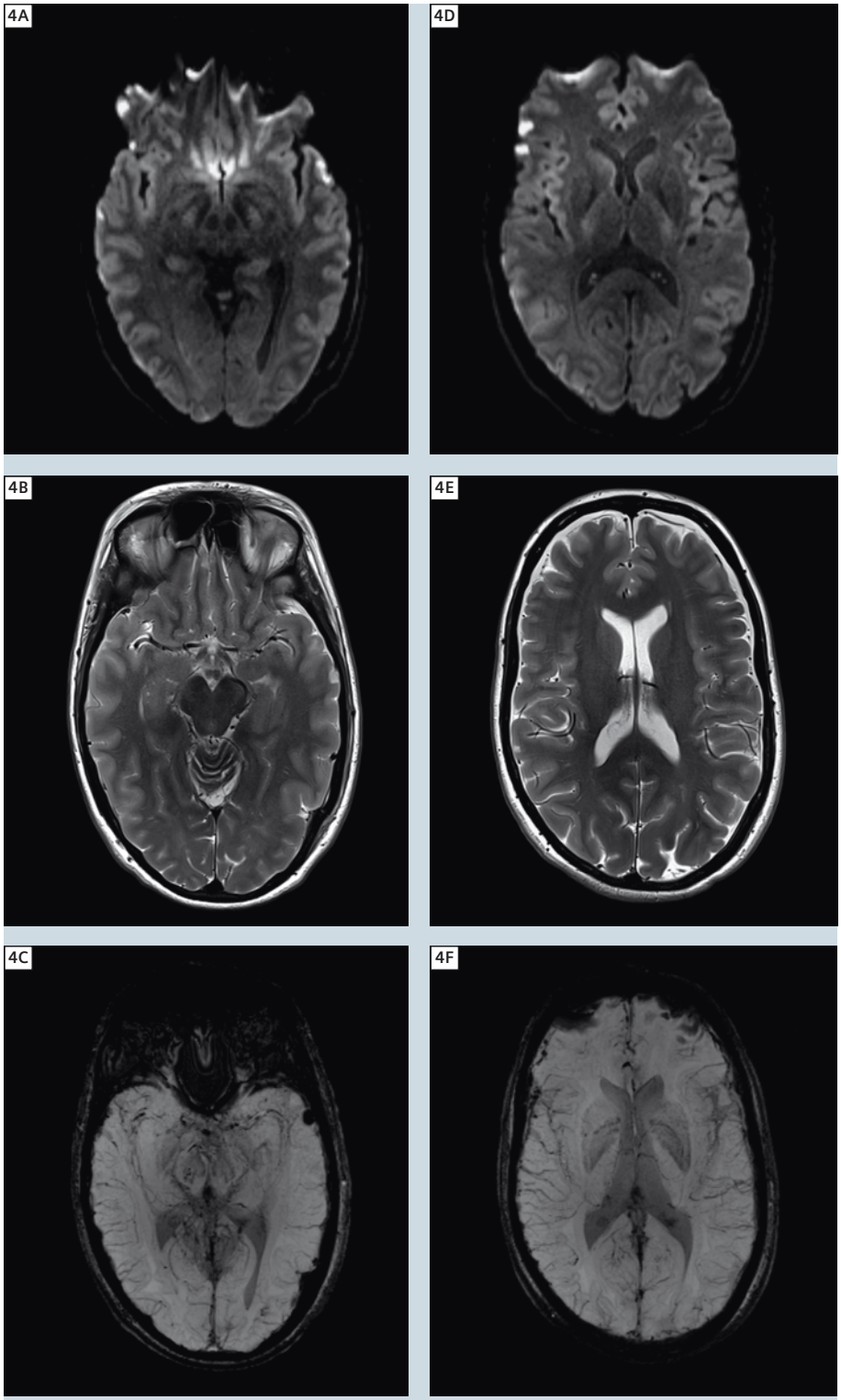

4 All images acquired at 3 Tesla. **A, D)** DWI **B, E)** T2w TSE 4 **C, F)** *syngo* SWI.

Case 5: Cerebral metastases in case of oesophageal adenocarcinoma

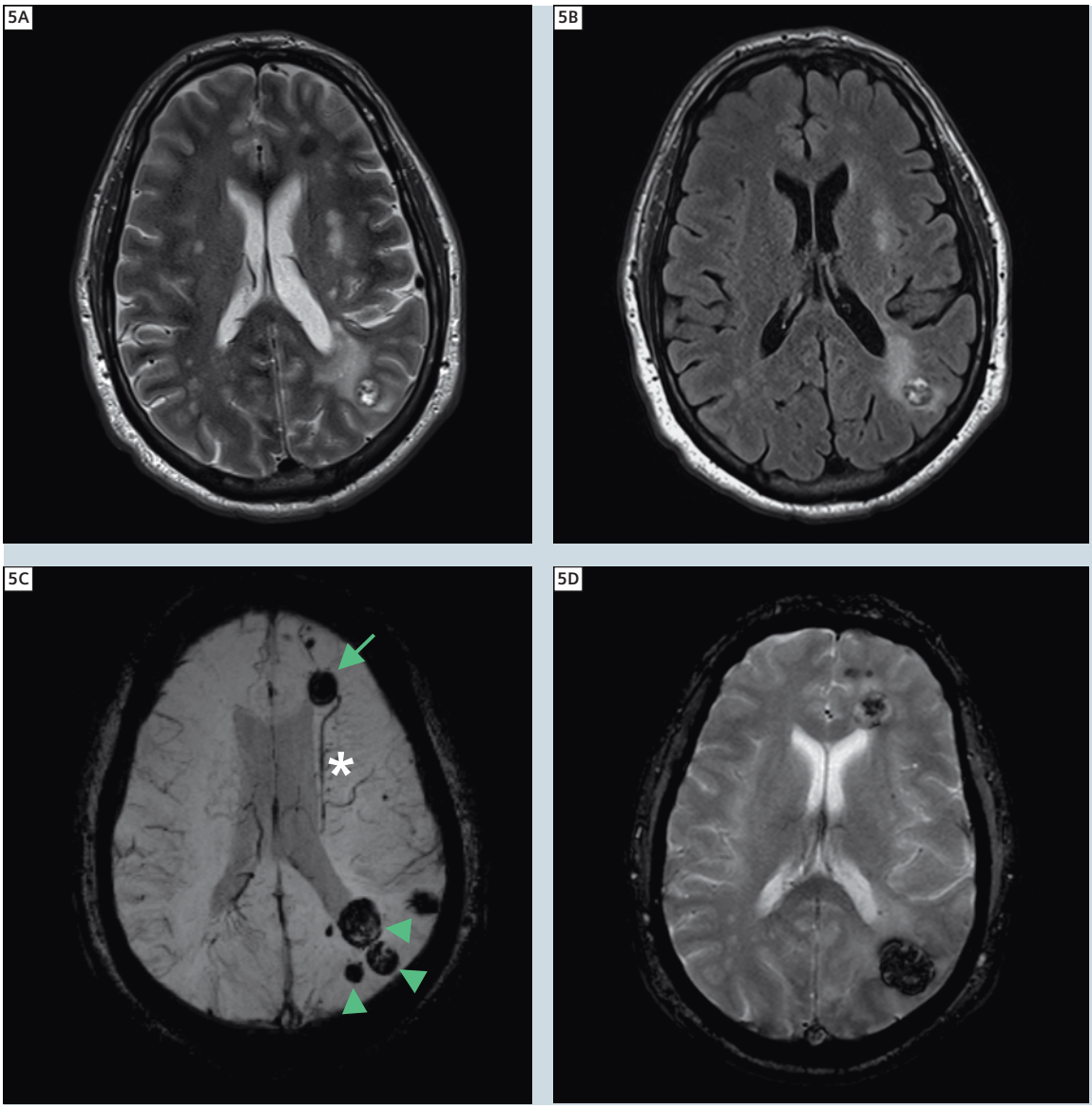

5 **A)** T2w TSE at 3 Tesla.
B) T2w FLAIR at 3 Tesla.
C) *syngo* SWI at 3 Tesla: cavernous haemangioma marked by arrow, DVA marked by asterisk, hemorrhagic metastases marked by arrowhead.
D) Follow-up after one month with a conventional T2* sequence at 1.5 Tesla.

Patient history

A 48-year-old male with oesophageal adenocarcinoma presented with right retro orbital pain for 8 weeks and was scanned for query cerebral metastases.

Sequence details

Pre- and post contrast T1 volume, axial T2, FLAIR, DWI, *syngo* SWI whole brain images, coronal T1, fat sat T2, post contrast fat sat T1 images of orbits and paranasal sinuses.

Imaging findings

No evidence of orbital mass or mass within the paranasal sinuses was demonstrated.
Numerous T2 hypointense lesions with marked signal dropout on SWI were evident throughout the left cerebral hemisphere. However, some of these were unaltered in appearance from the previous study from 2 years earlier and were consistent with cavernous haemangiomas. The others represent haemorragic metastases.

Discussion

The patient returned for a follow-up scan on our 1.5T MAGNETOM Avanto scanner 1 month later and standard T2* gradient echo imaging was performed. Compared to the 3T SWI, the standard gradient echo imaging at 1.5T is not as sensitive to the multiple haemorrhagic areas, failing to show some of the smaller lesions evident on the 3T SWI sequence.

Case 6: Haemorrhagic component of MCA infarction

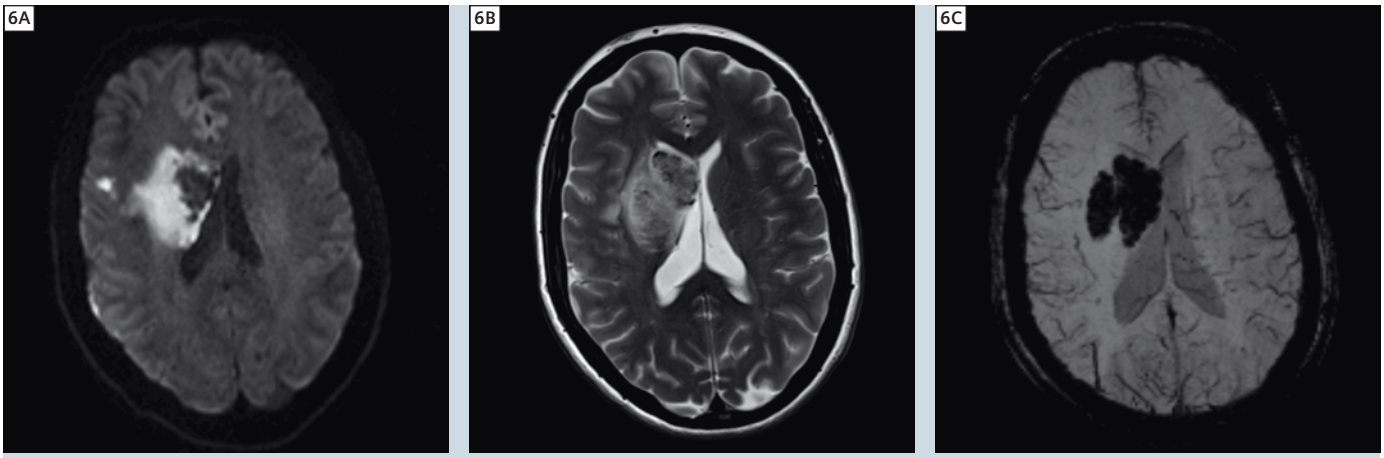

6 All images acquired at 3 Tesla. **A)** DWI **B)** T2w TSE **C)** *syngo* SWI

Patient history

A 48-year-old female presented to our emergency department with sudden onset of left face, arm and leg weakness. CT brain was reported as right middle cerebellar artery infarction. MRI was performed to confirm this finding.

Sequence details

Pre- and post contrast volume T1, axial FSE T2, FLAIR, *syngo* SWI, DWI images of the whole brain and 3D TOF MRA circle of Willis.

Imaging findings

Abnormal signal was seen within the right caudate head and lentiform nucleus with significant susceptibility artefact within these structures that was most consistent with the presence of blood products. The pathology is contained within the middle cerebral artery distribution and appearances on *syngo* SWI are most consistent with a cerebral infarction with haemorrhagic transformation.

Discussion

The SWI sequence demonstrated the full extent of the haemorrhagic component of the infarction better than any of the routine sequences. The presence of haemorrhage with stroke is important to demonstrate as it changes treatment options.

Case study discussion

syngo SWI has allowed smaller susceptibility lesions to be demonstrated than previously possible, in cases of vascular malformation, tumor, stroke, trauma and dementia.
In many cases cited in the literature, SWI was the only imaging sequence to show the abnormality due to its increased sensitivity to iron content.
In all 6 of our cases the SWI sequence demonstrated increased detail of the pathology compared with the routine imaging sequences. In cases 2, 4 and 5, some lesions appeared to be too small to see on other imaging sequences, indicating how the sensitivity of *syngo* SWI may benefit diagnosis.
The increased signal and susceptibility effects at 3T enhance the use of *syngo* SWI, allowing full brain coverage in a short amount of time.

References

1 *syngo* SWI powered by Tim. Hot Topic by Siemens Healthcare. Available online at www.siemens.com/magnetom-world (go to Publications > Hot Topics).
2 Susceptibility Weighted Imaging, Opening new doors to clinical applications of Magnetic Resonance Imaging – E. Mark Haacke PhD Comment: MRM, 2004 Sep;52(3):612-618.
3 Susceptibility-weighted MR imaging: a review of clinical applications in children. Tong KA, Ashwal S, Obenaus A, Nickerson JP, Kido D, Haacke EM. AJNR Am J Neuroradiol. 2008 Jan;29(1):9-17. Epub 2007 Oct 9. Review.
4 Susceptibility-weighted imaging to visualize blood products and improve tumor contrast in the study of brain masses. Sehgal V, Delproposto Z, Haddar D, Haacke EM, Sloan AE, Zamorano LJ, Barger G, Hu J, Xu Y, Prabhakaran KP, Elangovan IR, Neelavalli J, Reichenbach JR. J Magn Reson Imaging. 2006 Jul;24(1):41-51.
5 Reliability in detection of hemorrhage in acute stroke by a new three-dimensional gradient recalled echo susceptibility-weighted imaging technique compared to computed tomography: a retrospective study. Wycliffe ND, Choe J, Holshouser B, Oyoyo UE, Haacke EM, Kido DK. J Magn Reson Imaging. 2004 Sep;20(3):372-7.

Contact

Kate Negus
MRI Supervising Technologist
Barwon Medical Imaging
The Geelong Hospital
PO Box 281
Geelong, 3220, Victoria, Australia
Phone: +61 3 5226 7070
katen@barwonhealth.org.au

Assoc. Prof. Peter Brotchie, MBBS, Ph.D.
Director MRI
Barwon Medical Imaging
The Geelong Hospital
Geelong, 3220, Victoria, Australia
Phone: +61 3 5226 7032
peterbr@barwonhealth.org.au

Brain Dot engine

Standardized imaging across patients and institutions with the Brain Dot engine. Optimized workflow for increased throughput and examination consistency.

Patient 1, system A , incorrect head positioning (before AutoAlign)

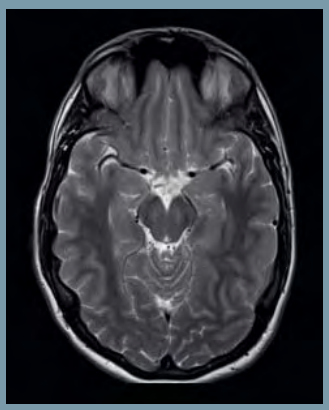

Patient 2, system B (before AutoAlign)

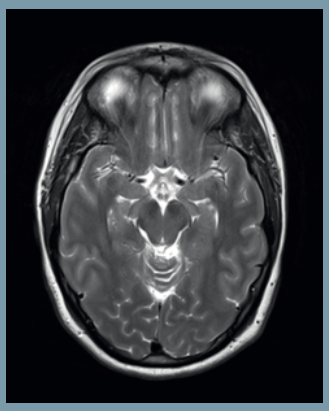

Follow-up , distinct deviaton of head axes (before AutoAlign)

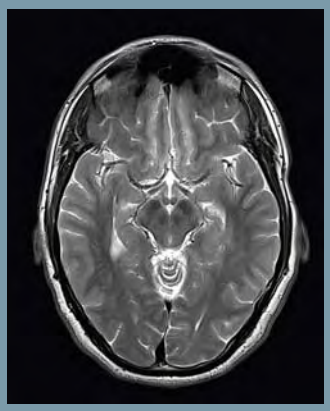

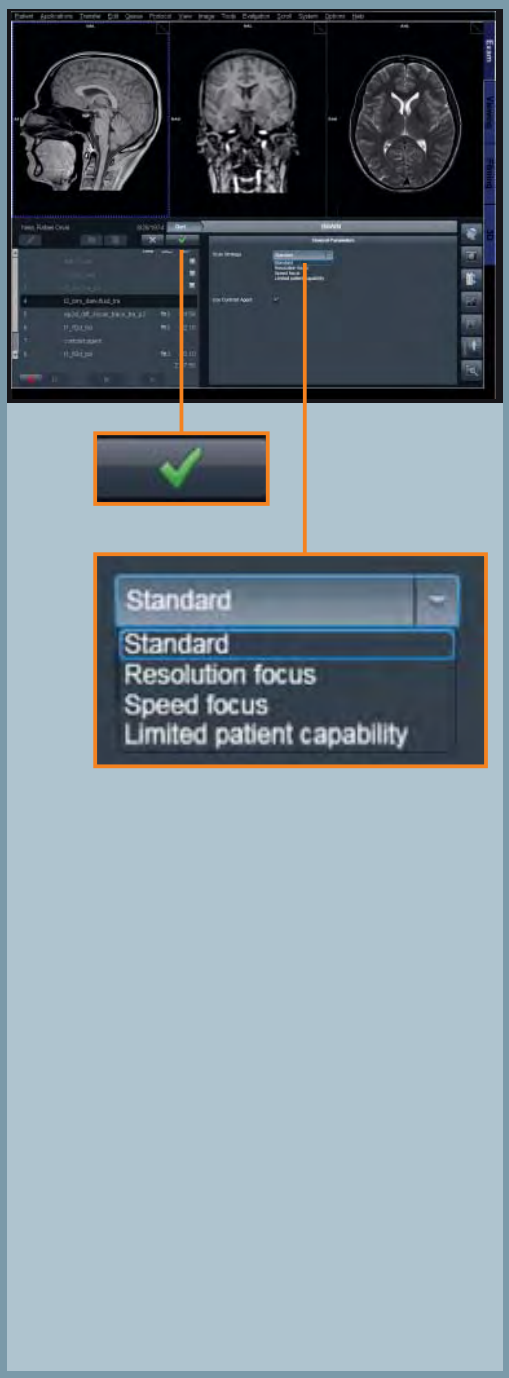

Arterial Spin Labeled Perfusion MRI

John A. Detre, M.D.

Center for Functional Neuroimaging, Department of Neurology and Radiology, University of Pennsylvania, Philadelphia, PA, USA

Perfusion refers to the delivery of oxygen and nutrients to tissues by means of blood flow and is one of the most fundamental physiological parameters. Disorders of perfusion also account for most of the leading causes of medical disability and mortality. While measurements of perfusion are of direct diagnostic value in vascular disorders, perfusion measurements also serve as biomarkers for a broader range of physiological and pathophysiological functions. A close coupling between cerebral blood flow and metabolism allows regional brain function to be assessed through measurements of cerebral perfusion and increased vascularity of neoplasms allows tumor perfusion to be used as a measure of tumor grade and to monitor the response to tumor therapy.

Classical tissue perfusion is measured using a diffusible tracer that can exchange between the vascular compartment and tissue. This yields a perfusion measurement in units of milliliters of blood flow per gram of tissue per unit time (ml/g/min). However, owing to the relative ease of inferring hemodynamic function from the passage of an intravascular tracer, the term "perfusion imaging" has also been applied to measurements of perfusion-related parameters such as mean transit time and blood volume that can be related to perfusion through the Central Volume Principle. In the field of MRI, most people associate the concept of perfusion imaging with dynamic susceptibility contrast imaging using a relaxation contrast agent. However, there are also several methods for the measurement of classical tissue perfusion using MRI. Diffusible tracers that can be monitored with MRI include fluorinated halocarbons [1], deuterated water ($^{2}H2O$) [2, 3], ^{17}O-water [4], and potentially ^{13}C labeled hydrocarbons.

Magnetically labeled endogenous blood water can also be used as a tracer for perfusion MRI. To accomplish this, the longitudinal magnetization of arterial blood water must be manipulated so that it differs from the tissue magnetization. It is quite analogous to the use of 15O-water for PET perfusion imaging except that the magnetic tracer decays with T1 instead of a radioactive decay and the ASL

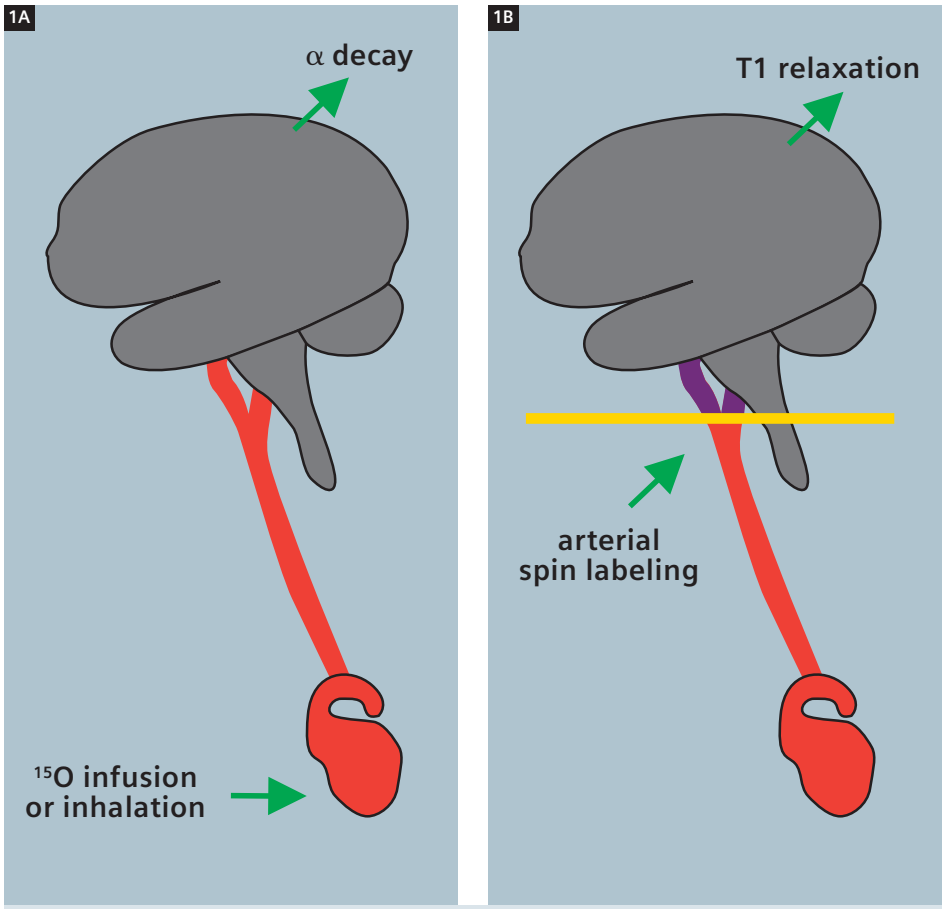

1 Concept of Arterial Spin Labeling (ASL), comparing 15O-PET (Fig. 1A)) and ASL (Fig. 1B) approaches. In ASL, endogenous arterial blood water is magnetically labeled instead of exogenously administered tracer, and the magnetic label decays with T1 instead of radioactive decay (α).

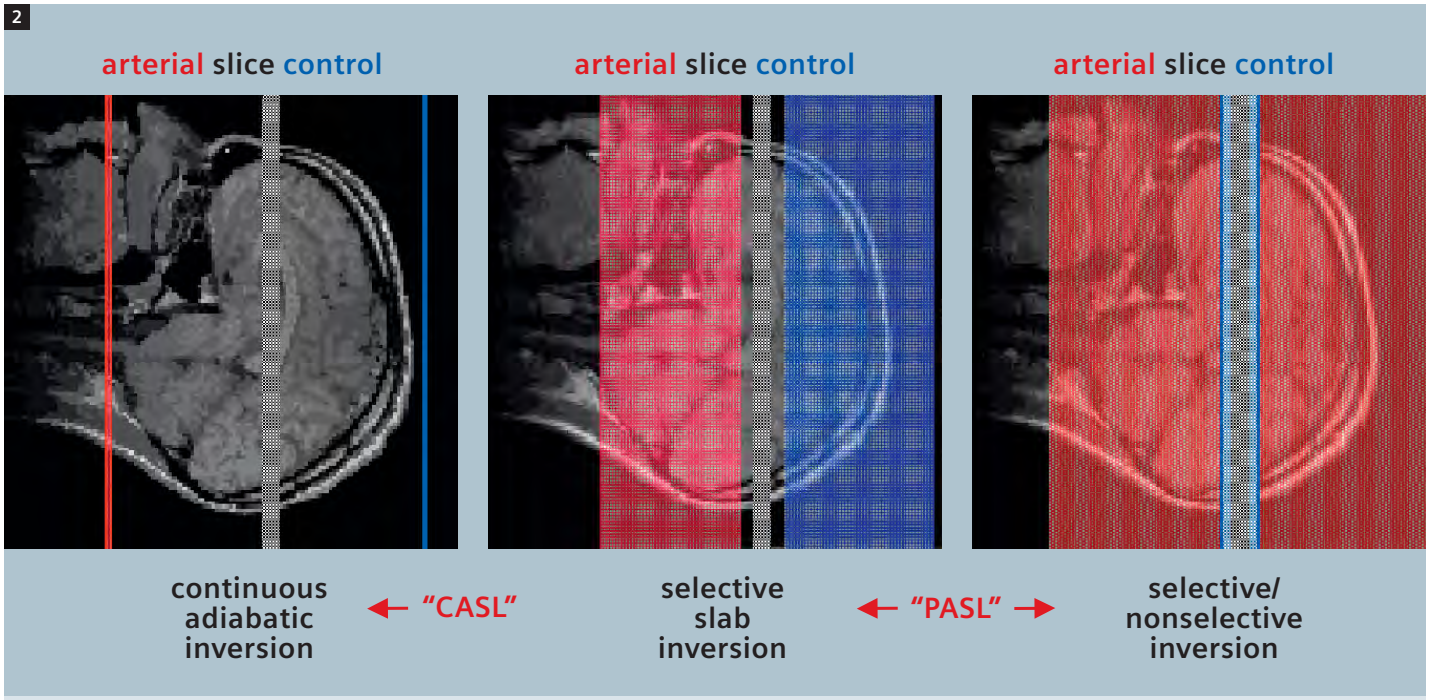

2 Schematic diagram illustrating arterial spin labeling strategies. Continuous ASL (CASL, left) labels arterial spins as they flow through a labeling plane. Pulsed ASL (PASL, middle and right) labels arterial spins using a spatially selective labeling pulse. Applications to single-slice imaging are illustrated for simplicity. Somewhat more complex schemes are used for multislice imaging.

approach is completely noninvasive. Because T1 relaxation is approximately 100 times faster than the radioactive decay rate of 15O, only a small amount of labeled water accumulates, though the temporal resolution is also correspondingly higher. The subtle difference between images acquired with and without arterial spin labeling (ASL) can be modeled to derive a calculated blood flow image showing perfusion in ml/g/min at each voxel. Key parameters required for ASL quantification include knowledge or assumptions about the T1 values in blood and tissue, the labeling efficiency, and the arterial transit time [5, 6]. ASL can be combined with any imaging sequence and theoretically provides a flow image that is completely independent of scanning parameters; As such, it represents one of the few MRI contrast mechanisms for which the physiological basis is really well understood. In practice, most ASL measurements are made with some compromises trading off sensitivity and convenience for a less pure measurement of tissue blood flow.

Arterial spin labeling can be accomplished using a variety of approaches and in nearly any organ. Most ASL has been carried out in the brain because the arterial supply is extremely well defined and perfusion to brain tissue is high. However, ASL studies have also successfully been carried out in kidney, lung, retina, heart, and skeletal muscle. The most common ASL approaches use either pulsed labeling (PASL) with an instantaneous spatially selective saturation or inversion pulse [7], or continuous labeling (CASL), most typically by flow driven adiabatic fast passage [8]. In some PASL methods, a spatially selective inversion pulse is administered to the tissue rather than to arterial blood [9]. More recently there have also been efforts label based on velocity rather than spatial selectivity for tissue arterial supply [10]. The first publication on ASL perfusion MRI actually used pseudocontinuous saturation to dephase arterial blood water in the neck of a rat [11]. Prior to that time, the idea of labeling arterial blood water had been considered primarily as a means for visualizing intraluminal flow in arteries and veins [12, 13]. Continuous labeling schemes allow brain magnetization to reach a steady-state that maximizes the signal difference between labeled and unlabeled conditions [14], though this occurs at the expense of both increased SAR deposition and magnetization transfer effects that complicate both the accurate measurement of the control (unlabeled) condition, and the extension to multislice imaging. Some groups have addressed this using a separate labeling coil [15], while others have pursued single coil approaches [16]. The myriad technical details of ASL implementation are beyond the scope of this article, but key advances have focused on improved labeling, improved measurements of the subtle effects of ASL on tissue signal, and improved modeling of measured signal changes in terms of tissue blood flow. For CBF, current tech-

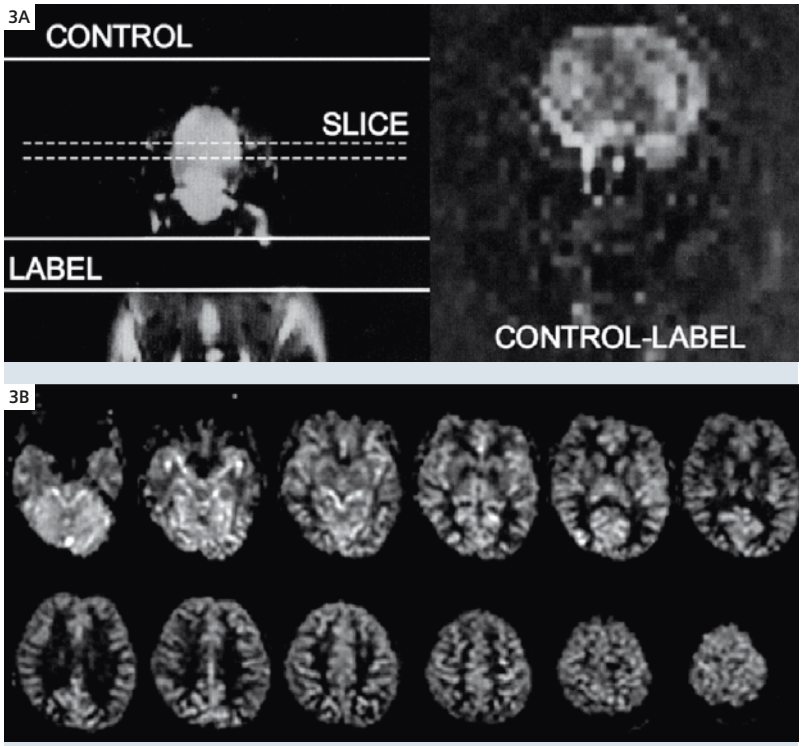

3 The original demonstration of ASL using pseudocontinuous ASL in the rat brain [11]. **(Fig. 3A)**
Multislice PASL of human brain acquired from a normal volunteer at 3T [18]. **(Fig. 3B)**

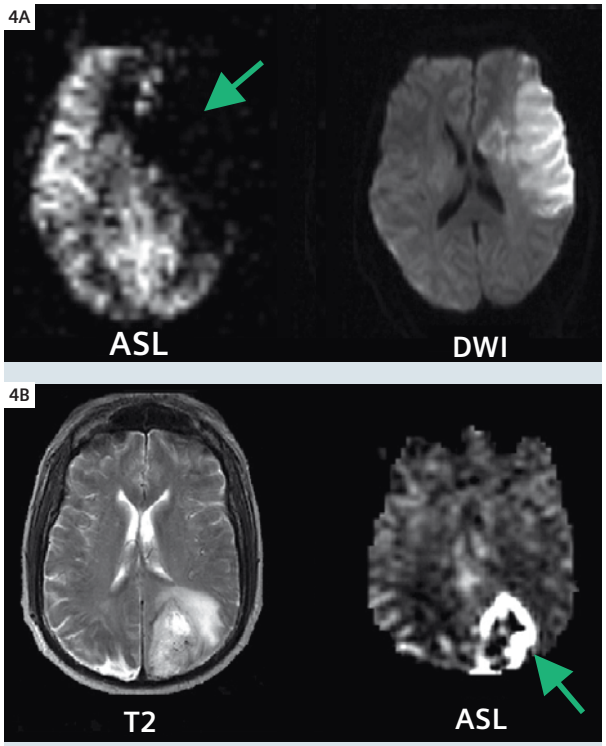

4 Representative clinical applications of ASL showing hypoperfusion in an acute stroke **(Fig. 4A)** and hyperperfusion in a glioblastoma **(Fig. 4B)**. For more details on clinical applications of ASL see [31].

nology provides a reasonably good whole-brain image in just a few minutes of scanning. ASL methods particularly benefit from high magnetic field trengths because not only is the sensitivity higher, but T1 also lengthens, allowing more label to accumulate [17, 18]. ASL methods also benefit from the increased sensitivity provided by multicoil receivers and are minimally degraded by parallel imaging [19]. The use of a body transmitter benefits PASL by allowing a larger region for arterial inversion but necessitates a more elaborate approach for CASL, termed pseudo-continuous labeling [20].

In clinical neuroscience, while the application of ASL perfusion MRI to the diagnosis and management of acute stroke is both obvious and feasible, the clinical utility of ASL is likely much broader since only a minority of acute stroke patients undergo MRI. ASL perfusion MRI could greatly enhance the evaluation of both TIA (Transient Ischemic Attack) and chronic cerebrovascular disease by quantifying regional CBF in specific vascular territories where interventions may be planned, or by allowing the effects of pharmacological therapies on CBF to be evaluated. Several approaches now also exist for selective arterial labeling, allowing the perfusion distribution of specific arteries to be assessed independently [21, 22]. A challenge in the application of ASL to cerebrovascular disorders is that sensitivity decreases in regions with very low CBF and the presence of prolonged arterial transit times that can create regions of apparent hyperperfusion when labeled spins remain in large vessels due to prolonged arterial transit times. This artifact is usually easy to recognize and can be verified by the addition of spoiler gradients that dephase coherently flowing spins. Arterial transit times can even be quantified by comparing ASL images with and without spoiler gradients [23], providing access to a novel physiological parameter that likely reflects the recruitment collateral flow sources. Another significant application of ASL is in degenerative diseases, where specific patterns of hypoperfusion may be used to aid in differential diagnosis of disorders such as Alzheimer's disease [24] and frontotemporal dementia [25]. Finally, as noted above, perfusion of brain tumors typically correlates with their grade and potentially their response to therapies [26]. Undoubtedly, the clinical availability of noninvasive and quantitative CBF imaging will lead to numerous additional applications as further experience with this modality develops.

In basic neuroscience, ASL perfusion MRI can be used to localize task activation in a manner similar to BOLD fMRI (Blood Oxygen Level Dependent functional MR Imaging). Indeed, ASL based contrast derived from inversion recovery imaging of task activation was included in one of the earliest reports of fMRI in human brain [28]. Although relative CBF can be inferred from ASL images acquired without control labeling, acquisition of both labeled and control pairs are required for quantification of CBF. While this reduces the temporal resolution of ASL perfusion fMRI as compared to BOLD fMRI, it also

dramatically changes the noise properties of the data, providing sensitivity over much longer timescales [29]. ASL perfusion fMRI can also be used as a measure of brain function at rest, independent of any sensorimotor or cognitive task, and reveals regional changes in brain function associated with development [30], behavioral states [31], or genetic traits [32]. Because ASL measures a purely biological parameter, it should also be particularly valuable for multisite studies examining brain function on a variety of scanner platforms or longitudinally.

A limitation in the widespread use and dissemination of ASL perfusion MRI has been the absence of product sequences provided by vendors. The recent development of an ASL product by Siemens should help alleviate this limitation, at least for Siemens users. Other vendors will hopefully follow suit. The Siemens ASL product provides a robust PASL sequence with echoplanar readout and online calculation of CBF maps from the acquired data. Many of us involved in the early development and validation of ASL perfusion MRI are eager to see it translated to routine clinical use.

Dr. Detre is an inventor of ASL technology and has received royalties from the University of Pennsylvania for its licensure.

References

1 Eleff, S.M., M.D. Schnall, L. Ligetti, M. Osbakken, V.H. Subramanian, B. Chance and J.S.J. Leigh, Concurrent measurement of cerebral blood flow, sodium, lactate, and high-energy phosphate metabolism using 19F, 23Na, 1H, and 31P nuclear magnetic resonance spectroscopy. Magn. Reson. Med., 1988. 7: p. 412-24.

2 Ackerman, J.J., C.S. Ewy, N.N. Becker and R.A. Shalwitz, Deuterium nuclear magnetic resonance measurements of blood flow and tissue perfusion employing 2H2O as a freely diffusible tracer. Proc Natl Acad Sci U S A, 1987. 84(12): p. 4099-102.

3 Detre, J.A., V.H. Subramanian, M.D. Mitchell, D.S. Smith, A. Kobayashi, A. Zaman and J.S. Leigh, Measurement of regional cerebral blood flow in cat brain using intracarotid 2H2O and 2H NMR imaging. Magn. Reson. Med., 1990. 14: p. 389-395.

4 Pekar, J., L. Ligeti, Z. Ruttner, R.C. Lyon, T.M. Sinnwell, P. van Gelderen, D. Fiat, C.T. Moonen and A.C. McLaughlin, In vivo measurement of cerebral oxygen consumption and blood flow using 17O magnetic resonance imaging. Magn Reson Med, 1991. 21(2): p. 313-9.

5 Alsop, D.C. and J.A. Detre, Reduced transit-time sensitivity in noninvasive magnetic resonance imaging of human cerebral blood flow. J. Cereb. Blood Flow Metab., 1996. 16: p. 1236-1249.

6 Buxton, R.B., L.R. Frank, E.C. Wong, B. Siewert, S. Warach and R.R. Edelman, A general kinetic model for quantitative perfusion imaging with arterial spin labeling. Magn Reson Med, 1998. 40(3): p. 383-96.

7 Wong, E.C., R.B. Buxton and L.R. Frank, Implementation of quantitative perfusion imaging techniques for functional brain mapping using pulsed arterial spin labeling. NMR Biomed, 1997. 10(4-5): p. 237-49.

8 Williams, D.S., J.A. Detre, J.S. Leigh and A.P. Koretsky, Magnetic resonance imaging of perfusion using spin inversion of arterial water. Proc. Natl. Acad. Sci. USA, 1992. 89: p. 212-216.

9 Kim, S.G., Quantification of relative cerebral blood flow change by flow-sensitive alternating inversion recovery (FAIR) technique: application to functional mapping. Magn. Reson. Med., 1995. 34: p. 293-301.

10 Wong, E.C., M. Cronin, W.C. Wu, B. Inglis, L.R. Frank and T.T. Liu, Velocity-selective arterial spin labeling. Magn Reson Med, 2006. 55(6): p. 1334-41.

11 Detre, J.A., J.S. Leigh, D.S. Williams and A.P. Koretsky, Perfusion imaging. Magn. Reson. Med., 1992. 23: p. 37-45.

12 Sardashti, M., D.G. Schwartzberg, G.P. Stomp and W.T. Dixon, Spin labeling angiography of the carotids by presaturation and simplified adiabatic inversion. Magn. Reson. Med., 1990. 15: p. 192-200.

13 Singer, J.R. and L.E. Crooks, Nuclear magnetic resonance blood flow measurements in the human brain. Science, 1983. 221(4611): p. 654-6.

14 Wong, E.C., R.B. Buxton and L.R. Frank, A theoretical and experimental comparison of continuous and pulsed arterial spin labeling techniques for quantitative perfusion imaging. Magn Reson Med, 1998. 40(3): p. 348-55.

15 Zaharchuk, G., P.J. Ledden, K.K. Kwong, T.G. Reese, B.R. Rosen and L.L. Wald, Multislice perfusion and perfusion territory imaging in humans with separate label and image coils. Magn. Reson. Med., 1999. 41: p. 1093-8.

16 Alsop, D.C. and J.A. Detre, Multisection cerebral blood flow MR imaging with continuous arterial spin labeling. Radiology, 1998. 208: p. 410-16.

17 Wang, J., D.C. Alsop, L. Li, J. Listerud, J.B. Gonzalez-At, M.D. Schnall and J.A. Detre, Comparison of quantitative perfusion imaging using arterial spin labeling at 1.5 and 4.0 Tesla. Magn Reson Med, 2002. 48(2): p. 242-54.

18 Wang, J., Y. Zhang, R.L. Wolf, A.C. Roc, D.C. Alsop and J.A. Detre, Amplitude-modulated Continuous Arterial Spin-labeling 3.0-T Perfusion MR Imaging with a Single Coil: Feasibility Study. Radiology, 2005. 235: p. 218-28.

19 Wang, Z., J. Wang, T.J. Connick, G.S. Wetmore and J.A. Detre, Continuous ASL perfusion MRI with an array coil and parallel imaging at 3T. Magn Reson Med, 2005. 54(3): p. 732-7.

20 Garcia, D.M., C. de Bazelaire and D. Alsop, Pseudo-continuous Flow Driven Adiabatic Inversion for Arterial Spin Labeling. ISMRM 13th Scientific Meeting Proceedings, 2005: p. 37.

21 Hendrikse, J., J. van der Grond, H. Lu, P.C. van Zijl and X. Golay, Flow territory mapping of the cerebral arteries with regional perfusion MRI. Stroke, 2004. 35(4): p. 882-7.

22 Werner, R., K. Alfke, T. Schaeffter, A. Nabavi, H.M. Mehdorn and O. Jansen, Brain perfusion territory imaging applying oblique-plane arterial spin labeling with a standard send/receive head coil. Magn Reson Med, 2004. 52(6): p. 1443-7.

23 Wang, J., D.C. Alsop, H.K. Song, J.A. Maldjian, K. Tang, A.E. Salvucci and J.A. Detre, Arterial transit time imaging with flow encoding arterial spin tagging (FEAST). Magn Reson Med, 2003. 50(3): p. 599-607.

24 Alsop, D.C., J.A. Detre and M. Grossman, Assessment of cerebral blood flow in Alzheimer's disease by spin-labeled magnetic resonance imaging. Ann Neurol, 2000. 47(1): p. 93-100.

25 Du, A.T., G.H. Jahng, S. Hayasaka, J.H. Kramer, H.J. Rosen, M.L. Gorno-Tempini, K.P. Rankin, B.L. Miller, M.W. Weiner and N. Schuff, Hypoperfusion in frontotemporal dementia and Alzheimer disease by arterial spin labeling MRI. Neurology, 2006. 67(7): p. 1215-20.

26 Wolf, R.L., J. Wang, S. Wang, E.R. Melhem, M. O'Rourke D, K.D. Judy and J.A. Detre, Grading of CNS neoplasms using continuous arterial spin labeled perfusion MR imaging at 3 Tesla. J Magn Reson Imaging, 2005. 22(4): p. 475-482.

27 Wolf, R.L. and J.A. Detre, Clinical neuroimaging using arterial spin-labeled perfusion magnetic resonance imaging. Neurotherapeutics, 2007. 4(3): p. 346-59.

28 Kwong, K.K., J.W. Belliveau, D.A. Chesler, I.E. Goldberg, R.M. Weisskoff, B.P. Poncelet, D.N. Kennedy, B.E. Hoppel, M.S. Cohen and R. Turner, Dynamic magnetic resonance imaging of human brain activity during primary sensory stimulation. Proc. Natl. Acad. Sci. USA, 1992. 89: p. 5675-5679.

29 Aguirre, G.K., J.A. Detre and D.C. Alsop, Experimental design and the relative sensitivity of BOLD and perfusion fMRI. Neuroimage, 2002. 15: p. 488-500.

30 Wang, Z., M. Fernandez-Seara, D.C. Alsop, W.C. Liu, J.F. Flax, A.A. Benasich and J.A. Detre, Assessment of functional development in normal infant brain using arterial spin labeled perfusion MRI. Neuroimage, 2008. 39(3): p. 973-8.

31 Wang, J., H. Rao, G.S. Wetmore, P.M. Furlan, M. Korczykowski, D.F. Dinges and J.A. Detre, Perfusion functional MRI reveals cerebral blood flow pattern under psychological stress. Proc Natl Acad Sci U S A, 2005. 102(49): p. 17804-9.

32 Rao, H., S.J. Gillihan, J. Wang, M. Korczykowski, G.M. Sankoorikal, K.A. Kaercher, E.S. Brodkin, J.A. Detre and M.J. Farah, Genetic variation in serotonin transporter alters resting brain function in healthy individuals. Biol Psychiatry, 2007. 62(6): p. 600-6.

Arterial Spin Labeling (*syngo* ASL)
Case Reports from Geneva University

Viallon Magalie, Ph.D.; Karl-Olof Lovblad, M.D., Ph.D.

Hopitaux, Universitaire de Genève, Switzerland

Case 1: Pediatric 1

Patient history

15-year-old female patient with known epilepsy.

Image findings / Results

On the T2-weighted images there are multiple bilateral hemispheric cortical and subcortical hyperintensities that are much more visible on the corresponding FLAIR images. On the ASL perfusion maps we have hypoperfusion in these areas.

Discussion

The multiple cortical and subcortical lesions correspond to tubera in a case of Tuberous Sclerosis of Bourneville.

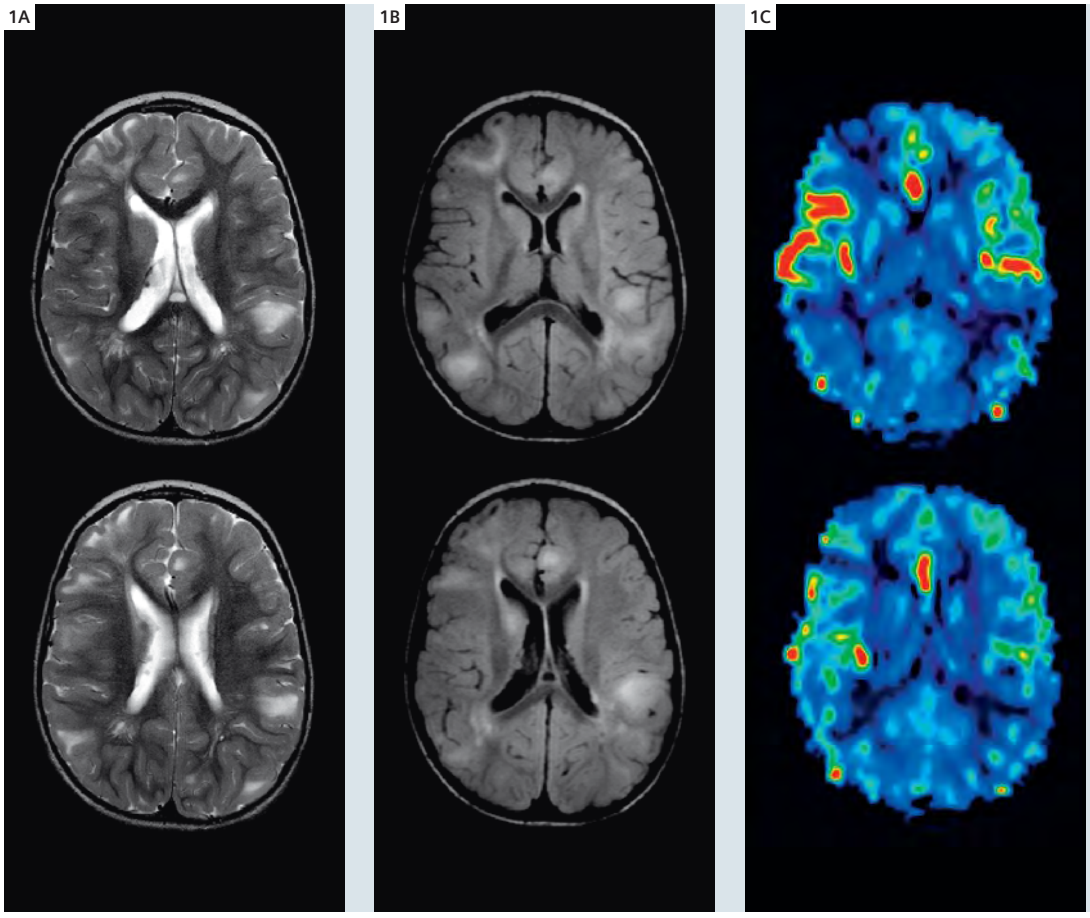

1A T2-weighted axial Turbo Spin Echo (TSE) image. Slice thickness 4 mm, TE/TR 101/4000 ms, BW 170 Hz/px, PAT factor 2, TF 19, FoV 150 x 200 mm, matrix 288 x 512, flip angle 145°.
1B Multiplanar reconstruction (MPR) Flair 3D sagittal 1 mm, TE/TR/TI 411/6000/2100 ms, BW 780 Hz/px, PAT factor 2, TF 266, FoV 234 x 250 mm, matrix 242 x 256, MPR slice thickness 4 mm, 176 slices.
1C Fair-QUIPSII arterial spin labeling sequence: TE/TR 13/5000 ms, BW 2230 Hz/px, matrix 64 x 64, FoV 220 mm, FatSat, slice thickness 6 mm, 14 slices, TI1 700 ms, TI2 1800 ms, T1 1496.5 ms, Partial Fourier 6/8, Lambda 0.9 mL/g, inversion efficiency 95%, flow compensation with flow limit 50 cm/sec, inferior Sat. Thk 100 mm, inferior sat gap 0 mm.

Case 2: Pediatric 2

Patient history

5-months-old* female with intractable epilepsy with 15 episodes per day.

*The safety of imaging infants under two years old has not been established.

Image findings / Results

Polymicrogyria of the left hemisphere on the T2-weighted images. On the ASL perfusion maps there is hypoperfusion in the left occipital lobe, which was also seen on FDG-PET (FluoroDeoxyGlucose-Positron Emission Tomography).

Discussion

Left-sided Hemimegalencephaly with polymicrogyria. The ASL data confirm the PET data which shows ictal hyper-perfusion in the left occipital lobe.

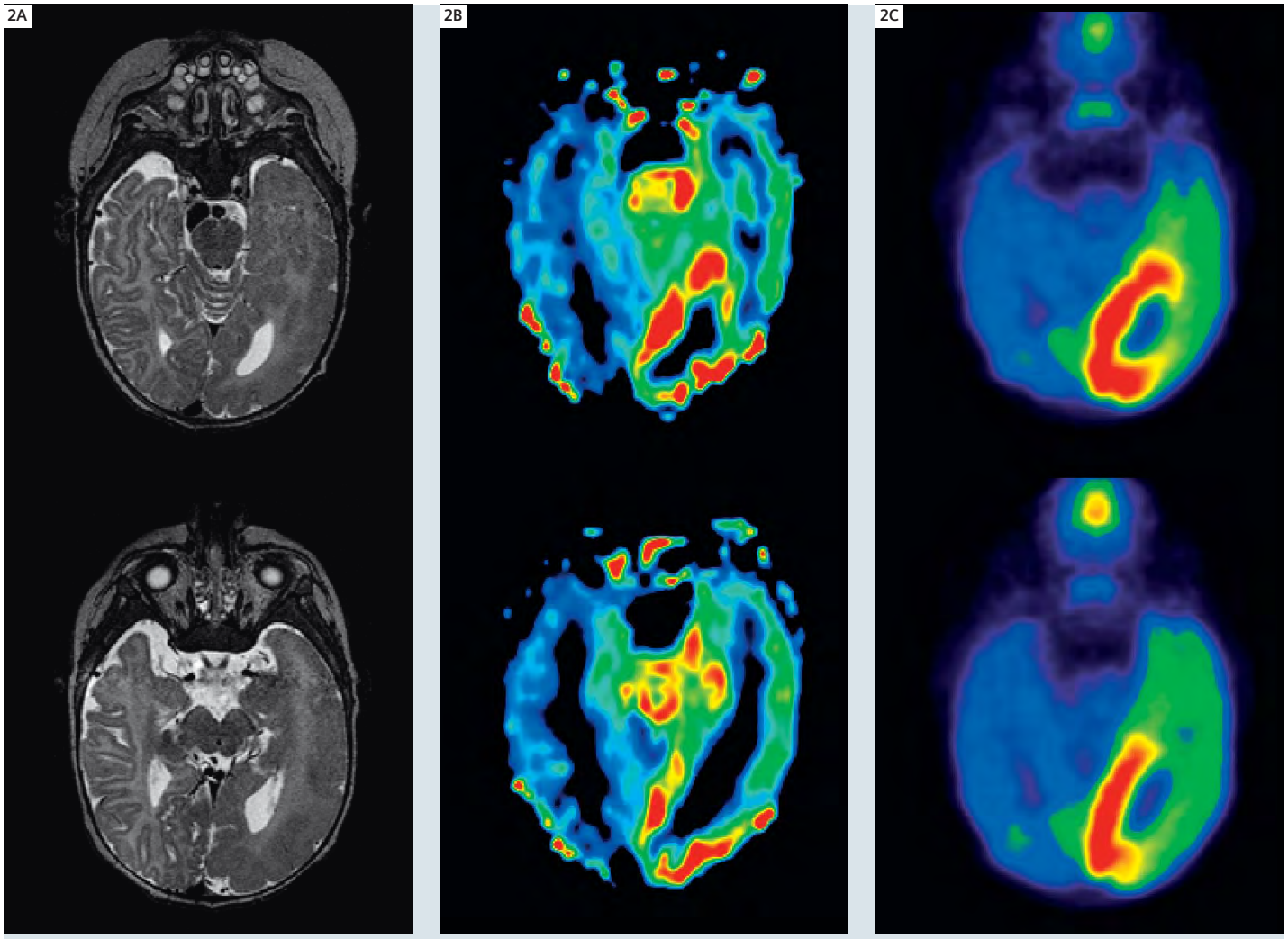

2A T2-weighted axial Turbo Spin Echo (TSE) image, slice thickness mm, TE/TR 101/4000 ms, BW 170 Hz/px, PAT factor 2, TF 19, FoV 150 x 200 mm, matrix 288 x 512, flip angle 145°. **2B** Fair-QUIPSII arterial spin labeling sequence: TE/TR 13/5000 ms, BW 2230 Hz/px, matrix 64 x 64, FoV 220 mm, FatSat, slice thickness 6 mm, 14 slices, TI1 700 ms, TI2 1800 ms, T1 1496.5, Partial Fourier 6/8, Lambda 0.9 mL/g, inversion efficiency 95%, flow compensation with flow limit 50 cm/sec, inferior Sat. Thk 100 mm, inferior sat gap 0 mm. **2C** F18-FDG PET-CT image with attenuation correction from CT data (Siemens Biograph Sensation 16), 80 MBq, 30 min post injection. These images show glucose metabolization which is linked to perfusion even though not being directly an image of CBF.

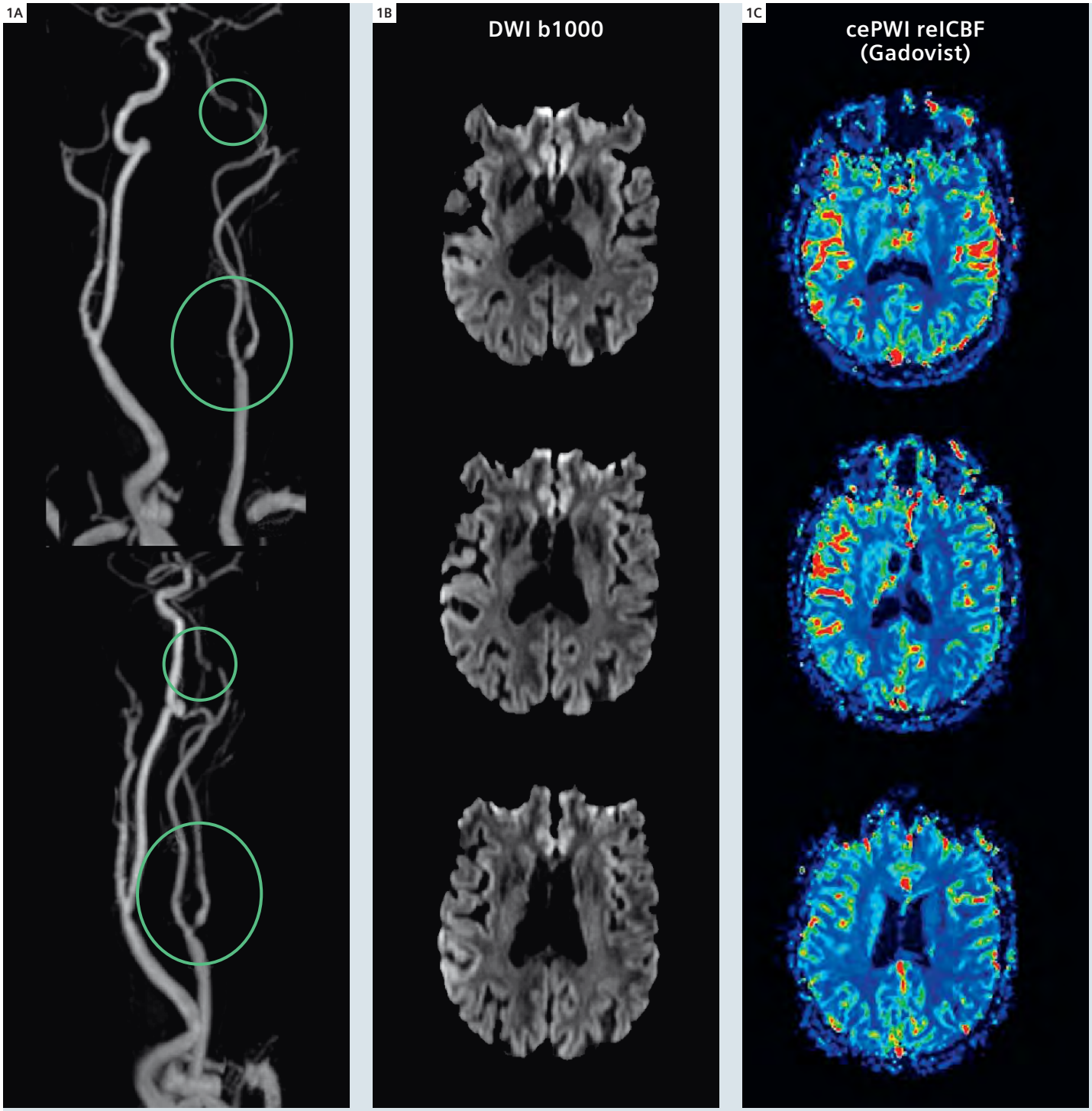

1A Contrast enhanced MR Angiography (ce-MRA): angiogram obtained from Flash3d-ce, voxel 0.8 x 0.8 x 0.8 mm, PAT factor 2, FoV= 263 x 300 mm, matrix 314 x 512, BW 650 Hz/px, flip angle 25°, 88 slices, centric reordering.

1B Diffusion-weighted imaging (DWI) b=1000, slice thickness 4 mm, TE/TR 92/5300 ms, BW 1240 Hz/px, PAT factor 2, FoV 208 x 230 mm, codage AP, matrix 157 x 192, flip angle 90°, 4 averages.

1C Contrast enhanced perfusion-weighed imaging (cePWI)*, relative cerebral blood flow (relCBF)*: relCBF parametric map calculated using *syngo* MR perfusion*, slice thickness 4 mm, TE/TR 92/4000 ms, BW 1370 Hz/px, PAT factor 2, FoV 200 x 200 mm, matrix 128 x 128, flip angle 90°.

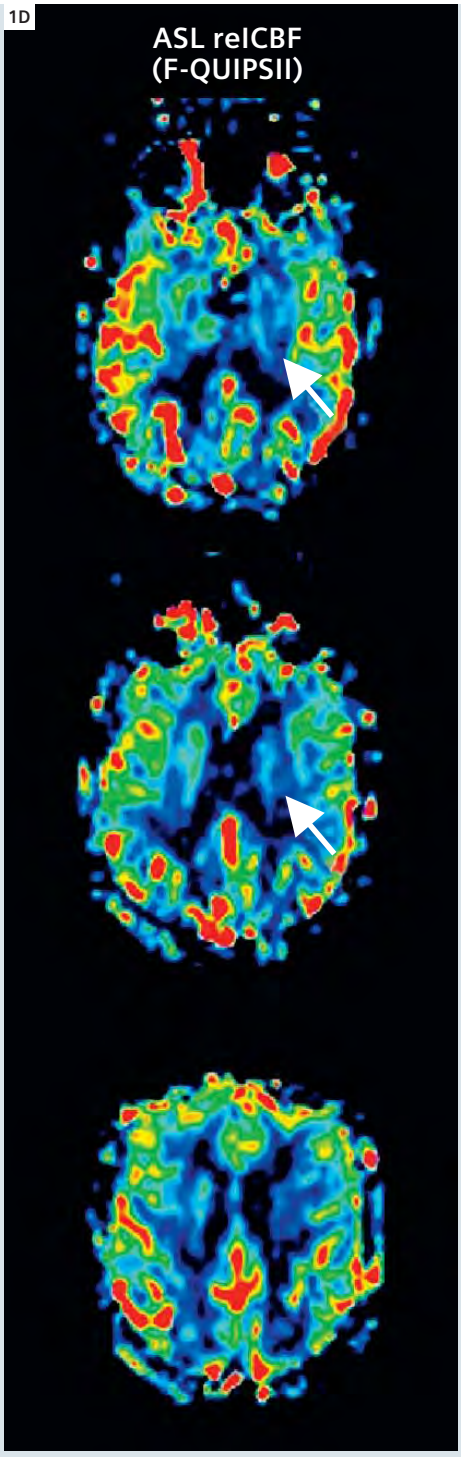

1D Arterial Spin Labeling (ASL) relCBF: Fair-QUIPSII ASL sequence: TE/TR 13/5000 ms, BW 2230 Hz/px, matrix 64 x 64, FoV 220 mm, FatSat, slice thickness 6 mm, 14 slices, TI1 700 ms, TI2 1800 ms, T1 1496.5 ms , Partial Fourier 6/8, Lambda 0.9 mL/g, inversion efficiency 95%, flow compensation with flow limit 50 cm/sec, inferior Sat. Thk 100 mm, inferior sat gap 0 mm.

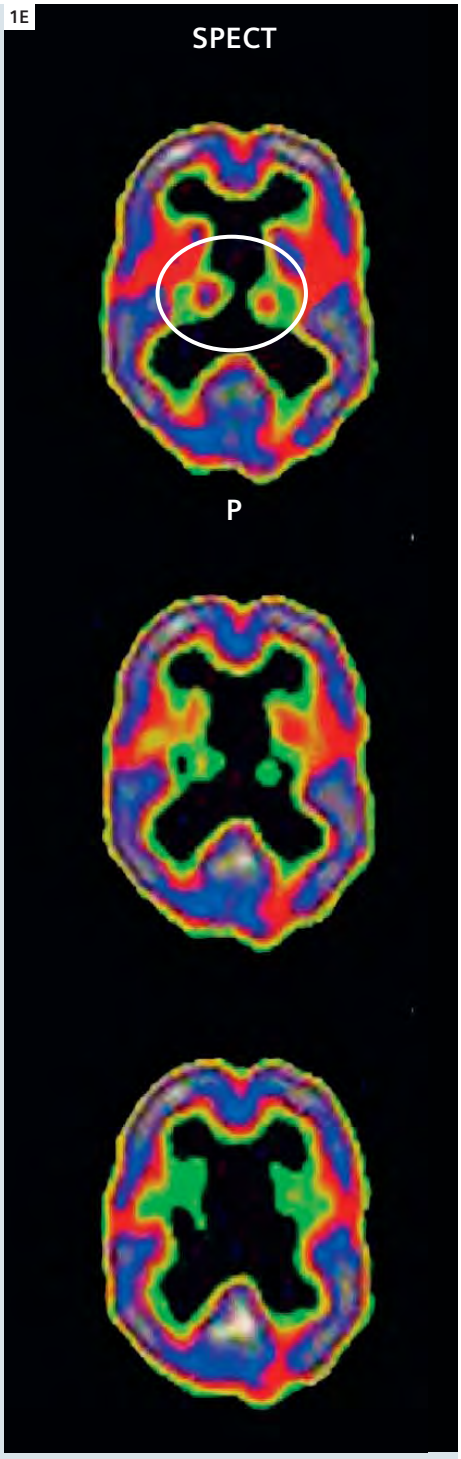

1E SPECT acquisition (Toshiba 3-heads) after injection of 369 MBq of 99 mTc-ECD. Post DIAMOX we observe an equalization of the perfusion of both hemisphere, pre DIAMOX, we have an increase perfusion on the right hemisphere.

Case 3: High grade stenosis on the left ICA

Patient history

Patient with left-sided carotid stenosis

Image findings / Results

High-grade left-sided carotid stenosis visible on contrast-enhanced MRA of the carotids. On DWI there are no ischemic lesions. On contrast-enhanced Perfusion* maps there is hypoperfusion in the left basal ganglia and internal capsule, which can be seen both on ASL maps and SPECT.

Discussion

The ASL findings correspond quite well to those identified on both SPECT and contrast-enhanced perfusion in a case of tight carotid stenosis. The enormous advantages of ASL in such a protocol is that it allows to both study perfusion prior to an injection of contrast agent dedicated to ceMRA.

Case 4: Stroke

Patient history

67-year-old male patient with dysphasia and right-sided hemiparesis.
The examination was performed on a MAGNETOM Trio, A Tim system, using a 12-channel head coil.

Image findings / Results

The DWI images show restricted diffusion in the left MCA territory, these changes can be seen on FLAIR and T2. On the ASL there is slight hyperperfusion* due to collateral flow, which cannot be seen on conventional contrast-enhanced perfusion imaging and SPECT images.

Discussion

In addition to the diffusion and standard MR sequences, ASL shows reperfusion in acute stroke* that cannot be seen on conventional MR perfusion images. Areas of cortical reperfusion due to collaterals were better assessed by ASL that seems to demonstrate hyperperfusion that might signal recanalization and/or collaterals. Moreover ASL correctly measures CBF even when BBB breaks down, which commonly occurs after a few days in stroke. Thus performing a protocol including ASL may allows one to better include/exclude patients for treatment: impacting on prevention by demonstrating hypoperfusion in carotid stenosis and improving treatment of ischemia by showing hemodynamic compromise.

The examinations were performed on a MAGNETOM Trio, using a 12-channel head coil.

Contact
Magalie Viallon, Ph.D.
Hopitaux Universitaire de Genève
Switzerland
Magalie.viallon@hcuge.ch

Karl-Olof Lovblad, M.D., Ph.D.
Hopitaux Universitaire de Genève
Switzerland
Karl-olof.lovblad@hcuge.ch

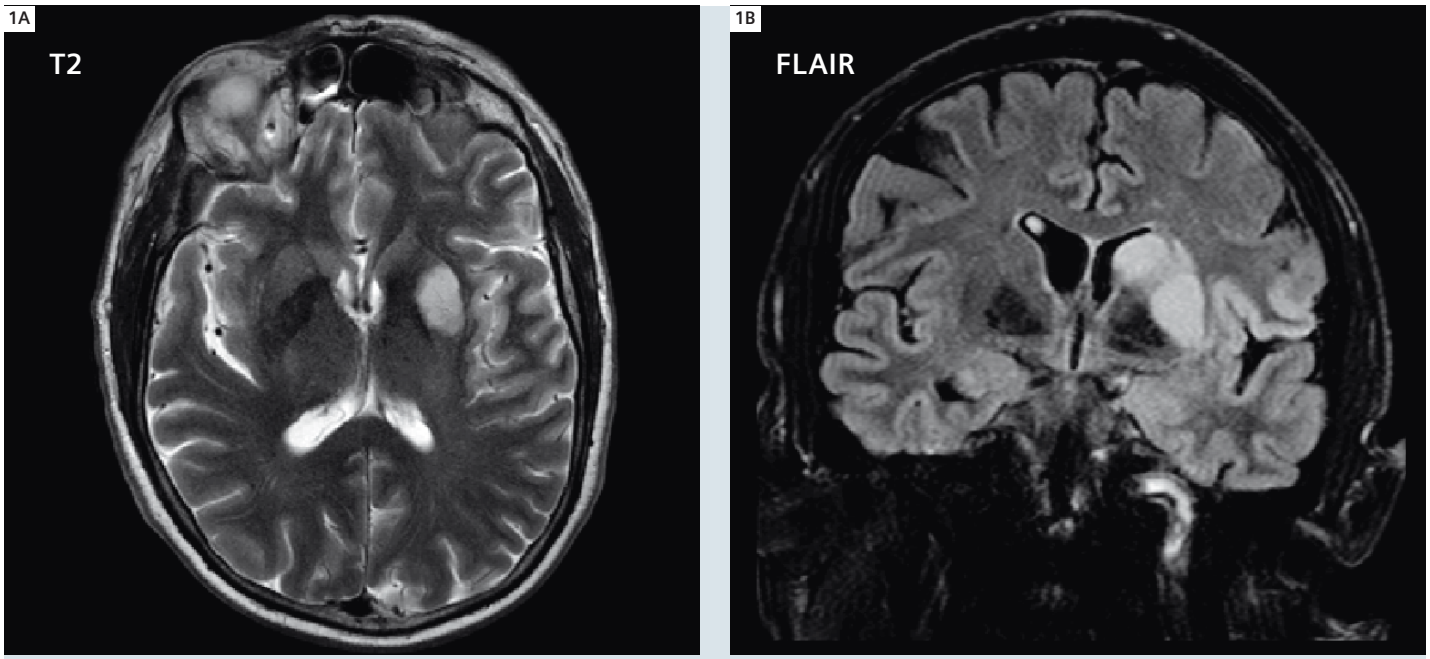

1A T2-weighted axial Turbo Spin Echo image: slice thickness 4 mm, TE/TR 101/4000 ms, BW 170 Hz/px, PAT factor 2, TF 19, FoV 150 x 200 mm, matrix 288 x 512, flip angle 145°. **1B** T2-weighted coronal FLAIR image: slice thickness 4 mm, TE/TR/TI 122/8500/2500 ms, BW 130 Hz/px, PAT factor 2, TF 13, FoV 200 x 230 mm, matrix 190 x 256, flip angle 150°.

*Works in progress (WIP). The information about this product is preliminary. The product is under development and not commercially available in the U.S., and its future availability cannot be ensured.

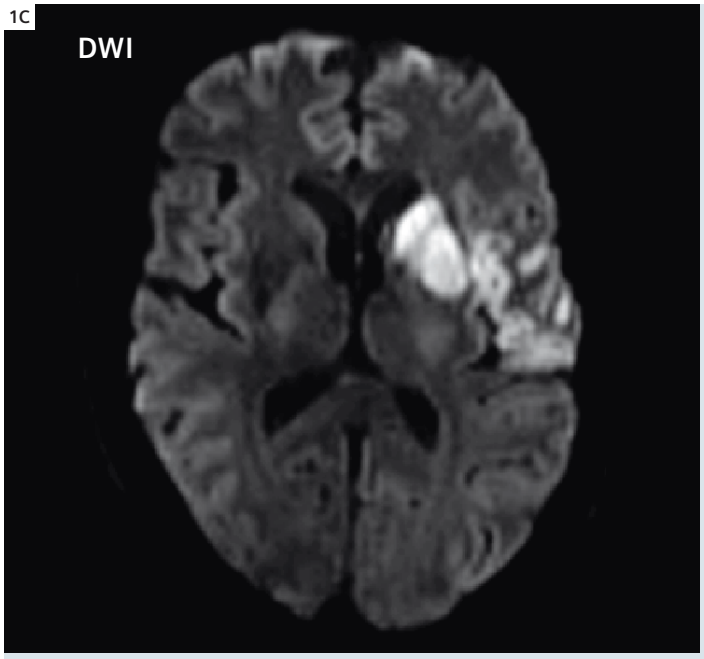

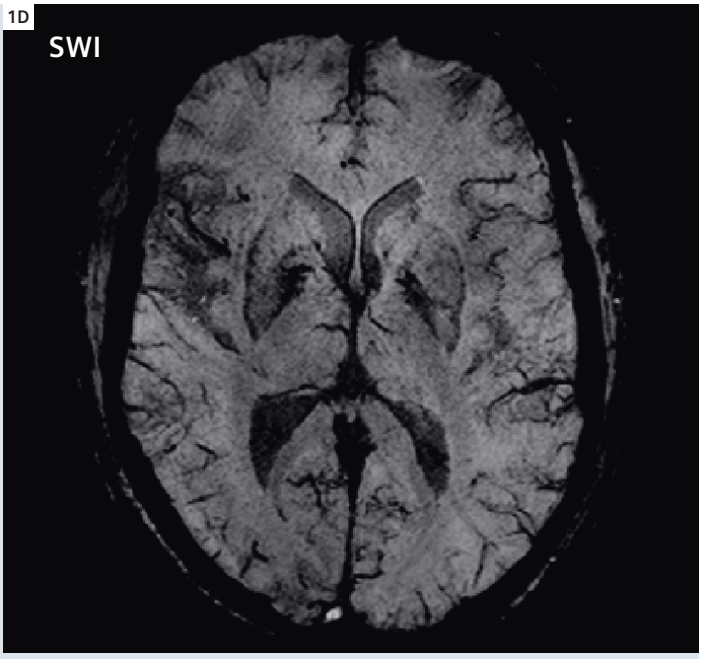

1C Diffusion-weighted image (DWI): b=1000, slice thickness 4 mm, TE/TR 92/5300 ms, BW 1240 Hz/px, PAT factor 2, FoV 208 x 230 mm, codage AP, matrix 157 x 192, flip angle 90°, 4 aver- **1D** ages. Susceptibility-weighted image (SWI): slice thickness 1.2 mm, TE/TR 20/34 ms, BW 110 Hz/px, PAT factor 2, FoV 175 x 200 mm, matrix 224 x 256, flip angle 15°, flow compensation, thin MinIP (minimum intensity projection) axial 8 mm, 60 slices.

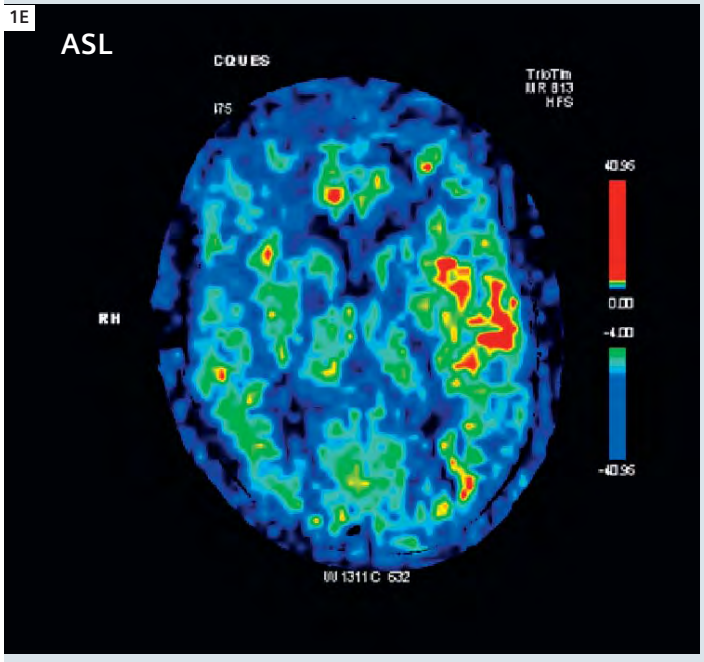

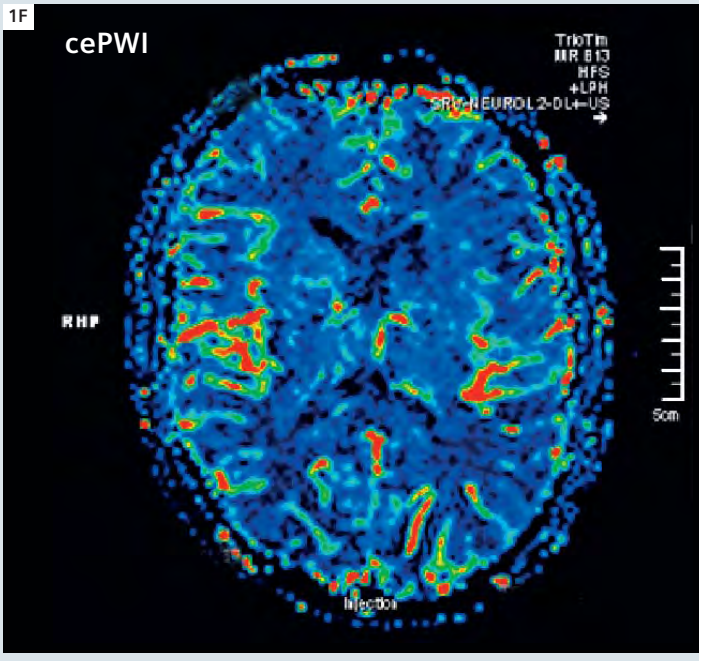

1E Arterial Spin Labeling (ASL) relCBF: Fair-QUIPSII arterial spin labeling sequence: TE/TR 13/5000 ms, BW 2230 Hz/px, matrix 64 x 64, FoV 220 mm, FatSat, slice thickness 6 mm, 14 slices, TI1 700 ms, TI2 1800 ms, T1 1496.5 ms, Partial Fourier 6/8, Lambda 0.9 mL/g, inversion efficiency 95%, flow compensation with flow limit 50 cm/s, inferior Sat. Thk 100 mm, inferior sat gap 0 mm.

1F Contrast enhanced perfustion-weighted image (cePWI)* relCBF: relCBF* parametric map calculated using *syngo* MR perfusion, slice thickness 4 mm, TE/TR 92/4000 ms, BW 1370 Hz/px, PAT factor 2, FoV 200 x 200 mm, matrix 128 x 128, flip angle 90°.

Case Report: Clinical Validation of Arterial Spin Labeling

Jessica A. Turner; Sumiko Abe; Liv MacMillan; Jerod Rasmussen; Steven G. Potkin

Brain Imaging Center, University of California, Irvine, CA, USA

Introduction

Arterial spin labeling (ASL) magnetic resonance imaging methods are perfusion-based imaging techniques; they provide quantitative measures of capillary blood flow rCBF (regional cerebral blood flow), in units of ml/100 g/min. Like positron emission tomography and certain other imaging methods, ASL measures can be either absolute (measuring overall flow), or relative (measuring changes in flow). However, ASL does not require injection of radioactive tracers or contrast agent, since it depends on the endogenous tracer of the spin-tagged blood. This allows it to be used in many clinical populations, and to be used repeatedly over shorter periods of time without any side effects observed with other exogenous tracer based methods. The basis of ASL is to use an appropriate RF pulse to tag all the blood in a particular location with a particular magnetization, i.e. an inversion (hence spin labeling). As the blood perfuses from the tagging location into the rest of the brain, the tagged blood changes the magnetization characteristics of the area, and thus can be measured [1]. ASL has been used successfully to measure blood flow in cardiovascular disorders and brain tumors [2–6]. Areas of high perfusion around a tumor, for example, can indicate where the growth is occurring most rapidly [7]. ASL can identify signs of stenosis which can be very difficult to otherwise identify non-invasively in the clinic [8]. These disorders which stem from structural changes closely involved with the cardiovascular system are obvious candidates for a study using ASL.

Here we would like to demonstrate how ASL can be useful in clinical settings.

The following protocol (referred to as "FBIRN-ASL protocol") was used:
FAIR QUIPSSII as pulsed ASL method,
TI2 = 1600 ms,
TI1 = 600 ms;
TR = 4 s,
TE = 12 ms;
flip angle 90 degrees;
24 slices, 4 mm thick, 1 mm gap.
P >> A phase encoding;
220 mm FOV,
base resolution 64,
phase partial Fourier 6/8,
ascending slice order,
AC–PC aligned.
Fat saturation was turned on;
the coil combine mode was
sum of squares.
The bandwidth was 2368 Hz/Px,
echo spacing 0.49.
We collected 105 measurements, which included an M0 reference scan. All studies were conducted using the 12-channel Siemens product Head Matrix coil. 3D PACE was used for real-time prospective motion correction.

Case 1

The subject is a 47-year-old male, who has been schizophrenic for 31 years, currently on antipsychotics and sleep aids. He had a self-report of a head injury at age 3 requiring both stitches and surgery, and another concussion with hospitalization in his teens. His schizophrenic symptoms are stable on his current medications. The head injury is not the current cause for treatment. The subject received T1- and T2-weighted anatomic scans, and an ASL scan using the FBIRN settings. The MRIs were reviewed by a radiologist to determine whether the internal brain damage required any current attention, and it was determined that it did not. The rCBF measures from the entire brain, from gray matter and from areas near the damage were measured for comparison both in their means and their variability. The T1 and T2-weighted images clearly showed areas of damage in the frontal lobes, with multiple fluid filled cysts, and dilation of the posterior sulci. There was no dilatation of the left frontal horn of the ventricles, which frequently is associated with atrophy, so general atrophy was not noted. The ASL images showed the expected distortion from the frontal cysts.

The rCBF measures both globally and from the entire grey matter of the subject were in general quite low, 45–47 ml/100 g/min (as compared to 58 ml/100 g/min for similarly aged healthy males, using a 1.5T multi-slice CASL method, in Parkes et al. (2004).) Areas near the cysts showed a higher variability in rCBF than did the overall grey matter measures.

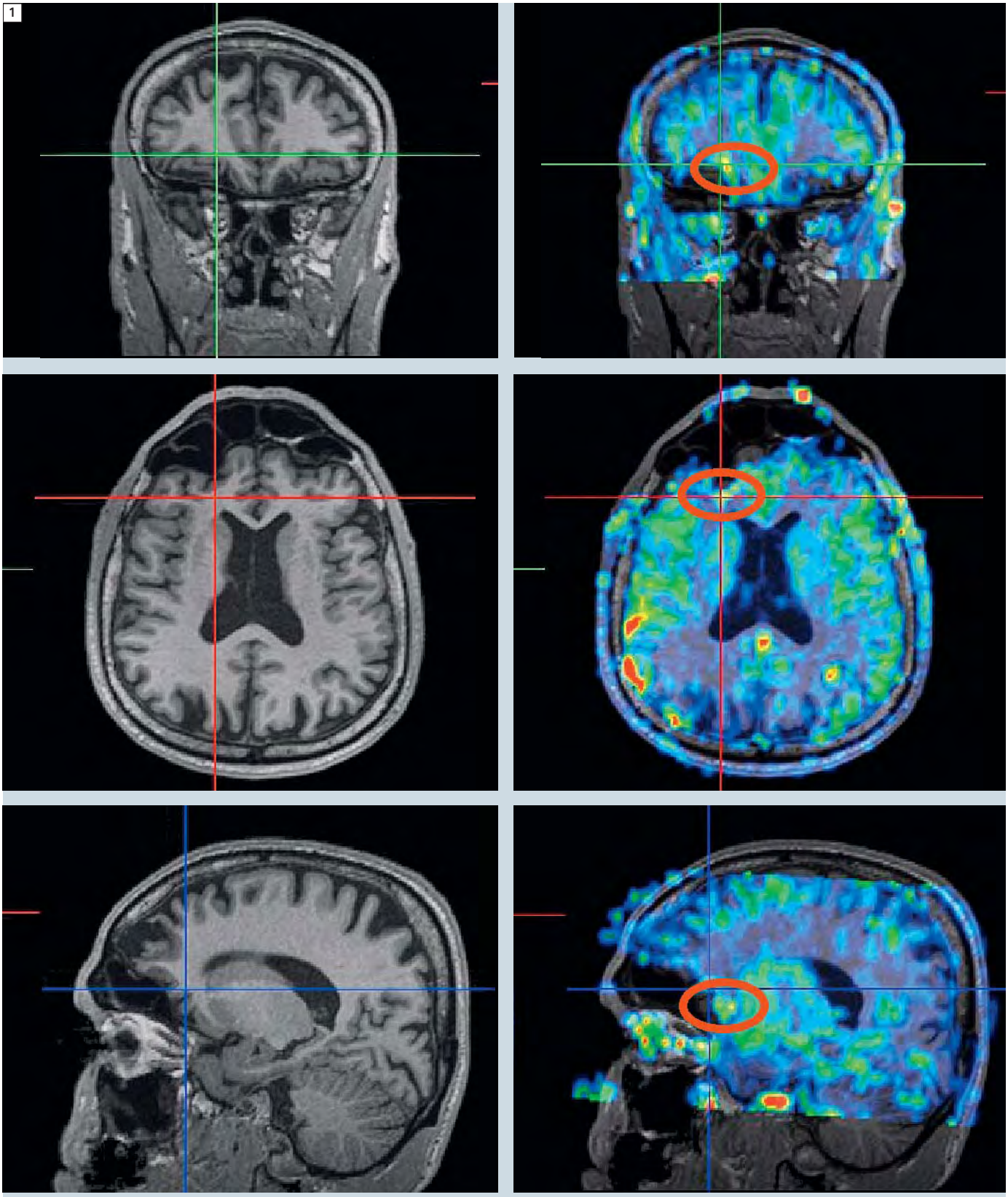

1 rCBF measurement around the area of brain damage. Left row is the anatomical scan and the right row shows the ASL rCBF measurement fused to the anatomical scan. The rCBF of the area around the brain damage is found to be higher.

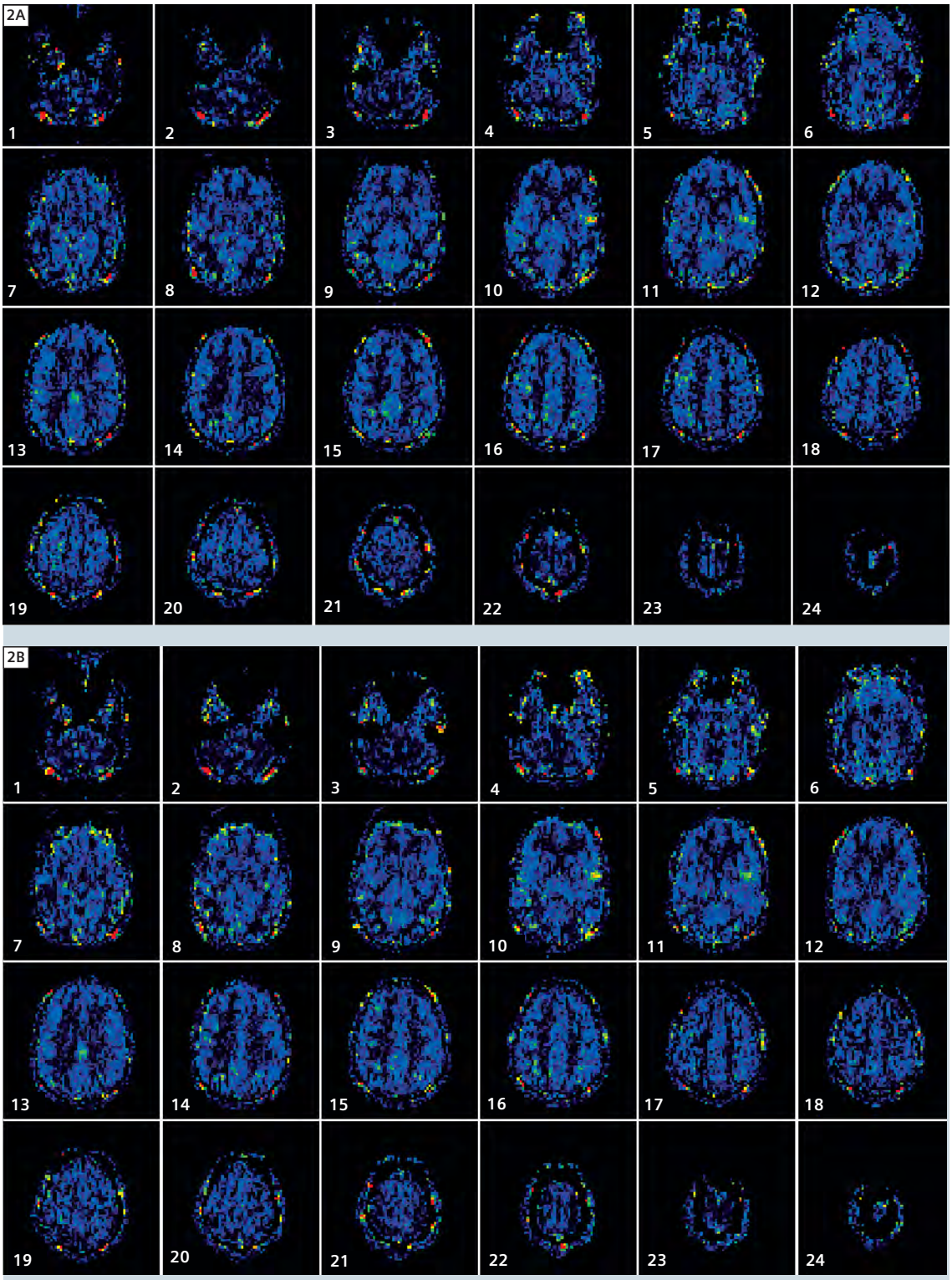

2A, B Representative images from the experiment. **(2A)** rCBF images when eyes open and **(2B)** when closed.

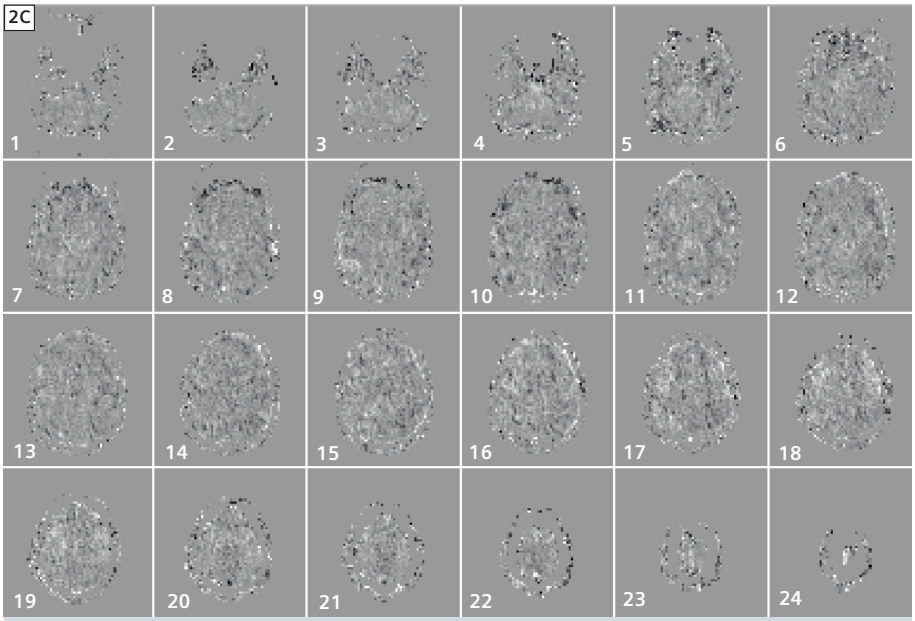

2C Difference images between eyes closed and eyes open.

Case 2

Three healthy subjects (ages 22 to 62) were scanned twice each in the FBIRN-ASL setting, once with eyes open and once with eyes closed. One subject was scanned twice in each condition. No motion correction was included during the scan.

Various rCBF measures were summarized from the rCBF images in each condition. The difference image (rCBF with eyes open – rCBF with eyes closed) was calculated for each subject. Head movement over the 105 image volumes was also measured in the two conditions. Overall, ASL flow within the grey matter mask increases very slightly with the eyes open. In three of the four cases, head movement was greater when the subject's eyes were closed.

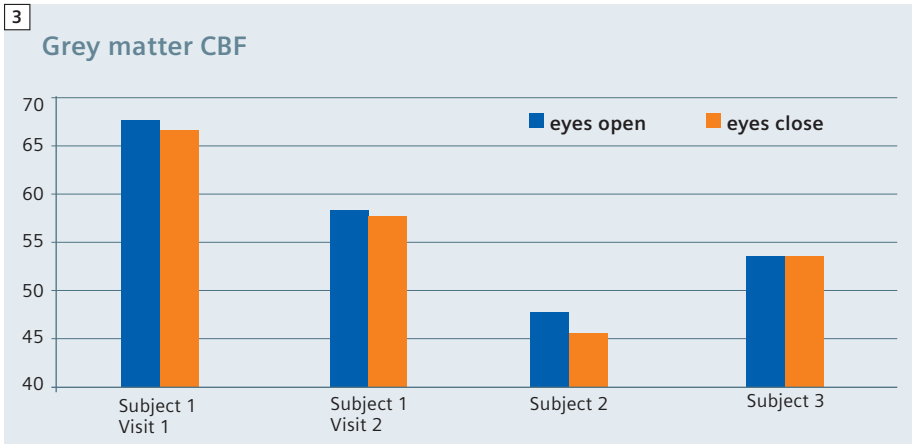

3 Grey matter rCBF [ml/100 g/min]. There is a consistent decrease in grey matter CBF when the eyes are closed.

Contact
Jessica A. Turner, Ph.D.
Project Manager, FBIRN
(www.nbirn.net)
Department of Psychiatry and
Human Behavior
University of California
Irvine, CA, 92617
USA
Phone: +1(949) 824-3331
Fax: +1(949) 824-3324
turnerj@uci.edu

References

1 Detre, J. A., Leigh, J. S., Williams, D. S., & Koretsky, A. P. (1992). Perfusion imaging. Magn Reson Med, 23(1), 37–45.

2 Deibler, A. R., Pollock, J. M., Kraft, R. A., Tan, H., Burdette, J. H., & Maldjian, J. A. (2008a). Arterial spin-labeling in routine clinical practice, part 2: Hypoperfusion patterns. AJNR Am J Neuroradiol.

3 Deibler, A. R., Pollock, J. M., Kraft, R. A., Tan, H., Burdette, J. H., & Maldjian, J. A. (2008b). Arterial spin-labeling in routine clinical practice, part 3: Hyperperfusion patterns. AJNR Am J Neuroradiol.

4 Noguchi, T., Yoshiura, T., Hiwatashi, A., Togao, O., Yamashita, K., Nagao, E., et al. (2008). Perfusion imaging of brain tumors using arterial spin-labeling: Correlation with histopathologic vascular density. AJNR Am J Neuroradiol, 29(4), 688–693.

5 Tourdias, T., Rodrigo, S., Oppenheim, C., Naggara, O., Varlet, P., Amoussa, S., et al. (2008). Pulsed arterial spin labeling applications in brain tumors: Practical review. J Neuroradiol, 35(2), 79–89.

6 Wolf, R. L., & Detre, J. A. (2007). Clinical neuroimaging using arterial spin-labeled perfusion magnetic resonance imaging. Neurotherapeutics, 4(3), 346–359.

7 Bartsch, A. J., Homola, G., Biller, A., Solymosi, L., & Bendszus, M. (2006). Diagnostic functional mri: Illustrated clinical applications and decision-making. J Magn Reson Imaging, 23(6), 921–932.

8 Detre, J. A., Samuels, O. B., Alsop, D. C., Gonzalez-At, J. B., Kasner, S. E., & Raps, E. C. (1999). Noninvasive magnetic resonance imaging evaluation of cerebral blood flow with acetazolamide challenge in patients with cerebrovascular stenosis. J Magn Reson Imaging, 10(5), 870–875.

Cerebral Blood Flow Imaging with 3D GRASE ASL Sequence Increases SNR and Shortens Acquisition Time

David A. Feinberg[1,2,3]; Matthias Günther[1,4,5]

[1]*Advanced MRI Technologies, LLC, Sebastopol, CA, USA*
[2]*University of California, Berkeley and San Francisco, CA, USA*
[3]*Redwood Regional Medical Group, Santa Rosa, CA, USA*
[4]*mediri GmbH, Heidelberg, Germany*
[5]*University Hospital Mannheim, Neurology, Heidelberg, Germany*

Abstract

Arterial Spin Labeling (ASL) is a technique capable of measuring cerebral blood flow (CBF) in humans. However, ASL is limited by low sensitivity given blood is ~3% by volume in brain parenchyma. Single-shot 3D GRASE ASL technique has made possible whole brain coverage with over twice the signal-to-noise ratio (SNR) of 2D EPI ASL. To achieve even higher spatial resolution in fast acquisitions, a segmented version of the 3D GRASE ASL sequence is combined with a 32-channel coil at 3 Tesla to achieve 128 and 256 matrix images in 1 to 2 minutes.

Introduction

In the early 1980s when the very first MRI blood flow images were shown at conferences, Nobel Prize laureate Prof. Paul Lauterbur commented, "As MR imaging techniques develop, blood flow imaging will advance with them." This is fortelling of the recent developments describing the uniquely powerful Arterial Spin Labeling (ASL) method of blood flow imaging [1–6], since it is very flexible and can be adapted to several different MR imaging sequences. Each imaging technique is differs in speed, image quality and ability to quantify blood flow. To be discussed below are the advantages of 3D sequences [1, 2, 26, 27] compared to 2D MRI in overcoming physiologic limitations in obtaining whole brain coverage. The 3D gradient and spin echo (GRASE) [1, 2, 18] readout scheme has advantages of refocusing many more signals than RARE / TSE / FSE or EPI sequences for higher SNR which translates into greatly reduced imaging time and much higher spatial resolution (Fig. 1). It has additional advantages of reduced susceptibility artifacts compared to Spiral and EPI techniques for improved image quality. Several examples of 3D GRASE ASL are presented here along with a fuller discussion of these differences.

What is ASL imaging?

To measure blood perfusion in brain tissue, it is necessary to quantify signal

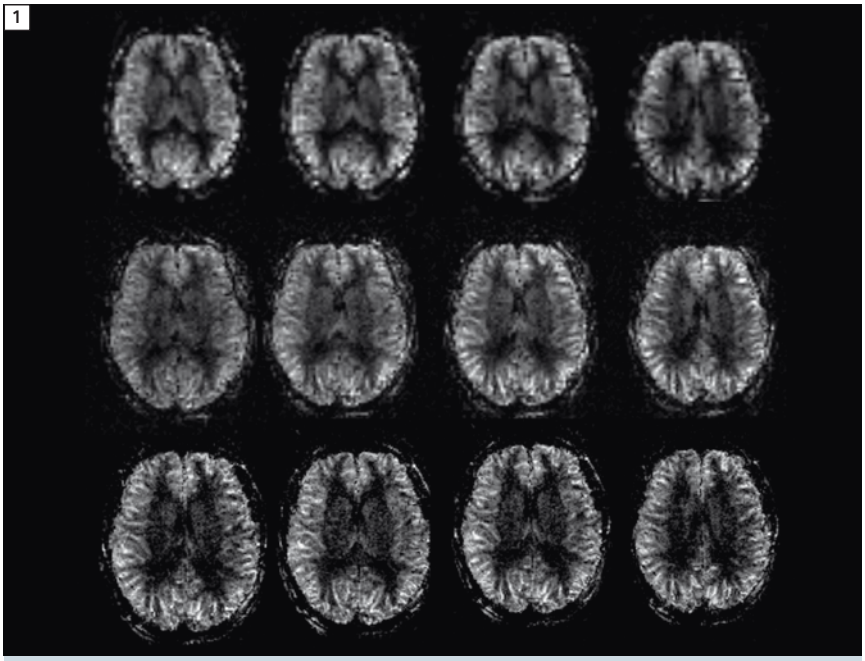

1 3D GRASE ASL with 32-channel coil **row 1)** 64 matrix, resolution 4 x 4 x 4 mm³ voxel, 26 images, 16 s, **row 2)** 128 matrix, resolution 2.5 x 2.5 x 2.0 mm³ in 1 min **row 3)** 256 matrix, resolution 1.5 x 1.5 x 3.0 mm³, 26 images, 2:04 min.

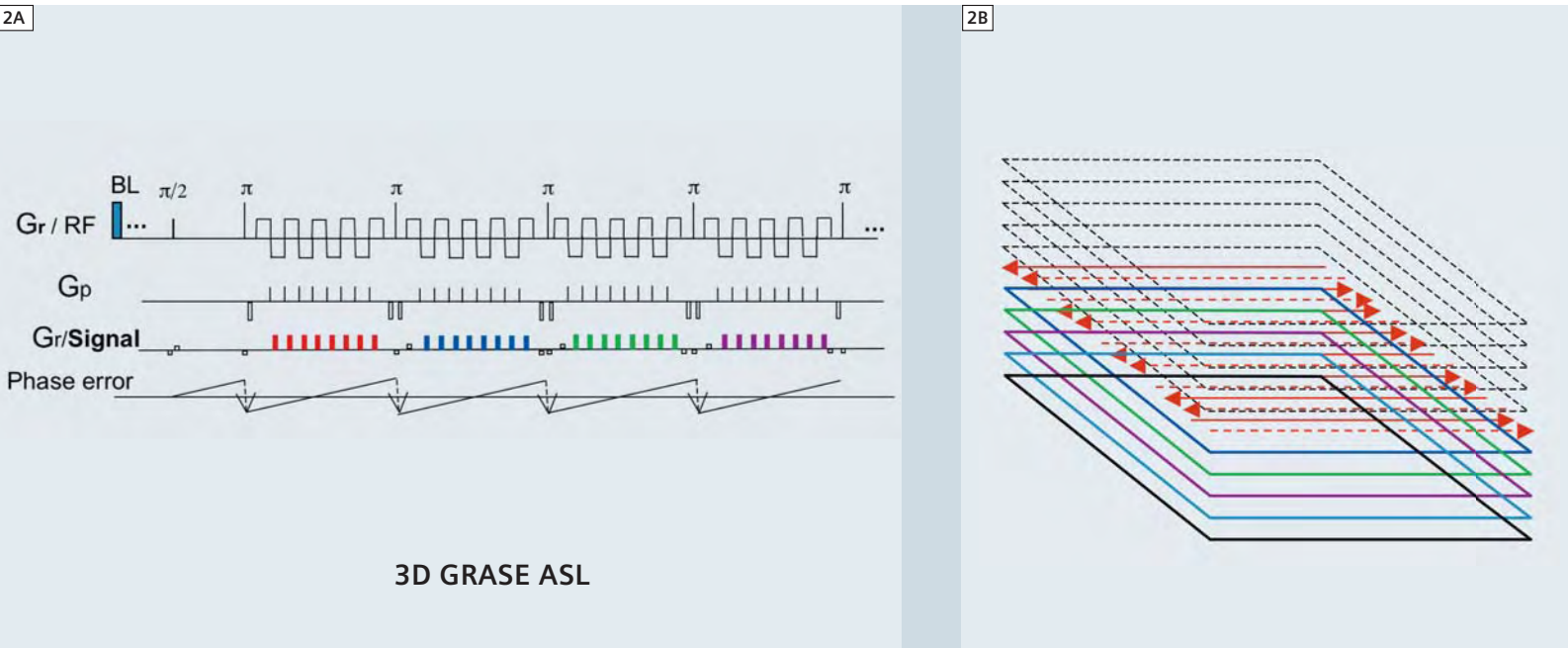

2 3D GRASE ASL. The 180° RF refocusing pulses (π) prevent large phase error. EPI type gradient refocusing (Gr) gives maximum number of signals, (BL) blood labeling and background suppression pulses.

changes independent of the signal from the partial volumed static brain tissue. ASL obtains two images, each with identical signals from brain tissue but different blood signal as affected by the presence / absence of blood labeling RF pulses (typically inversion RF pulses). Ideally, subtraction of the two images removes static brain tissue signal leaving only blood signal which intensity reflects hemodynamic parameters of cerebral blood flow (CBF) and the blood bolus arrival time (BAT) to the tissue. Critical to the success of ASL, the blood spin labeling is achieved by manipulating the longitudinal magnetization, which stores the "labeled" (tagged) spin magnetization with T1 decay (~1200–1500 ms) rather than with shorter T2 decay (~150 ms). The longer T1 decay enables enough time for the spins in blood to reach the brain tissue upstream from the arterial location of labeling. The tagging of the inflowing blood spins can either occur in a small localized region but over a long period of time of several seconds (continuous ASL [2, 3, 7, 9, 14, 24]) or at a larger region at a defined point in time (pulsed ASL [28–31]. After labeling preparation the tagged blood spins are given an inflow time TI to allow them to move into the microvasculature of the imaging region. A typical inflow time is 1500 ms. The beginning of the image readout sequence typically occurs with a 90° excitation pulse followed by either a gradient echo train sequence such as EPI or spiral, where the signal decays with T2* or by a spin echo based sequence like RARE or GRASE, where the signal decays with a combination of T2 and a component of stimulated echoes with longer T1 decay. As mentioned above, the measured signal will be dominated by brain tissue signal with blood signal being in the range of a few percent. Therefore, additional application of background suppression pulse schemes are incorporated to reduce the amplitude of static signal so errors in net subtracted signal is reduced for more reliable measurement of blood signal [32]. For quantification of cerebral blood flow several models exist [6, 12, 13] with the one-compartment model [12] being used most often. One of the most critical aspects of quantification is the variation of arrival times of the labeled blood bolus at different regions of the brain. Several techniques have been developed to reduce the sensitivity to this bolus arrival time (BAT) [4, 6]. Time-consuming sampling the inflow of the labeled blood into the tissue allows the measurement of BAT as an additional hemodynamical parameter. For whole brain application, this technique requires an efficient ASL technique, which provides sufficient SNR to reduce overall scan time and supports large region coverage.

2D and 3D ASL slice coverage limitations of hemodynamic timing

One of the major drawbacks of 2D EPI based ASL is a limitation on the number of images, preventing whole brain coverage. The EPI images are readout sequentially. With the acquisition of each EPI image ~50 msec, the blood inflow time of each slice increases with this time increment until the net range of inflow time is too large to ensure that the labeled blood is in the same vascular compartment in all slices. The 3D MRI sequences entirely overcome this problem because all images are readout

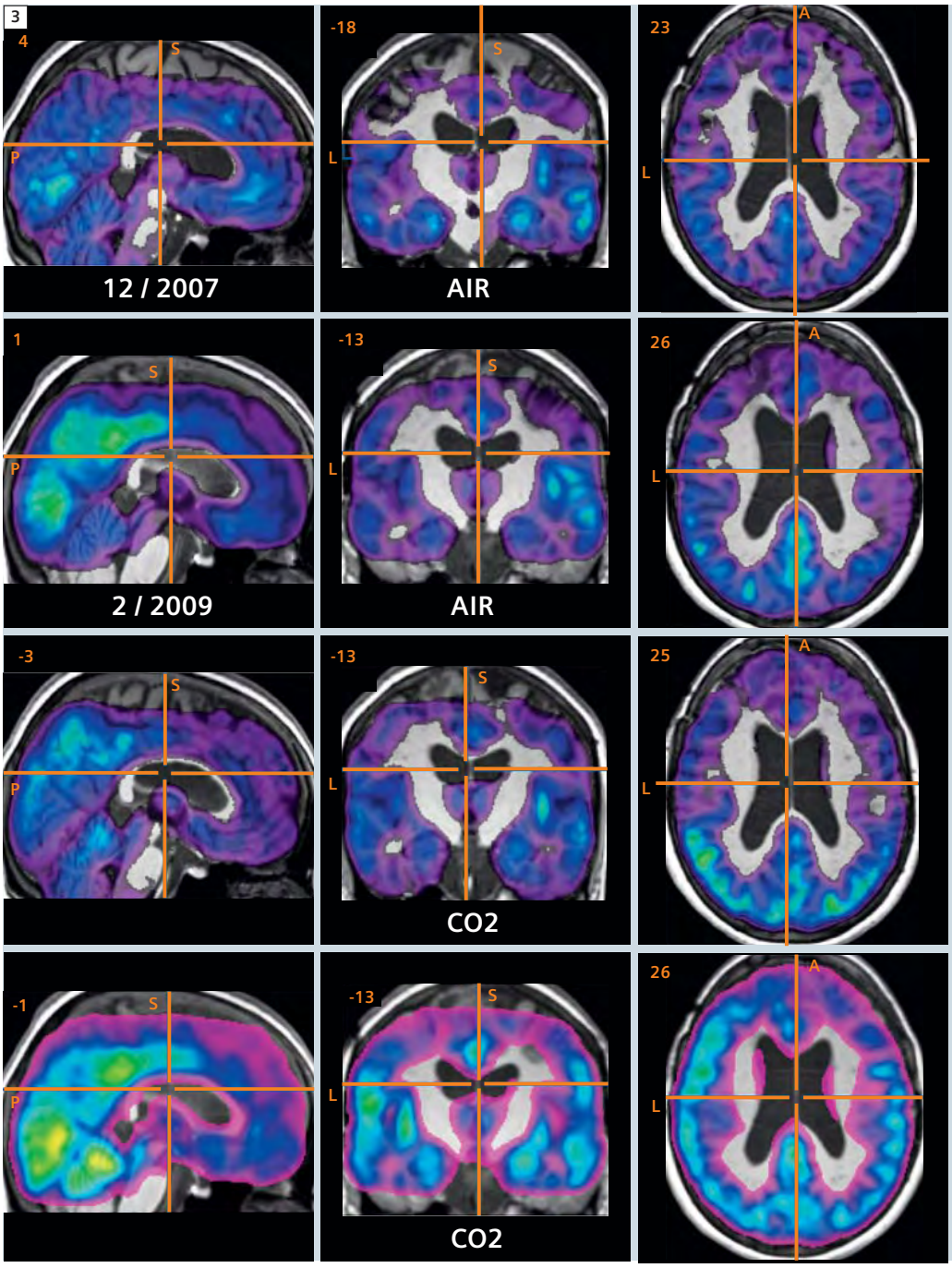

3 CBF maps of MoyaMoya patient.
Rows 1 and 2: control image while breathing air.
Rows 3 and 4: hypercapnia, CO_2 challenge.
Rows 1 and 3: 12/2007 pre-surgery.
Rows 2 and 4: 2/2009 post-surgery show greater vascular reactivity post-surgery. The CBF maps from 3D GRASE ASL overlaid on anatomic images.
(Courtesy of Rik Achten, GIfMI, UGent, Belgium.)

simultaneously rather than in temporal sequential order. The spins move into the brain tissue and at a specified time, all slices are encoded simultaneously beginning with a single 90 degree pulse covering a thick slab 3D volume [1, 27], not a single slice [11]. The echo train reads out all slices together which are then separated by a 3D Fourier Transform, which has additional sqrt(N) advantage of higher SNR compared to 2D EPI. Similarly, in a 3D readout the inversion pulse timing for background suppression is optimal for all slices, while in sequential 2D imaging there is variation between slices in the effectiveness of background suppression [32].

Artifacts in 3D GRASE compared to RARE, Spiral, EPI

Basically any echo train sequence can be used for 3D ASL readout but each differs in their number of echoes, accumulative phase errors causing susceptibility artifacts, and SNR efficiency [25, 17]. Echo volume imaging (EVI) is the 3D variant of EPI which has an echo train time lim-

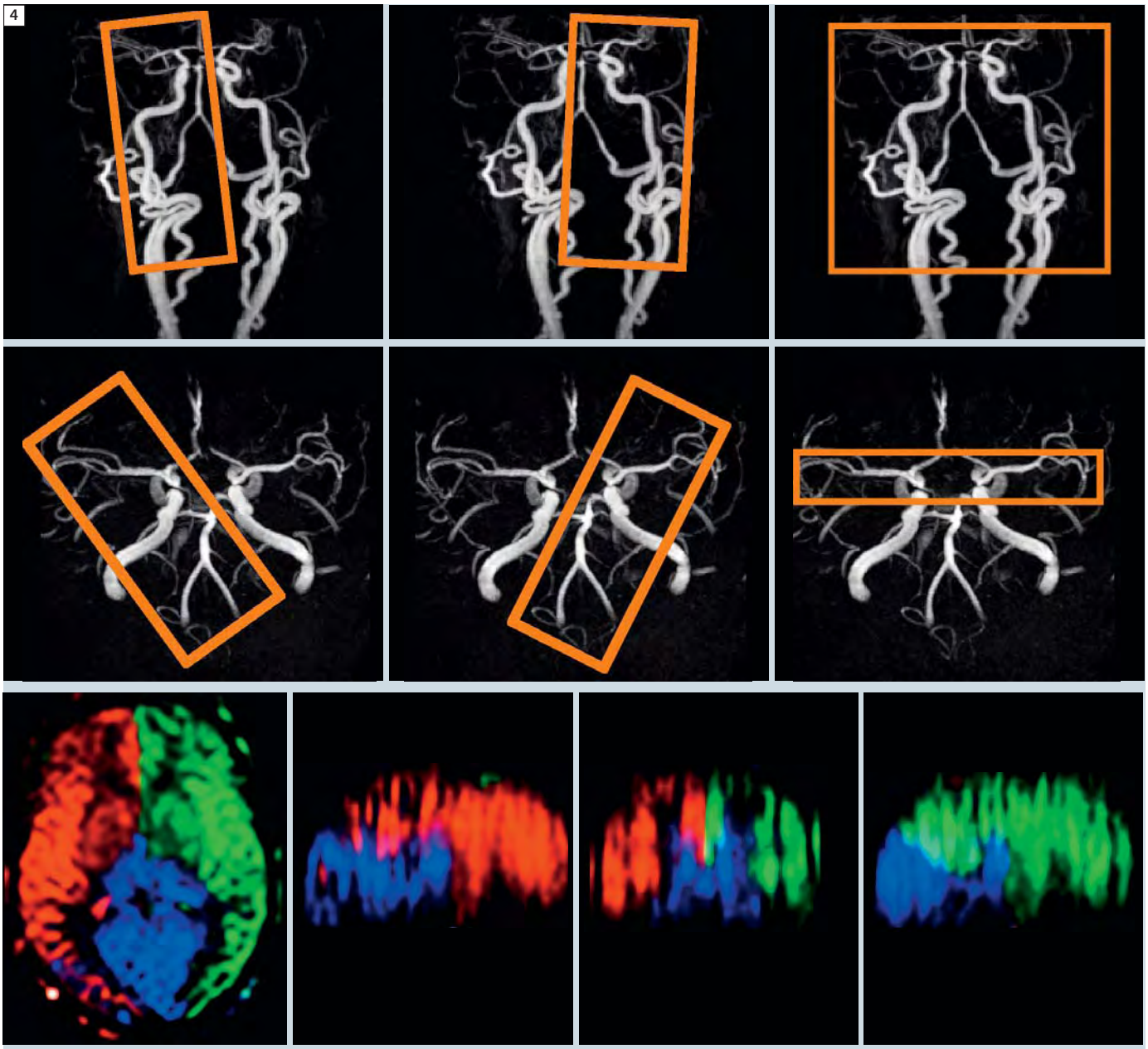

4 Color-coded visualization of vascular territories in transverse, sagittal and coronal orientation. Three excitation regions shown in MRA (yellow box) A–P (top) and C–C (middle).

ited to under ~80 ms due to rapid T2* decay and it has large phase errors leading to susceptibility artifacts with regions of signal loss (similar to spiral and rectilinear EPI). 3D GRASE sequences has many RF refocusing pulses which maintains a low level of phase error and permits a sustainable echo train for up to 300 ms. RARE / TSE has similar net sequence time, however, there is a large fraction of time spent on RF refocusing pulses, 1 per signal. GRASE uses switched gradient rephrasing of signals to produce several times as many signals as TSE, which translates into faster imaging time and higher SNR per imaging time. A similar and useful variant, Spiral RARE (or Spiral GRASE) also has efficiency advantages, however, it places the beginning of the spiral, the center of k-space, on a gradient echo position at the beginning of each time interval between RF pulses, increasing susceptibility weighting. Furthermore, non-Cartesian image reconstruction methods are required. The key to success of 3D GRASE has been its high SNR, low arti-

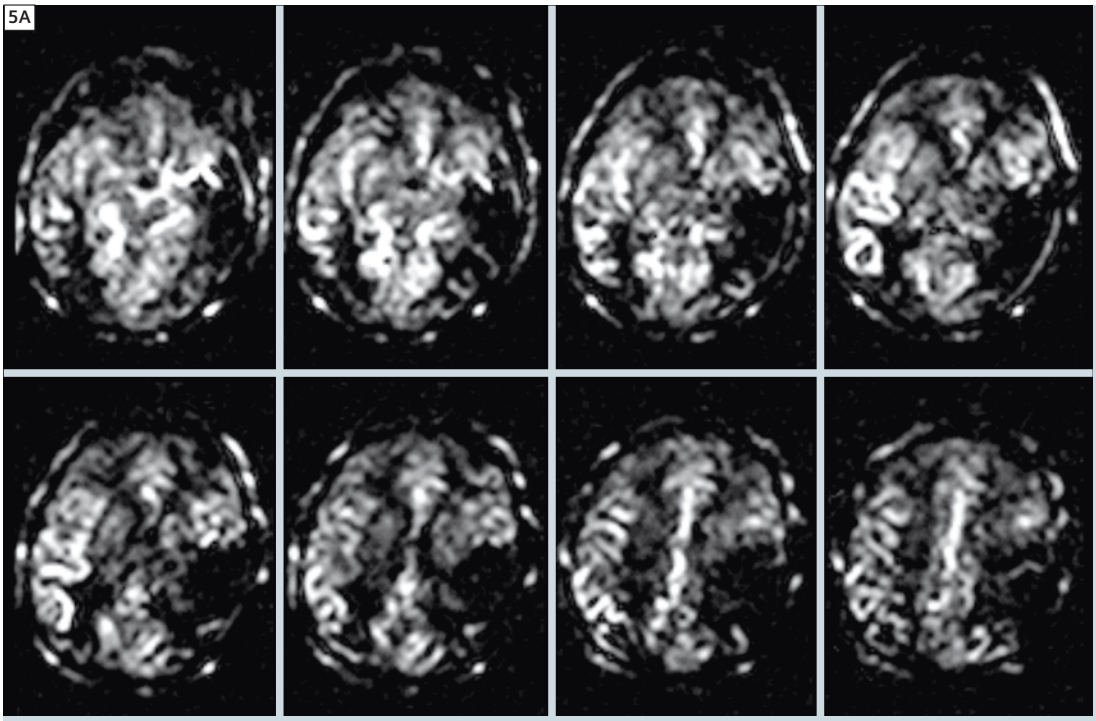

5 Single-shot 3D ASL of two patients with acute stroke. **A:** in left MCA territory,

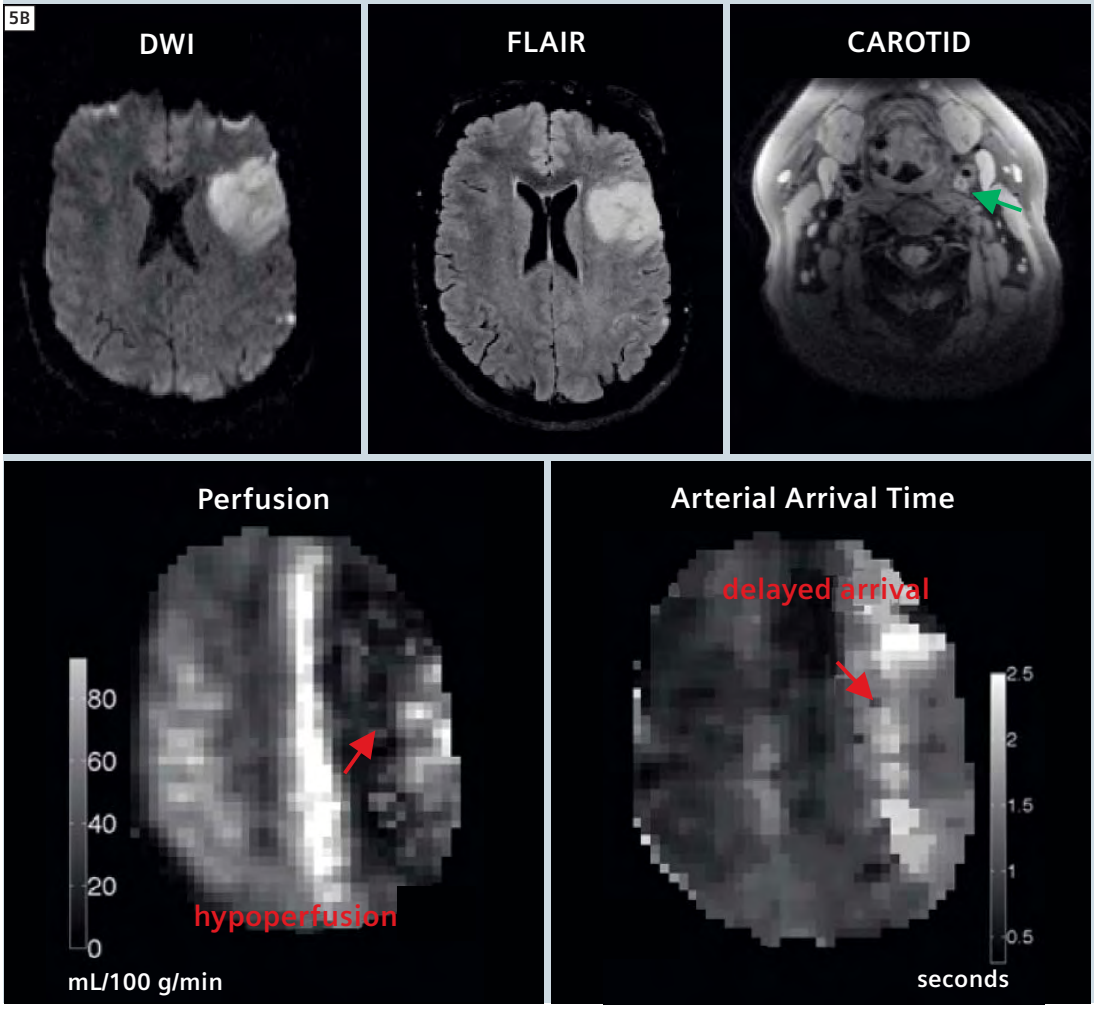

5B In second patient (48 hour) with hypoperfusion and delayed bolus arrival time (BAT) (red arrows) in ischaemic hemisphere, MRA reveals a near 100% occlusion in the left ICA (yellow arrow). *(Reproduced with permission of: BJ MacIntosh, P Jezzard et al., ISMRM 2009).*

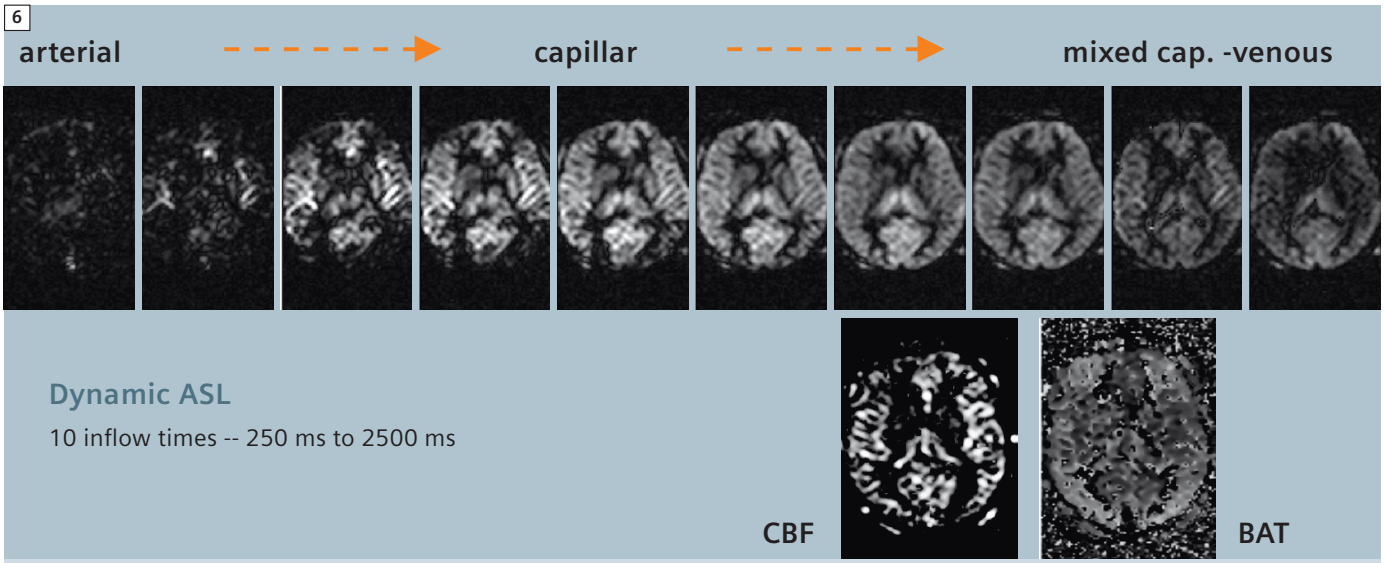

6 Dynamic ASL data acquisition with calculated CBF and BAT maps, 1 of 26 slices shown in a 3D whole brain coverage, inflow time (TI).

fact load due to the CPMG (Carr-Purrcell-Meiboom-Gill echos) timing, and whole brain coverage made possible with the simplified physiological timing in 3D acquisitions.

The source of high SNR and fast data acquisition of 3D GRASE

The number of echoes produced in a single echo train of EPI, TSE and GRASE is dependent on the rate of echo refocusing which is relatively slow in RF refocusing (~4 ms) versus fast with switched gradient refocusing (~0.2 ms). It is no less dependent upon the signal decay times of T2 and T1 stimulated echo compared to shorter T2* of EPI. In relative terms the number of refocused echoes is in EPI (2 signal / ms x 30 ms) 60 echoes, TSE (1 signal / 3 ms x 300 ms) 100 echoes, and 3D GRASE (1.5 signal / ms x 300 ms) 450 echoes. Therefore, EPI has the fastest rate of echo generation by means of gradient switching but the shortest 'echo train time', ETT, due to T2* decay. TSE has the slowest rate using RF refocusing but a long ETT, whereas 3D GRASE has the benefit of both a fast refocusing rate and a long ETT which are multiplicative for much higher net signal (Fig. 2). In addition to increasing spatial resolution and image speed, the image SNR is dependent on square root of N signals in the Fourier transform. Therefore, the relative SNR of EPI, TSE and 3D GRASE is sqrt(60), sqrt(100) and sqrt(450), 7.7, 10.0 and 21.2 respectively. The possible earlier TE of EPI to a lesser extent mitigates some of this large SNR disadvantage to 3D GRASE, which nets to nearly a factor of 2.5 higher SNR and, thus, 3D GRASE has a factor of 6–8 in scan time reduction (fewer signal averages) at constant SNR.

32-channel RF head coil effects speed and resolution

Utilizing a 32-channel coil yields another ~2 higher SNR in cortical brain regions for all imaging techniques, and these SNR gains are multiplied in 3D GRASE. This allows either extremely fast ASL acquisitions or higher resolution than previously achieved in ASL images at 3 Tesla [25] (Fig. 1).

The 32-channel coil has therefore been used to acquire larger matrix images with higher resolutions, with up to 256 matrix in reasonable scan times of 2 minutes. Instead of going to higher resolution, the reduced acquisition time can be used to sample variable inflow times to separately quantify CBF from bolus arrival time BAT using parametric curve fitting (Fig. 6). It should be noted that 3D GRASE can be combined with several different ASL encoding schemes [22, 24].

Resolving vascular territories in the brain

The images can be performed with separation of vascular territories by labeling different downstream vessels separately, (Fig. 4). Hadamard encoding has permitted to incorporate vascular territory sensitivity into an ASL protocol without loss of SNR compared to non-selective (standard) ASL to keep scan times in an acceptable range for clinical applications [21]. Stroke patients may be studied with 3D vascular territory ASL to evaluate changes occurring during recovery or to assess therapies (23). Patients with arterio-venous malformations (AVM) or aneurysms can have altered flow circuitry in the circle of Willis and downstream cerebral arteries identifiable as changes in vascular territory perfusion [20].

High spatial resolution ASL

The segmented sequence version of 3D GRASE ASL provides shorter RF pulse intervals in the CPMG spin echo sequence [27]. This reduces susceptibility artifact and concurrently shortens the time of

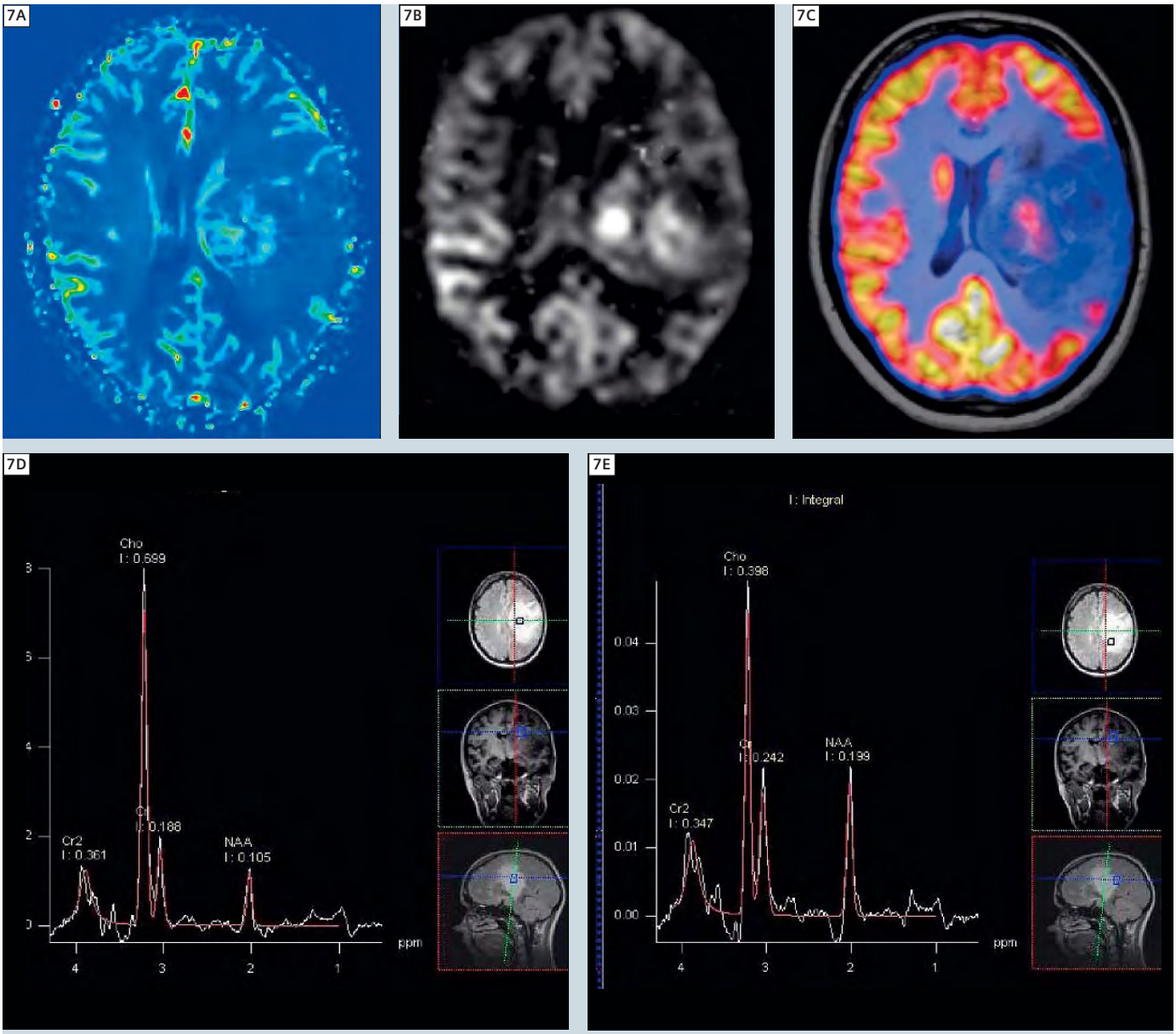

7 ASL perfusion of Glioma. **A:** Dynamic susceptibility contrast, increased perfusion in center of a recurrent Glioma, originally grade II, **B:** ASL CBF map from dynamic ASL, showing increased perfusion **C:** PET image fused to MRI. A biopsy was performed in the location of highest perfusion in ASL CBF and a grade III was diagnosed. **D, E:** At time of biopsy, MRS showed the Cho/Cr was highest in biopsy location. *(Courtesy of Rik Achten, GIfMI, UGent, Belgium.)*

each of several echo trains for reduced through-plane blurring compared to the single-shot sequences. Image distortions were also reduced using the 128 matrix instead of 64 matrix as the larger FOV allowed swapping the phase and read axes, placing the highly switched read axis onto the head's lateral axis with less physiologic stimulation to allow higher bandwidth and closer echo spacing for less distortions. One unexpected fortuitous finding is that the segmented 3D GRASE sequence does not have artifacts from CSF or brain motion and the labeling pulses normalizes blood inflow and the larger 3D volume further removes slice inflow artifacts.
The SNR gains from the 32-channel coil/receiver system enabled higher resolution ASL images. The ASL encoding used pulsed ASL (PASL) sequence with QUIPSS II (QUantitiativ Imaging of Perfusion using a Single Subtraction) variants and background suppression pulses, previously described [1].
One can incorporate the 3D ASL sequence into a clinical protocol, requiring only 8–16 second scan time for whole brain coverage at 4 mm isotropic resolution or 2–4 minutes to

obtain highly quantitative BAT and CBF maps (Fig. 6), useful for evaluation of therapeutic responses to drugs and surgical interventions (Fig. 3), following brain recovery after stroke (Fig. 5), or evaluation of tumors (Fig. 7).

In conclusion, with ASL scan times now reduced from ~15 minutes 6 years ago, to ~16 seconds for a whole brain slice coverage, perfusion images should become just another image contrast mechanism, utilized in all routine clinical screening brain studies. With such fast scans and no need for contrast agents, ASL based perfusion imaging is an important new contrast mechanism that may be used by the radiologist in all routine clinical brain screening studies. Already with these refinements, ASL is faster than CT perfusion contrast imaging, and avoids x-ray dosage and risks of iodinated contrast agent to the patient. The rapid automated image processing of ASL perfusion maps enables their practical use in emergency medical studies. The ability of MRI to rapidly show several different contrast mechanisms in images (T1-weighted, FLAIR, diffusion-weighted imaging (*syngo* DWI)) and now CBF from 3D ASL without contrast injections, further establishes MRI as an invaluable diagnostic examination of brain disease.

Acknowledgment: N.I.H. National Inst. Neurological Disease and Stroke: grant no. 5R44NS059223

References

1 Gunther, M., K. Oshio, and D.A. Feinberg, Single-shot 3D imaging techniques improve arterial spin labeling perfusion measurements. Magn Reson Med, 2005. 54(2): p. 491–8.
2 M. A. Fernandez-Seara, Z.W., J. Wang, M. Korczykowski, M. Guenther, D. Feinberg, J. A. Detre. 3T Pseudo-continuous ASL Perfusion fMRI with Background-Suppressed Single Shot 3D GRASE During Memory Encoding. in International Society for Magnetic Resonance in Medicine. 2006. Seattle.
3 Detre, J.A., et al., Perfusion imaging. Magn. Reson. Med., 1992. 23: p. 37–45.
4 Alsop, D.C. and J.A. Detre, Reduced transit-time sensitivity in noninvasive magnetic resonance imaging of human cerebral blood flow. J. Cereb. Blood Flow Metab., 1996. 16: p. 1236–1249.
5 Gonzalez-At, J.B., D.C. Alsop, and J.A. Detre, Perfusion and transit time changes during task activation determined with steady-state arterial spin labeling. Magn. Reson. Med., 2000. 43: p. 739–46.
6 Wong, E.C., R.B. Buxton, and L.R. Frank, Quantitative imaging of perfusion using a single subtraction (QUIPSS and QUIPSS II). Magn Reson Med, 1998. 39: p. 702–8.
7 Yang, Y., et al., Transit time, trailing time, and cerebral blood flow during brain activation: measurement using multislice, pulsed spin-labeling perfusion imaging. Magn Reson Med, 2000. 44(5): p. 680–5.
8 Ye, F.Q., et al., Correction for vascular artifacts in cerebral blood flow values measured using arterial spin tagging techniques. Magn. Reson. Med, 1997. 37: p. 226–35.
9 Alsop, D.C. and J.A. Detre, Multisection cerebral blood flow MR imaging with continuous arterial spin labeling. Radiology, 1998. 208: p. 410–16.
10 McLaughlin, A.C., et al., Effect of magnetization transfer on the measurement of cerebral blood flow using steady-state arterial spin tagging approaches: a theoretical investigation. Magn Reson Med, 1997. 37(4): p. 501–10.
11 Wang, J., et al., Comparison of quantitative perfusion imaging using arterial spin labeling at 1.5 and 4.0 Tesla. Magn Reson Med, 2002. 48(2): p. 242–54.
12 Wong, E.C., R.B. Buxton, and L.R. Frank, A theoretical and experimental comparison of continuous and pulsed arterial spin labeling techniques for quantitative perfusion imaging. Magn. Rason. Med., 1998. 40: p. 348–55.
13 Buxton, R.B., et al., A general kinetic model for quantitative perfusion imaging with arterial spin labeling. Magn Reson Med, 1998. 40(3): p. 383–96.
14 Williams, D.S., et al., Magnetic resonance imaging of perfusion in the isolated rat heart using spin inversion of arterial water. Magn Reson Med, 1993. 30(3): p. 361–5.
15 Wang, J., et al., Empirical analyses of null-hypothesis perfusion FMRI data at 1.5 and 4 T. Neuroimage, 2003. 19(4): p. 1449–62.
16 Feinberg, D.A. and K. Oshio, GRASE (gradient- and spin-echo) MR imaging: a new fast clinical imaging technique. Radiology, 1991. 181(2): p. 597–602.
17 Feinberg, D.A., B. Kiefer, and G. Johnson, GRASE improves spatial resolution in single shot imaging. Magn Reson Med, 1995. 33(4): p. 529–33.
18 Feinberg DA, Kiefer B, Litt AW. High resolution GRASE MRI of the brain and spine: 512 and 1024 matrix imaging. J Comput Assist Tomogr. 1995 Jan-Feb;19(1):1–7.
19 Luh, W.M., et al., QUIPSS II with thin-slice TI1 periodic saturation: a method for improving accuracy of quantitative perfusion imaging using pulsed arterial spin labeling. Magn Reson Med, 1999. 41(6): p. 1246–54.
20 Sallustio F, Kern R, Günther M, Szabo K, Griebe M, Meairs S, Hennerici M, Gass A. Assessment of intracranial collateral flow by using dynamic arterial spin labeling MRA and transcranial color-coded duplex ultrasound.Stroke. 2008 Jun;39(6):1894–7. Epub 2008 Apr 10.
21 Günther M. Efficient visualization of vascular territories in the human brain by cycled arterial spin labeling MRI. Magn Reson Med. 2006 Sep;56(3):671–5.
22 Fernández-Seara MA, Edlow BL, Hoang A, Wang J, Feinberg DA, Detre JA. Minimizing acquisition time of arterial spin labeling at 3T. Magn Reson Med. 2008 Jun;59(6):1467–71.
23 MacIntosh BJ, Pattinson KT, Gallichan D, Ahmad I, Miller KL, Feinberg DA, Wise RG, Jezzard P. Measuring the effects of remifentanil on cerebral blood flow and arterial arrival time using 3D GRASE MRI with pulsed arterial spin labelling.J Cereb Blood Flow Metab. 2008 Aug;28(8):1514–22. Epub 2008 May 28.
24 Fernández-Seara MA, Wang Z, Wang J, Rao HY, Guenther M, Feinberg DA, Detre JA. Continuous arterial spin labeling perfusion measurements using single shot 3D GRASE at 3 T.Magn Reson Med. 2005 Nov;54(5):1241–7.
25 McKinstry RC, Feinberg DA. Ultrafast magnetic resonance imaging. A new window on brain research. Science. 1998 Mar 20;279(5358):1965-6. No abstract available.
26 Feinberg DA, Ramanna S, Gunther M, Evaluation of new ASL 3D GRASE sequences using Parallel Imaging, Segmented and Interleaved k-space at 3T with 12- and 32-Channel coils. ISMRM, Honolulu, 2009
27 Talagala SL, Ye FQ, Ledden PJ, Chesnick S. Whole-Brain 3D Perfusion MRI at 3.0 T using CASL with a separate labeling Coil, Mag Res Med, 52: 131–140 (2004)
28 Edelman, R. R., B. Siewert, et al. (1994). "Signal targeting with alternating radiofrequency (STAR) sequences: application to MR angiography." Magn Reson Med 31(2): 233–8
29 Kwong, K. K., D. A. Chesler, et al. (1995). "MR perfusion studies with T1-weighted echo planar imaging." Magn Reson Med 34(6): 878–87.
30 Luh, W. M., E. C. Wong, et al. (1999). "QUIPSS II with thin-slice TI1 periodic saturation: a method for improving accuracy of quantitative perfusion imaging using pulsed arterial spin labeling." Magn Reson Med 41(6): 1246–54.
31 Wong, E. C., R. B. Buxton, et al. (1998). "Quantitative imaging of perfusion using a single subtraction (QUIPSS and QUIPSS II)." Magn Reson Med 39(5): 702–8.
32 Ye, F. Q., J. A. Frank, et al. (2000). "Noise reduction in 3D perfusion imaging by attenuating the static signal in arterial spin tagging (ASSIST)." Magn Reson Med 44(1): 92–100.

Contact
David Feinberg, M.D., Ph.D.
Advanced MRI Technologies
652 Petaluma Ave.,
J Sebastopol, CA, 95472
USA
david.feinberg@advancedmri.com

Tim 4G

32-Channel Head Coil

- **Superb functional and structural brain imaging**
- **Unsurpassed SNR and iPAT performance**
- **Two connectors only thanks to Dual-Density Signal Transfer technology***

*MAGNETOM Skyra only

Available for 3T MAGNETOM Skyra, 3T MAGNETOM Trio, 3T MAGNETOM Verio, 1.5T MAGNETOM Avanto and 1.5T MAGNETOM Espree.

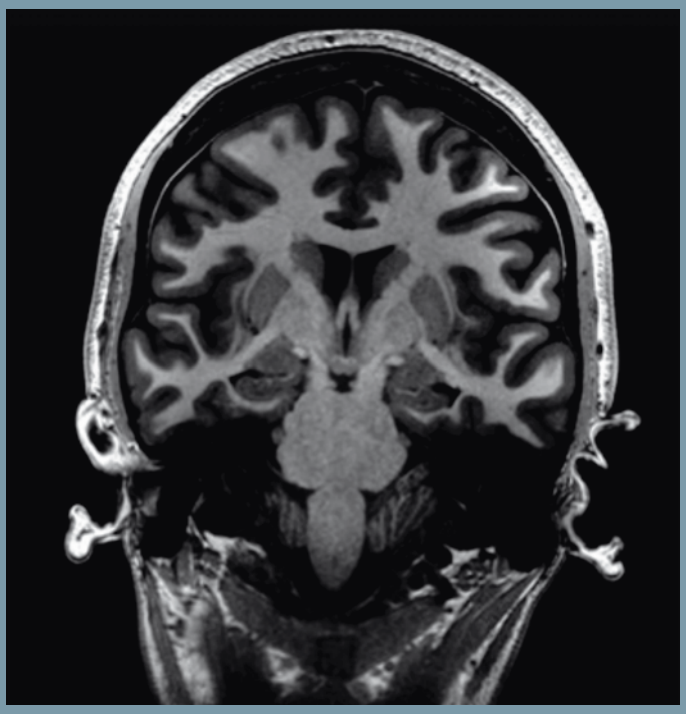

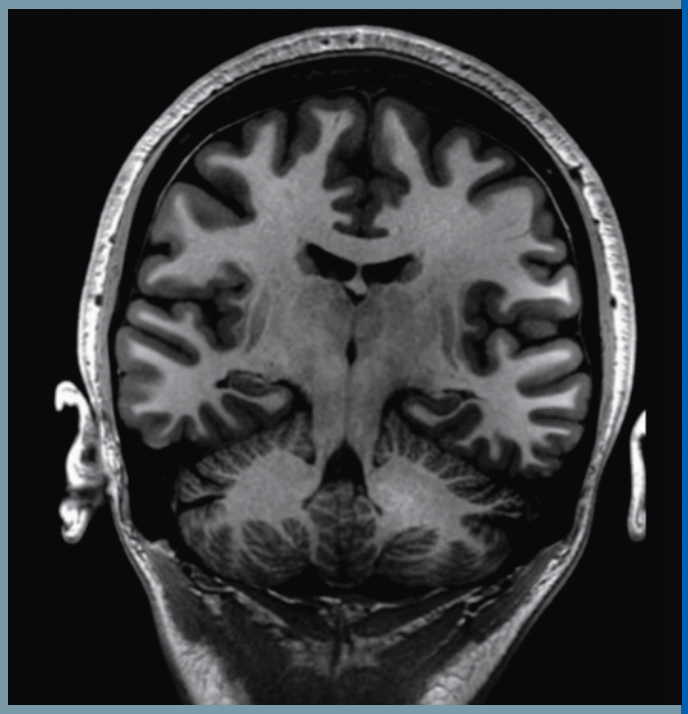

Images courtesy of MGH, Boston, USA

Diffusion-Weighted MR Imaging in Brain Tumor

L. Celso Hygino da Cruz Jr.; Emerson L. Gasparetto; Roberto C. Domingues; Romeu C. Domingues

CDPI e Multi-Imagem Ressonância Magnética, Rio de Janeiro – RJ, Brazil

Introduction

Primary neoplasms of the central nervous system (CNS) have a prevalence of between 15,000 and 17,000 new cases annually in the United States and are estimated to cause the deaths of 13,000 patients. Gliomas are the leading cause of primary CNS tumors, accounting for 40–50% of cases and 2–3% of all cancers[4]. Despite new treatment techniques, patients' survival still remains very low, varying between 16 and 53 weeks.
It is generally accepted that conventional magnetic resonance imaging (MRI) tends to underestimate the extent of the tumor, which can in turn lead to a suboptimal treatment. New functional magnetic resonance imaging sequences, such as diffusion tensor imaging (DTI) and diffusion-weighted imaging (DWI), have been widely used to evaluate such tumors.

Diffusion-weighted MR image

Diffusion-weighted imaging is based on the random or Brownian motion of water molecules in relation to their thermal energy.
DWI has been used to assess brain tumors and while it has had limited success as a definitive prognostic tool, its proponents suggest that in certain settings it can increase both the sensitivity and specificity of MR imaging.
One example of a specific arena in which DWI may be helpful is in distinguishing between brain abscesses and necrotic and cystic neoplasms on MRI. This differentiation is still a challenge on both clinical and radiological setting. The abscesses have a high signal on DWI and a reduced Apparent Diffusion Coefficient (ADC) within the cavity. This restricted diffusion is thought to be related to the characteristic of the pus in the cavity; this may in turn lead to reduced water mobility, lower ADC, and bright signal on DWI. By contrast, necrotic and cystic tumors display a low signal on DWI (similar to the CSF in the ventricles) with an increased ADC as well as isointense or hypointense DWI signal intensity in the lesion margins.

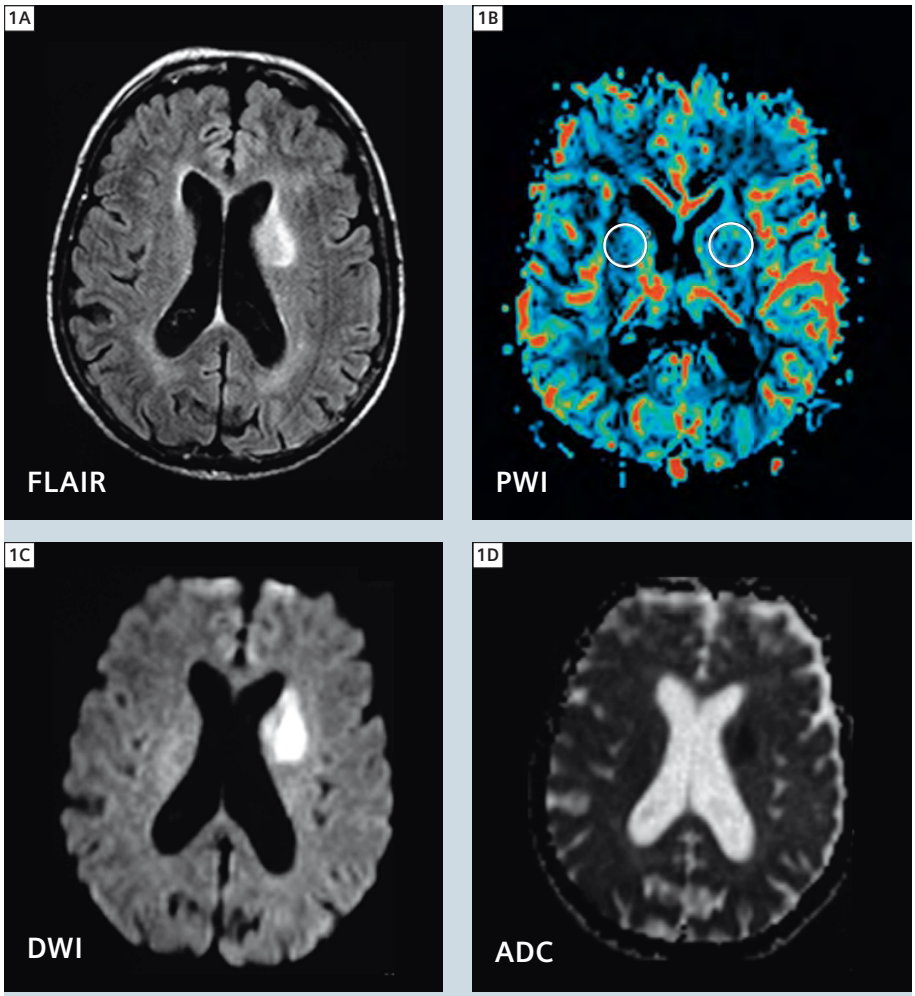

1 72-year-old female presented with mental and language disturbance, since 20 days. Enhancing lesion, low perfusion, restricted diffusion on DWI and ADC.
Diagnosis: Lymphoma

DWI is also an effective way of differentiating an arachnoid cyst from epidermoid tumors. Both lesions present similar signal intensity characteristic of cerebrospinal fluid (CSF) on T1 and T2 sequences. On DWI, epidermoid tumors are hyperintense – for they are solidly composed – whereas arachnoid cysts are hypointense, demonstrating high diffusivity. The ADC values of epidermoid tumors are similar to those of the brain parenchyma, whilst ADC values of arachnoid cysts are similar to those of CSF.
In certain settings diffusion-weighted imaging can increase both the sensitivity and specificity of MR imaging in the evaluation of brain tumors by providing information about tumor cellularity, which may in turn improve prediction of tumor grade. The mechanism in which DWI may help in the tumor grading is based on the fact that free water molecule diffusivity is restricted by cellularity increase in high-grade lesions. The reduction in extracellular space caused by tumor cellularity causes a relative reduction in the apparent diffusion coefficient (ADC) values. Perhaps most helpfully, high grade tumors have in some studies been found to have low ADC values, suggesting a correlation between ADC values and tumor cellularity. In some studies, however, ADC values found in high- and low-grade gliomas have overlapped somewhat. It is well known that the brain tumors, specially the gliomas, are heterogeneous. Usually within a same neoplasm grade, mostly high-grade, different histologic features of grades II–IV are presented. This limitation may also be explained by the fact that it is not only the tumor cellularity that is responsible for reducing the diffusibility.
Lymphoma, a highly cellular tumor, has hyperintensity on DWI and reduced ADC values. While meningiomas also have a restricted diffusion, displaying low ADC values, they rarely present difficulty in diagnosis. DWI can be somewhat helpful in distinguishing medulloblastoma from other pediatric brain tumors, as it seems to display restricted diffusion presumably because of the densely packed tumor cells and high nuclear-to-cytoplasm ratio. The solid enhancing portion of cerebellar haemangioblastomas demon-

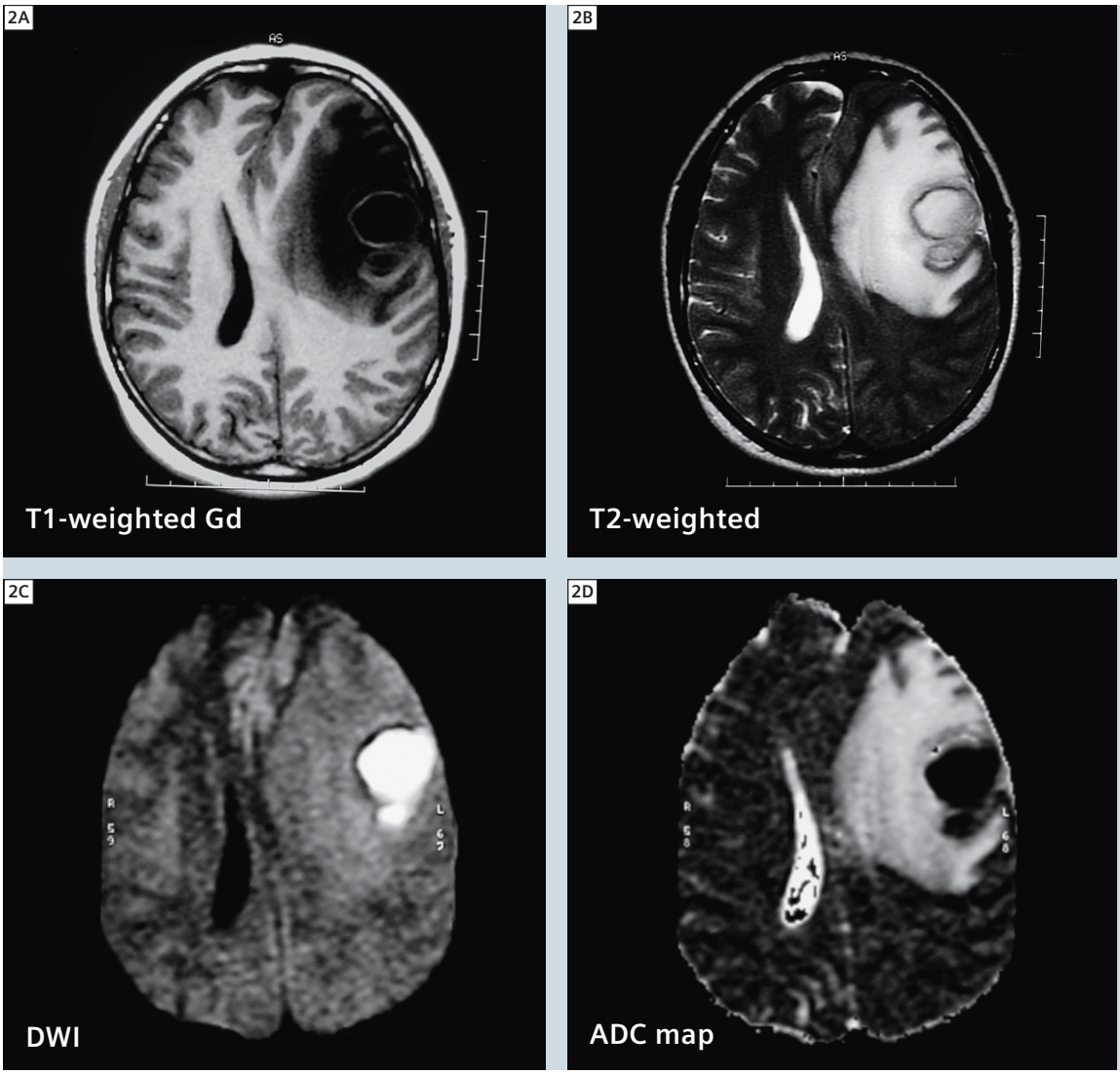

2 A bilobulated ring enhancing necrotic lesion, surrounded by vasogenic edema, demonstrating restricted diffusion within the lesion.
Diagnosis: Abscess

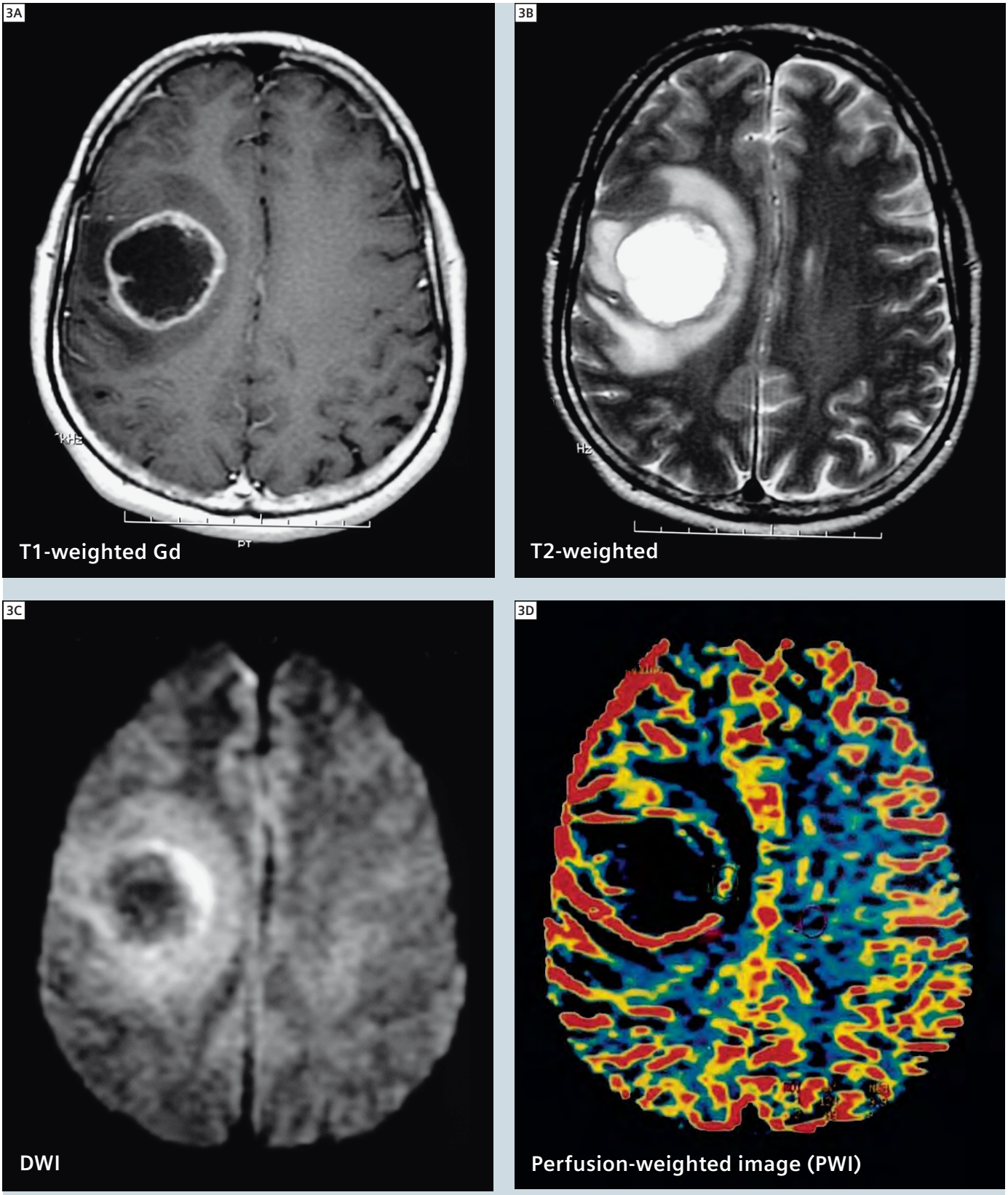

3 An expansive ring enhancing cystic/necrotic lesion, surrounded by vasogenic edema/infiltrative lesion, demonstrating restricted diffusion and high perfusion in its borders and unrestricted diffusion within the lesion.
Diagnosis: Glioblastoma Multiforme (GBM)

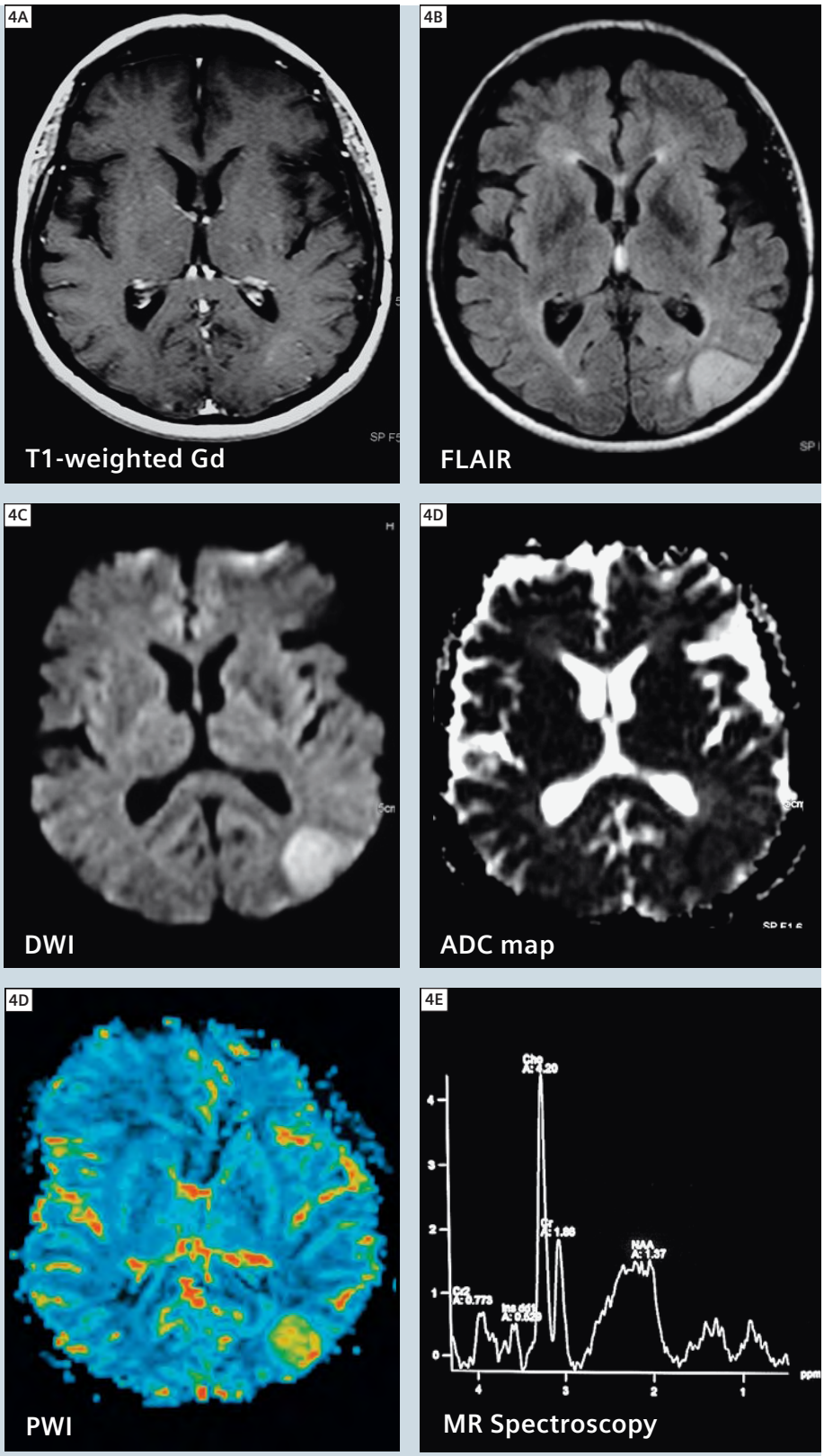

4 A non-enhancing cortical lesion, with high perfusion and restricted diffusion. MR-spectroscopy demonstrates a very high choline peak and low NAA.
Diagnosis: Anaplastic astrocytoma

strates high diffusibility, due to its rich vascular spaces.

Diffusion-Tensor MR image

The movement of water occurs in all three directions, and is assumed to behave in a manner physicists can describe using a Gaussian approximation. When water molecules diffuse equally in all directions, this is termed isotropic diffusion. In the white matter, however, free water molecules diffuse anisotropically, that is to say the water diffusion is not equal in all three orthogonal directions. The fractional anisotropy (FA) measures the fraction of the total magnitude of diffusion anisotropy. In addition to assessment of the diffusion in a single voxel, DTI has been used to attempt to map the white matter fiber tracts. A color-coded map of fiber orientation can also be determined by DTI. A different color has been attributed to represent a different fiber orientation along the three orthogonal spatial axes.

The precise determination of the margins of the tumor is of the utmost importance to the management of brain tumors. The goal of a surgical approach to the brain neoplasm is the complete resection of the tumor, coupled with minimum neurological deficit.

Since it is generally accepted that conventional MR imaging underestimates the real extent of the brain tumor, given its ability to verify neoplastic cells that infiltrate peritumoral areas of abnormal T2-weighted signal intensity, many practitioners are uncomfortable using only conventional MRI approaches. While this remains to be proven, it does appear from straightforward inspection that DTI is able to illustrate the relationship of a tumor with the nearby main fiber tracts. Because of this, many have begun to suggest that DTI might be used to aid in surgical planning and possibly aid radiotherapy planning, as well as to monitor the tumor recurrence and the response to the treatment.

Based on these findings, DTI seems to be of great value in the detection of FA values, variation in pure vasogenic edema and the combination of vasogenic edema

Continued on page 114

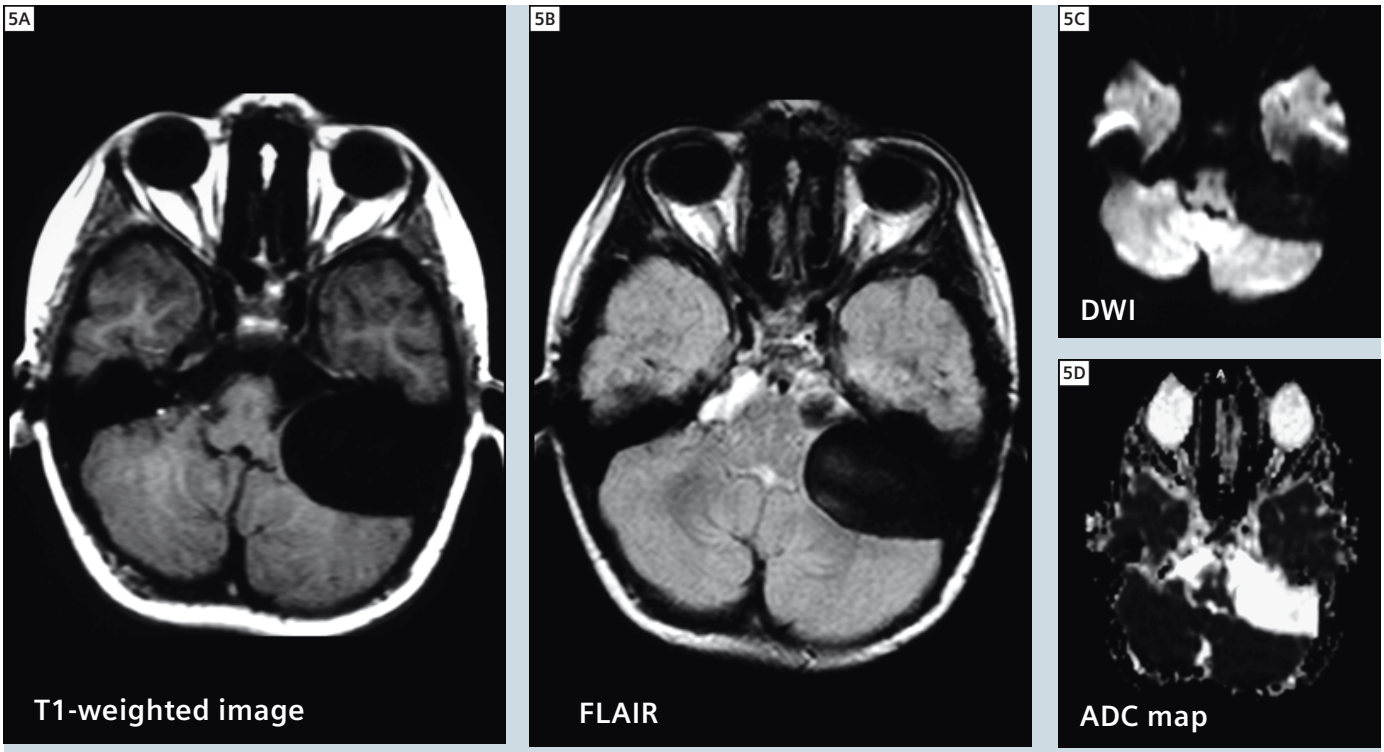

5 An expansive lesion in the left aspect of the posterior fossa, demonstrating similar signal intensity to CSF and high diffusibility.
Diagnosis: Arachnoid cyst

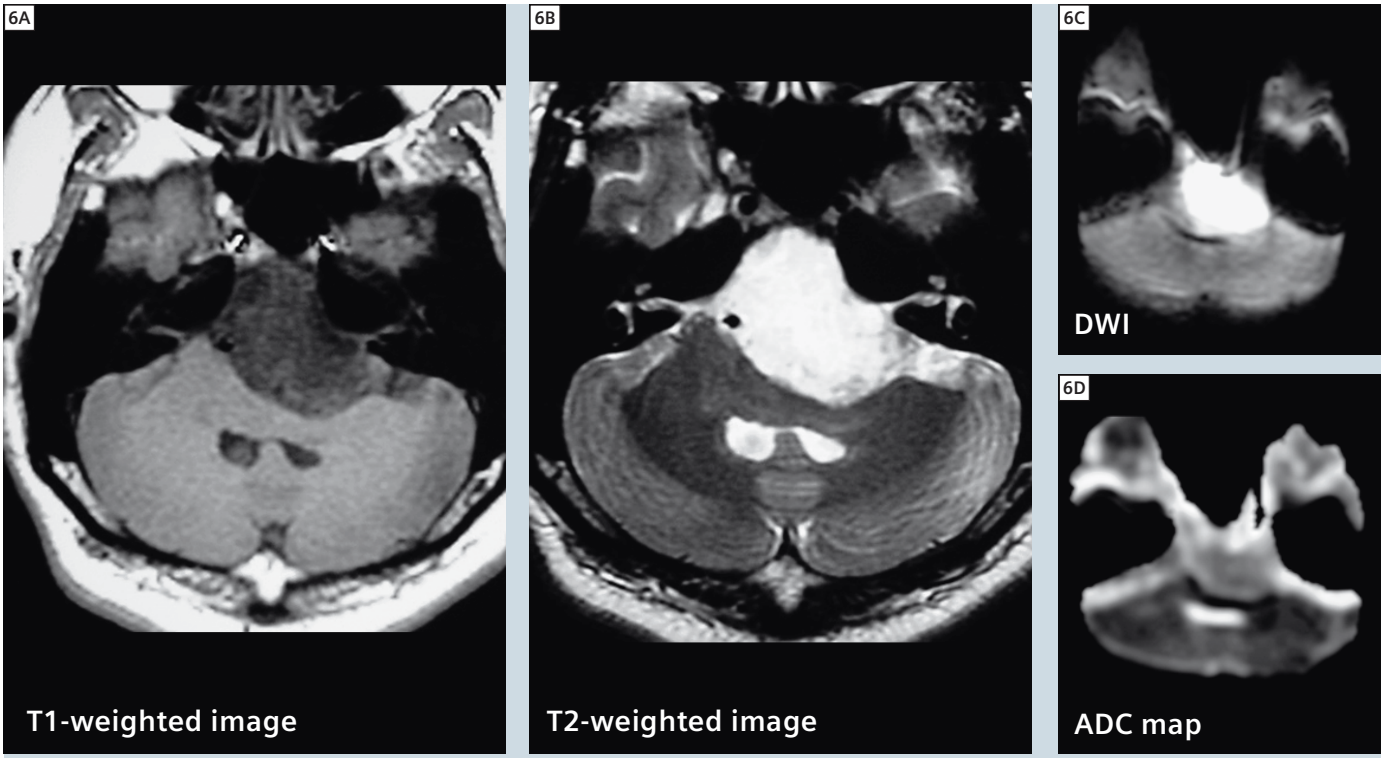

6 An expansive lesion in the left aspect of the posterior fossa, demonstrating similar signal intensity to CSF and high signal intensity on diffusion-weighted imaging (DWI). **Diagnosis:** Epidermoid

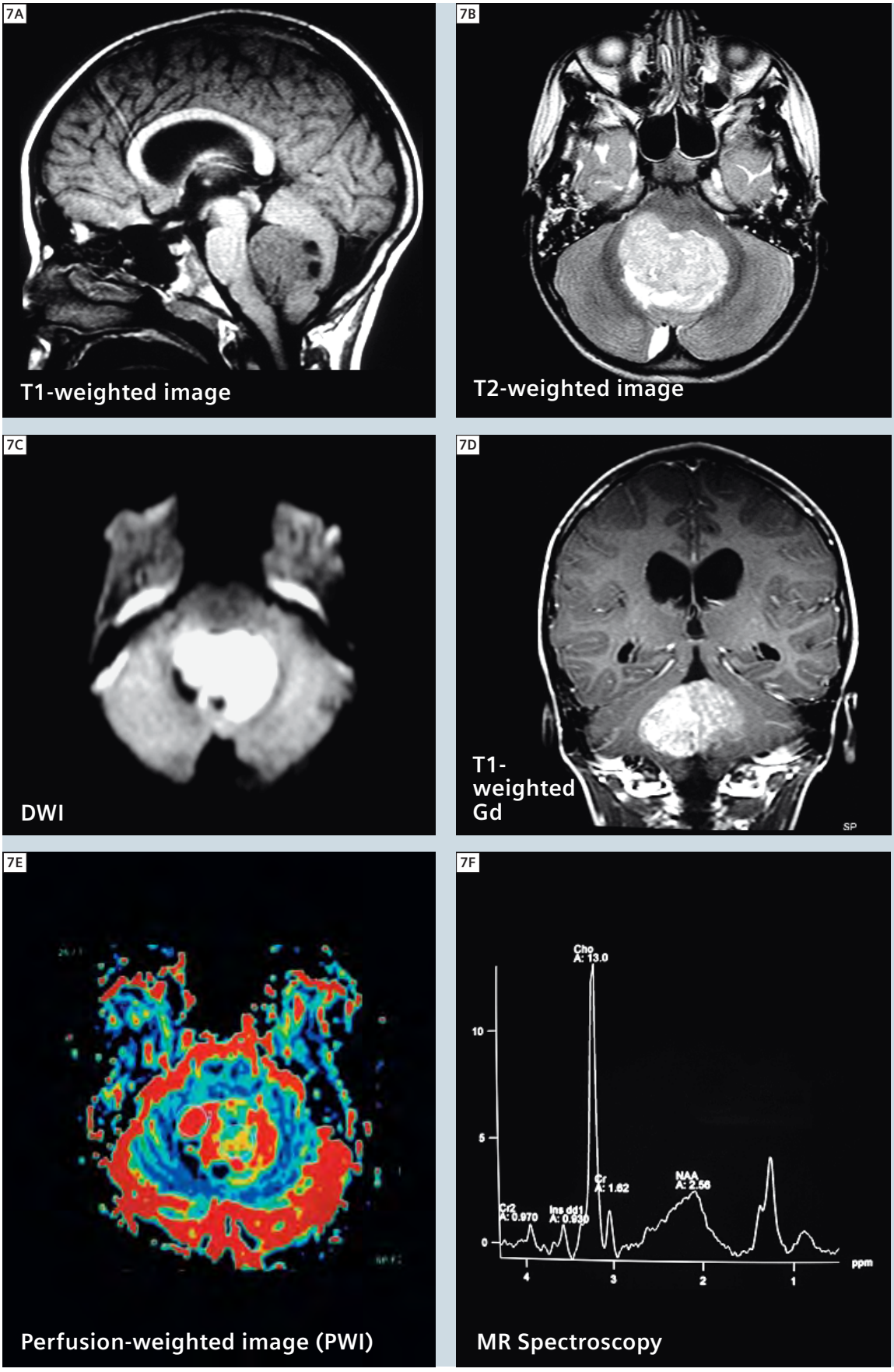

7 An expansive intraventricular enhancing lesion in the fourth ventricle, demonstrating restricted diffusion, hyperperfusion and a very high Choline peak, low NAA and lipids/lactate peak. **Diagnosis:** Medulloblastoma

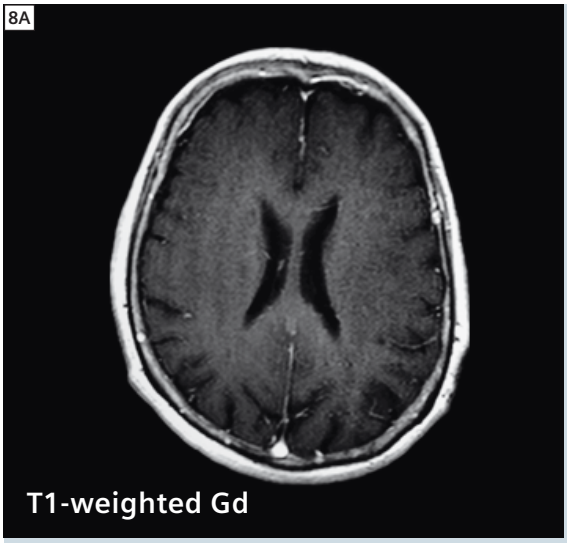

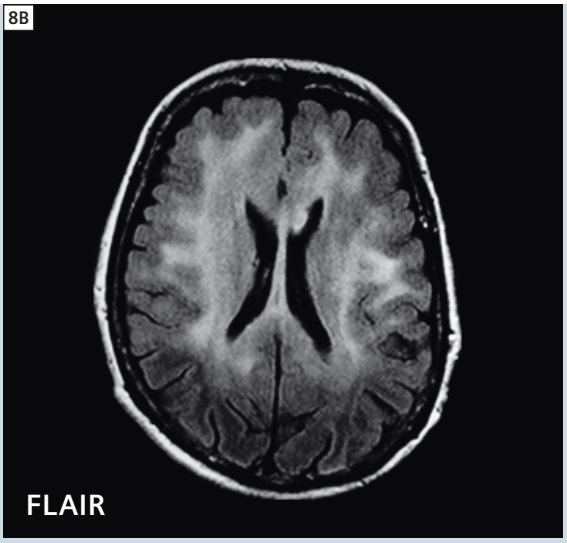

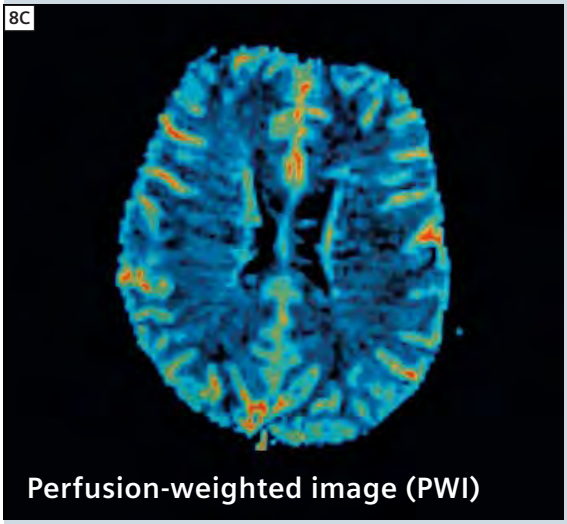

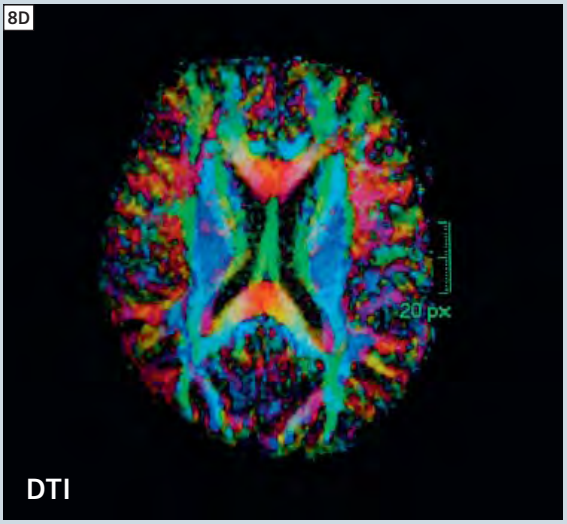

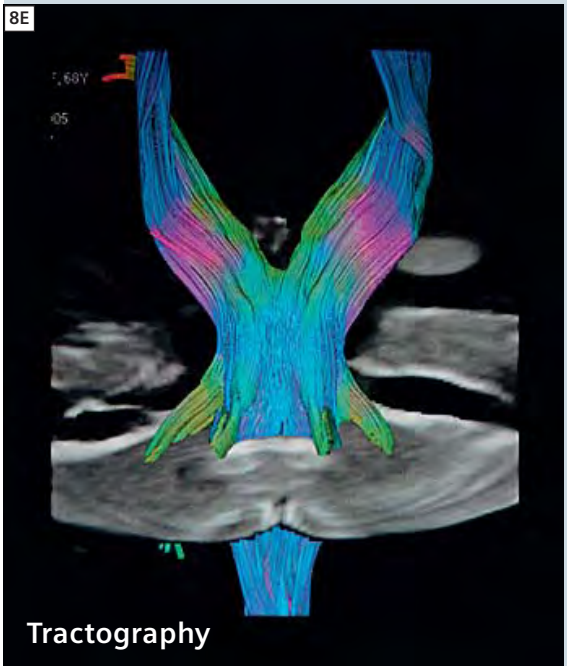

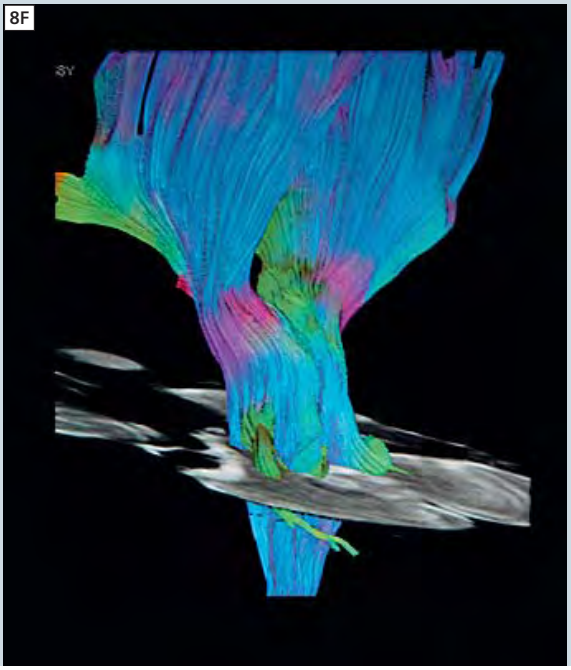

8 An infiltrative, non-enhancing white matter lesion, without hyperperfusion. Diffusion Tensor Imaging (DTI) demonstrates a reduction in FA values, preserving the direction of the main fiber tracts. **Diagnosis:** Gliomatosis cerebri

and extracellular matrix destruction. In conclusion, DTI may be able to distinguish high-grade gliomas from low-grade gliomas and metastatic lesions.

Pre-surgical planning

DTI appears to be the only non-invasive method of obtaining information about the fiber tracts and is able to suggest them three-dimensionally, though the validity of these suggestions remains to be carefully studied. Frequently, the involvement of the white matter tracts can be clearly identified in brain tumor patients by using both anisotropic maps (FA maps are the most widely used) and tractography. Based on DTI findings, resulting from studies of brain tumor patients, the white matter involvement by a tumor can be arranged into five different categories:

- Displaced: maintained normal anisotropy relative to the contralateral tract in the corresponding location, but situated in an abnormal T2-weighted signal intensity area or presented an abnormal orientation.
- Invaded: slightly reduced anisotropy without displacement of white matter architecture, remaining identifiable on orientation maps.
- Infiltrated: reduced anisotropy but remaining identifiable on orientation maps.
- Disrupted: marked reduced anisotropy and unidentifiable on oriented maps.
- Edematous: maintained normal anisotropy and normally oriented but located in an abnormal T2-weighted signal intensity area.

In short, DTI is gaining enthusiasm as a pre-operative MRI method of evaluating brain tumors closely related to eloquent regions. DTI appears to be particularly advantageous for certain types of surgical planning, optimizing the surgical evaluation of brain tumors near white matter tracts. Formal studies that demonstrate that DTI can successfully prevent post-operative complications have yet to be carried out but preliminary data appear promising.

Intracranial neoplasms may involve both the functional cortex and the corresponding white matter tracts. The preoperative identification of eloquent areas through noninvasive methods, such as blood-oxygen-level-dependent (BOLD) functional MR imaging (fMRI) and DTI tractography, offers some advantages. Increasingly, investigators are beginning to combine fMRI with DTI: this might allow us to precisely map an entire functional circuit. Even though fMRI locates eloquent cortical areas, the determination of the course and integrity of the fiber tracts remains essential to the surgical planning.

Limitations

While initial reports suggest advantages of DWI and DTI in the evaluation of patients with brain tumors, these reports are largely single-center, uncontrolled, preliminary findings. Therefore these results must be cautiously interpreted. Furthermore, there remain substantial technical hurdles, even though the rapid evolution of MRI systems is making ever more powerful approaches possible. Such improvements are particularly welcome given the limited signal-to-noise ratio of diffusion overall. Nevertheless, these initial data are promising.

Summary

Diffusion imaging appears to have the potential to add important information to pre-surgical planning. While experience is limited, DTI appears to provide useful local information about the structures near the tumor, and this appears to be useful in planning. In the future, DTI may provide an improved way to monitor intraoperative surgical procedures as well as their complications. Furthermore, the evaluation of the response of treatment to chemotherapy and to radiation therapy might also be possible. While diffusion imaging has some limitations, its active investigation and further study are clearly warranted.

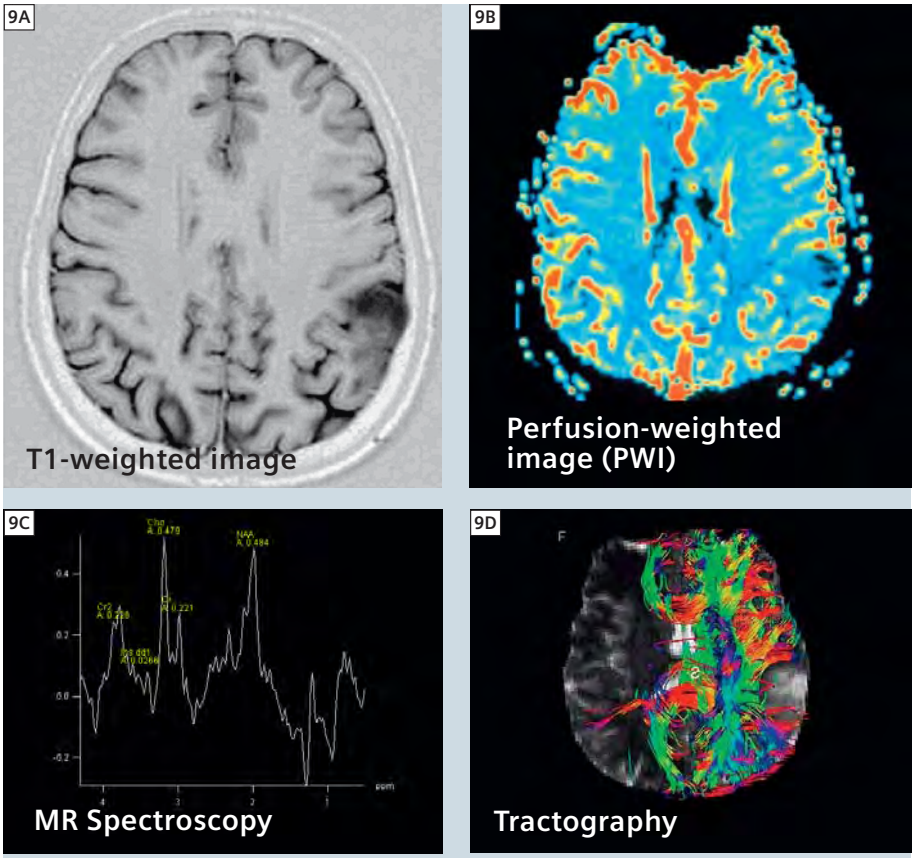

9 An expansive cortical lesion, with hypoperfusion. MR-spectroscopy demonstrates a high Choline peak and low NAA. The lesion seems to dislocate the main adjacent fiber tracts.
Diagnosis: Low grade Glioma

References

1 Berens ME, Rutka JT, Rosenblum ML. Brain tumor epidemiology, growth, and invasion. Neurosurg Clin North Am 1990; 1:1–18.

2 Jemal A, Thomas A, Murray T, et al. Cancer statistics2002.CA2002;52(1):23–47.

3 Felix R, Schorner W, Laniado M, et al. Brain tumors: MR imaging with gadolin-DPTA. Radiology 1985; 156:681–688.

4 Knopp EA, Cha S, Johnson G, et al. Glial Neoplams: Dynamic Contrast-enhanced T2*-weighted MR imaging. Radiology 1999; 211:791–798.

5 Brunberg JA, Chenevert TL, McKeever PE, Ross DA, Junck LR, Muraszko KM, et al. In vivo MR determination of water diffusion coefficients and diffusion anisotropy: Correlation with structural alteration in gliomas of the cerebral hemispheres. AJNR Am J Neuroradiol 1995;16:361–371.

6 Mori S, Frederiksen K, Van Zijl PCM, Stieltjes B, Kraut MA,Slaiyappan M, et al. Brain White Matter Anatomy of Tumor Patients Evaluated With Diffusion Tensor Imaging. Ann Neurol 2002; 51:377–380.

7 Price SJ, Burnet NG, Donovan T, Green HAL, Pena A, Antoun NM , et al . Diffusion Tensor Imaging of Brain Tumors at 3T: A potential tool for assessing white matter tract invasion. Clinical Radiology 2003; 58:455–462.

8 Schulder M, Maldjian JA, Liu WC, Holodny AI, Kalnin AT, Mun IK, et al. Functional image-guided surgery of intracranial tumors located in or near the sensorimotor cortex. J Neurosurg 1998; 89:412–418.

9 Holodny AI, Ollenschlager M. Diffusion imaging in brain tumor. Neuroimaging Clin N Am 2002; 12:107–124.

10 Barboriak DP. Imaging of brain tumors with diffusion-weighted and diffusion tensor MR imaging. Magn Reson Imaging Clin N Am 2003;11:379–401.

11 Tsuruda JS, Chew WM, Moseley ME, Norman D. Diffusion-weighted MR imaging of the brain : value of differentiating between extra-axial cysts and epidermoid tumors. Am J Neuroradiol 1990; 155:1049–1065.

12 Chen S, Ikawa F, Kurisu K, Arita K, Takaba J, Kanou Y. Quantitative MR evaluation of intracranial epidermoid tumors by fast fluid-attenuated inversion recovery imaging and echo-planar diffusion-weighted imaging. Am J Neuroradiol 2001; 22(6):1089–1096.

13 Laing AD, Mitchell PJ, Wallace D. Diffusion-weighted magnetic resonance imaging of intracranial epidermoid tumors . Aust Radiol 1999; 43:16–19.

14 Guo AC, Provenzale JM, Cruz Jr LCH, Petrella JR. Cerebral abscesses: investigation using apparent diffusion coefficient maps. Neuroradiology 2001;43:370–374, 2001.

15 Chang SC, Lai PH, Chen WL,Weng HH, Ho JT, Wang JS. Diffusion-weighted MRI features of brain abscess and cystic or necrotic brain tumors: comparison with conventional MRI. Clin Imaging 2002; 26(4):227–236.

16 Tien RD, Feldesberg GJ, Friedman H, Brown M, MacFall J. MR imaging of high-grade cerebral gliomas: Value of diffusion-weighted echo-planar pulse sequence. AJR Am J Roentgenol 1994;162:671–677.

17 Krabbe K, Gideon P, Wang P, Hansen U, Thomsen C, Madsen F. MR diffusion imaging of human intracranial tumours. Neuroradiology 1997; 39:483–489.

18 Le Bihan D, Douek P, Argyropoulou M, Turner R, Patronas N, Fulham M . Diffusion and perfusion magnetic resonance imaging in brain tumors. Top Mang Reson Imaging 1993; 5:25–31.

19 Tsuruda JS, Chew WM, Moseley ME, Norman D. Diffusion-Weighted MR imaging of extraaxial tumors. Magn Reson Med 1991; 19:316–320.

20 Cruz, Jr LCH; Sorensen AG. Diffusion tensor magnetic resonance imaging of brain tumors. Neurosurg Clin N Am 16(2005)115–134.

21 Cruz, Jr LCH; Sorensen AG. Diffusion tensor magnetic resonance imaging of brain tumors. Magn Reson Clin N Am 2006 May 14(2);183–202.

22 Stadnik TW, Chaskis C, Michotte A, Shabana WM, van Rompaey K, Luypaert R, et al. Diffusion-weighted MR imaging of intrcerebral masses: Comparison with conventional MR imaging and histologic findings. AJNR Am J Neuroradiol 2001; 22:969–976.

23 Guo AC, Cummings TJ, Dash RC, Provenzale JM. Lymphomas and high-grade astrocytomas: comparison of water diffusibility and histologic characteristics. Radiology 2002; 224(1):177–183.

24 Kono K, Inoue Y, Nakayama K, Shakudo M, Morino M, Ohata K, et al. The Role of Diffusion-Weighted Imaging in Patients with Brain Tumors. AJNR Am J Neuroradiol 2001; 22:1081–1088.

25 Koetsenas AL, Roth TC, Manness WK, Faeber EN. Abnormal diffusion-weighted MRI in medulloblastoma: Does it reflect small cell histology? Pediatric Radiol 1999;29:524–526.

26. Quadrery FA, Okamoto K. Diffusion-weighted MRI of haemangioblastomas and other cerebellar tumours. Neuroradiology 2003;45(4): 212–219.

27 Goebell E, Paustenbach S, Vaeterlein O, Ding X, Heese O, Fiehler J, Kucinski T, Hagel C, Westphal M, Zeumer H. Radiology 2006;239:217–222. Low-Grade and Anaplastic Gliomas: Differences in Architecture Evaluated with Diffusion-Tensor MR Imaging.

28 Inoue T, Ogasawara K, Beppu T, Ogawa A, Kabasawa H. Diffusion tensor imaging for preoperative evaluation of tumor grade in gliomas. Clin Neurol Neurosurg 2005;107:174–180.

29 Jellinson BJ, Field AS, Medow J, et al. Diffusion Tensor Imaging of Cerebral White Matter: A Pictorial Review of Physics, Fiber Tract Anatomy, and Tumor Imaging Patterns. AJNR Am J Neuroradiol 2004; 23:356–369.

30 Sha S, Bastin ME, Whittle IR, Wardlaw JM. Diffusion Tensor MR Imaging of High-grade cerebral gliomas. AJNR Am J Neuroradiol 2002; 23:520–527.

31 Witwer BP, Moftakhar R, Hasan KM, Deshmukh P, Haughton V, Field A, et al. Diffusion-tensor imaging of white matter tracts in patients with cerebral neoplasm. J Neurosurg 2002; 97:568–575.

32 Weishmann UC, Symms MR, Parker GJM, Clark CA, Lemieux L, Barker GJ, et al. Diffusion tensor imaging demonstrates deviation of fibers in normal appearing white matter adjacent to a brain tumour. J Neurol Neurosurg Psychiatry 2000; 68:501–503.

33 Holodny AI, Schwartz TH, Ollenschleger M, Liu WC, Schulder M. Tumor involvement of the corticospinal tract: diffusion magnetic resonance tractography with intraoperative correlation. J Neurosurg 2001; 95(6): 1082.

34 Holodny AI, Ollenschleger M, Liu WC, Schulder M, Kalnin AJ. Identification of the corticospinal tracts achieved using blood-oxygen-level-dependent and diffusion functional MR imaging in patients with brain tumors.

35 Krings T, Reiges MH, Thiex R, Gilsbach JM, Thron A. Functional and diffusion-weighted magnetic resonance images of space-occupying lesions affecting the motor system: imaging the motor cortex and pyramidal tracts. J Neurosurg 2001; 95(5):816–824.

36 Guye M, Parker GJM, Symms M, Boulby P, Wheeler-Kingshott CAM, Salek-Haddadi A, et al. Combined functional MRI and tractography to demonstrate the connectivity of the human primary motor cortex in vivo. Neuroimage 2003; 19:1349–1360.

Contact
L. Celso Hygino da Cruz Jr.
CDPI e Multi-Imagem
Ressonância Magnética
Rio de Janeiro, Brazil
celsohygino@hotmail.com

Clinical Applications of Diffusion Tensor Imaging

Tammie L. S. Benzinger, M.D., Ph.D.[1]; Robert C. McKinstry III, M.D., PhD.[2]; Chin-I Chen, M.D[1]; Agus Priatna, Ph.D.[3]

[1]*Mallinckrodt Institute of Radiology, Washington University School of Medicine, St Louis, Missouri, USA*
[2]*St. Louis Children Hospital, Mallinckrodt Institute of Radiology, Washington University School of Medicine, St Louis, Missouri, USA*
[3]*Siemens Medical Solutions, Malvern, PA, USA*

Introduction

Diffusion tensor imaging (DTI) is an emerging method for clinical neuroradiology. DTI allows for quantitative evaluation of the rate and direction of water motion within a voxel. In the brain, the axons of neurons form fiber tracts which impose directionality (anisotropy) on measurements of water diffusion. The aggregate diffusion of water within these tracts is quantified at each point by the diffusion tensor (D) [Stejskal and Tanner, 1965]. Multiple parameters can be derived from the diffusion tensor, including the „trace", Tr(D)= 1 + 2 + 3 = 3 × ADC (apparent diffusion coefficient), the relative anisotropy (RA, defined as the standard deviation of the three eigenvalues, normalized by the ADC), and the fractional anisotropy (FA, which is the standard deviation of the three eigenvalues normalized to the magnitude of the diffusion tensor). These secondary parameters are independent of the frame of reference and are very sensitive to white matter pathology [Alexander et al., 2007; Melhem et al., 2002].

Until recently, DTI required extensive off-line calculations to generate the tensor (D) and related parameter maps. However, using the current DTI packages available on the Tim (Total imaging matrix) platforms, DTI can now be performed as part of a routine clinical brain MRI, with Inline calculation of the D, ADC, and FA, and rapid off-line calculation of additional parameter maps as needed. We have developed a 25-direction DTI protocol with 25 b-values which can be run with isotropic 1 mm voxels at 3 Tesla in 4 minutes. We now include this as part of the standard imaging routine for pediatric and adult brain MRIs at St. Louis Children's Hospital and Washington University Medical Center.

Method

Imaging was performed at 3 Tesla MAGNETOM Trio, A Tim System or 1.5 Tesla MAGNETOM Symphony, A Tim System with Quantum gradient system using 12-channel Head Matrix coils. A single shot spin-echo echo planar imaging (EPI) was used for DTI acquisition at the Tim Trio with the following parameters: 60 slices without a gap, FoV = 190 mm, phase FoV = 100 %, slice thickness = 2 mm, base resolution = 96, phase resolution = 100 (that makes voxel size = 2 x 2 x 2 mm), phase partial Fourier = 6/8, TR = 9900 msec, TE = 102 msec, average = 1, b-value = 1400 sec/mm^2, bandwidth = 1080 Hz, EPI factor = 96, echo spacing = 1 msec. A similar protocol was setup for the Tim Symphony with 2.5 x 2.5 x 2.5 mm isotropic voxel. Average ADC map, trace weighted map, FA map, and tensor data were created inline. Post-processing was performed with Neuro 3D application package. The package has the capability of processing directional color encoded fractional anisotropy map (blue = SI direction, green = AP direction, and red = RL direction), tensor map, aligned tensor and anatomy data, aligned tensor and fractional anisotropy data, texture diffusion that maps the overall fiber tracts within the slices, and tractography.

Clinical cases

The following cases are some of the examples of the clinical applications of diffusion tensor imaging in pediatrics and adults which we have encountered in the course of routine clinical practice.

Case 1: Septo-optic dysplasia

A 14-year-old boy was admitted to the hospital with severe, chronic headaches. MRI shows absence of the septum pellucidum is consistent with his clinical diagnosis of septo-optic dysplasia. Moderate hydrocephalus and thinning of the corpus callosum were found. DTI show marked diminution, with significant reduction in the visual fiber tracts of the optic radiations but with persistent anisotropy (Fig. 1). These findings are concordant with his clinical presentation of intact visual function and are also in accordance with reports in the literature [Polizzi et al., 2006; Schoth et al., 2004]. Septo-optic dysplasia consists of a heterogenous deficits of midline brain structures which include absence or dysplasia of septum pellucidum, optic nerve and pituitary-hypothalamic dysfunction. In addition, the lesions may associate cerebral development malformations such as schizencephaly and polymicrogyria. A HESX1 gene mutation has been identified in familial septo-optica dysplasia. Clinical manifestations include diminished visual acuity, color blindness, nystagmus, microphthalmia, mental retardation, and endocrine disturbance.

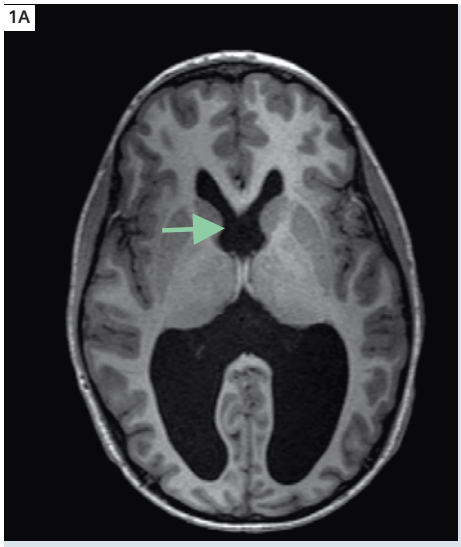

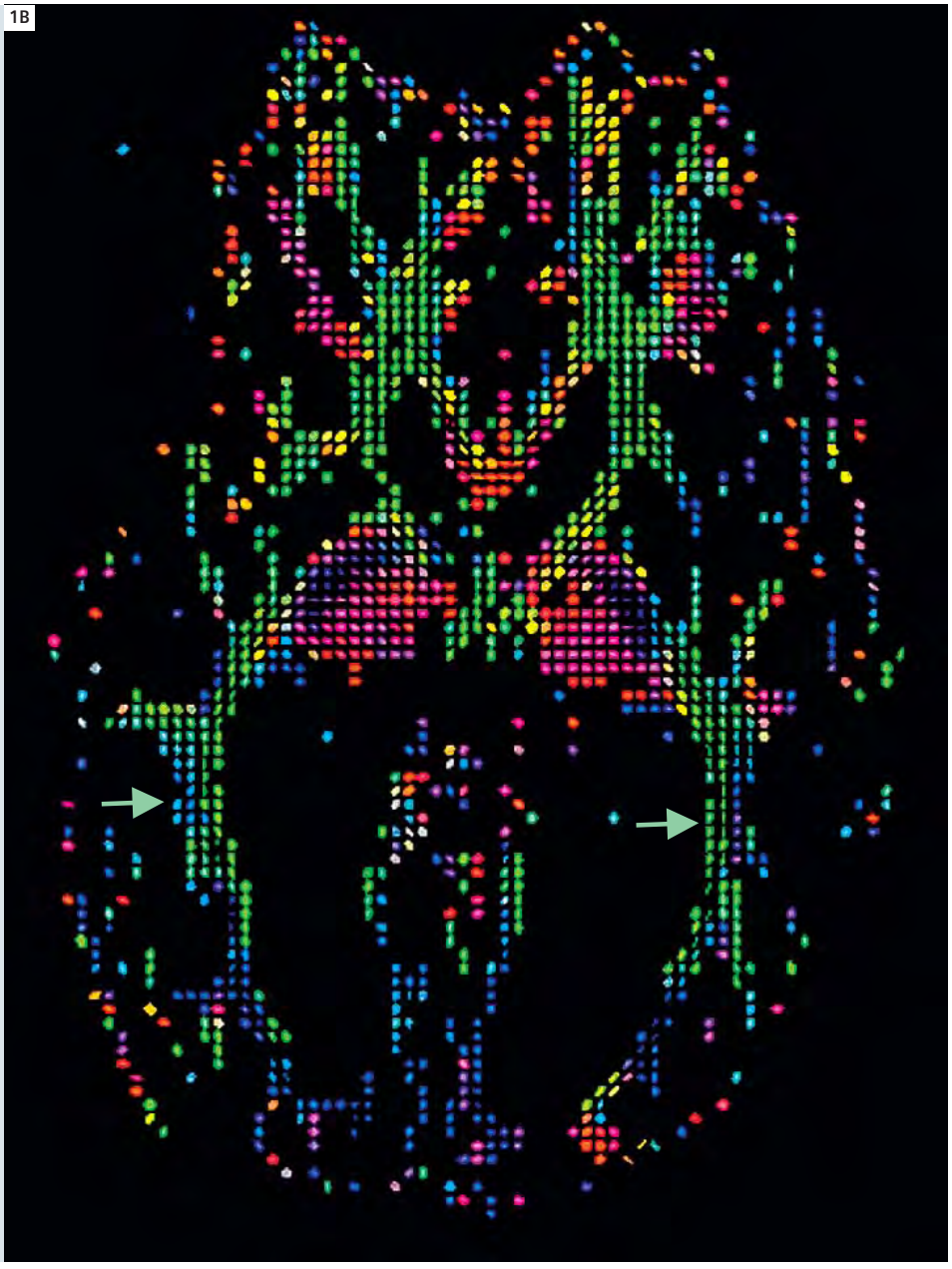

1 Septo-optic dysplasia. MR examinations were performed at 3T MAGNETOM Trio, A Tim System: **(A)** T1-weighted (MPRAGE) anatomic image demonstrating enlargement of the ventricles and absence of the septum pellucidum (arrow). **(B)** Tensor diagram computed from a 4 minute DTI scan performed with isotropic 2 mm voxels at 3 Tesla. The shape and color of the ellipsoids corresponds to the orientation of the white matter tract (anterior-posterior is green, transverse is red, and cranio-caudal is blue). The optic radiations (arrowheads) adjacent to the lateral ventricles are thin but intact.

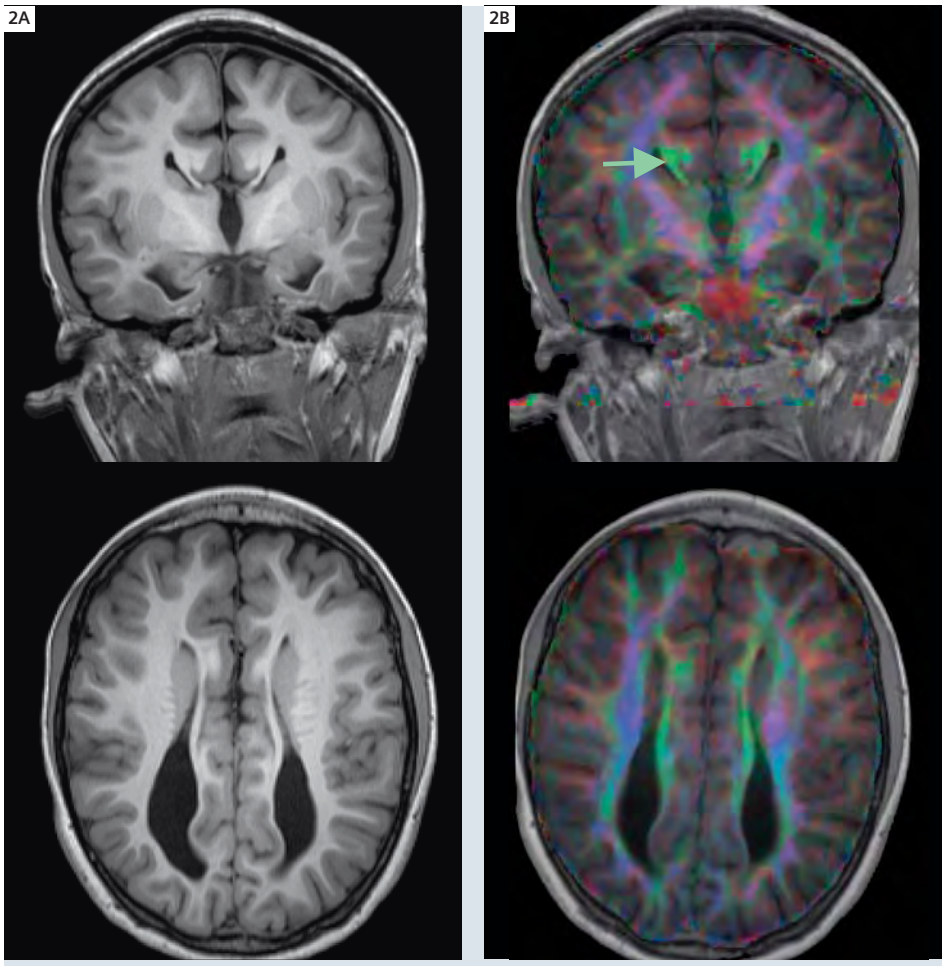

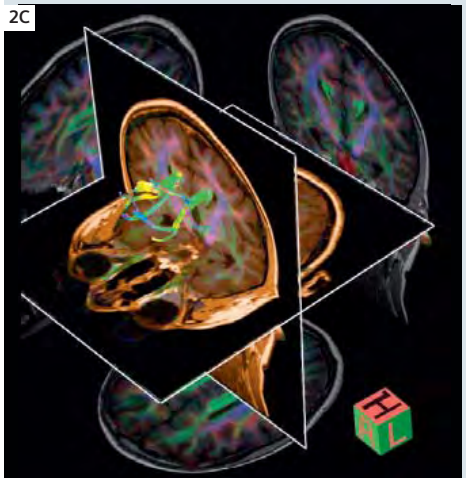

2 Agenesis of corpus callosum. MR exa-minations were performed at 3T MAGNETOM Trio, A Tim System. **(A)** T1-weighted images MPRAGE showing absense of the corpus callosum and parallel lateral ventricles.
(B) Color-encoded FA map merged with the anatomic images, using the Neuro3D software application. The linear white matter running in the anterior-posterior direction (Probst bundle) is identifed by the arrowhead.
(C) Tractography shows the bilateral Probst bundles (arrowhead) and no crossing fibers.

Case 2: Agenesis of corpus callosum

A 9-year-old girl was diagnosed with developmental delay and intractable seizures. MRI shows colpocephaly, parallel lateral ventricles, and agenesis of the corpus callosum. DTI shows no crossing fibers in the expected region of the corpus callosum (Fig. 2). With tractography, the orientation of the parallel Probst bundles are clearly identified. Tractography has recently been described as a useful imaging approach to callosal agenesis and dysgenesis [Tovar-Moll, 2007]. Agenesis of corpus callosum is a failure to develop the large bundle of fibers that connect the cerebral hemispheres. The complex disorder can result from any one of the multiple steps of callosal development, such as cellular proliferation and migration, axonal growth or glial patterning at the midline. Its subjacent mechanisms are still unknown. Patients can show variable presentations ranging from no symptoms to severe cognitive impairment [Paul et al., 2007].

Case 3: Schizencephaly

A 4-year-old girl has a past history of seizures. MRI (Fig. 3) shows a major malformation of cortical development involving the left motor strip, dorsal lateral premotor region, frontal operculum, frontal polar region, orbital frontal and lateral frontal regions, parietal operculum, and posterior temporal lobe. An associated left-sided schizencephaly is identified. The left lateral ventricle is mildly dilated. There is abnormal configuration of the central sulcus on the left. DTI shows diminished anisotropy of the underlying white matter region in subjacent to the malformation of cortical development [Eriksson et al., 2001; Trivedi, et al., 2006]. Schizencephaly presents a cleft in the cerebral cortex unilaterally or bilaterally, usually located in the frontal area. Associated septum pellucidum deficits are often found, suggesting that schizencephaly may share similar genetic mechanisms with septo-optic dysplasia. Mutation in the EMX2 gene can lead to schizencephaly. Clinical symptoms include seizures and mental impairment [Tanaka et al., 2000].

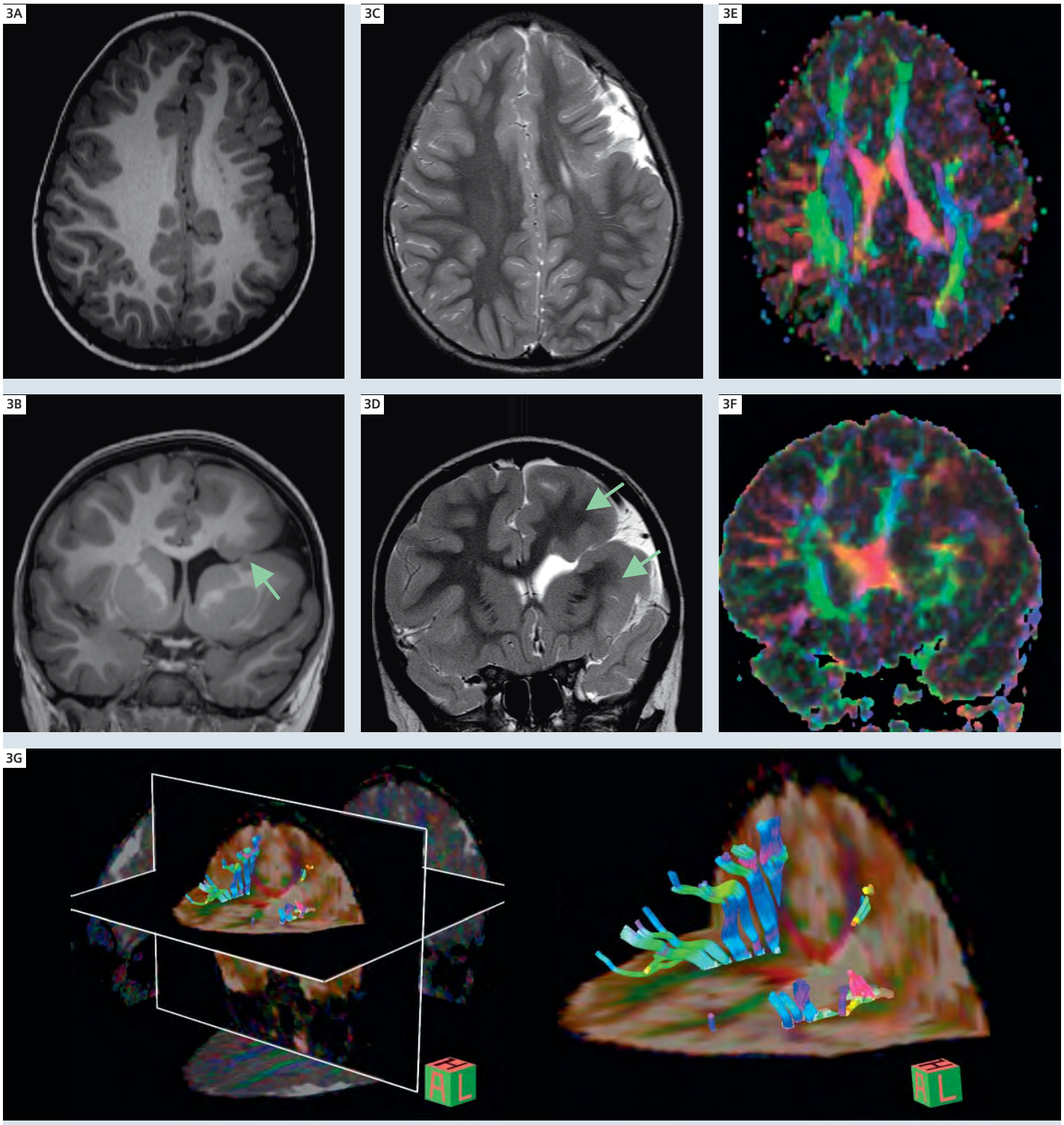

3 Schizencephaly. MR examinations were performed at 3T MAGNETOM Trio, A Tim System. T1 **(A, B)** and T2-weighted **(C, D)** transverse **(A,C)** and coronal images **(B, D)** demonstrating a large schizencephalic cleft in the left cerebral hemisphere (arrow). Accompanying this is an extensive malformation of cortical development (arrowheads). Although the white matter underlying the abnormal cortex appears normal on the clinical T1 and T2-weighted images, when the directional encoded FA map is superimposed on the anatomic images **(E, F)** there is complete loss of the normal (green and red) anisotropy in this white matter. **(G)** Tractography images show the tortuous fibers which do not cross the schizencephalic cleft.

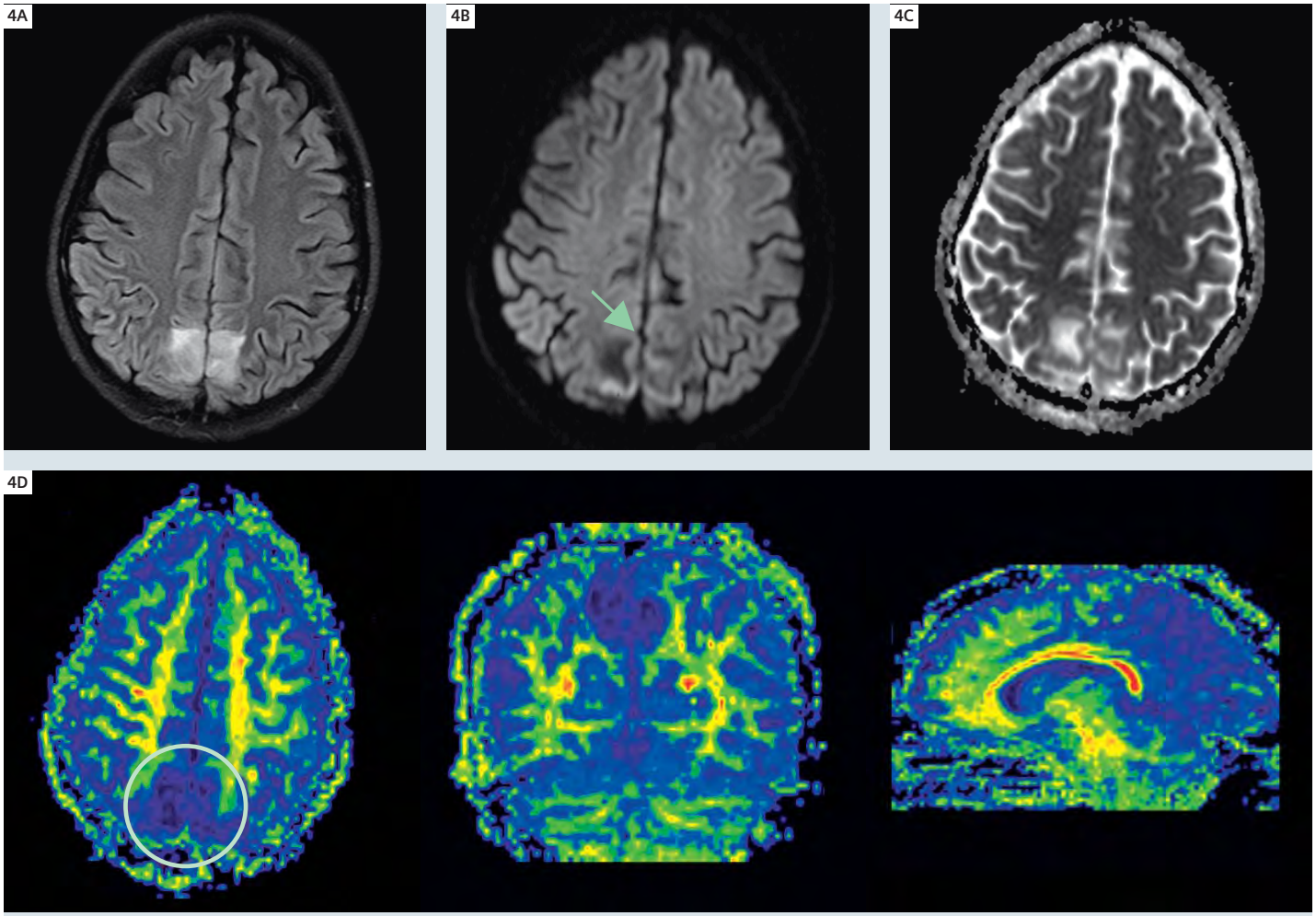

4 Reversible Posterior Leukoencepalopathy Syndrome (RPLS). MR examinations were performed at 3T MAGNETOM Trio, A Tim System: **(A)**, **(B)**, and **(C)** are the DarkFluid T2-weighted TSE, b = 0 image, and ADC map shows the area of restricted diffusion. **(D)** Fractional anisotropy, reformatted in transversal, coronal, and sagittal orientations shows loss of anisotropy in the right parietal lobe extending beyond the areas of T2 hyperintensity.

Case 4: Reversible Posterior Leukoencepalopathy Syndrome (RPLS)

A 13-year-old girl who with a past medical history of hypertension and end stage renal disease was transferred to pediatric ICU because of hypertensive seizure. MRI shows bilateral posterior parietal-occipital areas of T2 hyperintensity, with a focal area of reduced diffusion in the right parietal lobe. The FA parameter map derived from DTI demonstrates an area of abnormal anisotropy in the right parietal lobe which extends beyond the area of T2 hyperintensity (Fig. 4). Although restricted diffusion can has been reported in RPLS, the FA changes in the surrounding white matter have not previously been examined. Incorporating DTI into the routine clinical protocol will allow for larger research studies to be generated to further evaluate this finding [Mukherjee et al., 2001]. RPLS is a clinicoradiological entity which appears as reversible white matter edema predominantly involving the parietal and occipital lobes. The syndrome has been associated with a spectrum of disorders, including hypertensive encephalopathy, eclampsia, thrombotic thrombocytopenic purpura, acute renal failure, hemolytic-uremic syndrome, acute intermittent porphyria, and immunosuppressive drugs. The eitiology of RPLS is believed to be due to a breakdown of the blood-brain barrier with transudation of fluid and protein into the extravascular space resulting in cerebral edema [Min et al., 2006; Doelken et al., 2007].

Case 5: Pediatric demyelination

A 17-year-old boy was admitted with acute onset of headache, double vision, gait instability and nausea. MRI shows abnormalities on the right internal capsule, right periventricular, right mid brain, and right cerebellum. Eigenvalues of DTI show increased radial diffusivity but normal axial diffusivity at the lesion site, which is consistent with demyelinating disease (Fig. 5) and suggests myelin loss without axonal injury. As predicted by the DTI analysis, the child had an almost complete clinical recovery within a few weeks [Mukherjee et al., 2001; Song et al., 2002]. The central nerve system inflammatory demyelinating disorders of childhood include both self-limited (monophasic or recurrent acute disseminated encephalomyelitis ADEM, neuromyelitis optica NMO, clinical isolated syndrome CIS) and life-long (multiple sclerosis) conditions, which can be indistinguishable at the time of initial presentation. ADEM is an acute or subacute white matter disease of brain and spinal cord that often follows a viral illness or vaccination. MS results in recurrent episode and is more likely to develop significant disability [Inglese et al., 2002; Krupp, et al., 2007].

5A

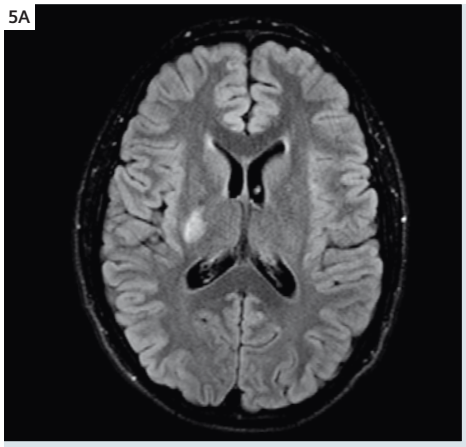

5B

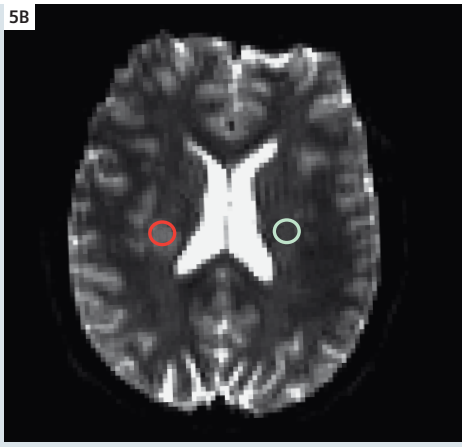

5C

ID	FA Mean / SDev	FA Size / Min / Max	ADC Mean / SDev	ADC Size / Min / Max	TraceW Mean / SDev	TraceW Size / Min / Max	b0 Mean / SDev	b0 Size / Min / Max
1	454.5 / 33.5	2 / 421 / 488	956.0 / 26.0	2 / 930 / 982	247.0 / 0.0	2 / 247 / 247	642.5 / 16.5	2 / 626 / 659
2	650.5 / 29.5	2 / 621 / 680	663.0 / 13.0	2 / 650 / 676	187.0 / 3.0	2 / 184 / 190	363.0 / 11.0	2 / 352 / 374

ID	Mean / SDev	Size / Min / Max	Mean / SDev	Size / Min / Max	Mean / SDev	Size / Min / Max	Mean / SDev	Size / Min / Max
1	1534.5 / 29.5	2 / 1505 / 1564	1062.0 / 46.0	2 / 1016 / 1108	206.0 / 8.0	2 / 198 / 214	624.5 / 4.5	2 / 620 / 629
2	1462.3 / 50.2	3 / 1392 / 1506	446.7 / 98.3	3 / 307 / 521	209.3 / 1.7	3 / 207 / 211	78.7 / 21.7	3 / 53 / 106

5D

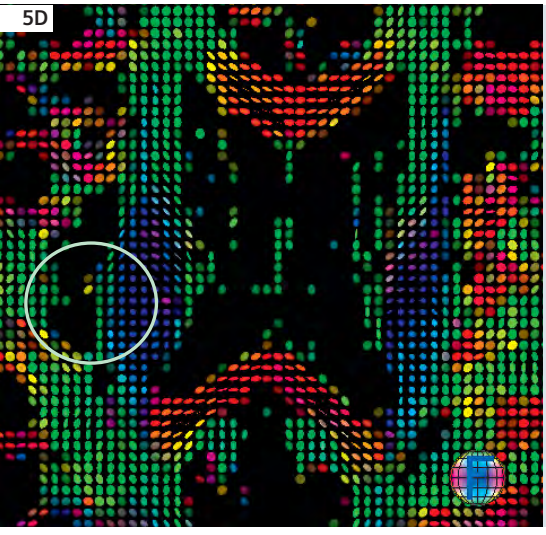

5E

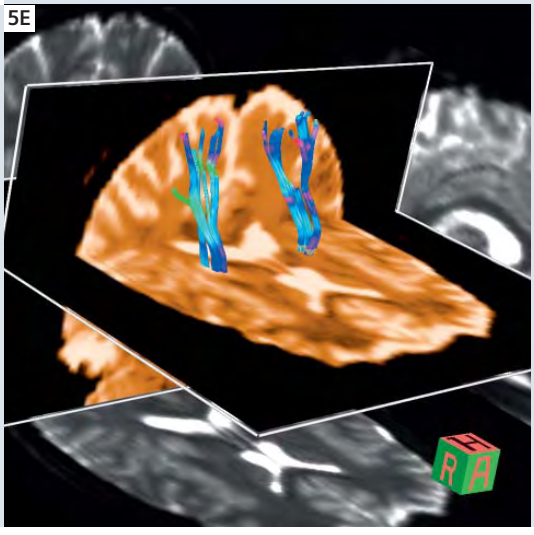

5 Pediatric demyelination. MR examinations were performed at 3T MAGNETOM Trio, A Tim System: **(A)** DarkFluid T2-weighted image shows abnormality on the right side of the brain. **(B)** DTI acquisition was acquired at 2 mm isotropic resolution. Regions of interest at normal (green) and lesion (red) sites were drawn at the diffusion image with b = 0. **(C)** Measurement shows increase in E2 and E3 (radial diffusivity) in the lesion site while the E1 (axial diffusivity) are the same bilaterally. **(D)** Tensor image shows the abnormality in the lesion site. **(E)** Tractography images show that the tracts in the lesion remain intact.

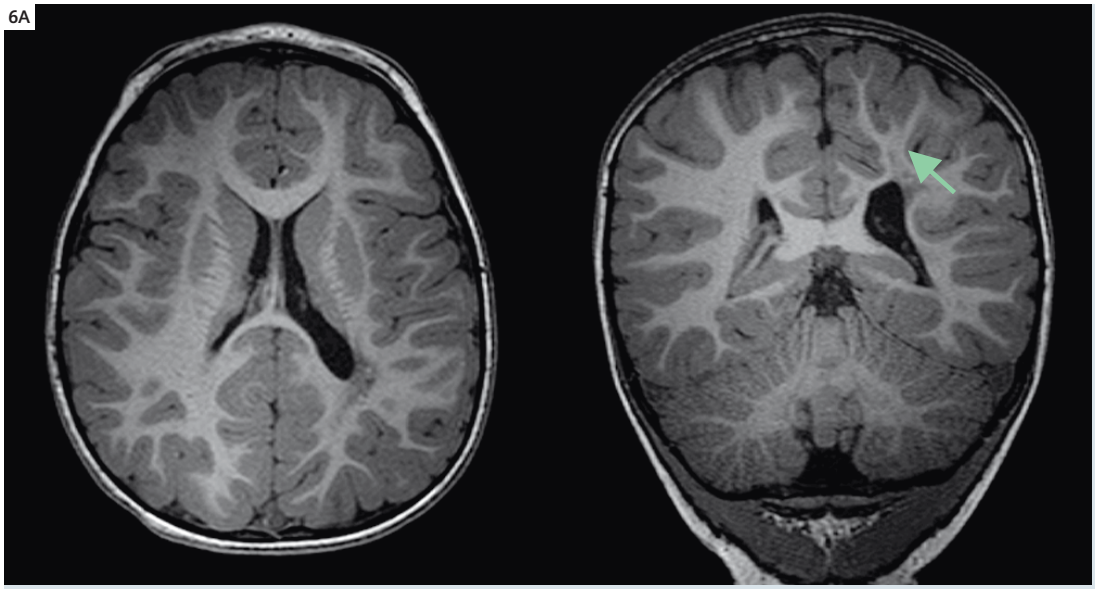

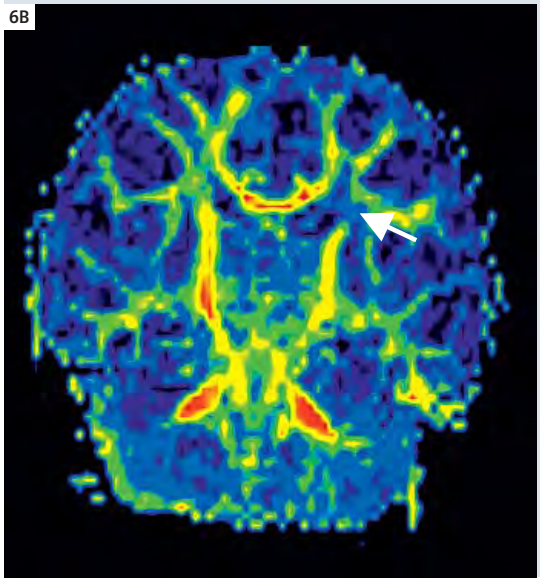

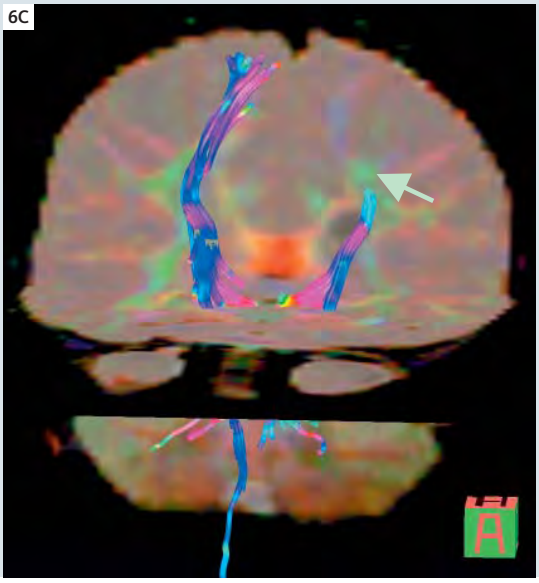

6 Periventricular Leukomalacia. MR examinations were performed at 3T MAGNETOM Trio, A Tim System:
(A) Isotropic 1 mm MPRAGE, reformatted to the transversal and coronal orientations showing the abnormality involving left peritrigonal white matter (arrowhead), with thinning of the white matter and ex-vacuo dilatation of the lateral ventricle.
(B) Coronal reformatted fractional anisotropy shows focal loss of anisotropy at the same location in the left periventricular white matter.
(C) Tractography shows interrupted fibers of the left corticospinal tract at the lesion site, explaining the patient's right hemiparesis.

Case 6: Periventricular leukomalacia

A 2-year-old girl has history of meningitis, right hemiplegia, and difficulty with balance. Her degree of disability was not immediately concurrent with the very minimal findings on the routine clinical MRI which shows mildly decreased T1 and focal increased T2 signal involving left peritrigonal white matter, and mild thinning of the posterior body of the corpus callosum. However, DTI shows the T2 hyperintense lesion corresponds to focal reduced anisotropy centered in a critical location in the left corticospinal tract. Tractography demonstrates interruption of the left corticospinal tract at this level, which is concurrent with the clinical finding of right hemiplegia (Fig. 6). Periventricular leukomalacia refers to the most common damage of the immature cerebral white matter in the perinatal period. It is related to the susceptibility of the periventricular white matter to focal ischemic, infective, or inflammatory destructive processes of neonates. Pathologically, it is characterized by focal necrosis in the periventricular region and diffuse reactive gliosis in the surrounding white matter [Folkerth, 2006; Nagae, 2006; Ward et al., 2006].

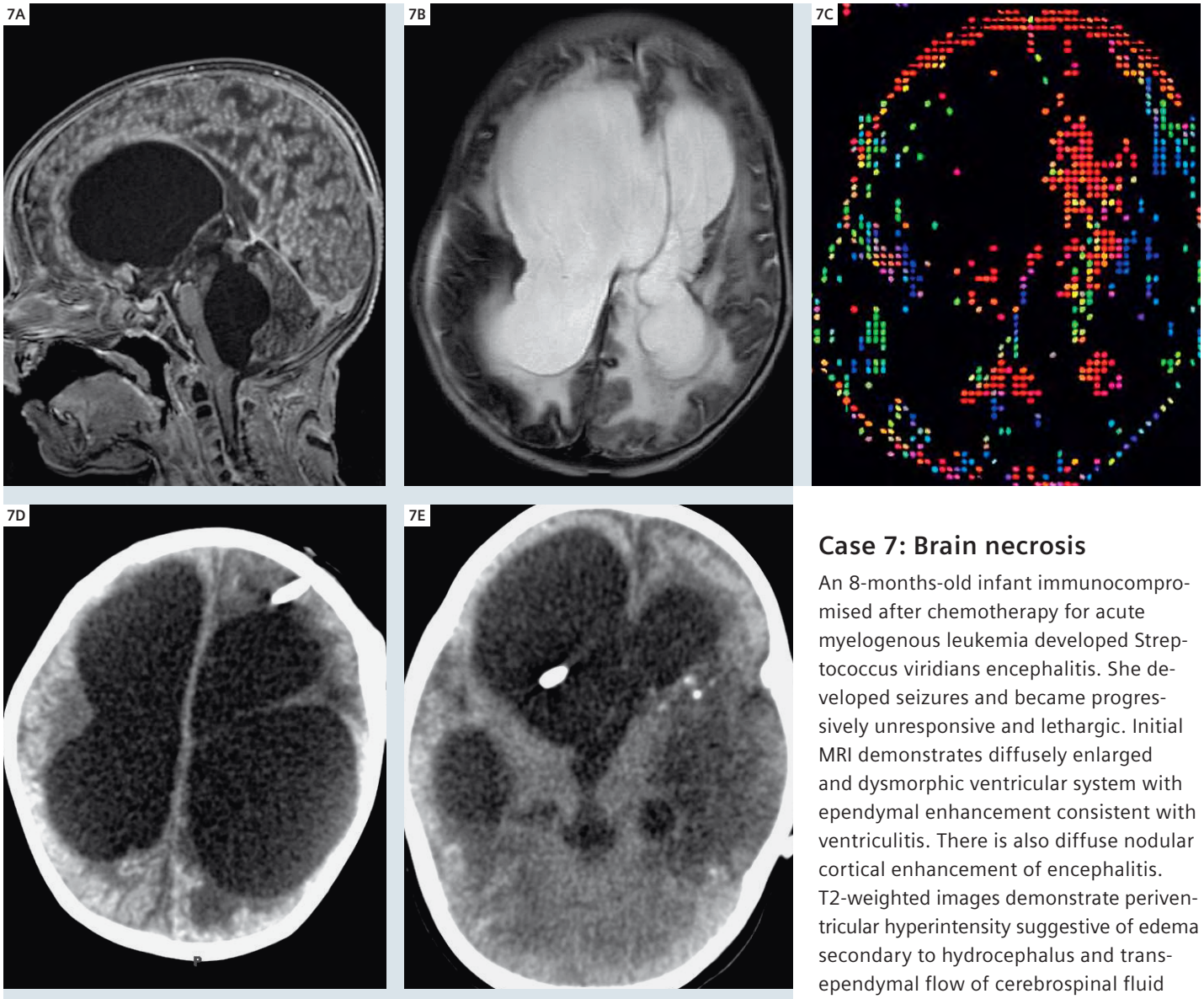

7 Brain necrosis. MR examinations were performed at 3T MAGNETOM Trio, A Tim System: **(A)** Post-contrast SE T1-weighted sagittal images of the brain demonstrate severe ventriculomegaly, periventricular ependymal enhancement, and diffuse granular enhancement of the cortex. These findings suggest severe ventriculitis and encephalitis. **(B)** Axial TSE T2-weighted images demonstrating ventriculomegaly and surrounding T2 hyperintensity of the white matter. In the setting of ventriculomegaly, the most common cause of periventricular white matter T2 hyperintensity is transependymal flow of CSF due to hydrocephalus. **(C)** Fractional anisotropy DTI with ellipsoid and color encoding demonstrates complete loss of normal periventricular white matter anisotropy (for comparison, see figure 5D). Inclusion of DTI in this routine clinical protocol thus suggested an alternate diagnosis of diffuse brain necrosis. **(D)** Non-contrast CT obtained 6 weeks after the initial MRI confirms initial imaging finding. Ventricular catheter failed to fully decompress the ventricles. There is loss of periventricular white matter and diffuse cerebral atrophy secondary to brain necrosis.

Case 7: Brain necrosis

An 8-months-old infant immunocompromised after chemotherapy for acute myelogenous leukemia developed Streptococcus viridians encephalitis. She developed seizures and became progressively unresponsive and lethargic. Initial MRI demonstrates diffusely enlarged and dysmorphic ventricular system with ependymal enhancement consistent with ventriculitis. There is also diffuse nodular cortical enhancement of encephalitis. T2-weighted images demonstrate periventricular hyperintensity suggestive of edema secondary to hydrocephalus and transependymal flow of cerebrospinal fluid (CSF). However, DTI demonstrates periventriular loss of anisotropy and near-total destruction of white matter tracts confirming brain necrosis (Fig. 7). This was confirmed by the patient's clinical course and subsequent imaging.

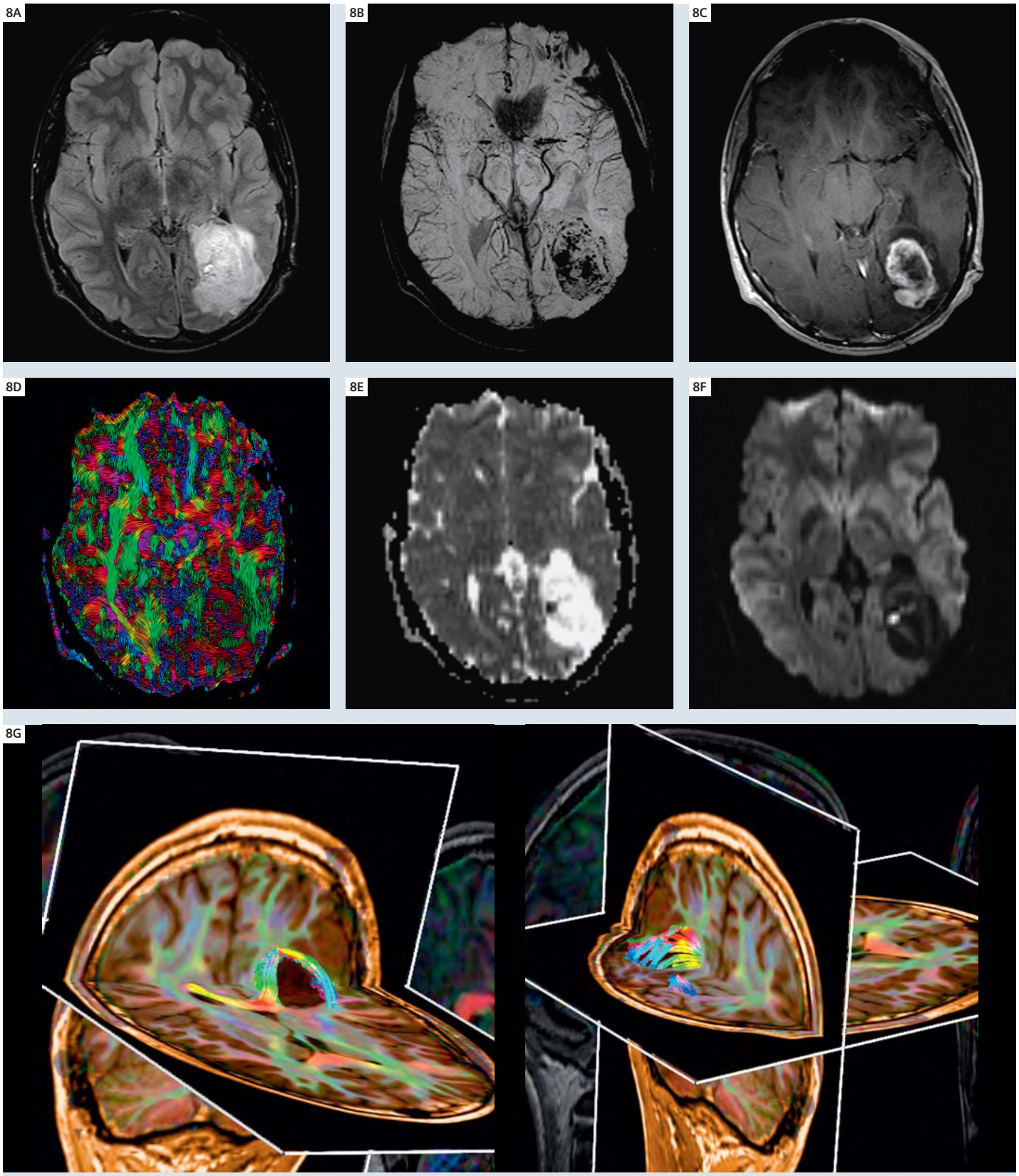

8 DNET tumor. MR examinations were performed at 3T MAGNETOM Trio, A Tim System: **(A)** DarkFluid T2-weighted image demonstrates focal T2 hyperintensity within the left temporooccipital lobe, displacing the trigone of the let lateral ventricle anteriorly. **(B)** Susceptibility weighted imaging (SWI) demonstrates central hemorrhage (signal loss) within the mass. **(C)** Postcontrast T1-weighted image demonstrates the left temporooccipital enhancing mass. **(D)** Texture diffusion showing the possible tracts within the slices. **(E)** and **(F)** are ADC map and trace-weighted images. **(G)** Tractography showing the tracts splitting and surrounding the tumor. This suggests a low grade primary glial neoplasm. Pathology confirmed this tumor to be a DNET.

Case 8: DNET tumor

A 16-year-old boy presented with seizures and was found to have a contrast enhancing mass at the left temporo-occipital lobe (Fig. 8). Susceptibility-weighted imaging (SWI) demonstrated internal hemorrhage within the mass. DTI deomstrated central reduced diffusion and displacement (rather than interruption) of the surrounding axon bundles. Prior to DTI, the differential diagnosis based upon conventional MR imaging would suggest primary glial neoplasm. Displacement, rather than disruption, of the fiber bundles at DTI is suggestive of lower grade neoplasm, which was confirmed at pathology to be a dysembryoplastic neuroepithelial (DNET) tumor. DNETs are pathologically benign cortical lesions that often arise in the temporal lobe. They usually are found in children and young adults with seizures that tend to become refractory to medical treatment. These lesions have many different imaging characteristics [Cruz et al., 2006; Koeller et al., 2006].

Case 9: Corpus callosum epidermoid cyst

A 46-year-old female presented to the emergency room with dizziness, fatigue, and nausea. MRI demonstrated a 4 cm mass mass arising from the posterior body of the corpus callosum. The mass was lobulated and had a heterogeneous appearance, decreased signal on T1, increased signal on T2, increased signal on diffusion-weighted imaging (DWI) and suppression of signal on the DarkFluid sequence. There was minimal post contrast enhancement of the mass. These characteristics are typical of an epidermoid cyst. DTI shows that the corpus callosum tracts are splayed superiorly, anteriorly and posteriorly with respect to the mass. The splenium is not involved (Fig. 9). The DTI findings are features of low grade lesions. Epidermoid cysts are benign slow-growing tumors which contain keratin, cellular debris and cholesterol, and lined with stratified squamous epithelium. Epidermoid cysts are most commonly located in the cerebellopontine angle cistern and the parasellar regions. Most are asymptomatic but may occasionally result in mass effect, cranial neuropathy, or seizure [Osborn et al., 2006]. Here we report a case of an epidermoid cyst that involves the body of the corpus callosum which is an unusual location.

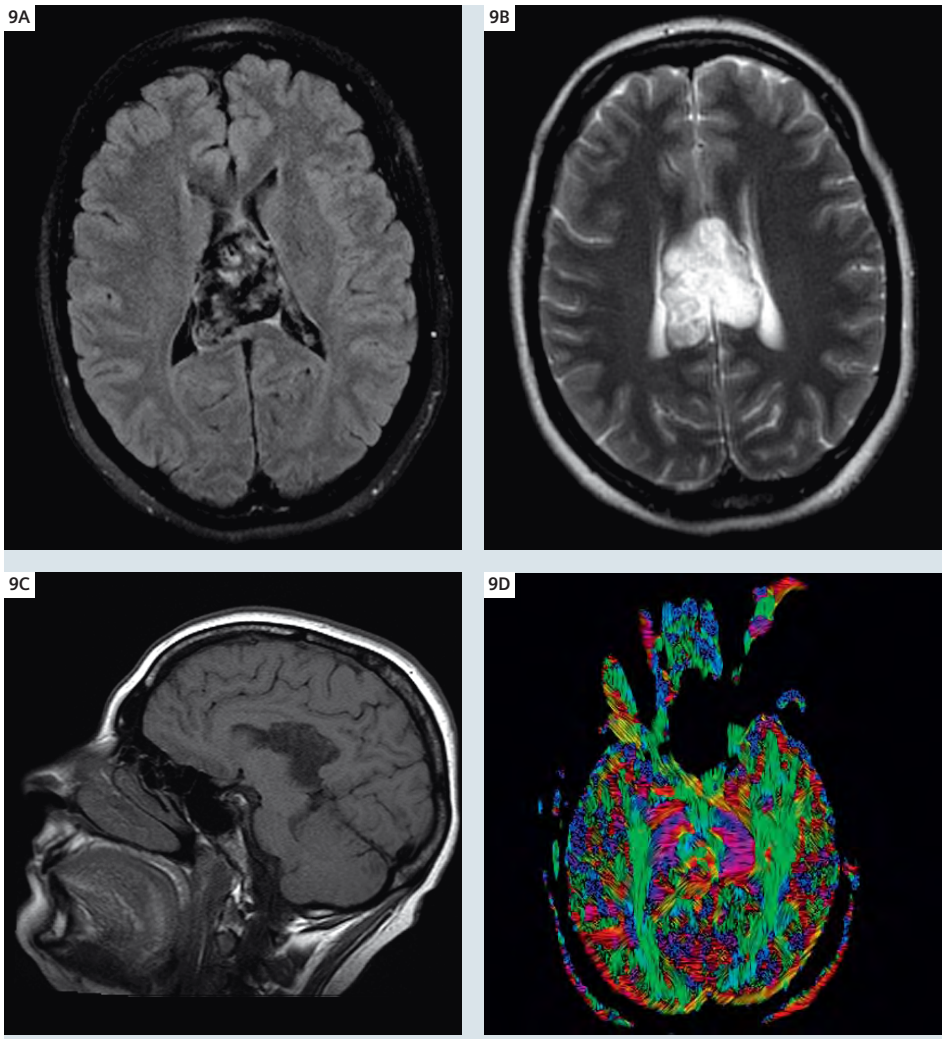

9 Corpus callosum epidermoid cyst. MR examinations were performed at 1.5T MAGNETOM Symphony, A Tim System: **(A)**, **(B)**, **(C)** are DarkFluid T2-weighted TSE, T2-weighted BLADE, and T1-weighted spin echo images respectively, demonstrating the mass associated with the posterior body of corpus callosum.

Continued on page 126

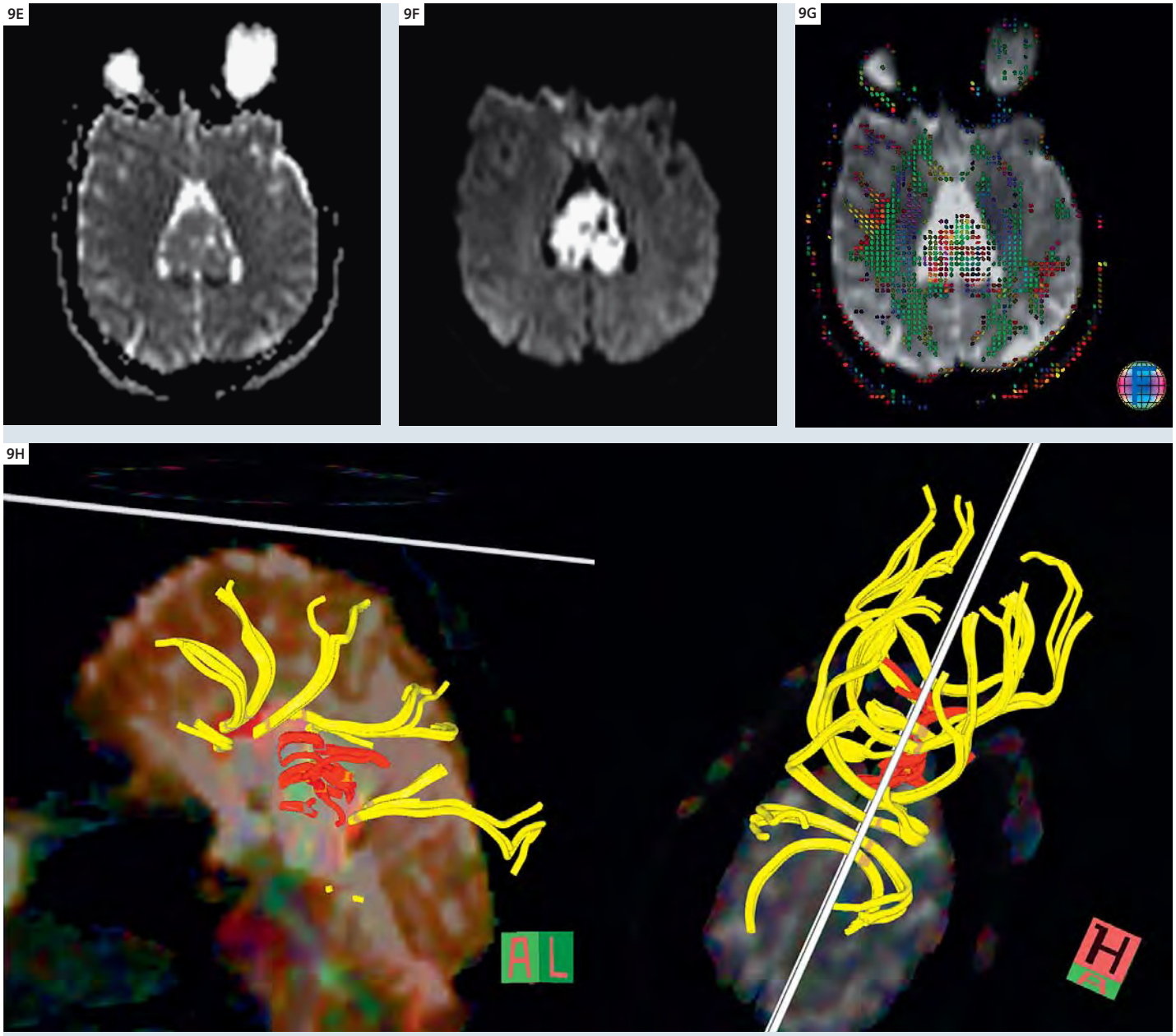

9 Corpus callosum epidermoid cyst **(D)**, **(E)**, **(F)**, **(G)** are the texture diffusion, ADC map, trace-weighted, and aligned tensor and anatomy still showing anisotropic diffusion surrounding the mass. **(H)** Tractography shows intact fibers of the corpus callosum (yellow) displaced superiorly above the mass (red). In this case, tractography proved useful for presurgical planning.

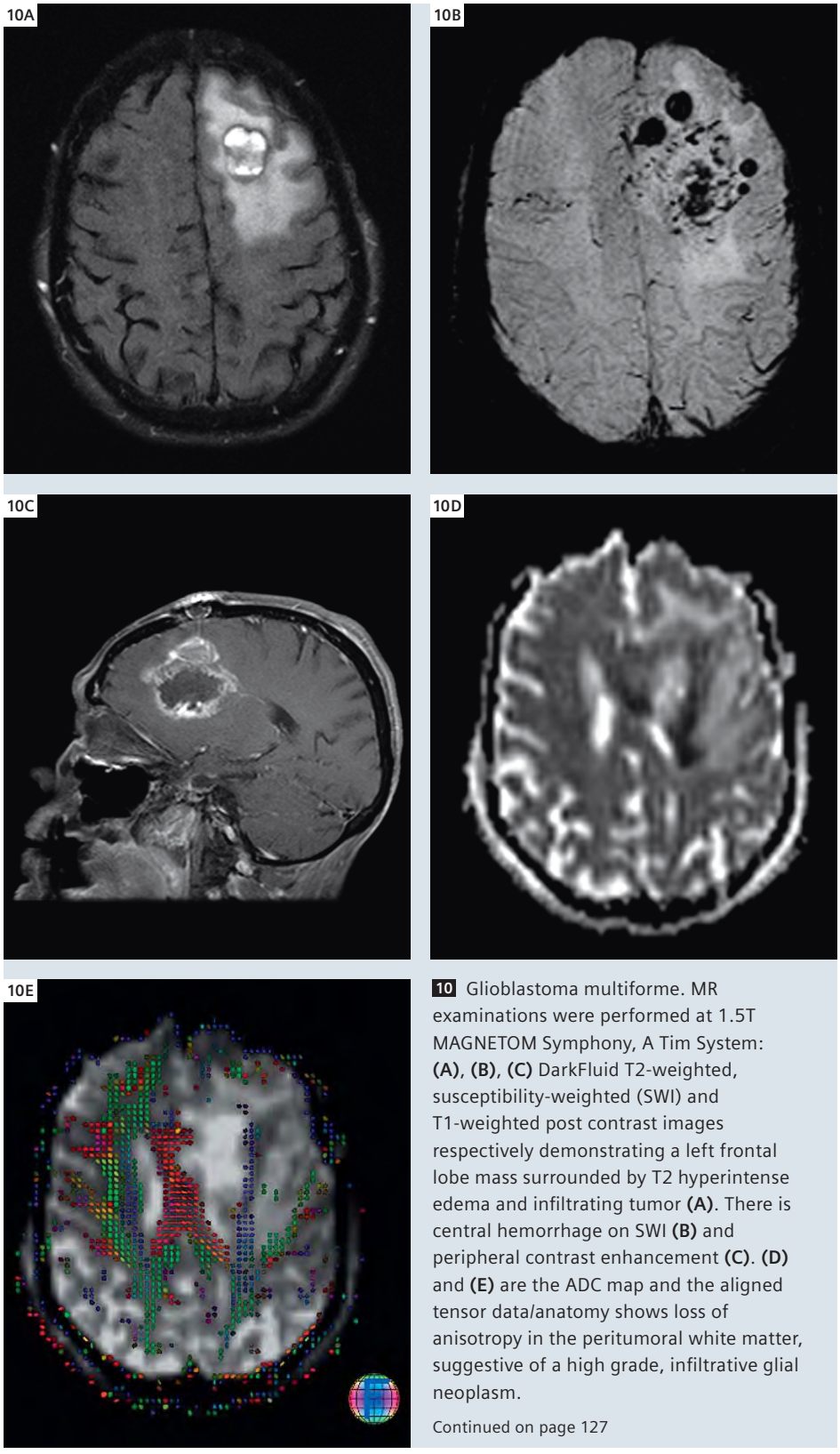

10 Glioblastoma multiforme. MR examinations were performed at 1.5T MAGNETOM Symphony, A Tim System: **(A)**, **(B)**, **(C)** DarkFluid T2-weighted, susceptibility-weighted (SWI) and T1-weighted post contrast images respectively demonstrating a left frontal lobe mass surrounded by T2 hyperintense edema and infiltrating tumor **(A)**. There is central hemorrhage on SWI **(B)** and peripheral contrast enhancement **(C)**. **(D)** and **(E)** are the ADC map and the aligned tensor data/anatomy shows loss of anisotropy in the peritumoral white matter, suggestive of a high grade, infiltrative glial neoplasm.

Continued on page 127

Case 10: Glioblastoma multiforme (GBM)

An 83-year-old woman was admitted with right limb weakness. MRI demonstrated a T2 hyperintense, hemorrhagic, contrast enhancing mass of the left frontal lobe. DTI shows disruption, rather than displacement, of left frontal white matter tracts, suggestive of a high grade glial neoplasm (Fig. 10). Biopsy confirmed the diagnosis of glioblastoma multiforme (GBM). Gliomas of astrocytic origin (astrocytomas) are classified into four grades pilocytic astrocytoma (grade I), astrocytoma (grade II), anaplastic astrocytoma (grade III) and glioblastoma multiforme (GMB) (grade IV), with different biological behaviour and degree of malignancy. Glioblastoma (GBM), the most common primary intracranial malignancy, is a morphologically diverse neoplasm with poor prognosis despite multimodality therapy [Roberts et al., 2005].

Conclusion

We have developed a fast, high resolution DTI protocol for whole brain DTI for implementation in routine clinical practice. Using standard Siemens DTI software at the scanner and standard post-processing, we routinely obtain 2 mm (3T) or 2.5 mm (1.5T) isotropic DTI with 25 b-values for all brain MRIs performed on Tim systems at Washington University. This adds less than 5 minutes to the brain MRI protocol. Post-processing for FA is performed inline at the scanner and is evaluated for all patients. Additional parameter maps and tractography for selected cases is performed with an additional 5–20 minutes of post-processing. The DTI is of high quality, and is obtained with additional averages (up to 10 to 20 minutes of total scanning time) for subjects involved in research studies. All of the cases presented in this review were identified during the course of routine clinical practice in a one month interval. On a daily basis, we are discovering new utility for DTI in our practice, with direct impact on current patient care.

10F

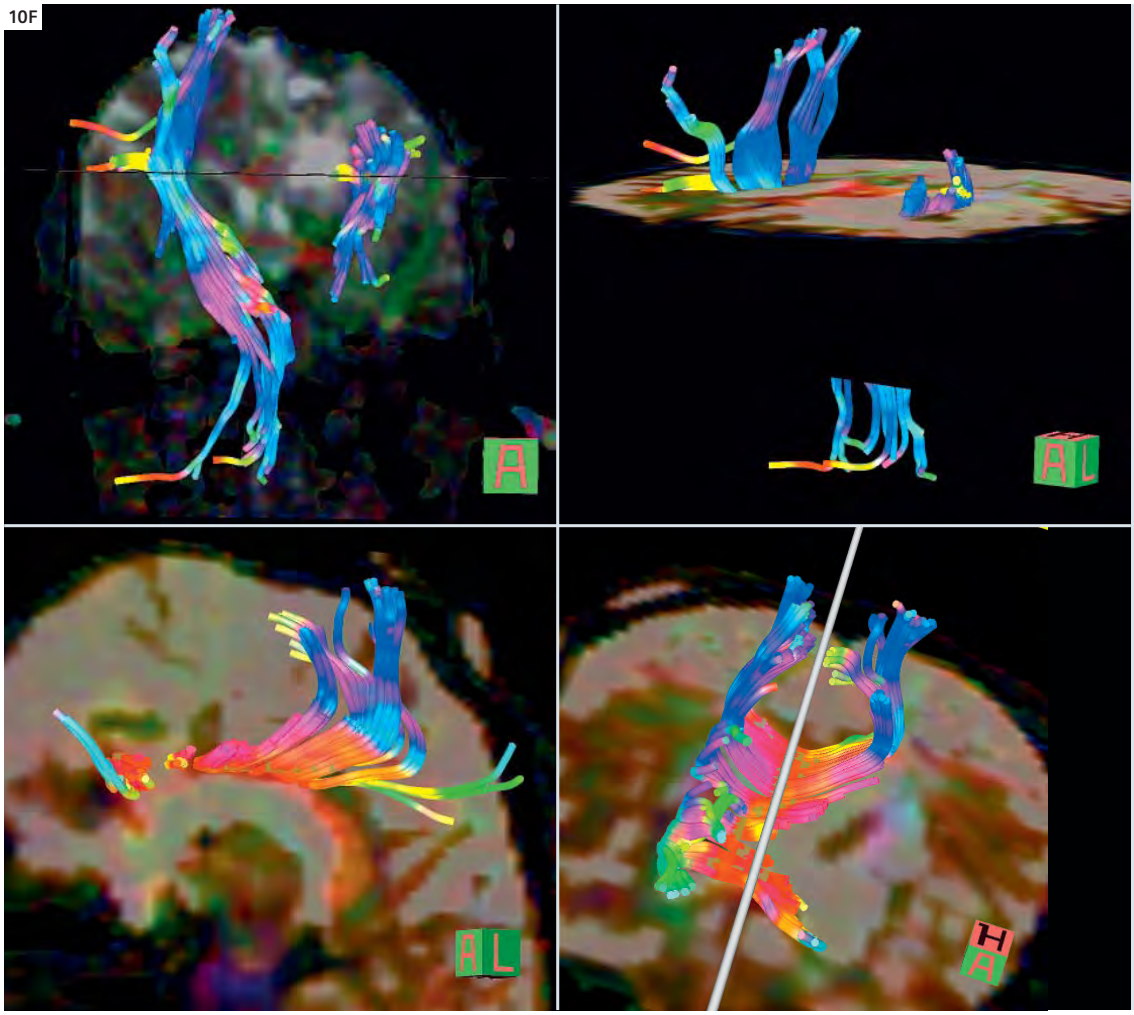

10 (F) Tractography images show the interrupted fibers around the tumor as would be expected for a high grade GBM (in contrast to the intact fibers around the low grademasses in figures 8 and 9). GBM was confirmed at pathology.

References

1 Alexander AL, Lee JE, Lazar M, Field AS.Diffusion tensor Imaging of the Brain. Neuroptherapeutics; 2007 July; 4:316-329.

2 Cruz LC Jr, Sorensen AG. Diffusion tensor magnetic resonance imaging of brain tumors. Magnetic Resonance Imaging Clinic North America. 2006 May; 14(2):183-202.

3 Doelken et al. Differentiation of cytotoxic and vasogenic edema in a patient with reversible posterior leukoencephalopathy syndrome using diffusion-weighted MRI. Diagn Interv Radiol 2007; 13: 125-128.

4 Eriksson S, Rugg-Gunn FJ, Symms MR, Barker GJ, Duncan JS. Diffusion tensor imaging in patients with epilepsy and malformations of cortical development. Brain 124: 617-626. 2001.

5 Folkerth RD. Periventricular Leukomalacia: Overview and Recent Findings. Pediatric and Developmental Pathology 2006;9; p3-13.

6 Inglese et al. Magnetization Transfer and Diffusion Tensor MR Imaging of Acute Disseminated Encephalomyelitis. AJNR 2002; 23; 267-272).

7 Koeller et al. Dysembryoplastic neuroepithelial tumors: MR appearance. AJNR 1992 Sep-Oct;13(5): 1319-25.

8 Krupp et al. Consensus definitions proposed for pediatric multiple sclerosis and related disorders. Neurology 2007; 68 (suppl 2): S7-12.

9 Melhem, ER, Mori, S, Mukundan, G, Kraut, M, Pomper, MG, van Zijl, PC

10 Diffusion Tensor MR Imaging of the Brain and White Matter Tractography, Am. J. Roentgenol. 2002 178: 3-16.

11 Min et al. Reversible Posterior Leukoencephalopathy in Connective Tissue Diseases. Semin Arthritis Rheum 2006: 35: 388-395.

12 Mukherjee P, McKinstry RC. Reversible posterior leukoencephalopathy syndrome: Evaluation with diffusion tensor imaging. Radiology. 2001 Jun;219(3):756-65.

13 Nagae LM. Diffusion Tensor Imaging in Children with Periventricular Leukomalacia: Variability of Injuries to White Matter Tacts. AJNR; 28; 1213-22, 2006.

14 Osborn et al. Intracranial Cysts: Radiologic-Pathologic Correlation and Imaging Approach. Radiology; 2006; vol 239; No. 3. p652-664.

15 Paul, LK et al. Agenesis of the corpus callosum: genetic, developmental and functional aspects of connectivity. Nature Reviews Neuroscience. 2007 April, vol 8, p287-299

16 Polizzi A, Pavone, P, Iannetti, P, Manfre, L, and Ruggieri, M. Septo-optic dysplasia complex: A heterogenous malformation syndrome. Pediatric Neurology Vol 34, No. 1, 2006.

17 Roberts TP, Liu F, et al. Fiber density index correlates with reduced fractional anisotropy in white matter of patients with glioblastoma. AJNR Am J Neuroradiol. 2005 Oct;26(9):2183-6.

18 Schoth, Felix, Krings, Timo. Diffusion-tensor imaging in septo-optic dysplasia. Neuroradiology, Vol 46, No 9, Sept 2004.

19 Song SK, Sun SW, Ramsbottom MJ, Chang C, Russell J, Cross AH. Dysmyelination revealed through MRI as increased radial (but unchanged axial) diffusion of water. Neuroimage. Nov 2002;17(3):1429-1436.

20 Stejskal EO, Tanner JE. Spin diffusion measurements: spin echoes in the presence of a time-dependent field gradient. J Chem Phys 1965;42:288 -292.

21 Tanaka et al. Genetics of brain development and malformation syndromes. Current Opinion in Pediatrics 2000, 12: 523-528.

22 Tovar-Moll F, Moll G, de Oliveira-Souza R, Bramati I, Andreiuolo PA, Lent R Neuroplasticity in Human Callosal Dysgenesis: A Diffusion Tensor Imaging Study, Cerebral Cortex Advance Access published on March 1, 2007, DOI 10.1093/cercor/bhj178. Cereb. Cortex 17: 531-541.

23 Trivedi R, Gupta RK, el al. Diffusion tensor imaging in polymicrogyria: a report of three cases. Neuroradiology. 2006 Jun; 48(6): 422-7.

24 Ward P, Counsell S, et al. Reduced fractional anisotropy on diffusion tensor magnetic resonance imaging after hypoxic-ischemic encephalopathy. Pediatrics. 2006 Apr;117(4):e619-30. Epub 2006 Mar 1.

Expert Talks

Don't miss the talks of experienced and renowned experts covering a broad range of MRI imaging

Imaging of the young brain – which technique for which referral?

Michael Ditchfield, M.D.
Monash Children's, Clayton, Australia

Acquisition and evaluation of perfusion data

Heiko Meyer
Siemens Healthcare, Erlangen, Germany

Peripheral nerve imaging from head to toe

Meng Quan-Fei
Hospital of Sun Yat-sen University, Guangzhou, China

Clinical Applications of DTI

Tammie L. S. Benzinger
Washington School of Medicine, St. Louis, USA

Effective utilization of fMRI in routine clinical practice

Helmut Rumpel
Singapore General Hospital, Singapore

Visit us at **www.siemens.com/magnetom-world**

Go to **Education > e-trainings & Presentations**

Diagnostic Relevant Reduction of Motion Artifacts in the Posterior Fossa by *syngo* BLADE Imaging

T. von Kalle[1]; B. Blank[2]; C. Fabig-Moritz[1]; P. Müller-Abt[1]; M. Zieger[1]; K. Wohlfarth[3]; P. Winkler[1]

[1]*Department of Pediatric Radiology, Olgahospital Klinikum Stuttgart, Germany*
[2]*Department of Pediatric Oncology, Hematology and Immunology, Olgahospital Klinikum Stuttgart, Germany*
[3]*Siemens Healthcare, Erlangen, Germany*

1

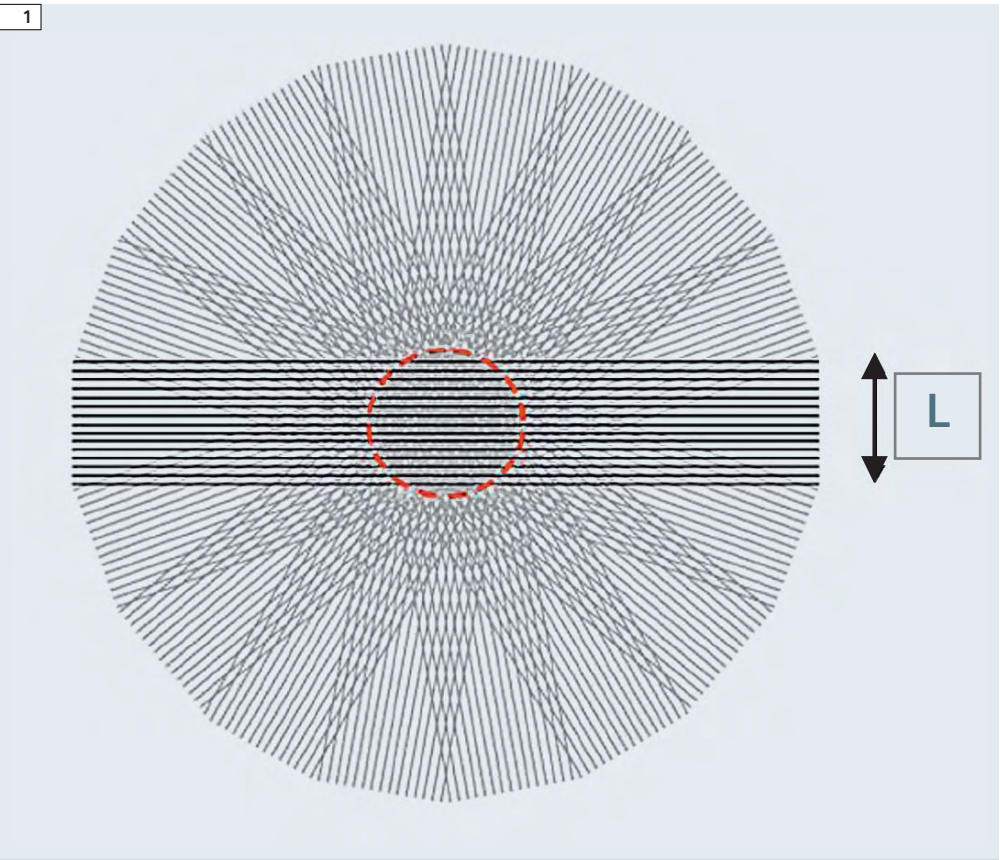

1 k-space trajectory in BLADE imaging. The k-space is covered by a series of blades each of which consists of the lowest phase encoding lines. The centre of the k-space (red circle) with diameter L is resampled for every blade. Data are then combined to a high resolution image.

Although movement and pulsation artifacts are a frequent problem in daily routine [1–4] especially in the diagnostics of pediatric patients, only few articles on this topic can be found in the literature. According to our experience mainly MR images of the posterior fossa, the cerebellum and the brain stem, may be significantly impaired by artifacts from pulsatile flow of blood or cerebrospinal fluid even without patient head movement [5, 6]. Sedation or general anesthesia rarely influence these pulsation or flow artifacts. However, accurate assessment of small brain lesions is essential in many pediatric patients, especially in those with malignant brain tumors. MR imaging with "rotating blade-like k-space covering" (BLADE) and "Periodically Rotated Overlapping Parallel Lines with Enhanced Reconstruction" (PROPELLER) have been shown to effectively reduce artifacts in healthy volunteers and adult patients [7, 8, 9], as well as in pediatric patients [4, 10] and therefore have the potential to reduce the frequency of anesthesia in children. As these MR techniques reduce motion artifacts by fast segmental image acquisition combined with mathematical algorithms, we assumed that it might at

the same time reduce the visibility of small brain lesions. We therefore compared the image quality of two T2-weighted fluid attenuated inversion recovery (T2w FLAIR) sequences with different k-space trajectories (conventional Cartesian and BLADE) with respect to artifacts and depiction of small hyperintense brain lesions [5].

Imaging techniques

We used a 1.5T scanner (MAGNETOM Avanto, Siemens Healthcare, Erlangen, Germany) and the Siemens 12-channel head matrix coil.
For each patient we compared two sequences with transverse 4 mm sections (gap 10%) that were applied in identical slice positions:
1. The T2w FLAIR standard sequence, a spin-echo sequence with conventional rectilinear Cartesian k-space trajectories (image parameters: TI 2500 ms, TR 9000 ms, TE 100 ms, BW 150 Hz/pixel, turbo factor 19, TA160 s, FOV 230 x 230 mm, matrix 256 x 256).
2. The BLADE FLAIR sequence with rotating blade-like k-space trajectories (image parameters: TI 2500 ms, TR 9000 ms, TE 107 ms, BW 250 Hz/pixel, turbo factor 29, TA 260 s, BLADE-Coverage 130 %, FOV 230 x 230 mm, matrix 256 x 256).
During the acquisition of both sequences children were encouraged not to move their head. They were offered video films or audio programs during the examination.

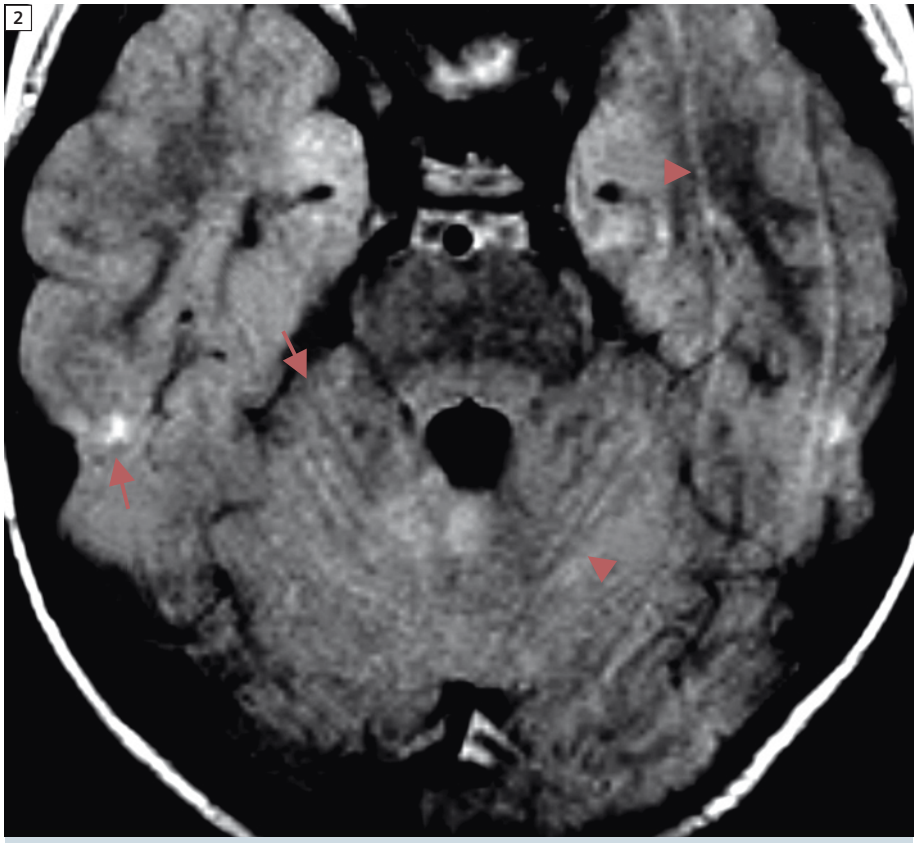

2 Movement artifacts caused by head movements (arrowheads) and pulsation artifacts caused by pulsatile flow (arrows). T2w FLAIR sequence with conventional rectilinear k-space trajectories.

BLADE technique

syngo BLADE is the product name of the motion insensitive Siemens turbo-spin-echo sequence which utilizes the PROPELLER k-space trajectory [11].
The technique is approved for diagnostic MR examinations of patients. It consists of blade-like rotating k-space coverage. During each echo train of a BLADE sequence the lowest phase encoding lines of a conventional rectilinear k-space are acquired. The number of lines, which depends on the length of the echo train, determines the resolution of the image. During the acquisition process the direction of this "blade" is rotated around the k-space centre such that the complete series covers the whole k-space (Fig. 1). Images can be displayed with or without an additional motion correction algorithm.

Patients

The typical hyperintense white matter abnormalities in the cerebellum of patients with neurofibromatosis type 1 (NF 1) [12] served the purpose of our study to assess and compare the visibility of small and low contrast lesions.
We re-evaluated images of children with NF 1, who had been routinely scanned for optic pathway gliomas and who had been examined with T2w FLAIR sequences of both techniques. 26 patients, 10 girls and 16 boys from 2 years 7 months to 17 years (median age 8 years 5 months) were included in the study.

Image evaluation

Four experienced pediatric radiologists independently assessed unlabeled images of both FLAIR sequences of each patient. Structures of the posterior fossa, cerebellum and brain stem, were evaluated according to the presence of movement artifacts (caused by head movements) or pulsation artifacts (caused by pulsatile flow of blood and/or cerebrospinal fluid) (Fig. 2), their differentiation from lesions, and their delineation from the surrounding tissue by contrast (difference in signal intensities) and edge definition (clearly or poorly defined margins) as has been described elsewhere

Table 1: Scores for movement and pulsation artifacts, and the differentiation of artifacts and lesions in the posterior fossa.

	Conventional		*syngo* BLADE	
	yes	no	yes	no
Movement	29	75	4	100
Pulsation	99	5	25	79
Differentiation lesion/artefacts	53	30	81	2

Yes = artifacts present, lesions and artifacts distinguishable. No = artifacts not present, lesions and artifact not distinguishable. Maximum score for each sequence = 104. Last line. Patients with neither artifacts nor lesions were excluded. Results of statistical tests cf Table 2.

[5] The transverse diameters of the largest and smallest lesions were measured in both sequences of each patient. Signal intensities of a representative lesion and the adjacent normal brain tissue were measured. [5]

Discussion

Techniques with rotating blade-like k-space covering (BLADE) [9], with periodically rotated overlapping parallel lines with enhanced reconstruction (PROPELLER) [8,10], and with k-space alignment similar to a trellis [13] have been shown to effectively reduce artifacts in T1- and T2-weighted images. Studies on pediatric [4] and adult patients [7] found a comparable detectability of lesions in contrast-enhanced T1-weighted images of FLAIR BLADE sequences and conventional spin-echo sequences. However, image quality and delineation of small or poorly delineated lesions in MR images in T2-weighted FLAIR acquired with these techniques have not been systematically studied.

In our study, all observers found more pulsation artifacts than movement artifacts in images of both the conventional and the *syngo* BLADE sequence (Table 1). Artifacts were reported significantly less often in images acquired with BLADE technique than in images with rectilinear k-space trajectory (Table 1 and 2). These results confirm that artifacts caused by pulsation, flow and motion are significantly reduced by the BLADE technique in comparison to the standard sequence with conventional

Table 2: Posterior fossa. Comparison of conventional vs. BLADE images. McNemar's test. p-values for each observer. Cohen's kappa for interobserver agreement.

	Presence of movement artifacts	Presence of pulsation artifacts	Differentiation of lesions and artifacts	Delineation of lesions	
				Edge definition	Contrast
Observer 1	0.03	0.02	0.04	> 0.05	> 0.05
Observer 2	0.02	0.00002	0.002	0.0027	0.0009
Observer 3	0.041	0.000007	0.001	> 0.05	> 0.05
Observer 4	0.013	0.00002	0.013	> 0.05	> 0.05
Cohen's kappa	0.34	0.37	0.72	0.11	0.01

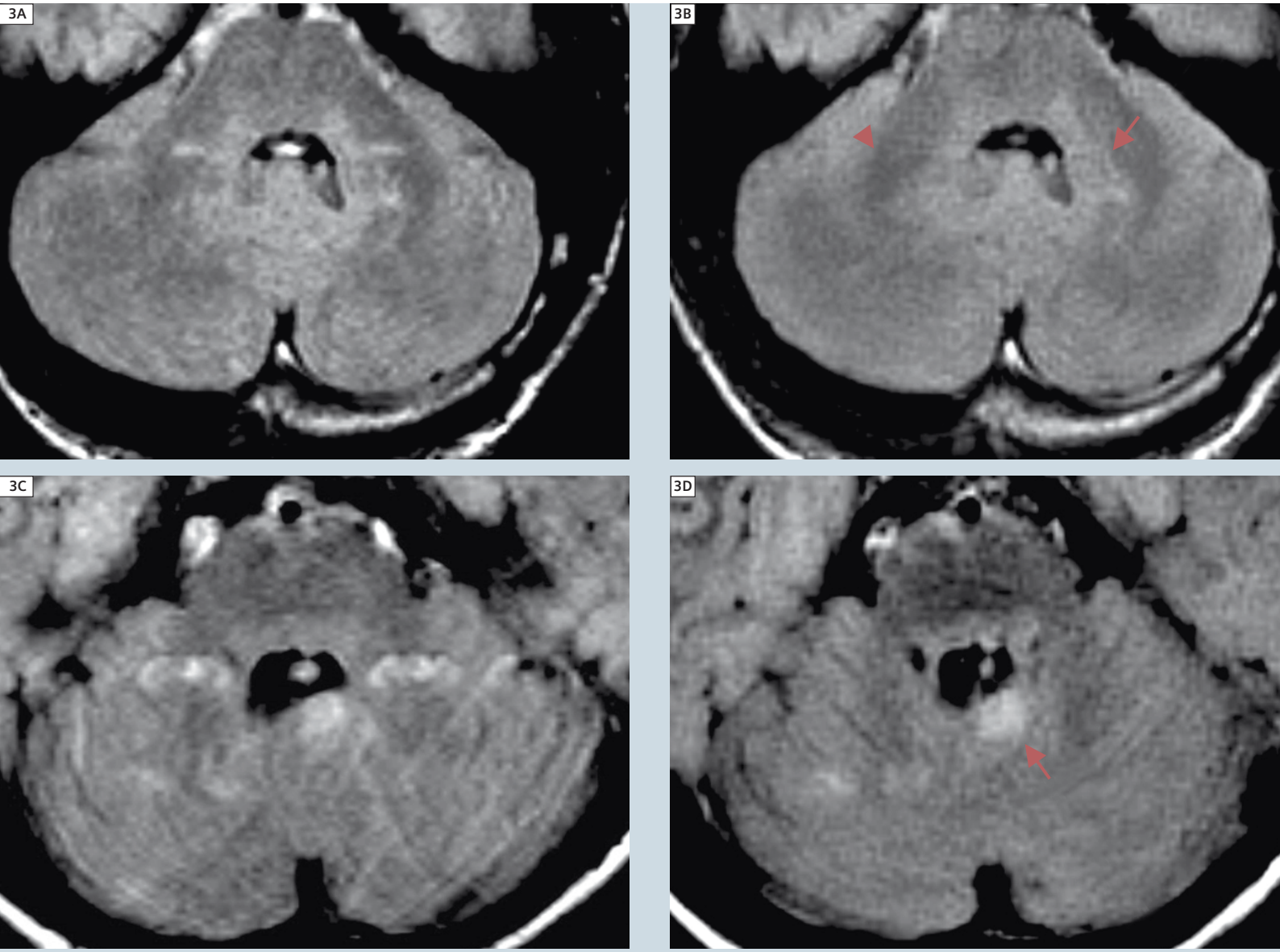

3 T2w FLAIR images of the posterior fossa of two different patients. Rectilinear k-space coverage (left), BLADE (right). Lesions typical of neurofibromatosis type 1: low contrast confluent (arrowhead), high contrast round (arrow). Artifacts and lesions not reliably distinguishable in conventional images (left).

rectilinear k-space covering. As the children were encouraged not to move during the examination, there were only moderate to minor movement artifacts even in conventional T2w FLAIR images. Pulsation artifacts were more frequent and more severe in conventional images and sometimes also present in BLADE images. Ratings of subtle movement artifacts in conventional images and subtle pulsation artifacts in BLADE images led to an only fair interobserver agreement (Cohen's kappa < 0.4, Table 2). These artifacts did not disturb the depiction of lesions.

There was good observer agreement (Cohen's kappa 0.74, Table 2) that artifacts compromised the assessment of lesions more often and more severely in conventional T2w FLAIR images than in BLADE images. In 6 of all 26 patients (23%) observers agreed that in conventional T2w FLAIR images they could not differentiate lesions from artifacts in the posterior fossa, rendering nearly a fourth of the examinations with conventional k-space trajectory inadequate for a reliable diagnosis. In none of the BLADE sequences more than one observer considered artifacts and lesions to be indistinguishable (Fig. 3).

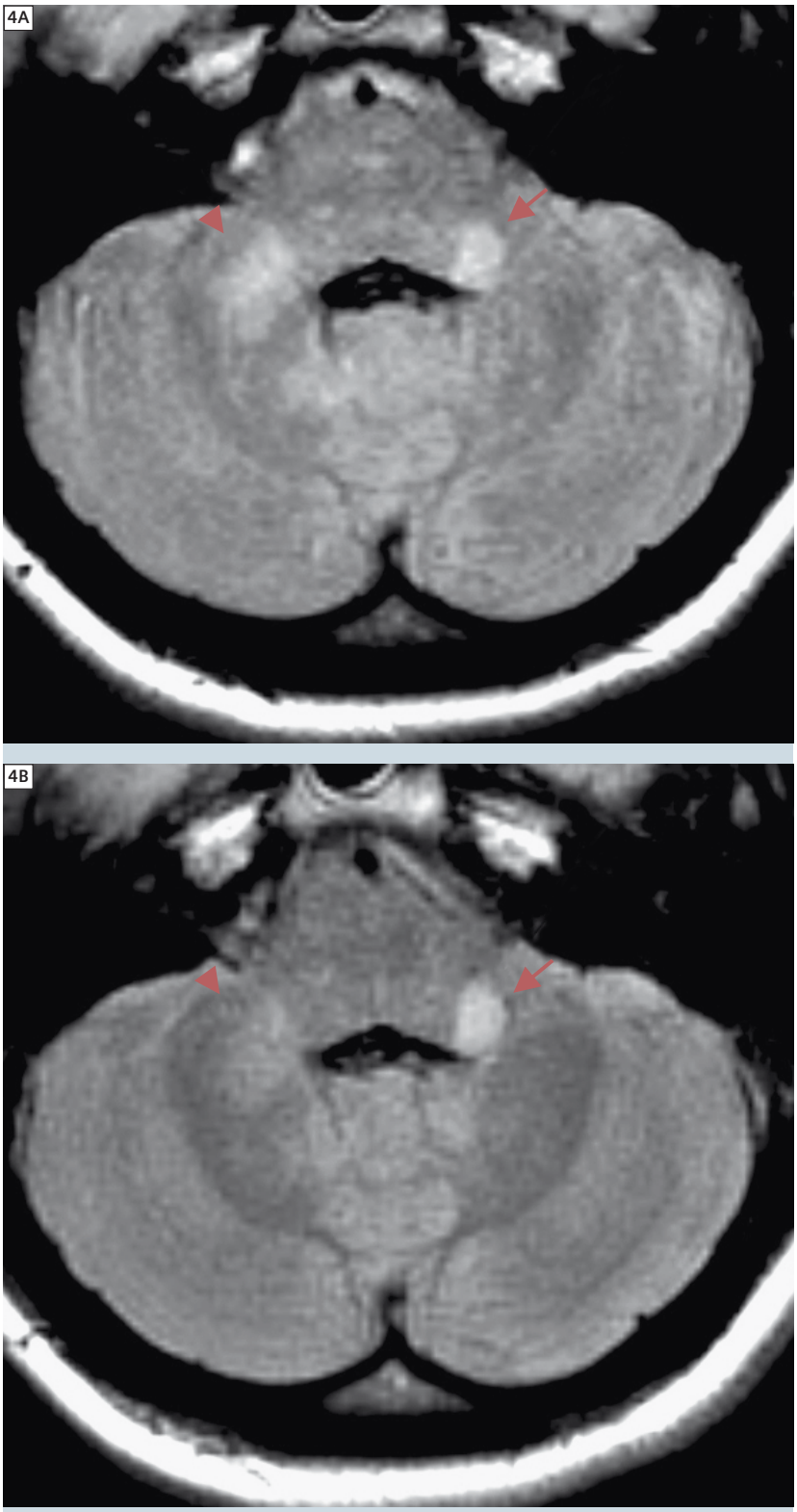

4 Absence of major artifacts and comparable visibility of lesions in images of both techniques (T2w FLAIR: rectilinear k-space top, BLADE bottom), low contrast confluent (arrowhead), high contrast round (arrow).

As Gill et al. reported for their sample [12], most hyperintense lesions in the thalami, brain stem and cerebellum were confluent or diffuse with poorly defined edges. A smaller number of lesions were well circumscribed with edges that were distinct from the adjacent normal tissue. Mean ratios of signal intensities were only slightly lower in the posterior fossa than in cerebrum and midbrain.

If lesions were not obscured by artifacts, visibility of lesions with both clearly and poorly defined edges appeared to be comparable in images of both techniques (Fig. 4). Observers' comparisons of both imaging techniques according to contrast and edge definition did not reveal consistently significant differences for lesions of the posterior fossa (Table 2). There only was a tendency to better edge definition in BLADE images. Visibility of lesions also was independent of size. Even the smallest lesions of our sample (2–3 mm) were equally depicted by both techniques.

BLADE technique is based on standard image acquisition techniques and therefore has the advantage of providing image characteristics equal to standard sequences. As an alternative to *syngo* BLADE imaging, pulsation artifacts may be identified by a second data acquisition after changing the phase encoding direction [1] or the slice orientation, with the disadvantage of a longer examination time and the higher risk of movement artifacts. Reduction of motion artifacts in non-sedated children can also be achieved by rapid sequences (e.g. single shot techniques) which, in neuroimaging, have the disadvantages of a poorer differentiation of gray and white matter [3, 10,14] and a lower spatial resolution [15].

Observers of our study had the subjective impression that the appearance of FLAIR BLADE images differed slightly from that of conventional images which did not impair image quality and lesion detectability (Figs. 3 and 4). These subtle differences have already been reported for PROPELLER technique [2]. BLADE images might therefore be identified by experienced radiologists despite "blinding". We have, however, not identified bias due to this fact in our study.
In our study, data acquisition time and image reconstruction time together were approximately 2–3 minutes longer for *syngo* BLADE sequences than for conventional FLAIR sequences. The advantage of artifact reduction by the BLADE technique clearly outweighed the prolonged duration.
There are limitations of our retrospective study: We were not able to measure the degree of patients' movements. Therefore, like other investigators [2, 4, 9], we can only assume that these parameters were similar in statistical mean throughout the examination. As both sequences were performed successively, pulsation and flow artifacts were also assumed as unchanged for both acquisitions. For our retrospective analysis we had to accept that in addition to the k-space trajectory some of the parameters of both sequences were not identical. As the BLADE technique benefits from long echo trains, a turbo factor had been chosen that was larger than that of our routine T2w FLAIR sequence. However, a change of these parameters would have had only minor influence on motion artefacts, and presumably would not have changed the quality of results. Prospective studies of a larger patient group could avoid these shortcomings.

Conclusion

BLADE technique reduces movement and pulsation artifacts in T2w FLAIR images without relevant loss of image quality. It therefore markedly improves depiction of small and low contrast brain lesions in children in the posterior fossa of pediatric patients. This can be crucial especially in patients after surgery of malignant brain tumors. In the absence of major artifacts lesions of all sizes were depicted in comparable quality by both techniques.

References

1 Böck JC, Neumann K, Sander B, Schmidt D, Schörner W (1991) Prepontine artifacts due to pulsation of cerebrospinal fluid in T_2-weighted coronal MRI. Clinical relevance, incidence and a technique for efficient artefact suppression. RoeFo 154: 202-205.
2 Forbes KP, Pipe JG, Bird CR, Heiserman JE (2001) PROPELLER MRI: Clinical testing of a novel technique for quantification and compensation of head motion. J Magn Reson Imaging 14: 215-222.
3 Penzkofer AK, Pfluger T, Pochmann Y, Meissner O, Leisinger G (2002) MR imaging of the brain in pediatric patients: Diagnostic value of HASTE sequences. AJR 179: 509-514.
4 Alibek S, Adamietz B, Cavallaro A, Stemmer A, Anders K, Kramer M, Bautz W, Staatz G (2008) Contrast-enhanced T1-weighted fluid-attenuated inversion-recovery BLADE Magnetic Resonance Imaging of the brain: An alternative to spin-echo technique for detection of brain lesions in the unsedated pediatric patient? Acad Radiol 15: 986-995.
5 Von Kalle T, Blank B, Fabig-Moritz C, Müller-Abt P, Zieger M, Wohlfarth K, Winkler P (2009) reduced artefacts and improved assessment of hyperintense brain lesions with BLADE MR imaging in patients with neurofibromatosis type 1. Pediatr Radiol 39: 1216-1222.
Kallmes DF, Hui FK, Mugler JP III (2001) Suppression of cerebrospinal fluid and blood flow artifacts in FLAIR MR imaging with a single-slab three-dimensional pulse sequence: Initial experience. Radiographics 221: 251-255.
6 Naganawa S, Satake H, Iwano S, Kawai H, Kubota S, Komada T, Kawamura M, Sakurai Y, Fukatsu H (2008) Contrast-enhanced MR imaging of the brain using T1-weighted FLAIR with BLADE compared with a conventional spin-echo sequence. Eur Radiol 18: 337-342.
7 Forbes KP, Pipe JG, Karis JP, Heiserman JE (2002) Improved image quality and detection of acute cerebral infarction with PROPELLER diffusion-weighted MR imaging. Radiology 225:551-555.
8 Wintersperger BJ, Runge VM, Biswas J, Nelson CB, Stemmer A, Simonetta AB, Reiser MF, Naul LG, Schoenberg SO (2006) Brain magnetic resonance imaging at 3 Tesla using BLADE compared with standard rectilinear data sampling. Invest Radio 41: 586-592.
9 Forbes KP, Pipe JG, Karis JP, Farthing V, Heiserman JE (2003) Brain imaging in the unsedated pediatric patient: Comparison of periodically rotated overlapping parallel lines with enhanced reconstruction and single-shot fast spin-echo sequences. AJNR 24: 794-798.
10 Pipe JG (1999) Motion correction with PROPELLER MRI: Application to head motion and free-breathing cardiac imaging. Magn Reson Med 42: 963-969.
11 Gill DS, Hyman SL, Steinberg A, North KN (2006): Age-related findings on MRI in neurofibromatosis type 1. Pediatr Radiol 36: 1048-1056.
12 Maclaren JR, Bones PJ, Millane RP, Watts R (2008) MRI with TRELLIS: a novel approach to motion correction. Magn Res Imaging 26: 474-483.
13 Iskandar BJ, Sansone JM, Medow J, Rowley HA (2004) The use of quick-brain magnetic resonance imaging in the evaluation of shunt-treated hydrocephalus. J Neurosurg (Pediatrics 2) 101: 147-151.
14 Ba-Ssalamah A, Schick S, Heimberger K, Linnau KF, Schibany N, Prokesch R, Trattnig S (2000) Ultrafast magnetic resonance imaging of the brain. Magn Reson Imaging 18: 237-43.

Contact
Thekla v. Kalle, M.D.
Department of Pediatric Radiology
Olgahospital Klinikum Stuttgart
Bismarckstr. 8
70176 Stuttgart
Germany
Phone: +49 (0) 711/ 278-04
t.vonkalle@klinikum-stuttgart.de
www.klinikum-stuttgart.de

Case Report:
Brain Spectroscopic Imaging at 3T with the 32-Channel Phased-Array Head Coil

Ovidiu C. Andronesi[1]; Dominique Jennings[1]; Nouha Salibi[2]; A. Gregory Sorensen[1]

[1]Athinoula A. Martinos Center for Biomedical Imaging, Department of Radiology, Massachusetts General Hospital, Boston, MA, USA
[2]Siemens Medical Solutions USA, Charlestown, MA, USA

Introduction

The newly developed 32-channel phased-array head coil [1, 2] has shown clear advantages for high resolution imaging, functional MRI (fMRI), perfusion and diffusion imaging of brain [3]. Known for its low intrinsic sensitivity, MR spectroscopic imaging (MRSI, also named chemical shift imaging or CSI [4]) is an obvious application that can benefit from the increased signal-to-noise ratio (SNR) provided by the 32-channel technology. Increased SNR will improve the current performance and reliability of MRSI, which will help in the realization of its full clinical potential. MRSI can study a wealth of in vivo metabolic processes that are complementary to the information derived from water imaging. However, obtaining clinically beneficial MRSI data is challenged by the much lower metabolite concentration compared to water, which in turn often imposes long scanning times.
Here we present brain MRSI data from a volunteer and from a brain tumor patient acquired at 3T with the standard 12-channel Head Matrix coil and with the recently released 32-channel phased-array head coil. The SNR of the 32-channel coil can be flexibly traded for reduced scan time and/or increased resolution of MRSI, or it can be used to improve the accuracy and reliability of spectral data.

Methods

All measurements were conducted on the same whole body 3T scanner (MAGNETOM Trio, A Tim System, Siemens, Erlangen) using similar MRSI/MRI protocols. One healthy volunteer and one high-grade glioma patient were studied after informed consent approved by IRB protocols at our institution.
For both subjects, one high resolution 3D structural scan (0.9 mm isotropic) was acquired with a multi-echo MPRAGE (MEMPRAGE) [5, 6] sequence (TR = 2.5 s, TI = 1.2 s, TE1/TE2/TE3/TE4 = 1.59/3.19/4.79/6.39 ms, FA = 7°, NA = 1) to identify the anatomy and position the volume of interest (VOI) for the CSI measurement. In the case of the glioma patient a single dose of Gd-DTPA (Magnevist) was bolus injected before the MEMPRAGE. In order to ensure the same CSI slice prescription when changing coils, an AutoAlign scout [7] was run prior to the spectroscopy measurement. The 2D CSI slice position was approximately at the same level from the skull base for the volunteer and for the patient. In both subjects the VOI could be positioned roughly in the center of the reference MEMPRAGE image. The hybrid 2D CSI protocol consisted of a PRESS [8] pre-selected VOI surrounded by 8 outer volume saturation bands (OVS) [9, 10] placed around the skull for lipid suppression. The WET (Water Enhanced Through T1 Effects) [1] method was used for water suppression (30 Hz bandwidth). Acquisition parameters were common for both subjects: FOV of 200 x 200 x 15 mm^3, VOI 80 x 80 x 15 mm^3, weighted elliptical phase encoding (16 x 16 matrix size yielding a voxel size of 12.5 x 12.5 x 15 mm^3), TR = 1.5 s, TE = 30 ms, NA = 4 (TA = 7:12 min), 1250 Hz bandwidth and 1024 points for the time-domain.
In addition, in the volunteer case two more 2D CSI data sets were recorded when using the 32-channel coil:
1) having the same resolution (16 x 16 matrix) and NA = 2 (TA = 4:45 min), and
2) increasing the resolution (20 x 20 matrix) and NA = 1 (TA = 6:26 min).

During data processing the data were interpolated to a 32 x 32 matrix. Processing included: k-space Fourier transformation and a spatial 50 Hz Hanning filter, subtraction of the residual water signal, time domain 1 Hz exponential apodization, zero filling to 2048 points, Fourier transformation of the time domain signals, frequency shift correction as well as phase correction and baseline correction. Data were quantified either with the fitting routine from *syngo* MR B15A or exported to jMRUI3.0 software [12] and fitted using the AMARES algorithm with soft constraints [13]. Shimming of the unsuppressed water signal from the VOI was performed with each coil until similar T2* (45 ms) and linewidth (9 Hz) values were obtained for both subjects to achieve similar spectral quality. However, in the case of the 32-channel coil convergence towards the optimal shim was slower and the shim values were higher suggesting either a slight increase in the distortion of the main magnetic field homogeneity (possibly due to the more compact geometry compared to the 12-channel coil), or an influence on the shimming algorithm of the less uniform receive profile for the 32-channel coil.

Volunteer results

The need for averaging due to low SNR represents one of the main reasons for the increased scanning times in MRSI. To demonstrate the SNR gain of the 32-channel coil and how this can be traded to reduce scan time and/or increase resolution, three different protocols were compared on an adult (40 years age) healthy volunteer:
1) NA = 4, 16 x 16 weighted elliptical phase encode matrix (TA = 7:12 min);
2) NA = 2, 16 x 16 weighted elliptical phase encode matrix (TA = 4:45 min);
3) NA = 1, 20 x 20 weighted elliptical phase encode matrix (TA = 6:26 min).
The reference scan obtained with the 12-channel Head Matrix coil was acquired using the first protocol and the parameters described in the methods section.
Protocols 1 and 2 produced similar SNR with the 32-channel coil, resulting in an average gain of 3–4 times across all voxels and all metabolites compared to the reference CSI acquired with the 12-channel Head Matrix coil. A somewhat smaller SNR gain of 2–3 folds was obtained with protocol 3. Figure 1 shows examples of the 2D-CSI data acquired following protocol 2 for 32-channel coils (Figs. 1A, B) and protocol 1 for 12-channel Head Matrix (Figs. 1C, D). The spectra are scaled to the same intensity (vertical axis) and frequency (horizontal axis) ranges. Enlarged views of spectra from the voxels highlighted in red are shown in figures 1A and 1C.

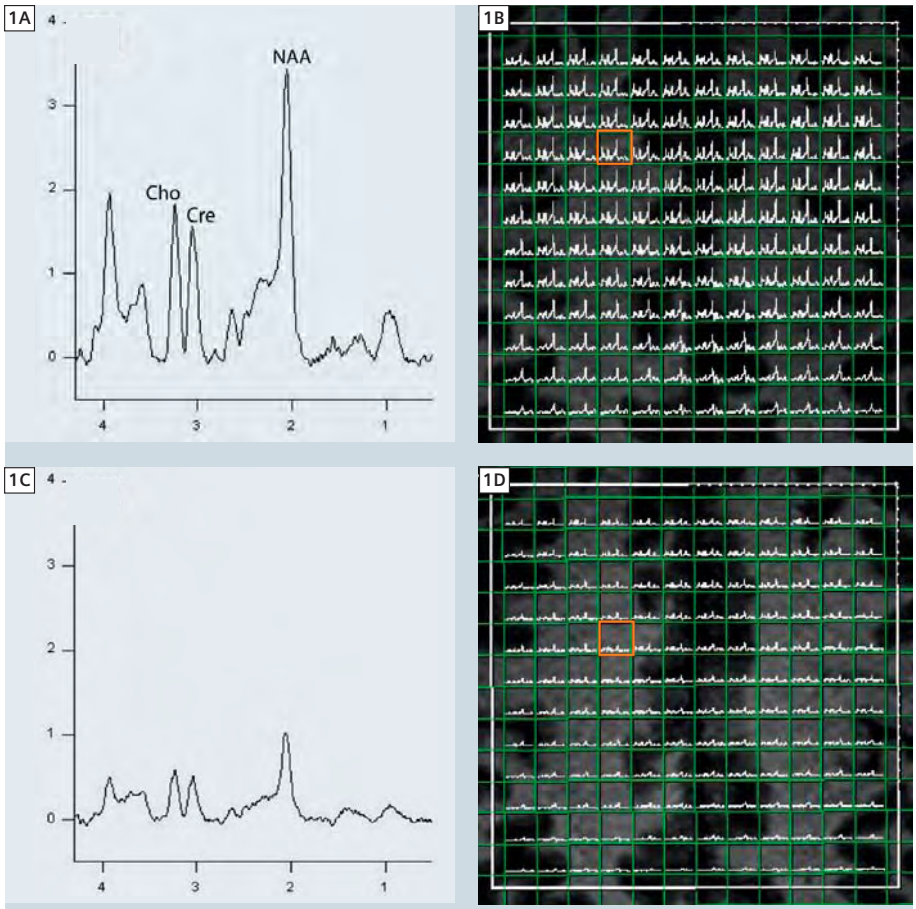

1 CSI data sets from a healthy volunteer acquired with the 32-channel phased-array head coil (upper row, NA = 2, TA = 4:45 min) and with the 12-channel Head Matrix coil (lower row, NA = 4, TA = 7:12 min). The spectra shown in 1A and 1C originate from the voxels highlighted in red in the CSI matrix (1B and 1D, respectively).

Patient results

One young patient (24 years age) with a recurrent high-grade glioma enrolled in a phase II study of a new antiangiogenic drug was imaged with structural, perfusion and diffusion-weighted imaging [14] which were followed by 2D CSI. All data were obtained within the same visit after 1 day of treatment. All the necessary data were first collected using the 32-channel coil. After switching to the 12-channel coil only the AAscout, MEMPRAGE and the CSI protocols where repeated, adding in total an extra 15 minutes to the scan time, including the time needed for changing coils. No extra Gd-DTPA dose was injected. For consistency with the previous visits, the 2D CSI measurement with the 32-channel coil was performed with the protocol 1 (NA= 4, TA = 7:12 min). The same protocol was also employed with the 12-channel Head Matrix coil.

The patient results of Figure 2 demonstrate a 3–4 fold increase in SNR with the 32-channel coil, which is similar to the increase in SNR observed in the volunteer data. The spectra are scaled to the same intensity and frequency range. The data in the upper (lower) row are obtained with the 32(12)-channel coil. Examples of tumor (Figs. 2A, D) and healthy (Figs. 2B, E) brain spectra are shown from the highlighted voxels (red

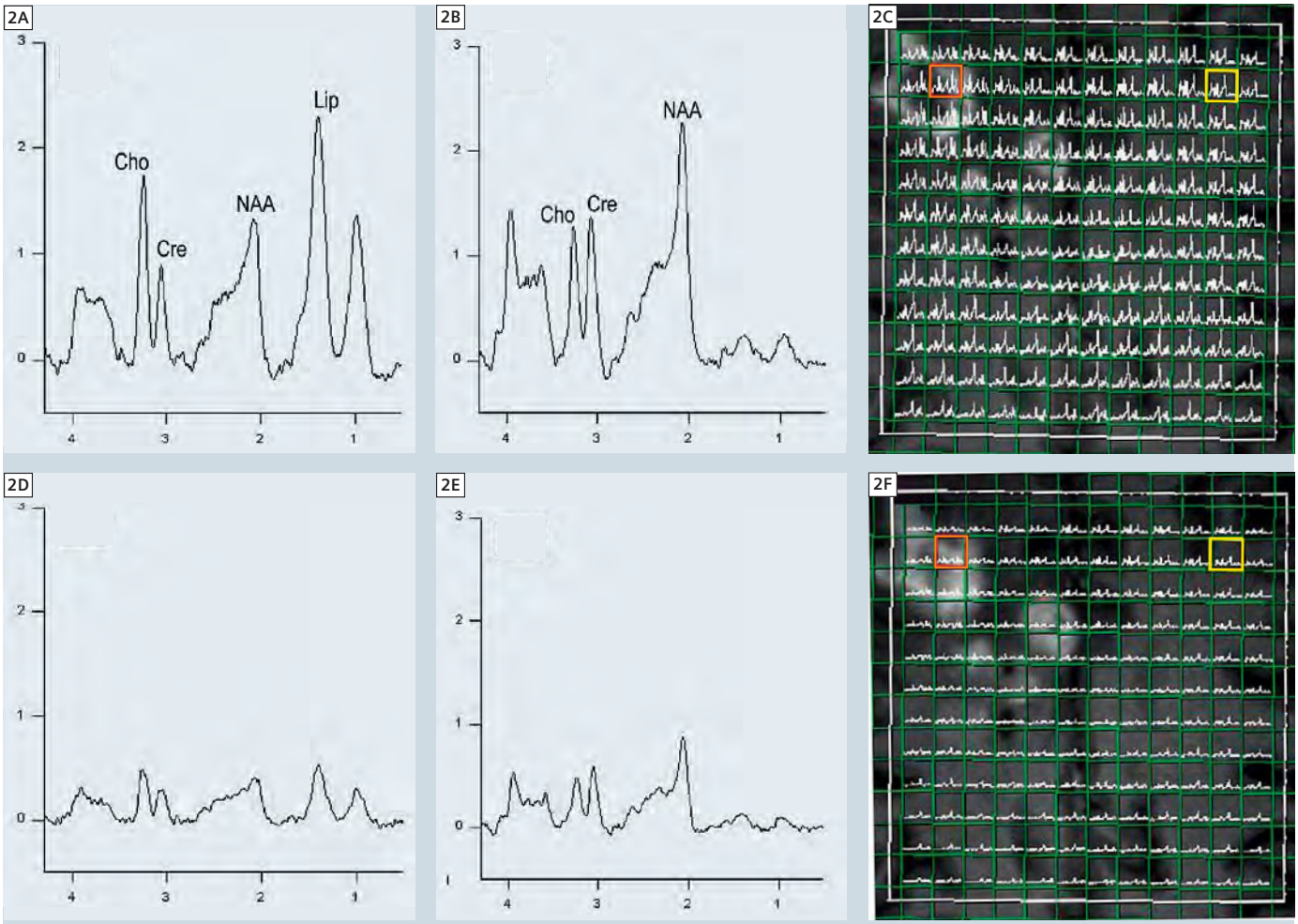

2 CSI data sets from a high-grade glioma patient acquired with the 32-channel phased-array head coil (2A–C) and with the 12-channel Head Matrix coil (2D–F). The same protocol with TR = 1.5 s, TE = 30 ms, NA = 4, TA = 7:12 min was employed. Tumor spectra are shown in 2A and 2D, originating from the red highlighted voxels (2C and 2F, respectively). Spectra of the healthy contra-lateral side are presented in 2B and 2E (yellow voxels in 2C and 2F, respectively).

and yellow, respectively) in the corresponding 2D CSI data matrix (Figs. 2C, F). A large contribution from lipid signal is found in the tumor. The particular position of the tumor in the anterior part of the VOI reduces the possibility of contamination with lipid signal from the skull due to the direction of the chemical shift error displacement from posterior to anterior (i.e. posterior voxels are more likely to be contaminated with lipid signal from skull). A close inspection of the voxels inside and outside the VOI reveals reduced lipid signals outside the VOI. The highest lipid signals are within the lesion; it was concluded that a lipid metabolite map can be reliably computed as demonstrated in figures 3B and 3E. As evident from spectra of Figs. 2A and D the tumor is characterized also by decreased NAA and increased Cho levels, confirming together with the lipids findings a high-grade glioma [15, 16]. A Cho/NAA map was calculated and overlaid on the Gd-DTPA enhanced image. Figure 3 shows the corresponding Cho/NAA maps (Figs. 3A, D), lipid maps (Figs. 3B, E) and post-Gd MEMPRAGE reference image (Figs. 3C, F), where the upper (lower) row data are obtained with the 32(12)-channel coil.

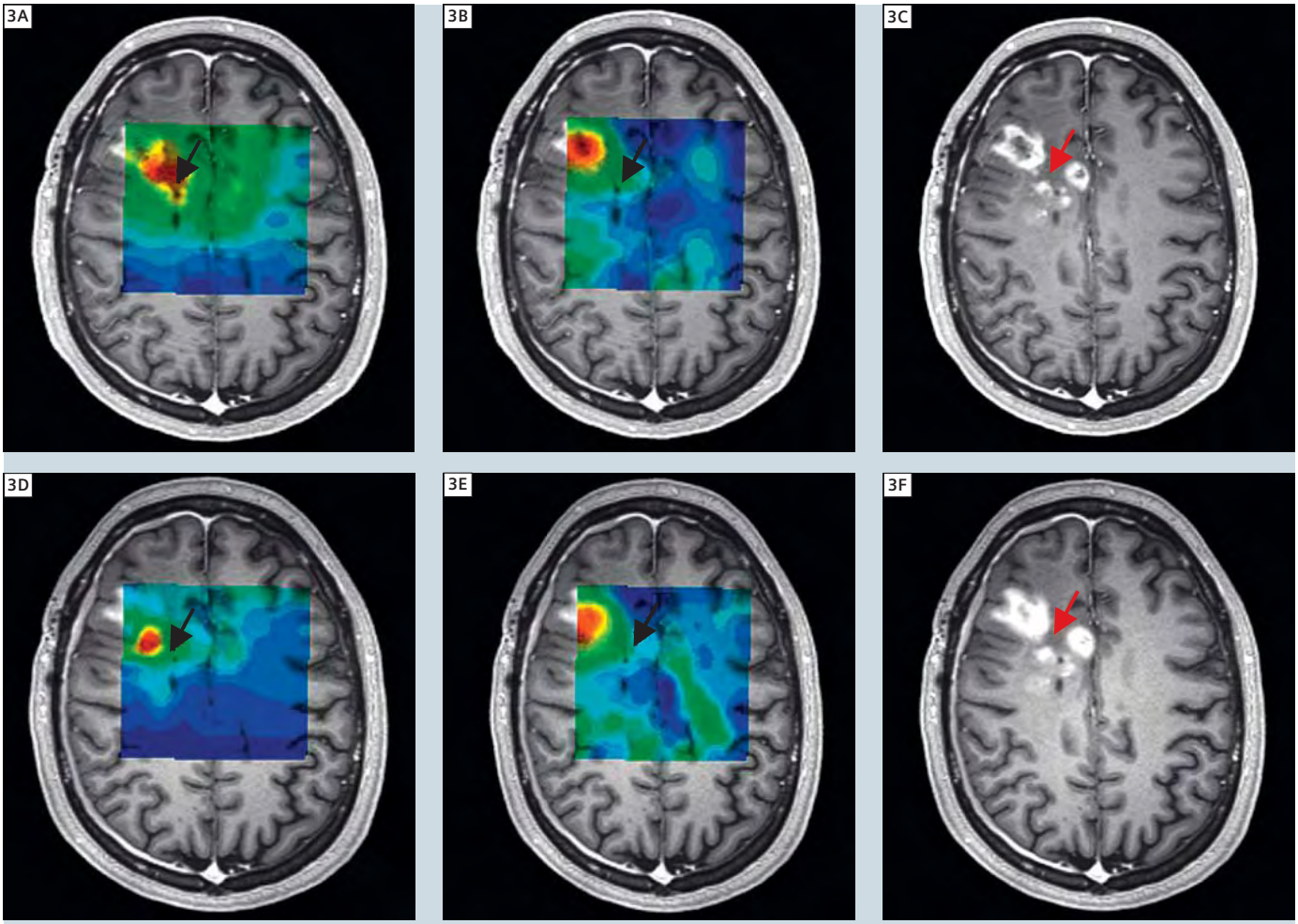

3 Metabolite maps and Gd-DTPA enhanced images for a high-grade glioma patient obtained using the 32-channel phased-array head coil (upper row) and the 12-channel Head Matrix coil (lower row). Cho/NAA maps are computed in 3A, D and lipid maps in 3B, E. The black arrows (3A, B, D, E) indicate areas where the 32-channel coil detects changes more reliable than the 12-channel coil. The red arrows (3C, F) point to the region of decreased intensity among the three main Gd enhancing lesions.

The maps obtained with the 32-channel phased-array head coil (Figs. 3A, B) have a better coverage of the extent of the lesion probed by the Gd image (Fig. 3C) as indicated by the black arrows. Interestingly the lipid map (Fig. 3B) overlaps well over the largest Gd enhancing lesion, while the increase of Cho/NAA ratio (Fig. 3A) seems to be more confined to the space among the three main Gd enhancing lesions, which corresponds to a region of reduced intensity in the MEMPRAGE image (Figs. 3C, F, red arrows) as compared to the contra-lateral normal side. However the extent of the Cho/NAA is better defined than the region of reduced intensity, possibly pointing to the most active part of the tumor that needs to be followed during the course of the treatment.

Conclusion

Data obtained from a healthy volunteer and from a patient with glioma indicate that CSI measurements with the 32-channel phased-array head coil can reduce by half the acquisition time (number of averages) while maintaining a 3–4 times gain in SNR compared to the 12-channel Head Matrix coil. SNR gain is also possible when simultaneously increasing the spatial resolution (with a larger phase encoding matrix) and reducing the scan time (number of averages).

Clinical benefits are demonstrated in the patient data, which show that possible hot spots of the tumors can be more reliably identified. Metabolite maps of the 32-channel coil conform better to the Gd enhancing lesions and the peritumoral regions.

The advantages reported here with the use of a 32-channel coil in the evaluation of tumors are also relevant to other brain spectroscopy applications including stroke, psychiatric or neurodegenerative diseases. The improved SNR and reliability, and the shorter scan times are likely to increase the clinical use of MR spectroscopy. They will also have considerable impact on the development of functional (dynamic) MR spectroscopy [17] and its clinical applications. Besides reducing scan times, increasing resolution and improving accuracy, innovative ideas could utilize image encoding with the geometry of large phased arrays coils [1]; latter could then improve the chemical shift displacement error that still hampers MRSI signal localization using slice selective excitation and gradient encoding.

Acknowledgements

I would like to thank Michael Hamm and Josef Pfeuffer from Siemens Medical Solutions USA Inc. for their assistance during this project.

References

1 Wald LL, Wiggins G. Highly parallel detection for MRI. MAGNETOM Flash 2008;38(1):34–44.
2 Stapf J. 32-Channel phased-array head coil. MAGNETOM Flash 2008;38(1):45.
3 Runge VM. 32-Channel head coil imaging at 3T Case Reports from Scott and White Clinic and Hospital. MAGNETOM Flash 2008;39(2):38–42.
4 Brown TR, Kincaid BM, Ugurbil K. NMR Chemical-Shift Imaging in 3 Dimensions. Proceedings of the National Academy of Sciences of the United States of America-Biological Sciences 1982;79(11):3523–3526.
5 Mugler JP, Brookeman JR. 3-Dimensional Magnetization-Prepared Rapid Gradient-Echo Imaging (3D MPRAGE). Magnetic Resonance in Medicine 1990;15(1):152–157.
6 van der Kouwe AJW, Benner T, Salat DH, Fischl B. Brain morphometry with multiecho MPRAGE. Neuroimage 2008;40(2):559–569.
7 van der Kouwe AJW, Benner T, Fischl B, et al. On-line automatic slice positioning for brain MR imaging. Neuroimage 2005;27(1):222–230.
8 Bottomley PA. Spatial Localization in NMR-Spectroscopy Invivo. Annals of the New York Academy of Sciences 1987;508:333–348.
9 Moonen CTW, Sobering G, Vanzijl PCM, Gillen J, Vonkienlin M, Bizzi A. Proton Spectroscopic Imaging of Human Brain. Journal of Magnetic Resonance 1992;98(3):556–575.
10 Duyn JH, Gillen J, Sobering G, Vanzijl PCM, Moonen CTW. Multisection Proton MR Spectroscopic Imaging of the Brain. Radiology 1993;188(1):277–282.
11 Ogg RJ, Kingsley PB, Taylor JS. WET, a T-1-Insensitive and B-1-Insensitive Water-Suppression Method for in-Vivo Localized H-1-NMR Spectroscopy. Journal of Magnetic Resonance Series B 1994;104(1):1–10.
12 Naressi A, Couturier C, Devos JM, et al. Java-based graphical user interface for the MRUI quantitation package. Magnetic Resonance Materials in Physics Biology and Medicine 2001;12(2–3):141–152.
13 Vanhamme L, van den Boogaart A, Van Huffel S. Improved method for accurate and efficient quantification of MRS data with use of prior knowledge. Journal of Magnetic Resonance 1997;129(1):35–43.
14 Batchelor TT, Sorensen AG, di Tomaso E, et al. AZD2171, a pan-VEGF receptor tyrosine kinase inhibitor, normalizes tumor vasculature and alleviates edema in glioblastoma patients. Cancer Cell 2007;11(1):83–95.
15 Griffin JL, Shockcor JP. Metabolic profiles of cancer cells. Nature Reviews Cancer 2004;4(7):551–561.
16 Hakumaki JM, Poptani H, Sandmair AM, Yla-Herttuala S, Kauppinen RA. H-1 MRS detects poly-unsaturated fatty acid accumulation during gene therapy of glioma: Implications for the in vivo detection of apoptosis. Nature Medicine 1999;5(11):1323–1327.
17 Ross B, Lin A, Harris K, Bhattacharya P, Schweinsburg B. Clinical experience with C–13 MRS in vivo. Nmr in Biomedicine 2003;16(6–7): 358–369.

Contact
Ovidiu C. Andronesi
Athinoula A. Martinos Center
for Biomedical Imaging
Department of Radiology
Massachusetts General Hospital
Boston, MA, 02114
USA
ovidiu@nmr.harvard.edu

Relevant clinical information at your fingertips

From technology to clinical applications, you will find all the latest news on Siemens MR at

www.siemens.com/magnetom-world

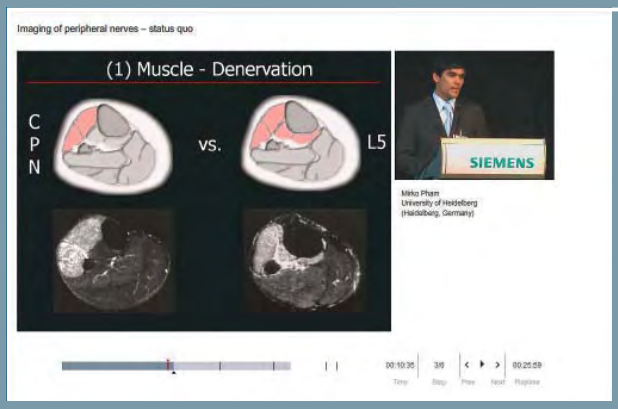

Don't miss the talks of international experts on Magnetic Resonance Imaging.

Go to
Education > e-trainings & Presentations

The Centerpiece of the MAGNETOM World Internet platform consists of our users' clinical results. Here you will find case reports and clinical methods.

Go to
Clinical Corner > Case Studies

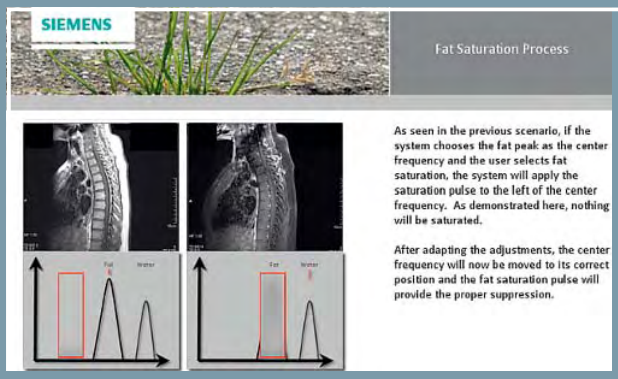

Just a mouse click away you will find application videos and useful tips allowing you to optimize your daily MR examinations.

Go to
Clinical Corner > Application Tips

For the whole range of clinical MR information visit us at

www.siemens.com/magnetom-world

3T MRI in Pediatrics: Challenges and Clinical Applications

Charuta Dagia; Michael Ditchfield, M.D.

Department of Medical Imaging, The Royal Children's Hospital & Murdoch Children's Research Institute Melbourne, Australia

Reprinted from European Journal of Radiology, 68 (2008) 309–319, with permission from Elsevier.

1. Introduction

The primary reason for increasing the magnetic field strength in magnetic resonance imaging (MRI) is to take advantage of the linear relationship between field strength and the signal-to-noise ratio (SNR). By increasing the signal that is obtained in MRI there is improvement in either the spatial or temporal resolution or both [1–4]. In pediatrics* there are a number of unique challenges which improved spatial and/or temporal resolution assist in overcoming. The challenges of high field MRI remain relevant in the pediatric setting. These include the altered T1 contrast, artefacts and safety issues, including specific absorption rate (SAR). These challenges also create opportunities with improvement in MR angiography (MRA), arterial spin labelling (*syngo* ASL), functional MRI (fMRI), susceptibility-weighted imaging (*syngo* SWI), and MR spectroscopy (MRS), all of which have distinctive applications in pediatrics.

This review will try to address basic considerations for pediatric 3T MR imaging, list the frequent and potential future applications, and discuss the challenges and restrictions.

2. What are the challenges of imaging children?

The four main challenges in imaging children are: (1) anatomical challenges, (2) developmental issues, (3) physiological challenges and (4) behavioural challenges.

2.1. Anatomical challenges

In children, normal structures are smaller than in adults. However, we often forget how small they are compared to the average adult. An average term neonate weighs 3.5 kg, with brain 25% of the adult size [5]. A premature neonate at 24 weeks gestation may weigh as little as 0.5 kg, with a very small brain. Other anatomical structures that we image such as the inner ear, cranial nerves, brachial plexus, biliary tree, peripheral joints and blood vessels are very small in children. The improved SNR at higher field strength allows the acquisition of thinner slices and improved spatial detail of these structures.

2.2. Developmental issues

With development and maturation, in addition to growth, there are changes in the appearance of many structures. This is especially true for the brain, bones and cartilage. The brain sulcation and myelination of the white matter tracts develop rapidly in the neonatal period, the changes being more dramatic in the premature (Fig. 1A and B). In the joints, with maturation there is conversion of the epiphyseal and apophyseal cartilage to bone. These changes are better visualised with improved spatial resolution as the structures involved are often small and the changes subtle.

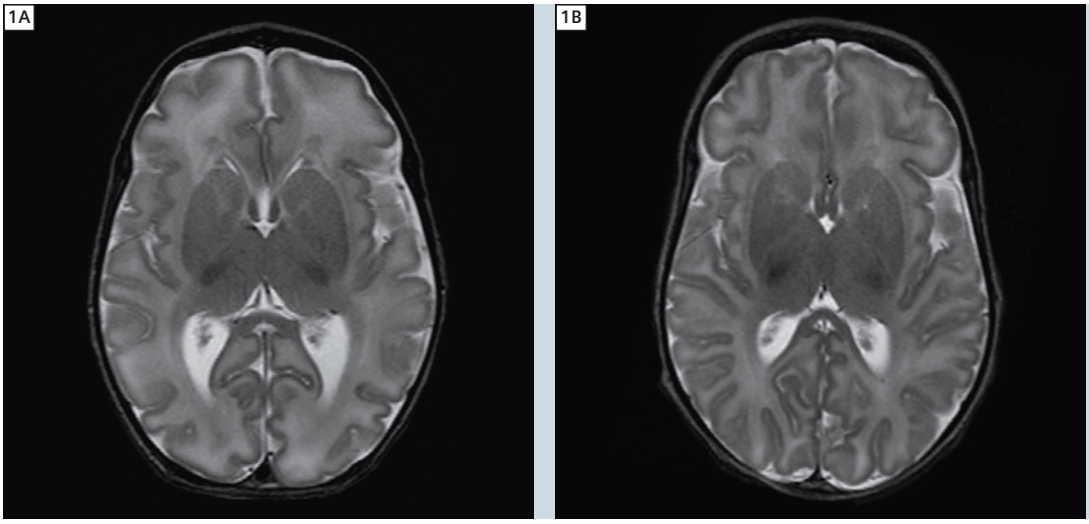

1 Axial T2 images from serial 3T MRI brain studies of a premature infant (34 weeks gestation) obtained 7 days **(A)** and 6 weeks **(B)** after birth demonstrate temporal maturation of the sulcal pattern, and progressive myelination in the posterior limbs of internal capsules and ventro-lateral thalami.

*The safety of imaging fetuses / infants has not been established.

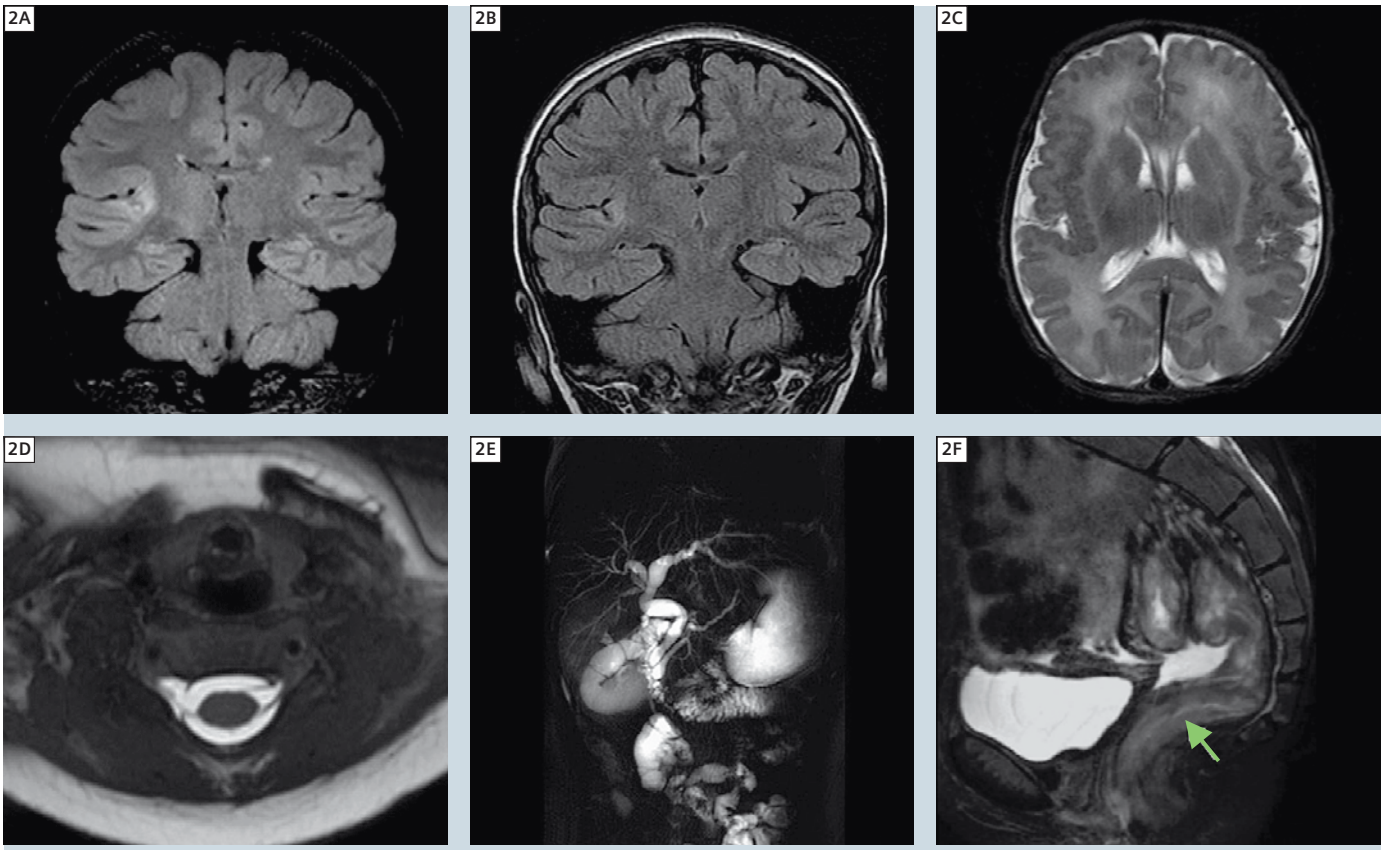

2 Histologically confirmed cortical dysplasia: coronal T2 FLAIR images from MRI brain study performed at 3T **(A)** demonstrates ill-defined increased signal in the right insular cortex and adjacent white matter, much better appreciated than on **(B)** the earlier study performed at 1.5T, **(C)** axial T2 image of a term neonate with polymicrogyria, **(D)** axial T2 TrueFISP MRI of the cervical spine in a 3-month-infant demonstrates avulsed right C6 ventral nerve root and traumatic pseudo-meningocoele due to obstetric brachial plexus palsy, **(E)** MRCP of a patient with a choledochocele and **(F)** sagittal T2 TSE images demonstrate recto-sigmoid wall oedema and thickening due to inflammatory bowel disease.

2.3. Physiological challenges

In children the blood flow, pulse and respiratory rates are considerably faster. The normal heart rate in a neonate can be as high as 140/min, and the respiratory rate up to 40/min. Children are also unable to hold their breath satisfactorily until they are about 8 years of age [6]. These parameters are significant for cardiac, chest and abdominal imaging and benefit from the shorter scan times as a result of the improved temporal resolution.

2.4. Behavioural challenges

One of the greatest challenges in children is getting them to cooperate adequately for a diagnostic MRI study. Younger children usually require sedation or general anaesthesia for a successful scan. This involves some inherent risk, requires specialised staff, MR compatible anaesthetic and monitoring equipment. It is also slow and expensive [7]. The need for anaesthesia can be reduced by the use of bean bags, timing the scan with feeds and sleeping, education and practice sessions with dedicated educational play therapy staff, MRI toys and where possible a practice MRI unit [6]. The chance of these succeeding is greater if the scan times are shorter which can be achieved at higher field strength due to the improved temporal resolution.

3. How good is 3T at imaging children?

3.1. Can it do the basics?

With continuing hardware advances such as the availability of dedicated receiver coils, new pulse sequences and parallel imaging techniques, the 3T MRI unit can be used for imaging of all the organ systems evaluated on the 1.5T system [3,8]. Many pediatric MRI applications benefit from the increased signal at 3T (Fig. 2A–F; Table 1). Others, involving anatomic regions such as the heart, chest and abdomen are inherently prone to 3T artefacts, which must be controlled – these are discussed later in the article.

3.2. Is the SNR doubled?

The primary benefit of imaging at high field strength is the increased SNR. This is a direct consequence of the increase in MR signal resulting from greater number of protons aligned with the main magnetic field [2]. The signal increases four-fold when going from 1.5 to 3T. However, the noise is also doubled. So theoretically, the SNR should increase two-fold at 3T, when compared to 1.5T. However, this assumes fully relaxed T1

conditions and a constant bandwidth and flip angle [9].
The observed SNR gain is influenced by numerous factors including receiver coil design, B_0 and B_1 field homogeneity and radiofrequency (RF) flip angle limitations governed by increased RF power deposition [10]. In practice, in controlling for chemical shift, susceptibility and SAR at 3T, the bandwidth is usually increased and the flip angle reduced. In addition, at 3T the relaxation times are altered, and the T1 of tissues is longer [11,12]. If the TR is kept constant, there will be a reduction in SNR. Increasing the TR to compensate for the longer T1 will increase the acquisition time [2]. Therefore, the signal-to-noise gain is always less, (typically 1.7–1.8-fold), and this gain varies for different tissues [10,13].

3.3. How fast?

The improvement in SNR can be used to reduce the scan time. However, as discussed above, the observed SNR gain is less than two-fold, so it is not possible to image at twice the speed. Nevertheless, imaging is faster at 3T. In our practice this has not allowed us to reduce the need for general anaesthesia routinely at 3T. In isolated instances, however, this has been possible. However, it has allowed us to perform sequences more routinely than is possible at 1.5T, due to the inherently longer scan times. This has been particularly true for MR spectroscopy (MRS) [2], whole body MRI and diffusion-weighted imaging (*syngo* DWI), including diffusion tensor imaging (*syngo* DTI) and 3D imaging, including 3D dynamic vascular imaging – these are discussed in detail later.

3.4. What resolution can be achieved?

The SNR gain can also be used to increase spatial resolution. This has improved the imaging quality of small structures in children (Table 1).We have also been able to diagnose subtle abnormalities, which were earlier missed at

Table 1: Pediatric applications that benefit from the improved spatial and temporal resolution.

	Application	Examples of specific diseases
Neonate	All structures	
Nervous system	Brain Inner ear Cranial nerves Brachial plexus	Cortical dysplasia, migrational abnormalities Congenital sensory neural hearing loss Neuritis, e.g. bells palsy Birth trauma
Abdomen	Biliary tree	Sclerosing cholangitis, post liver transplant assessment
Musculoskeletal system	Small joints Polyarthropathy	Post reduction of dislocated hips in DDH, pre operative congenital deformity correction Haemophilia
MR angiography	Vasculitis Vascular malformations Congenital heart disease	Takayasu's arteritis, Moya Moya, Kawasakis disease Characterising type of vascular malformation Pulmonary arterial and aortic abnormalities, anomalous pulmonary venous return
Whole body MRI	Neoplasia Bone infarction Multifocal diseases Osteoporosis (compression fractures)	Neuroblastoma, lymphoma, leukaemia, ewings sarcoma Sickle cell disease, post chemotherapy and steroid therapy Chronic recurrent multifocal osteomyelitis, polymyositis Metabolic bone disease, steroid therapy

Table 2: How the opportunities of high field MRI can be applied in different organ systems.

Opportunity	Central nervous system	Musculoskeletal system	Cardiovascular system
SNR	Improved DWI, DTI, fMRI	Small joints, cartilage structure	Improved temporal resolution
Longer T1	Improved MRA	Improved MRA	Improved MRA, ASL, myocardial tagging
Susceptibility	Improved fMRI, SWI	Improved detection of calcification	Potential BOLD imaging
Chemical shift	Improved MRS	Improved MRS and fat saturation	Potential MRS

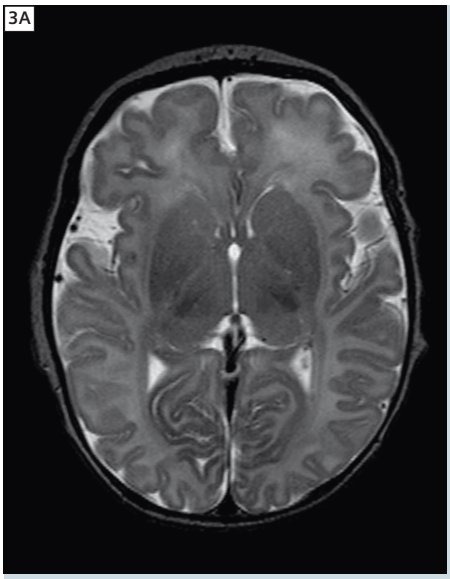

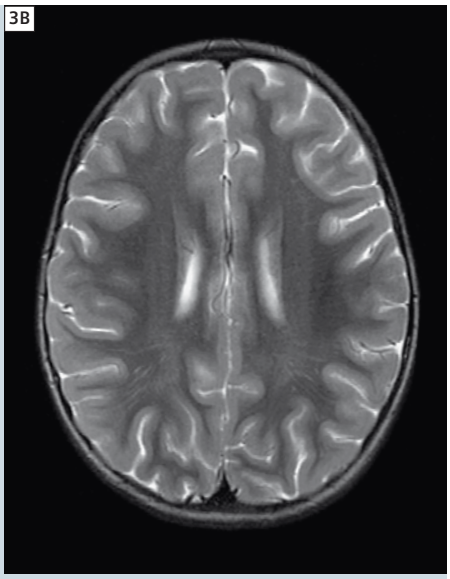

3 Axial T2 TSE MRI brain images obtained at 3T: the claustrum **(A)** is well demonstrated in this term neonate, **(B)** the perivascular spaces are routinely visualised at 3T.

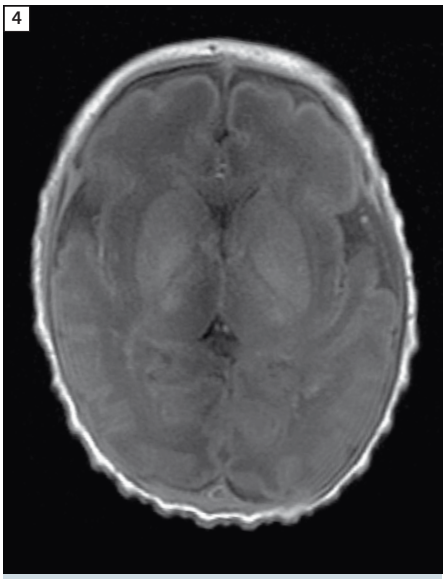

4 Axial T1 image from MRI brain study of a neonate. The image contrast is less due to the prolonged T1 time, and the high water content of non-myelinated white matter.

1.5T (Fig. 2A and B). As with the differences in image contrast when compared to 1.5T, it is also important to familiarise oneself with the normal structures that are routinely visualised at 3T, e.g. the claustrum and multiple perivascular spaces on brain studies (Fig. 3A and B).

4. What are the challenges and opportunities at 3T?

The improved signal at 3T confers indisputable advantages. However, further improvements with newer sequences and dedicated coils for imaging neonates and premature infants are routinely required to realise the full potential of 3T. In addition, the increased energy deposition raises important safety concerns. The primary challenges are due to longer T1 relaxation times, the effect on T2 and T2*, and the greater chemical shift. Each of these factors play a different role depending on the region studied, and also create opportunities in the form of important clinical applications as discussed below and in Table 2.
T1 or the longitudinal relaxation time varies for different tissues; but is generally longer at higher field strength for a specific tissue type. The T1 times of different tissues increase to varying degrees (Table 3). For instance, the T1 relaxation time of brain parenchyma is increased by up to 40% when compared to imaging at 1.5T. Other tissues with significant magnetisation transfer also demonstrate increments of 20–40%, whereas for cerebrospinal fluid, the change is negligible (Table 3). For some tissues the T1 is even higher, for example an increase of up to 73% is reported for the kidneys [3].

4.1.1. Challenges due to longer T1

The increase in tissue T1 time will usually cause a decrease in image SNR [3]. In addition, the T1 values of different tissues tend to become more uniform at higher field strengths [14–16], with the result that the T1 images show less contrast between tissues. The pulse sequence parameters used at 1.5T require modification when applying to 3T [17]. These adaptations help minimise the intrinsic 3T image contrast losses. Knowledge of T1 values of different tissues at 3T will help select TR, TE, flip angle and inversion time to optimise image contrast [2] (Tables 3 and 4). The longer relaxation times affect T1 imaging of the neonatal brain. The neonatal brain inherently has high water content, especially in the white matter, making grey–white differentiation difficult. This is compounded at 3T due to the decreased T1 contrast (Fig. 4). It is less of a problem in older children, after myelination is complete. The decreased grey–white contrast can be improved by appropriate use of TR, TE and flip angle and the use of sequences such as T1 FLAIR.

4.1.2. Advantages of longer T1

a) MRA: The longer T1 relaxation times allow better background suppression for MRA techniques, with a larger signal difference, or greater contrast, between blood vessels and the surrounding tissues [17]. This improves vessel visualisation both with time of flight (ToF) (Fig. 5) and contrast enhanced MRA (ceMRA). With ceMRA, the signal difference between blood and unenhanced tissue is further increased as the relaxivity of paramagnetic MR contrast agents is only slightly reduced at 3T [17]. Improved MRA has reduced the need for conventional angiography at our institution.

b) Post contrast imaging: For post contrast imaging in general, the improved contrast resolution at 3T and the rela-

Table 3: Increase in T1 times of different tissues at 3T vs. 1.5T [4, 8, 27, 32, 33]

Tissue type	% T1 increase	Examples of tissue T1 times (ms) at 1.5T	at 3T
Brain – grey matter	Up to 62%	960	1331
Brain – white matter	Up to 42%	700	832
CSF	Negligible change	Negligible change	Negligible change
Myocardium	43%	1030	1471
Blood	34%	1200	1500
Bone marrow	30%	290–550	370–590
Skeletal muscle	Up to 40%	860–1130	900–1420
Cartilage	10%	1020–1060	1170–1240
Synovial fluid	27%	2850	3620
Fat	20%	290–340	370–380
Liver	Up to 41%	493	641
Spleen	20%	790	950
Kidney	73%	652	774

tively less marked change in the relaxivity of paramagnetic contrast agents when compared to the surrounding parenchyma can permit a reduction of gadolinium doses and potentially enable earlier detection of inflammatory and neoplastic diseases [18–20].

5 MoyaMoya disease. MIP of time-of-flight MR brain angiogram demonstrates marked irregularity, narrowing of several vessels of the circle of Willis, with collateral neovascularisation.

c) Arterial spin labelling: ASL enables perfusion imaging without contrast and is potentially a very useful technique in children. Blood is labelled magnetically and then followed into the brain. At 3T the label lasts longer due to the longer T1 tissue relaxation times [21] and there is a potential three-fold increase in the SNR with this technique. In addition, the rate of blood flow is faster in children so that the label can also pass further through the vascular bed before fading. ASL has enormous potential in vasculitic conditions such as Moya Moya disease. Moya Moya disease manifests with progressive irregularity, stenoses and obliteration of intracranial arteries and neo-vascularisation by collaterals that have a 'puff-of-smoke' appearance on angiography (Fig. 5). Treatment is surgical creation of burr-holes to promote collateral formation via intra- to extracranial anastomoses. The timing of surgery is important to ensure the best possible outcome as collateralisation is optimal in the presence of a degree of tissue ischaemia, but delay can result in stroke. Serial imaging is used for assessment of the intra-cranial vasculature. ASL potentially has an important role in identifying parenchyma that is at risk of ischaemia, and to determine the optimal timing of surgery.

4.1.3. Effect on T2 and T2*

Tissue T2 values tend to decrease with field strength. However, tissue contrast on T2 images is not as significantly affected as T1 images [8]. Some recent reports suggest up to 10% decrease in T2 relaxation times at 3T, compared to 1.5T [16, 22, 23]. This further reduces the SNR gain for long TE sequences [17]. T2* decay, on the other hand, is considerably shorter at 3T due to microscopic field inhomogeneities which increase linearly with field strength.

Table 4: Adapting (1.5T) parameters to circumvent important 3T specific challenges.

	Effect	Compensation	Effect of compensation (trade off)
↑T1 value	↓T1 tissue contrast	Increasing TR Parallel imaging techniques IR or MT sequences	↑Scan time ↓SNR
↓T2* values	Change T2* contrast	↓TE	↓SNR
↑Chemical shift	Artefact at fat–soft-tissue interfaces and MRS mis-registration	Doubling the readout bandwidth ↓FOV Fat suppression ↓Voxel Size	↓SNR, permits↑, number of slices acquired for given TR ↓SNR Allows imaging at low readout bandwidth, SNR remains high
↑SAR	↑Body temperature	SAR monitor (legal limits) Special RF pulses ↓FOV Longer sequence duration ↓Flip angle ↓Number of slices Longer TR	 ↓SNR
↑Magnetic susceptibility	Image distortion, dark bands	Frequency encode parallel to long axis of implant Remove cause ↓Voxel size ↓Slice thickness ↓TE ↑Receiver bandwidth ↑Spatial resolution ↑ETL (TSE better than SE) Parallel imaging Shimming GRE sequence most affected	 ↓SNR ↓SNR ↑SAR ↓SNR
B_1 inhomogeneity	Bright central region, signal loss	B_1 insensitive (Adiabatic) pulses Shimming Dielectric pads	
↑Signal	↑Flow artefact	Saturation band Phase encode direction other than AP Gradient moment nulling Cardiac gating	

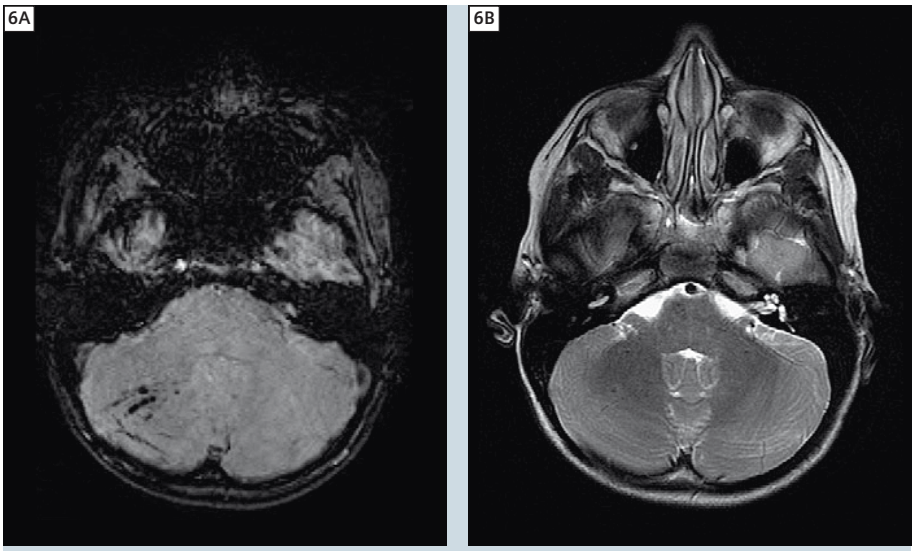

6 **(A)** Foci of profound signal loss due to haemosiderin on the susceptibility-weighted image on follow-up MRI brain study after trauma **(B)** these are only identified in retrospect on the axial T2 images.

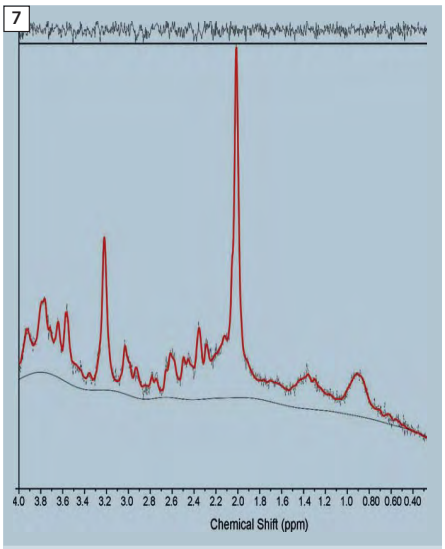

7 3T proton MRS (TE 30 PRESS) from the parietal white matter of a child with guanidinoacetate methyltransferase (GAMT) deficiency demonstrating a dramatic reduction in the creatine peak.

4.1.4. T2* related artefacts or susceptibility artefacts

The susceptibility effect is a materials' tendency to distort the applied magnetic field, and increases linearly with field strength. It occurs at air, bone or soft-tissue interfaces; and can cause areas of signal loss, inhomogeneous fat saturation and geometric distortion [24] (Figs. 6A and 8D). It is commonly seen near the paranasal sinuses in brain imaging, due to bowel gas in abdominal imaging, and with metallic implants, especially dental hardware in teenage children. The effect can be quite marked at 3T and was initially considered a major limitation to the clinical utility of high field MRI. The detrimental effect of susceptibility from macroscopic structures can be controlled at 3T by a number of techniques. The cause should be removed if possible. Appropriate shimming directly reduces field inhomogeneity. Decreasing the voxel size and TE and increasing the bandwidth can reduce this artefact, but with a concomitant decrease in SNR. Parallel imaging also reduces susceptibility, with a reduction in SNR [2] (Table 4). This decrease is adequately compensated by the increased signal at 3T.

4.1.5. T2* applications

The increased susceptibility at 3T has a number of advantages:

a) Functional MRI: fMRI relies on the ability to detect the blood deoxyhaemoglobin levels (BOLD effect), a T2* dependent technique. The greater susceptibility at high field strengths produces increased sensitivity for fMRI. fMRI has important applications in pediatric neuroimaging, especially in the preoperative assessment of children with intractable epilepsy and brain tumors, to minimise the resection of functional parenchyma.

b) Susceptibility-weighted imaging: The increased susceptibility at 3T increases the sensitivity to haemorrhage and calcification, which is exploited with *syngo* SWI. *syngo* SWI is very sensitive in identifying haemorrhagic foci in the brain (Fig. 6A and B). Specific pediatric applications include non-accidental injury, birth trauma and diffuse axonal injury due to vehicular accidents. Calcification is also easier to detect and is useful for characterising masses such as dysembryoplastic neuroepitheleal tumors.

SWI is also useful in children with haemosiderosis. Abnormal tissue iron deposition at an early age is most commonly due to recurrent transfusions in thalassemia major. Myocardial iron deposition can be fatal due to arrythmias and cardiomyopathy. This is prevented by judicious use of chelating agents, which have significant side-effects. Imaging at 3T can potentially increase the sensitivity for myocardial and liver iron quantification. This is useful to guide therapy – specifically, to optimise the dose of chelating agents and the timing of initiation of therapy.

4.2. Chemical shift

The chemical shift effect is increased two-fold at 3T compared to 1.5T [8, 25], and can result in pronounced artefacts, however, it can also be exploited for MRS.

4.2.1. Chemical shift artefact

Chemical shift artefact is caused by spatial mis-registration of fat and water, and causes a dark band at fat–soft tissue interfaces. It causes problems with MRS (discussed in detail later) and in abdominal imaging, where it can obscure subtle bowel wall changes in early inflammatory disease. This artefact is controlled by doubling the bandwidth [8, 26], or by decreasing the FOV [26]. Both of these

reduce SNR (SNR∝1/√BW), however, this loss is adequately compensated for by the increased signal at 3T [26]. The artefact can also be reduced by fat saturation, decreasing the voxel size and altering the TE.

4.2.2. MR spectroscopy

In the pediatric setting MRS is performed as a problem-solving tool, to answer specific questions. It is important for the work up of metabolic disorders. With significant overlap in the presentation of different conditions, MRS provides valuable information for the individual patient when considered in the appropriate clinical context. It can be diagnostic in certain entities, such as creatine deficiency syndromes (Fig. 7), useful to indicate disease activity, as in Leigh's disease and also to monitor response to treatment.
It is also helpful to characterise space-occupying lesions and to determine the extent of infiltrative spread (Fig. 8).
In neonates and pre term infants, MRS is performed for assessment of biochemical changes with brain maturation related to location and development, in order to detect brain injury (Fig. 9), and to distinguish hypoxic insults from metabolic/neurodegenerative conditions.

4.2.3. MRS: 3T advantages

Greater chemical shift is the basis of improvement in MRS at 3T, with increased frequency spread of individual peaks resulting in improved metabolite identification. In addition, the amount of signal derived from each metabolite is increased, so the metabolite peaks are easier to differentiate from background noise. The increased signal also enables faster acquisition times [8] which makes it more realistic in children, and especially neonates, who may not tolerate a longer sequence. The voxel size can also be reduced both with single voxel and multi voxel MRS, reducing the likelihood of contamination from subcutaneous/retro orbital fat in peripherally located lesions.

4.2.4. MRS: 3T challenges

Performing MRS at high field strength has quite a few advantages – but at the same time, there are several issues to consider when applying the 1.5T parameters and experience at 3T. The increased chemical shift also causes specific constraints for 3T MRS, whether using single or multi voxel techniques. Specifically, problems with misregistration (which results in poor lactate inversion at 3T, discussed later); and artefacts from increased susceptibility near bony structures, air sinuses and soft-tissue interfaces [25] are more pronounced than at 1.5T.
The greatest gain in SNR occurs at MRS using short TE – the latter is also the most useful in the assessment of metabolic diseases, as it is possible to detect metabolites with short T2 relaxation times, and there is little need for T2 correction. However, the general disadvantages of short TEMRS are also relevant at 3T, i.e., the overlap of lipid and lactate peaks, and distortion of the baseline due to the effect of eddy currents [27]. Hence, spectra are usually obtained at two TE values.
3T MRS at intermediate TE suffers from variable lactate inversion, which complicates the distinction of lactate from lipids – an important consideration, especially in the neonatal period as an additional sign of hypoxia. At long TE MRS the signal benefit at 3T compared to 1.5T becomes negligible [27] and the baseline is smoother, which limits detection

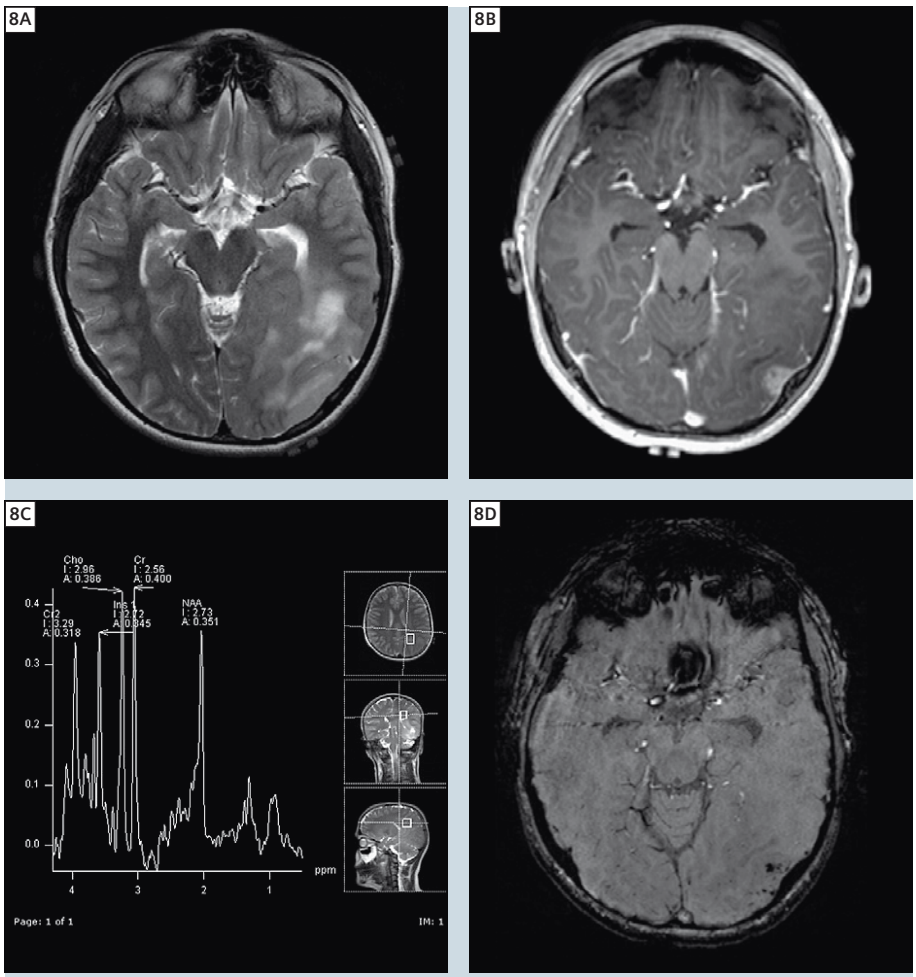

8 Glioblastoma Multiforme: Axial images from MRI brain study performed for right homonymous hemianopia demonstrate **(A)** gyral thickening, ill-defined increased T2 signal and indistinct grey-white differentiation in the left parieto-occipital region. **(B)** Cortically based enhancement **(C)** MR spectroscopy demonstrates marked elevation of choline away from the small central enhancing area – this is useful to delineate tumor extent, and distinguish infiltrative spread from peri lesional oedema. **(D)** Foci of signal dropout from blood degradation products. Note the skull base susceptibility artefact.

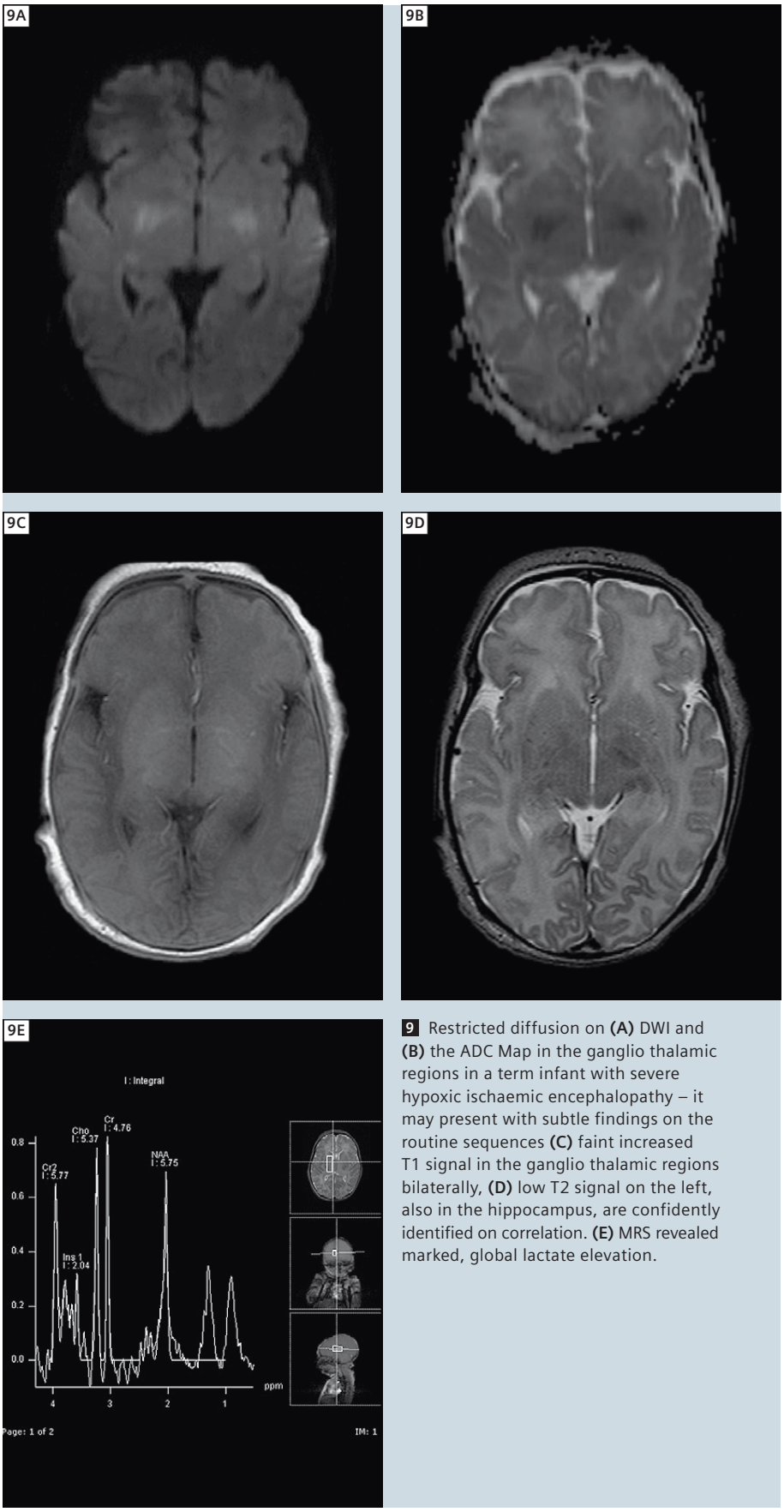

9 Restricted diffusion on **(A)** DWI and **(B)** the ADC Map in the ganglio thalamic regions in a term infant with severe hypoxic ischaemic encephalopathy – it may present with subtle findings on the routine sequences **(C)** faint increased T1 signal in the ganglio thalamic regions bilaterally, **(D)** low T2 signal on the left, also in the hippocampus, are confidently identified on correlation. **(E)** MRS revealed marked, global lactate elevation.

of smaller metabolite peaks. However, in the hypoxic setting, it is the preferred second acquisition as lipids in the voxel are neutralised, and confident assessment of lactate levels is possible.

4.3. B_1 inhomogeneity

B_1 inhomogeneity produces regions of reduced signal in the centre of the imaged object. This effect is caused by a combination of (A) variable and reduced RF penetration depth as the magnetic field strength increases and (B) dielectric tissue properties cause resonance phenomena that appear as standing waves when half the wavelength is in the order of the object size.
This is an important 3T artifact, is unpredictable and depends on the body shape and organ size. It is less of a problem in smaller children, as the tissue depth for RF penetration is less and the organ size smaller. It can affect abdominal MR images of older children. Appropriate shimming is helpful to move these dark bands away fromthe region of interest. Dielectric pads can help with this artifact and newer B_1 insensitive (Adiabatic) pulses have been developed with the latest MRI machines.

4.4. Safety issues

4.4.1. Specific absorption rate

SAR reduction is a very important factor that permits the clinical use of 3T MRI. It is a measure of the amount of energy deposited by an RF field in a given mass of tissue, and is constrained by FDA guidelines. As the power required for excitation increases with increasing frequency (and thus field strength); the SAR increases with field strength. This is according to the formula SAR∝Bo2 [10]. Therefore, using equivalent parameters, there is a four-fold increase in SAR at 3T compared to 1.5T.
The SAR increase is greater in fast spin echo sequences due to the multiple refocussing pulses and with RF intense pulse sequences such as FLAIR [25].
It also increases with gradient echo sequences that have a very short TR (e.g. TrueFISP). SAR is related to the flip angle according to the formula SAR∝(flip angle)2 [2]. Fast contrast

enhanced 3D angiography using a high flip angle; and fully rephased gradient echo techniques which yield optimum signal at high flip angle excitation with short TR easily reach SAR limits at 3T. The SAR can be reduced by using special RF coil designs such as transmit/receive array coils, by reducing the number of slices, by having a delay between sequences, or by the use of parallel imaging techniques. The choice of sequence can also reduce SAR, by using a smaller flip angle or echo train length, or an increased bandwidth or TE. However, reducing the flip angle or increasing the bandwidth alters tissue contrast. Specialised RF pulses that vary the flip angle throughout the sequence (e.g. hyperecho [28]) can reduce the SAR by up to four-fold (Table 4).
SAR potentially can create issues with temperature control, especially in neonates. They are kept wrapped in the scanner to keep them warm, however, the greater energy deposition has the potential to further increase body heat. Temperature monitoring (either skin or rectal) is therefore useful, but requires MR compatible probes. Although this is a potential issue at 3T, in practice it has not been anymore problematic when compared to scanning at 1.5T.

4.5. Specific applications that benefit from high field strength: whole body MRI, DWI & DTI and 3D imaging

The reduced scan times enable wider coverage while maintaining adequate SNR, and these advantages make whole body MRI and *syngo* DTI feasible at 3T.

4.6. Whole body MRI

There is an inherent advantage of the smaller patient size in pediatric whole body MR imaging, as the total number of acquisitions required is less than for adults. Whole body MRI in children is primarily used for oncologic screening to assess the skeletal spread [14], by obtaining overlapping STIR coronal sections (Fig. 10). An estimate of the total tumor burden, including soft-tissue involvement can be performed. It has a role in pediatric haematologic malignancies such as leukaemia and lymphoma [29], round cell tumors especially neuroblastoma, and skeletal tumors such as Ewings sarcoma [30]. Myelofibrosis, and also the response to therapy can be assessed. Non-oncologic applications include multifocal muscle disease, screening the osteoporotic skeleton for fractures, multiple bone infarcts, assessment of total body fat stores or whole body MR angiography (e.g. Takayasu's arteritis) [31].

4.6.1. Diffusion weighted (DWI) and diffusion tensor imaging (DTI)

The improved SNR at 3T means that higher B values (>1000 s/mm^2), thinner slices and imaging in a greater number of directions are possible, thereby improving DWI. Magnetic susceptibility artefact is more pronounced with EPI, and may be a problem with DWI at higher field strengths [32], especially with dental braces that are common in older children. This can be con trolled – to an extent – with volume shimming, parallel imaging techniques, and bandwidth adjustment.
In the neonatal period, *syngo* DWI is very important for the assessment of hypoxic ischaemic encephalopathy, as it may present with subtle findings on the routine sequences (Fig. 9). It is also useful in the context of pediatric stroke, including vasculitis and sickle cell disease; also with traumatic brain injury and demyelinating disorders.
The benefit of DTI, when compared to conventional DWI, is the capability to determine white matter fibre orientation within collimated bundles – this directional information is displayed using 2D directionally encoded color anisotropy images or by 3D fibre tractography (Fig. 11). Also, qualitative measures derived fromDTI, i.e., mean diffusivity and fractional anisotropy (FA) are rotationally invariant, and thus, in theory, not affected by changed head position or fibre orientation.
DTI is becoming increasingly important in the preoperative assessment of patients with brain tumors. Relationship of the mass with important white matter tracts can be demonstrated, and thus assist the surgeon in preserving function, while maximising lesion resection. With further advances, tractography can potentially enable more comprehensive assessment of other neural tract or pathway specific conditions, such as post delivery brachial plexus injuries; and aberrant connectivity in structural brain malformations.

10 Coronal T2 STIR whole body MRI for metastatic neuroblastoma.

4.7. 3D imaging and 3D dynamic MRA

The greater SNR enables faster acquisition of 3D data sets which are now routinely performed in our practice at 3T,

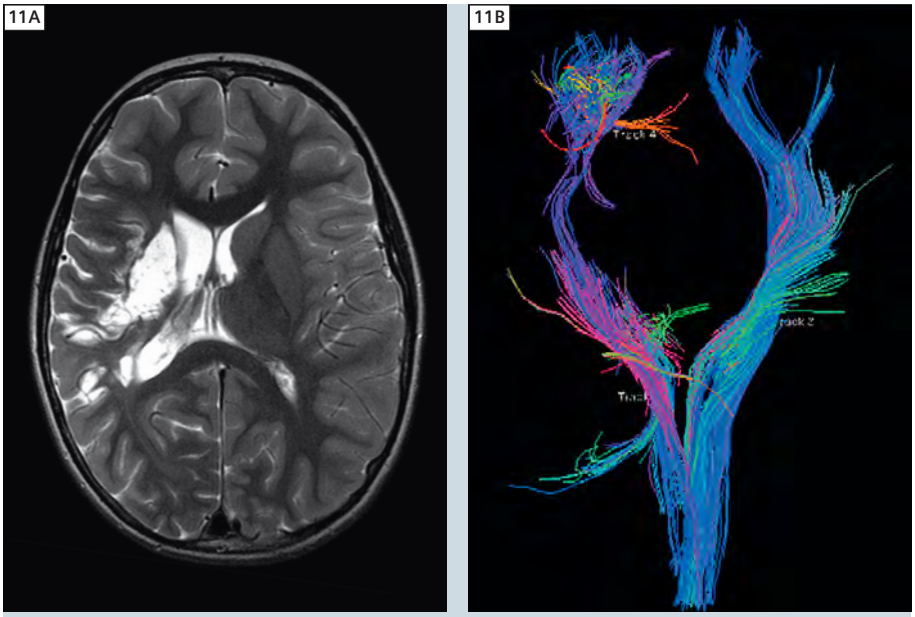

11 Sequela of right middle cerebral artery embolic occlusion secondary to traumatic internal carotid artery dissection. **(A)** Axial T2 image demonstrates cystic encephalomalacia and volume loss **(B)** disruption of the major white matter tracts (color coded) as depicted by tractography.

especially for post contrast imaging. Dynamic 3D imaging has also become practical with applications such as TWIST which enables sub-second time sequential 3D imaging.We have used this technique to evaluate the flow through complex vascular malformations, for planning treatment.

4.8. Challenging high field regions: cardiac and spinal imaging

There are definite advantages in having greater SNR for cardiac and spinal imaging, however, both regions have several high field issues, which come together to make these areas particularly challenging.

4.8.1. Cardiac imaging at 3T

The major indications for pediatric cardiac MR imaging are for assessment of ventricular function, the major vessels and post-operative anatomy in the context of congenital heart disease. However, all types of pathology including coronary artery abnormalities, cardiomyopathy, infiltrative disorders and cardiac tumors are imaged.

3T cardiac MRI has potential for improved coronary artery evaluation, and delayed enhancement imaging in conditions such as cardiomyopathy and assessment for arrythmogenic right ventricular dysplasia – these may be SNR-limited at lower field strengths.

Steady state free procession (TrueFISP) imaging, is very important in cardiac MRI at 1.5T. For the best TrueFISP imaging the TR is kept as short as possible (<4 ms), the flip angle as high and uniform as possible (all of which increase the SAR), and the magnetic field must be homogeneous (which is challenging at 3T). At 1.5T, the TrueFISP sequence is already at the SAR limit and to reduce the SAR at 3T, the flip angle must be reduced. This makes the blood pool darker and reduces the contrast between the blood pool SNR.

B_1 inhomogeniety artefact, susceptibility artefact and off resonance effects tend not to be a significant problem with cardiac imaging at 1.5T, however, occur unpredictably and can be severe at 3T [33]. Field inhomogeniety can be controlled by tight shimming and frequency correction.

Application of parallel imaging techniques may increase the clinical utility of 3T cardiac MRI. Higher acceleration factors enable smaller acquisition windows, and support segmented acquisition schemes, an advantage for the higher heart rates of pediatric patients. Also, the energy deposition can be reduced due to fewer phase-encoding steps [33]. Improved MRA at 3T is very useful in the assessment of the major arteries and veins which are very important in children with congenital heart disease. This is particularly true of the pulmonary arteries, which commonly require assessment in the neonatal period.

4.8.2. Spine imaging

T1 imaging of the spinal cord is difficult at 3T. T1 prolongation results in reduced contrast between the grey and white-matter. This is accentuated in pediatric imaging due to the increased water content of neural tissue, especially before myelination is complete. In addition, CSF signal intensity at 3T is greater than at 1.5T which means there is reduced contrast between the spinal cord/conus and the surrounding CSF.

Gradient sequences such as T1 FLAIR may lessen the problems associated with T1 lengthening, with the potential of optimum contrast at 3T, at normal as well as abnormal tissue interfaces [26]. Studies comparing post-contrast T1 spin echo and gradient images have yielded equivocal results with regard to lesion conspicuity and detection – this may be overcome by acquiring one of each, in different planes [26]. In addition, CSF flow artefacts increase with higher field strength, due to the increased signal and spatial misregistration. The highly pulsatile CSF flow in children can cause a severe artefact which can obscure important pathology, such as leptomeningeal tumour spread. Gradient moment nulling may prove to be useful for CSF flow compensation [11]. Cardiac gating may also be used to overcome these effects [9].

5. Conclusion

3T MRI is being increasingly performed for clinical purposes. The signal increases four-fold when compared to imaging at 1.5T, and can translate to an observed SNR gain of 1.7–1.8. The increased SNR

is a significant advantage in pediatrics – improved spatial and temporal resolution assist in overcoming the major anatomic, physiologic and behavioural challenges of imaging children. Rapid changes with development and maturation can also be better assessed.

The challenges inherent to imaging at high field strength remain pertinent – important among these are the altered T1 contrast, artefacts and safety issues, especially SAR. These necessitate modification of the imaging protocols used at 1.5T. Ongoing physicist input, and technical support is essential. Hardware advances especially improved gradients, dedicated coils and sequences are very useful in this regard. The above mentioned challenges also create opportunities at 3T, with improvement in MRA, *syngo* ASL, *syngo* SWI, fMRI and MRS – all of which have distinctive applications in pediatrics. The SNR gain can be used as a trade-off, when compensating for the altered relaxation times and 3T specific artefacts.

3T MRI has the potential to image all the systems in pediatrics. Optimising the parameters with due consideration to specific pediatric features, such as the increased water content of non myelinated brain, is essential. Some 3T artefacts inherent to specific anatomic regions, like the dielectric effects encountered in adult abdominal imaging, are less problematic in pediatrics due the smaller size. On the other hand, the neonatal brain and pediatric spine are difficult to image at 3T. Several factors also limit cardiac imaging at present. Further improvements in coil technology and newer sequences may help overcome the challenges that remain.

Contact
Michael Ditchfield, M.D.
The Royal Children's Hospital
Femington Road, Parkville
Viktoria, Australia, 3052
michael.ditchfield@rch.org.au

References

1 Akisik FM, Sandrasegaran K, Aisen A, et al. Abdominal MR imaging at 3.0 T. Radiographics 2007;27(5):1433–44.
2 Barth MM, Smith MP, Pedrosa I, et al. Body MR imaging at 3.0 T: understanding the opportunities and challenges. Radiographics 2007; 27(5):1445–64.
3 Soher BJ, Dale BM, Merkle EM. A review of MR Physics: 3T versus 1.5T. Magn Reson Imag Clin N Am 2007;15(3):277–90.
4 Zimmerman RA, Bilaniuk LT, Pollock AN, et al. 3.0 T versus 1.5T. Paediatr Brain Imag 2006; 16(2):229–39.
5 Kliegman RM, Behrman RE, Jenson HB, et al. Nelson Textbook of Pediatrics. 18th ed. Saunders; 2008. p. 41.
6 Hallowell LM, Stewart SE, de Amorim e Silva CT, et al., Reviewing the process of preparing children for MRI. Pediatr Radiol. 2008;38(3)271–79.
7 Stokowski LA. Ensuring safety for infants undergoingmagnetic resonance imaging. Adv Neonatal Care 2005;5(1):14–27.
8 Schick F. Whole-body MRI at high field: technical limits and clinical potential. Eur Radiol 2005;15(5):946–59.
9 Gonen O, Gruber S, Li BS, et al. Multi-voxel 3D proton spectroscopy in the Brain at 1.5T versus 3.0 T: signal-to-noise ratio and resolution comparison. AJNR Am J Neuroradiol 2001;22:1727–31.
10 Wen H, Denison TJ, Singerman RW, et al. The intrinsic signal-to-noise ratio in human cardiac imaging at 1.5, 3 and 4 T. J Magn Reson 1997; 125(1): 65–71.
11 Barker PB, Hearshen DO, Boska MD. Single-voxel proton MRS of the human brain at 1.5T and 3.0 T. Magn Reson Med 2001;45:765–9.
12 Thulborn KR. Clinical rationale for very-high-field (3.0 Tesla) functional magnetic resonance imaging. Topics Magn Reson Imag 1999;10(1):37–50.
13 Merkle EM, Dale BM. Abdominal MRI at 3.0 T: the basics revisited. AJR Am J Roentgenol 2006; 186(6):1524–32.
14 Michaeli S, Garwood M, Zhu XH, et al. Proton T2 relaxation study of water, Nacetylaspartate, and creatine in human brain using Hahn and Carr-Purcell spin echoes at 4 T and 7 T. Magn Reson Med 2002;47(4):629–33.
15 Ethofer T, Mader I, Seeger U, et al. Comparison of longitudinal metabolite relaxation times in different regions of the human brain at 1.5 and 3Tesla. Magn Reson Med 2003;50(6):1296–301.
16 de Bezelaire CMJ, Duhamel GD, Rofsky NM, et al. MR imaging relaxation times of abdominal and pelvic tissues measured in vivo at 3.0 T: preliminary results. Radiology 2004;230:652–9.
17 Bernstein MA, Huston III J, Lin C, et al. High-resolution intracranial and cervical MRA at 3.0 T: technical considerations and initial experience. Magn Reson Med 2001;46(5):955–62.
18 Bernstein MA, Huston III J, Ward HA. Imaging artifacts at 3.0 T. J Magn Reson Imag 2006; 24(4):735–46.
19 Fernandez-Seara MA, Wehrli FW. Postprocessing technique to correct for background gradients in image-based R*2 measurements. Magn Reson Med 2000;44(3):358–66.
20 Wood M, Hardy P. Proton relaxation enhancement. J Magn Reson Imag 1993;3:149–56.
21 Martirosian P, Klose U, Mader I, et al. FAIR True-FISP perfusion imaging of the kidneys. Magn Reson Med 2004;51(2):353–61.
22 Gold G, Han E, Stainsby J, et al. Musculoskeletal MRI at 3.0 T: relaxation times and image contrast. AJR Am J Roentgenol 2004;183:343–51.
23 Stanisz G, Odrobina E, Pun J, et al. T1, T2 relaxation and magnetisation transfer in tissue at 3T. Magn Reson Med 2005;54(3):507–12.
24 Tin Ging Ma H, Local experience of MR imaging with 3T (TRIO) equipped with TIM. Biomed Imag Interv J 2007;3(1):12–39.
25 Bronson J. High-field MRI: is it time for 3T? Imag Econ 2004. Available via http://www.imagingeconomics.com/issues/articles/2004-02 04. asp.
26 Shapiro MD. MR imaging of the spine at 3T. Magn Reson Imag Clin N Am 2006;14(1):97–108.
27 Kim J-h, Chang K-H, Na DG, et al. 3T 1H-MR spectroscopy in grading of cerebral gliomas: comparison of short and intermediate echo time sequences. AJNR Am J Neuroradiol 2006;27:1412–8.
28 Hennig J, Scheffler K. Hyperechoes. Magn Reson Med 2001;46:6–12.
29 Iizuka-Mikami M, Nagai K, Yoshida K, at al. Detection of bone marrow and extramedullary involvement in patients with non-Hodgkin's lymphoma by whole-body MRI: comparison with bone and 67 Ga scintigraphies. Eur Radiol 2004;14(6):1074–81.
30 Mazumdar A, Siegel MJ, Narra V, et al. Whole body fast inversion recovery MR imaging of small cell neoplasms in pediatric patients: a pilot study. AJR 2002;179:1261–6.
31 Laffan EE, O'Connor R, Ryan SP, et al. Whole-body magnetic resonance imaging: a useful additional sequence in pediatric imaging. Pediatr Radiol 2004;34(6):472–80.
32 Phalke VM, Gujar S, Quint DJ. Comparison of 3.0 T versus 1.5T MR: imaging of the spine. Neuroimag Clin N Am 2006;16(2):241–8.
33 Nael K, Fenchel M. Cardiac MR imaging: new advances and role of 3T. Magn Reson Imag Clin N Am 2007;15(3):291–300.

3T MR Imaging of Peripheral Nerves Using 3D Diffusion-Weighted PSIF Technique

Avneesh Chhabra[1], M.D.; Theodore Soldatos[1], M.D.; Aaron Flammang[1]; Wesley Gilson[1]; Abraham Padua[2]; John A Carrino[1], M.D., M.P.H.

[1]Johns Hopkins University, Baltimore, MD, USA
[2]Siemens Healthcare, MR RD Management, Malvern, PA, USA

High-resolution magnetic resonance (MR) Neurography is a novel imaging technique, which enables multiplanar imaging of peripheral nerves, as well as diagnosis and localization of entrapment and non-entrapment peripheral neuropathies related to etiologies, such as inflammation, tumor and trauma. Typically, MR Neurography techniques utilize a combination of fat-saturated T2-weighted, short inversion time recovery (STIR), or T2 spectral adiabatic inversion recovery turbo spin echo (T2 SPAIR TSE) images for the detection of the nerve signal, contour and size changes, as well as T1-weighted spin echo or fluid attenuated long inversion recovery (FLAIR) images for the anatomic assessment of the involved areas, based on the abundant intra- and perineural fat. However, the diagnostic ability of conventional MR Neurography is limited in the evaluation of smaller peripheral nerves of the axial and appendicular skeleton, where the similar caliber and T2 signal intensity of peripheral nerves and adjacent vessels render discrimination of the above structures difficult, if not impossible. Since nerve injuries and entrapments commonly lead to effacement of perineural fat in the area of involvement, T1-weighted images are often not helpful. In addition, an attempt to suppress

Table 1: Acquisition parameters for 3D-PSIF at 3T

The typical acquisition parameters employed for the 3D-PSIF sequence in a Siemens 3T MAGNETOM Verio scanner. The spatial resolution of this technique yields 0.9 x 0.9 x 0.9 mm voxel sizes and, whenever possible, this dimension is preserved. When examining areas requiring larger or smaller coverage, the scan matrix and the FOV are adjusted accordingly. This and number of slices are all that is changed. Scan time is typically kept below 6 minutes 30 seconds through the use of parallel acquisition. High quality thin MIP projections are rendered for display purposes.

Acquisition parameter	Value
Slabs	1
FOV	172 mm
Slice thickness	0.9 mm
TR	12 ms
TE	4.1 ms
Averages	1
Coil	8-channel knee coil
PAT	GRAPPA 2
Flip angle	30
Fat suppression	Water Excitation Normal
Diffusion mode	Phase
Diffusion moment mT/m*ms	85
Diffusion directions	1
Dimension	3D
Elliptical scanning	On
Asymmetric echo	Off
Receiver bandwidth	230 Hz/Px
Acquisition time	4 min 37 sec

vascular signal with saturation bands often fails in distal locations of the body, as the peripheral nerves frequently course through various obliquities.
Due to recent advances in 3T MR imaging with incorporation of optimized extremity coils and new pulse sequences, 3-dimensional high-resolution and high-contrast demonstration of the peripheral nerves is possible.
The 3-dimensional diffusion-weighted sequence based on reversed fast imaging with steady-state precession (3D-PSIF) has been recently implemented in high-resolution MR Neurography imaging protocols and has a potential to overcome most of the above mentioned challenges in small peripheral nerve imaging. The 3D-PSIF is a balanced gradient echo steady-state free precession (SSFP or PSIF) sequence with inherent features of a spin-echo sequence, as compared with other unbalanced spoiled or refocused gradient-echo techniques, such as fast low-angle shot (FLASH), fast field-echo, and gradient recall acquisition using steady-states (GRASS or FISP). Therefore, the 3D-PSIF sequence demonstrates less influence of local magnetic field inhomogeneities on the spin relaxation. The water-excitation technique enables uniform fat suppression and is unaffected by the chemical shift effect. Although 3D-PSIF may also be performed without fat saturation, fat-suppressed images usually provide better nerve-to-background contrast ratio. In addition, the application of diffusion moment provides suppression of water signal. In most cases, a diffusion moment value of 80–90 mT/m*ms provides an acceptable compromise in peripheral nerve-to-background contrast and image signal-to-noise ratios (SNR). Since the signal depends strongly on the steady-state condition, all moving structures, such as flowing blood, demonstrate a loss of signal intensity. As a result, the high T2 signal intensity of peripheral nerves is effectively differentiated from the nulled signal of adjacent vessels (Figs. 1, 2). Although 3D-PSIF images provide predominantly T2 contrast, there is a potential to perform post-contrast imag-

1 Sagittal 3D-PSIF image of the forearm and wrist demonstrates the median nerve (arrow) along its entire course.

2 Coronal 3D-PSIF image of the lumbosacral plexus demonstrates excellent discrimination of the nerve roots from adjacent soft-tissue structures.

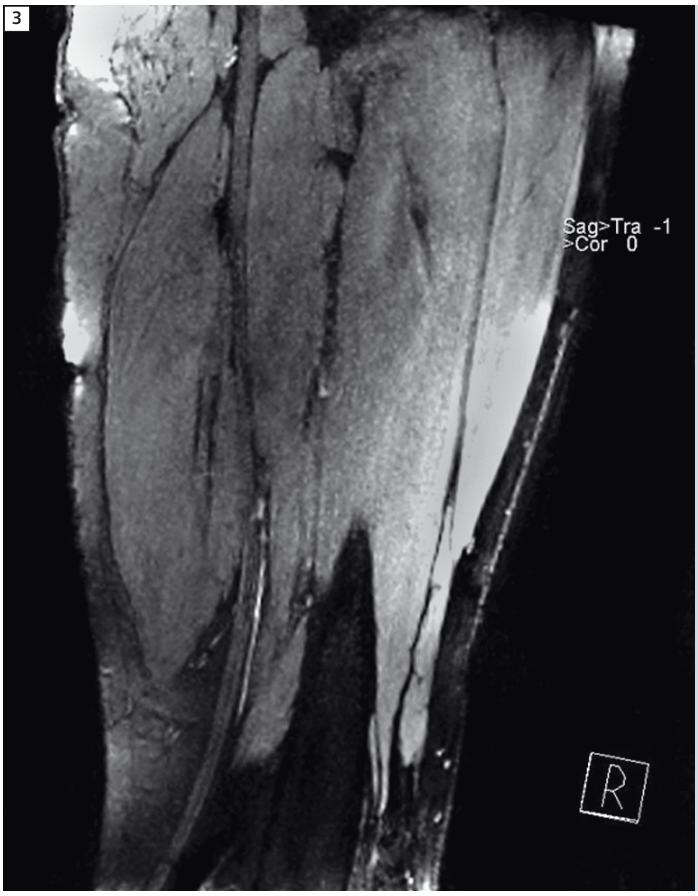

3 Coronal 3D-PSIF maximum intensity projection (MIP) of the thigh demonstrates the course of the sciatic nerve.

ing following administration of intravenous gadolinium. In 3D-PSIF imaging, the acquisition of isotropic voxels enables the data set to be reformatted into any imaging plane without significant loss of resolution. The latter feature may provide confirmation of anatomic continuity, as well as identification of branching, focal enlargement, course deviation and/or displacement of peripheral nerves. In addition, maximum intensity projections (MIPs) can be employed to further enhance the conspicuity of the nerves and provide images, which can be distributed to referring physicians for better depiction and understanding of nerve anatomy and pathology (Fig. 3). Table 1 displays the typical acquisition parameters employed for the 3D-PSIF sequence in a Siemens 3T MAGNETOM Verio scanner. In clinical practice, 3D-PSIF has proven more efficient than the conventional STIR and T2 SPAIR TSE sequences in differentiating small peripheral nerves from adjacent vessels. In the extremities, and particularly distal to the knee and elbow joints, the commonly encountered T2 hyperintense subcutaneous and/or fascial edema restricts the identification of small peripheral nerves on conventional T2-weighted sequences. In contrast, the inherent diffusion sensitive gradients of 3D-PSIF enable selective suppression of the water signal of the stationary subcutaneous and fascial edema, thus improving the conspicuity of small peripheral nerves in the above areas. On the other hand, the inherent high TE values of 3D-PSIF images result in lower SNR as compared to conventional fat-saturated T2-weighted images, which remain superior in delineating the fascicular structure of the nerves. In post-contrast imaging, as compared to the three-dimensional volumetric interpolated breathhold examination (3D VIBE) sequence, the 3D-PSIF technique provides better visualization of the nerve fascicles, as well as more adequate assessment of the anatomic relationship between fascicles and enhancing intraneural and/or extraneural tumors.

In summary, the 3D-PSIF sequence with high spatial resolution and high contrast provides reliable and objective identification of peripheral nerve anatomy and may be incorporated as part of the high-resolution MR study of peripheral nerves, whenever accurate nerve localization and/or pre-surgical evaluation are required.

→ **Don't miss the talks on peripheral nerve imaging on www.siemens.com/magnetom-world**

- Imaging of peripheral nerves – status quo by Mirko Pham University of Heidelberg, Germany
- Peripheral nerve imaging from head to toe by Meng Quan-Fei. The First Affiliated Hospital of Sun Yat-sen University, Guangzhou, China

Contact
John A. Carrino, M.D., M.P.H.
Associate Professor of Radiology and Orthopedic Surgery
Section Chief, Musculoskeletal Radiology
The Russel H. Morgan Department of Radiology and Radiological Science
601 North Caroline St. /JHOC 5165
Baltimore, MD 21287-0856
USA
carrino@jhmi.edu

syngo fMRI

- Easy paradigm and protocol selection
- Full control of temporal and spatial filtering
- Functional dataset in less than 5 minutes
- Dynamic t-maps and GLM statistics
- Display of statistics and 3D motion correction in real-time
- HD resolution, high luminescence flat panel monitor

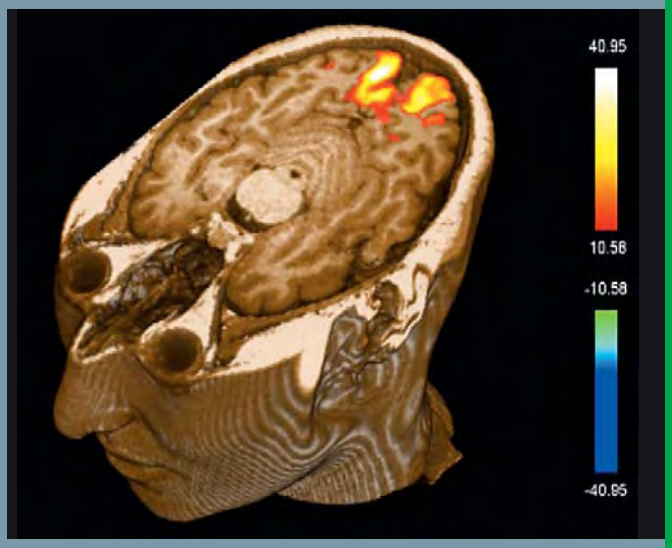

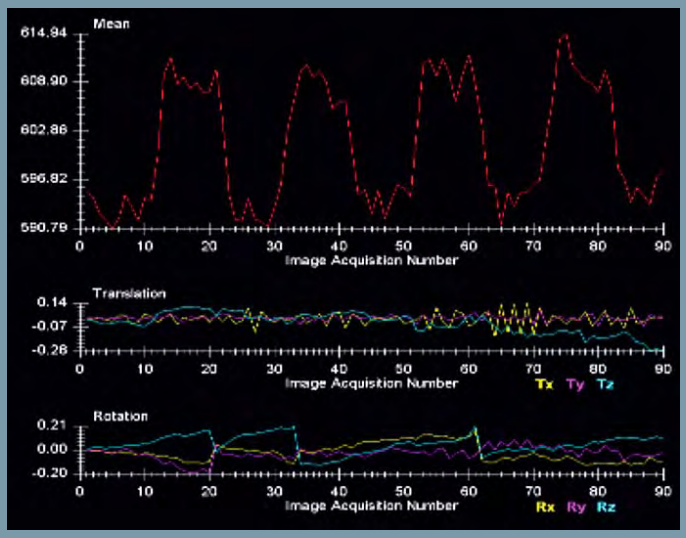

Integrated Whole Body MR/PET Imaging. First Examples of Clinical Application

A. Drzezga; A.J. Beer; S. Fürst; S. Ziegler; S.G. Nekolla; M. Schwaiger

Technische Universität München, Klinik und Poliklinik für Nuklearmedizin, Klinikum rechts der Isar, Munich, Germany

Introduction

Over the last decade, development of hybrid-imaging instrumentation has been among the innovations with the strongest impact on diagnostic imaging in clinical everyday routine. The driving force behind these developments is the considerable extent to which several different imaging modalities show complementary rather than redundant features. Consequently, it is logical to bundle the particular strengths of different modalities, and to compensate particular deficits of one modality with capabilities of another by combination of the different modalities into one hybrid instrument. Hybrid PET/CT entered the market in around 2000 and became a major success, thereby quickly obviating the demand for PET-only scanners. This success has been strongly driven by oncological applications, combining the high sensitivity of PET with the anatomical precision of CT. The coupling of ^{18}F-FDG, a tracer for metabolic activity with CT, has especially proved highly valuable: FDG-PET allows the sensitive detection of tumor cells and the estimation of their viability (e.g. for therapy control); CT complements the exact anatomic localization of suspect lesions and has a very high sensitivity for small lesions which are missed by PET due to limited resolution or movement artifacts (e.g. in the lung).

However, CT has some specific limitations, the most apparent being the relatively low soft-tissue contrast. This represents a disadvantage particularly for diagnostic questions directed to body regions which are defined by a complex regional arrangement of different adjacent soft tissue structures, e.g. the brain, the head-and-neck region or the pelvis. In contrast to CT, MR-imaging is distinguished by the ability to provide excellent soft-tissue contrast. This is the main reason why corresponding diagnostic problems are typically directed to MRI as the first-line imaging procedure of choice rather than to CT. This includes questions concerning e.g. neurological disorders, brain tumors, conditions in the head and neck region, abdominal/hepatic and pelvic masses and musculoskeletal problems.

For many of these diagnostic questions, PET has demonstrated a high added value as a complementary test in itself, whilst frequently being performed in addition to mandatory MRI-tests (see A. Padhani 'Multiparametric imaging of tumors – an emerging paradime', MAGNETOM Flash #45 3/2010, Research Supplement). Thus, the value of a combination of PET with MRI seems obvious. However, the development of such hybrid MR/PET instrumentation has been hampered for a long time primarily by technical obstacles which have been harder to overcome compared to the combination of PET and CT. Whereas the latter both represent modalities working with radiation (although in different wavelengths) and can thus be combined more easily, PET and MRI are based on entirely different image acquisition principles. The strong magnetic field required for MR-image acquisition is severely affecting the acquisition of the PET-signal. In particular, the conventional photomultiplier technique commonly used for obtaining the PET signal does not work properly in a magnetic field. To circumvent this limitation, platforms have been developed in which spatially separate MR- and PET-scanners are connected by means of a moving table. The patient is positioned on this table and undergoes first PET and then MR imaging, without having to get up from the table between the scans. However, these solutions do not allow simultaneous image acquisition and they are of course associated with lengthy examination protocols and with the risk of patient movement.

With the introduction of the so-called APDs (Avalanche Photodiodes) into PET-

instrumentation this problem has been solved more elegantly. APDs function in strong magnetic fields and can be used to substitute conventional photomultipliers to acquire information in the MR-scanner. The advent of this technology has allowed the industry to produce a first generation of hybrid MR-scanners in which a true integration of both modalities in a single machine has been realized (see H. Quick 'Whole-body MR/PET hybrid imaging' page 88 in this issue of MAGNETOM Flash). This principle was first successfully demonstrated by means of small head-only PET-scanners (PET-insert) which have been installed in conventional MR-scanners (see T. Beyer et al. 'MR/PET-hybrid imaging for the next decade', MAGNETOM Flash #45 3/2010 Research Supplement). Several studies have been performed in this prototype system since and proved the practicability of the concept [1–4].
On the basis of this prototype, a dedicated whole-body MR/PET system has now been developed. In November 2010, the world's first integrated clinical whole-body MR/PET scanner (Siemens Biograph mMR) was installed in the Department of Nuclear Medicine at the Technische Universität München (TUM), in Munich, Germany. The scanner is now operated by a consortium between the directors of Nuclear Medicine (Prof. Dr. Markus Schwaiger) and Radiology (Prof. Dr. Ernst Rummeny) from TUM and the directors of Nuclear Medicine (Prof. Peter Bartenstein) and Radiology (Prof. Dr. Maximilan Reiser) from the Ludwig-Maximilians-Universität, München. The setup of the first scanner of this type in Germany (and of three identical scanners which will be established in 2011 in Essen, Leipzig and Tübingen) has been made possible by funding of the German Research Foundation (DFG, Deutsche Forschungsgemeinschaft).
The Biograph mMR MR/PET-scanner is constituted by a high end 3T MR-scanner which harbours a fully functional state-of-the-art PET system within the gantry. The PET-system covers a field of view (25.8 cm) which is larger than in any other existing PET-camera. This allows to obtain multimodal (MR&PET) image information simultaneously in an extended region and to cover the entire body with a limited number of bed positions in short time. For further technical details on the system see page 88 in this issue of MAGNETOM Flash.

Opportunities of the MR/PET-system

From a clinical point of view, this system offers a number of obvious advantages:

1. **Reduction in examination time**
   In comparison to clinical CT-examinations, MR-scans can often be relatively time-consuming. The recently introduced whole-body MR/PET scanner now allows the acquisition of MR and PET information in a truly simultaneous approach, i.e. in regional alignment at exactly the same time, thereby reducing not only the number of examination appointments (i.e. the visits patients have to make to the imaging department) but also cutting the required examination time approximately in half (as compared to two separate examinations). This option of 'one-stop shop' examinations represents a major gain in patient comfort for patients requiring both MR and PET examinations and also reduces the required time of the medical personnel to acquire the requested imaging information.
2. **Regional coregistration**
   The acquisition of PET and MR-information in exactly overlapping anatomical positions also offers clear advantages: Precise coregistration of the PET-signal with the underlying anatomical information is assured as the risk of patient movement or changes in organ position (e.g. in bowel positions, different bladder filling status) between the acquisition of the two modalities is reduced, and thus potential misalignment is minimized. Due to the lack of radiation exposure by the MR-image acquisition, anatomical scans can be added/repeated to achieve optimal anatomical information.
3. **Simultaneity of acquisition**
   The newly introduced integrated MR/PET scanners for the first time allow truly simultaneous acquisition of imaging information from two different modalities of the same region at the same time. This opens a completely new dimension in hybrid imaging. Even established PET/CT technology only allows the acquisition of CT and PET in the same system but not at exactly the same time and region, as the two modalities/acquisition procedures are cascaded one after the other. The simultaneous acquisition of MR and PET information opens the opportunity to address many new scientific questions, which may be translated into clinical application, e.g. to cross-evaluate the value of different imaging tests under identical examination conditions or to improve understanding of disease pathophysiology by shedding light on the interrelation between different pathological processes. Simultaneous acquisition may also allow the following of organ and/or patient movement over time allowing for motion correction [2] and also the combination of information on motility with other functional information provided by PET (e.g. information on viability/perfusion derived from PET-imaging with information on wall movement in cardiac examinations).
4. **Exposure to ionizing radiation**
   Radiation exposure based on clinical imaging tests is currently a much-discussed topic. Compared to PET/CT, hybrid MR/PET offers the chance to reduce ionizing radiation exposure without loss of diagnostic information. MRI will probably allow anatomical allocation of the PET-signal with comparable precision as known from CT. In some cases the combination of PET-imaging with appropriate diagnostic MR-imaging procedures may be of superior diagnostic value with considerably lower radiation exposure as compared to the combination of PET and diagnostic CT.

5. **Complementary/superior diagnostic value of MR/PET compared to PET/CT**
   It is well known that MRI has complementary features to CT. The most obvious being the higher soft-tissue contrast. As mentioned above, combined MR/PET may be of obviously higher diagnostic value compared to PET/CT for indications and in body regions which would usually be approached using MRI rather than CT (see clinical examples below). In this regard MR/PET may represent a complementary imaging technique to PET/CT in the future just as MR itself represents a complementary imaging technique to CT nowadays.
6. **Opportunities for scientific applications**
   The MR/PET-system opens a large number of potential scientific applications. Among these is the unique option to establish previously unknown interrelations between different measures of pathology and physiology in the human body such as structure and function, perfusion and metabolism, tissue diffusivity and cell proliferation etc. This may allow to improve the understanding of healthy organ function and to detect causal relationships in disease pathogenesis potentially leading to new therapeutic approaches.
   For clinical diagnosis, combined MR/PET may allow the development of integrated multiparametric markers for more sensitive and more specific diagnosis, therapy planning and evaluation [5]. Several previous studies using separate modalities point to a potentially high scientific and clinical benefit from multimodal imaging approaches using MR/PET [e.g. 5–7].

Challenges of the MR/PET system

Like every new system, combined MR/PET still has a number of apparent challenges:

1. **Attenuation correction**
   In PET/CT systems, low-dose CT scans are used to estimate the expected attenuation of the radiation emitted from a specific body region. In contrast to CT, MR imaging does not provide information on tissue specific photon absorption, but rather on tissue type/class. However, it has been demonstrated that by means of a set of specific MR-sequences (Dixon imaging or chemical shift imaging) suitable attenuation maps can be calculated, which allow an approximation of 511 keV photon attenuation correction with sufficient reliability [8]. The dual point VIBE T1-weighted Dixon sequence used for attenuation correction in the Biograph mMR can be acquired quickly for each bed position (e.g. in the thorax during one breath-hold), practically not increasing the examination time. However, the current approach of tissue classification with the Dixon sequence is not yet fully satisfying, it is prone to metal artifacts, attenuation by bones is not considered and truncation artifacts may occur due to the limited transaxial field-of-view of the MR/PET scanner (particularly of the upper limbs). The compensation for these artifacts is currently a matter of ongoing research. Moreover, it can be anticipated that different sequences for attenuation correction will be used in specific areas of the body. For the head e.g., bone probably cannot be neglected completely for truly accurate AC, especially for the skull base. Therefore in this region, the application of ultrashort TE (UTE) sequences might be favourable, which allows for delineation of the bone, thus leading to more exact attenuation maps (μ-maps) as compared to the Dixon imaging approach.
2. **Anatomical allocation of PET-findings**
   The low dose CT scan of the whole body as acquired in conventional PET/CT provides limited diagnostic information but it allows a rough anatomical allocation of suspect PET-findings with sufficient reliability in many cases. For precise attribution diagnostic contrast-enhanced CT scans can be acquired in very short time and provide excellent anatomical information. By contrast, MR-sequences can be comparably slow and it may not be feasible to always acquire whole-body MR-information with high resolution in due time. However, it seems likely that the Dixon-sequences used for attenuation correction of the PET-data also can be used for anatomical allocation of PET-findings with very satisfying results. These whole-body images can then be complemented by added high-resolution MR-sequences in particular regions of interest.
3. **MR-specific diagnostic limitations**
   It is expected that MR/PET will be inferior to PET/CT for indications which are commonly addressed with better diagnostic value by CT, e.g. small pulmonary lesions. It remains to be evaluated for which indications MR/PET is superior or equal to PET/CT and for which indications PET/CT will remain the method of choice.
4. **Workflow**
   The high costs for this type of imaging instrumentation will require elaborate logistics regarding patient flow, occupancy of the scanner, selection of examination procedures etc., to assure efficient utilization of the scanner. The combined acquisition of MR and PET information defines the need for specially educated medical personnel experienced with both modalities.
5. **Design of suitable imaging protocols**
   The large number of available MR-sequences and of different PET-tracers exponentiates the number of potential combinations of imaging tests. This will define the need to develop optimized imaging algorithms for specific diagnostic questions, which ensure the selection of the most beneficial combinations.

Examples for clinical applications

1. Oncology

Case 1 Patient with a cervical Non-Hodgkin lymphoma.

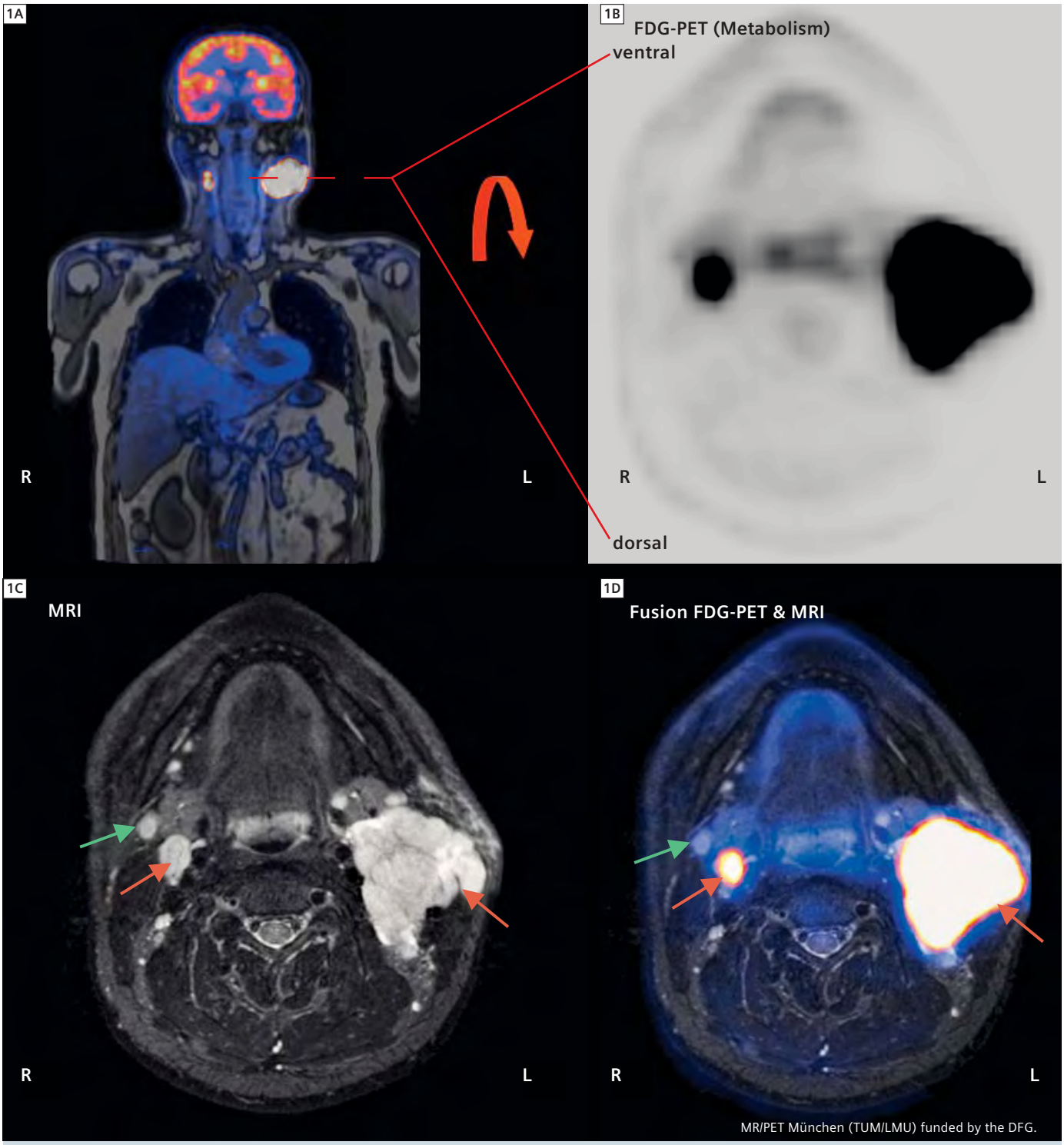

1 **A:** Overview using the opposed phase of the MR AC Dixon sequence. **B:** Axial slice of the ^{18}F-FDG-PET image, demonstrating tumor-suspect increased metabolism in two lesions (left and the right lateral). **C:** Axial MRI (STIR sequence) demonstrating the high tissue contrast. Several cervical lymph nodes are apparent, some enlarged. **D:** Overlay of PET and MRI, easily tumor-typical (red arrows) and non tumor-typical findings (green arrow) can be identified and allocated anatomically.

Case 2 Patient with a Neuroendocrine tumor.

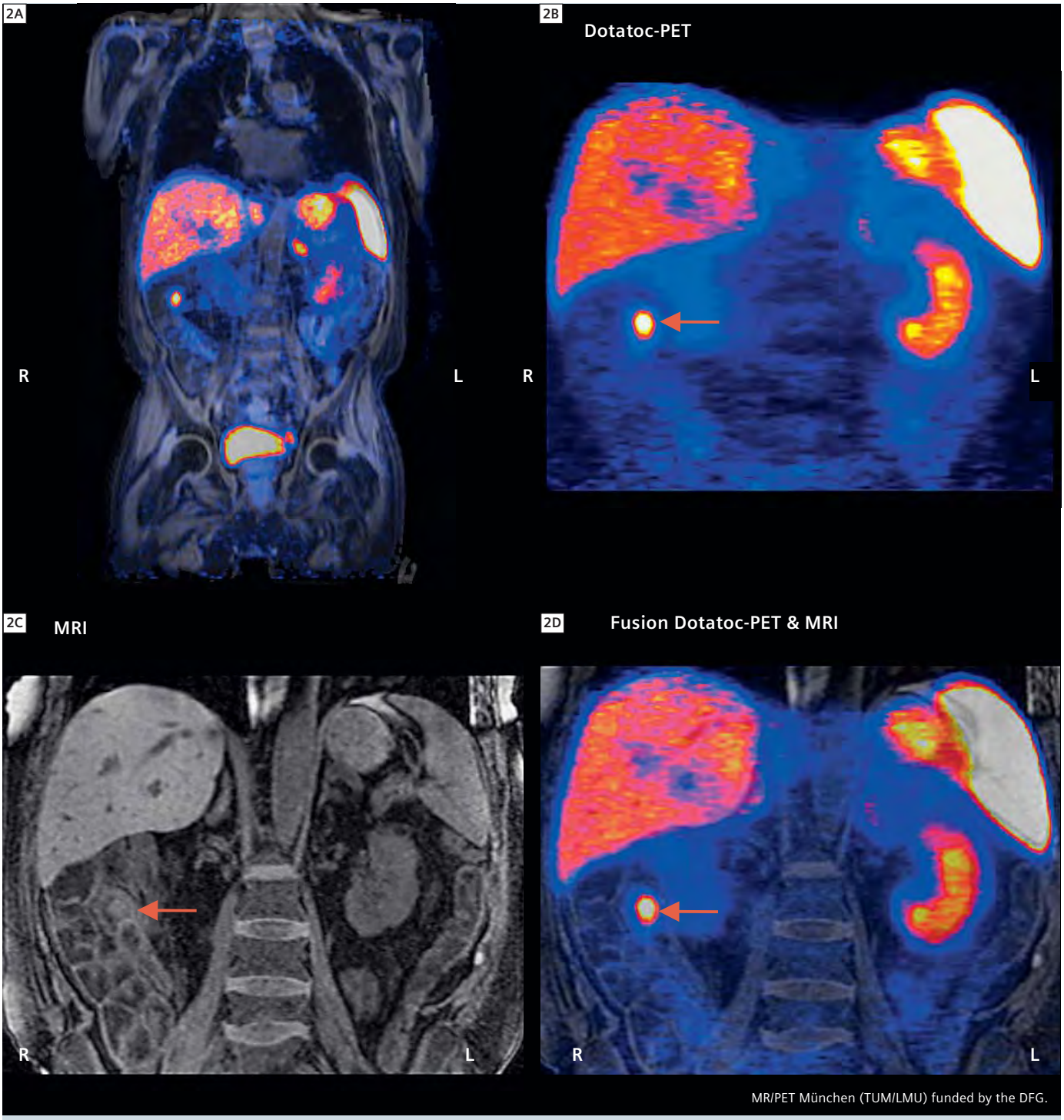

2 **A:** Overview using the water image of the MR AC Dixon sequence. Note the area of intense focal tracer uptake in the right upper quadrant of the abdomen, projecting on the region of the terminal ilium. There is a small bladder diverticulum of the left lateral bladder wall with tracer retention as accidental finding. **B:** PET-findings with ^{68}Ga-DOTATOC, a tracer binding to somatostatine-receptors which are expressed frequently on neuroendocrine tumors. An intense focal tracer-uptake can be found in the abdomen. **C:** MR-image, fat-suppressed coronal T1w breathold VIBE sequence. **D:** Fusion of PET and MR-findings. An excellent identification and anatomical allocation of the tumor is possible by combination of PET and MRI findings. No additional suspect lesions are apparent.

Case 3 Patient with bone metastases of a prostate cancer.

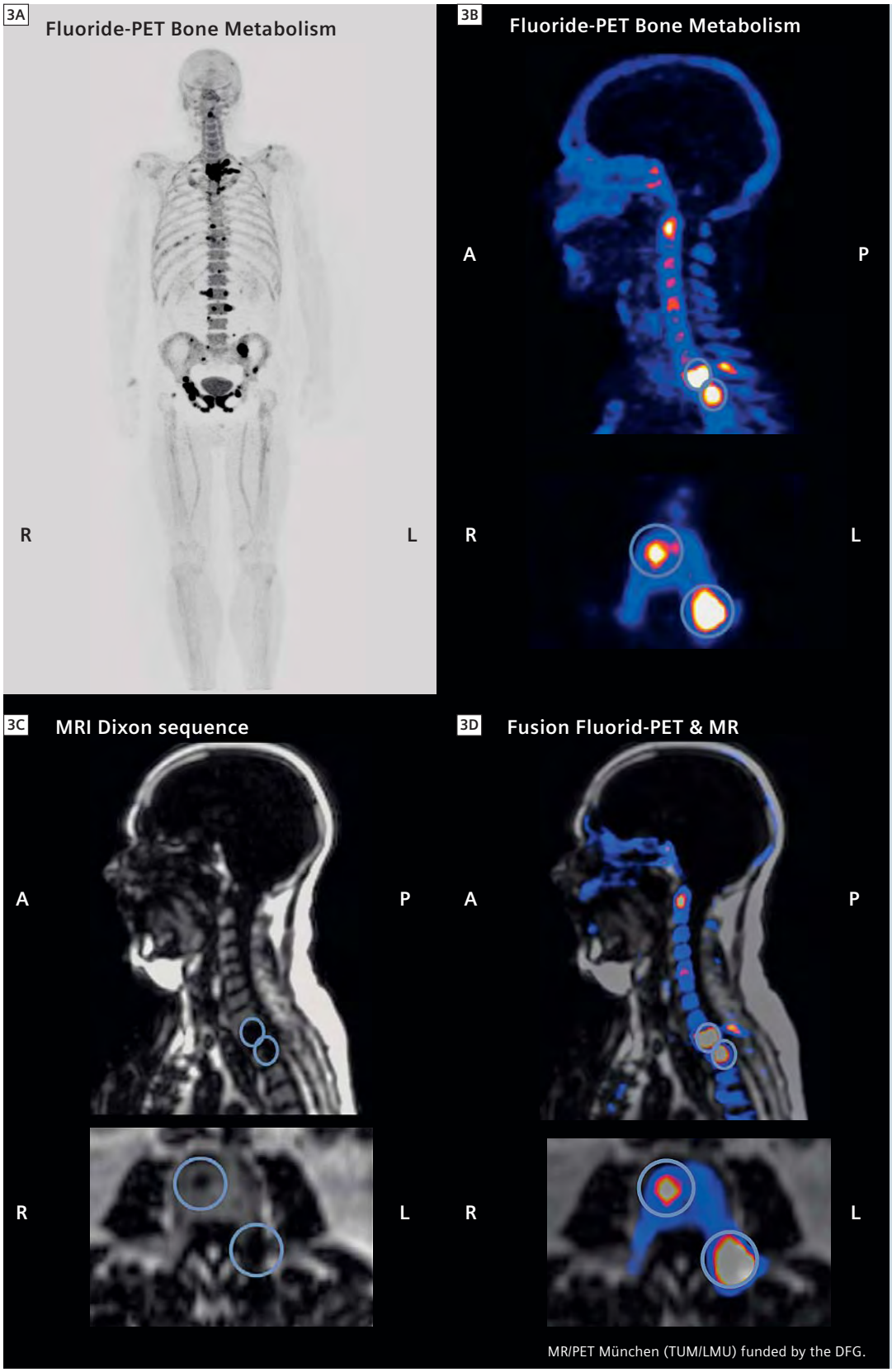

MR/PET München (TUM/LMU) funded by the DFG.

3 **A:** Overview of the ^{18}F-Fluoride PET scan. **B:** PET-findings. **C:** MR-image, sagittal fat-weighted MR AC Dixon sequence. **D:** Fusion of PET and MR-findings. Upper row: sagittal slices, Lower row: axial slices. The Fluoride-PET scan shows a number of suspect lesions in the skeleton, likely corresponding to bone metastases of the prostate-cancer. On the MR- and the fusion-images it is apparent that in the region of the increased PET-tracer uptake, displacement of the bone marrow has occurred, underlining the suspicion of bone metastases.

2. Neurology

Case 4 Patient with a glioblastoma multiforme.

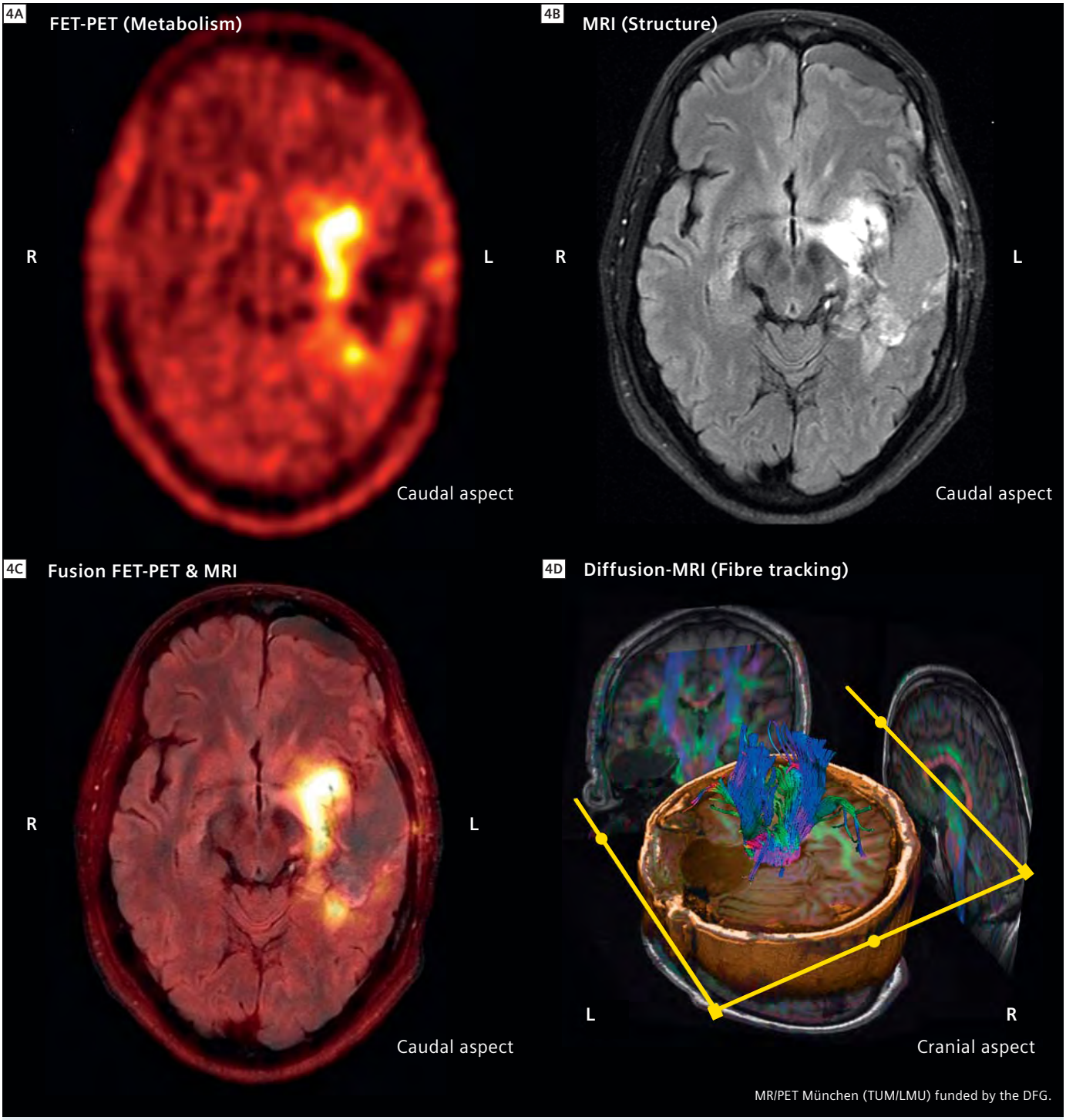

4 **A:** ^{18}F-FET PET scan. The tracer FET represents a measure of the amino acid metabolism and allows the sensitive identification of brain tumor tissue which is characterized by high amino acid turnover, in contrast to healthy brain tissue. A strong tracer uptake is visible around a previous resection area, suspect for remaining/recurrent brain tumor tissue. **B:** MR-image, axial FLAIR-sequence, demonstrating a region of hyper intensity around the area of resection, potentially representing edema and/or gliosis, but also vital tumor tissue cannot be excluded. Moreover, a left frontopolar hygroma is seen. **C:** Fusion of PET and MR-findings, allowing excellent anatomical allocation of the vital tumor tissue in reference to anatomical structures and abnormalities in the MR-image. **D:** Fibre-tracking based on a diffusion-tensor MR dataset, demonstrating the course of neuronal axons alongside the resection area.

Case 5 Patient with Alzheimer's disease.

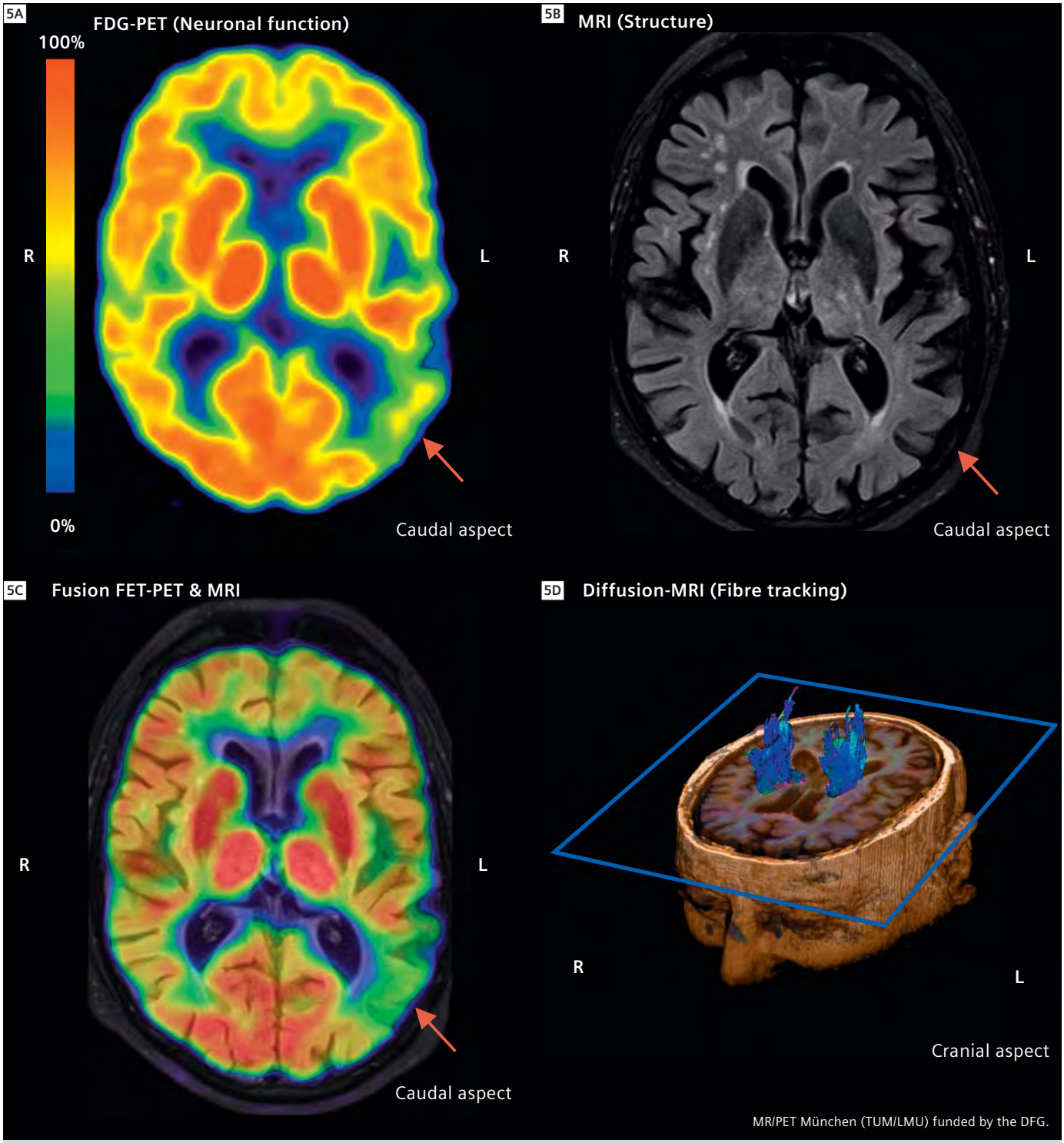

5 **A:** ^{18}F-FDG-PET of the brain, which represents a measure of neuronal function. Areas with reduced neuronal function in consequence of ongoing neurodegenerative processes are displayed in green-yellow (left temporoparietal cortex, see red arrow), healthy brain regions in orange-red. **B:** MR-image, axial FLAIR-sequence. Brain anatomy can be displayed in high resolution, cerebral atrophy is apparent in widespread regions, predominantly on the left side. **C:** In the MR/PET fusion regional allocation of hypometabolism and brain substance loss is possible. **D:** Fibre-tracking based on a diffusion-tensor MR dataset, demonstrating the course of neuronal axons in the brain of the patient.

3. Cardiology

Case 6 MR/PET of the heart.

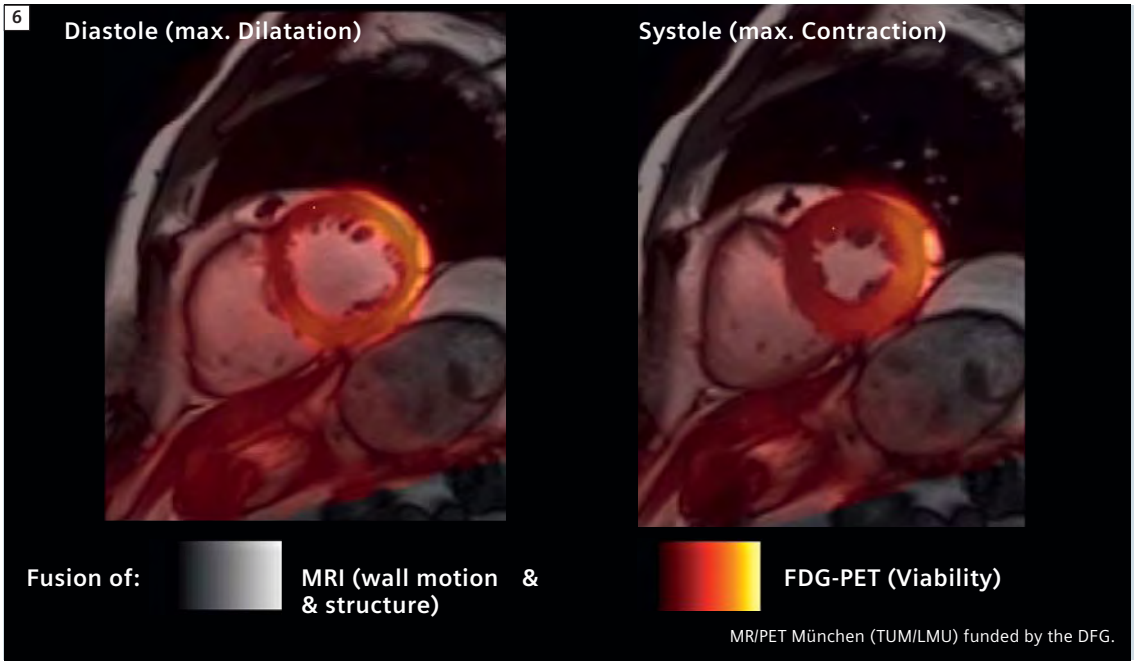

6 Assessment of the metabolism of cardiac tissue with the tracer ^{18}F-FDG allows the identification of viable myocardium. Simultaneous acquisition of wall motion and myocardial anatomy can be performed using MRI. The combination allows the exact attribution of functional aspects to underlying regional metabolic conditions/viability.

Conclusions

- First clinical imaging studies demonstrate successful clinical applicability of integrated whole body MR/PET.
- Attenuation correction of the PET signal using appropriate MR-derived attenuation maps appears to be feasible with sufficient reliability for most cases. Some problems (lack of accurate bone-detection, truncation artifacts) are a matter of ongoing research.
- From a diagnostic perspective, superiority of MR/PET compared to PET/CT can be foreseen for indications/body regions, which would preferably be approached by MRI rather than by CT, due to the superior soft tissue contrast of MRI. Examples are:
  Oncology: Head and neck tumors, masses in the pelvis/abdomen (e.g. prostate cancer), carcinoma of unknown primary, whole-body imaging
  Neurology: Brain tumors, epilepsy, dementia, stroke
  Cardiology: Regional function (wall motion) and scar detection (late enhancement) versus myocardial perfusion and tissue viability
- It remains to be evaluated for which indications MR/PET is superior or equal to PET/CT and for which indications PET/CT will remain the method of choice. MR/PET will probably be inferior to PET/CT for indications which are commonly addressed with better diagnostic value by CT, e.g. pulmonary lesions.
- The expected high costs for this type of imaging procedure will require elaborate logistics regarding patient flow, examination procedures, occupancy of the scanner etc., to ensure efficient utilization.
- The large number of available MR-sequences and of different PET-tracers exponentiates the number of potential combinations of imaging tests. This will define the need to develop optimized imaging algorithms for specific diagnostic questions.

References

1 Catana, C., et al., MRI-assisted PET motion correction for neurologic studies in an integrated MR-PET scanner. J Nucl Med. 52(1): p. 154-61.
2 Catana, C., et al., Toward implementing an MRI-based PET attenuation-correction method for neurologic studies on the MR-PET brain prototype. J Nucl Med. 51(9): p. 1431-8.
3 Herzog, H., et al., High resolution BrainPET combined with simultaneous MRI. Nuklearmedizin. 50(2).
4 Schlemmer, H.P., et al., Simultaneous MR/PET imaging of the human brain: feasibility study. Radiology, 2008. 248(3): p. 1028-35.
5 Beer, A.J., et al., Radionuclide and hybrid imaging of recurrent prostate cancer. Lancet Oncol. 12(2): p. 181-91.
6 Metz S, Ganter C, Lorenzen S, van Marwick S, Herrmann K, Lordick F, Nekolla SG, Rummeny EJ, Wester HJ, Brix G, Schwaiger M, Beer AJ. Phenotyping of tumor biology in patients by multimodality multiparametric imaging: relationship of microcirculation, alphavbeta3 expression, and glucose metabolism. J Nucl Med. 2010 Nov; 51(11):1691-8. Epub 2010 Oct 18.
7 Drzezga A, Becker AJ, Van Dijk K, Sreenivasan A, Talukdar T, Sullivan C, Schultz AP, Sepulcre J, Putcha D, Greve D, Johnson KA, Sperling RA. Neuronal dysfunction and disconnection of cortical hubs in non-demented subjects with elevated amyloid-burden. Brain. 2011, in press.
8 Martinez-Moller, A., et al., Tissue classification as a potential approach for attenuation correction in whole-body PET/MRI: evaluation with PET/CT data. J Nucl Med, 2009. 50(4): p. 520-6.

Contact
Alexander Drzezga, MD
Technische Universität München
Klinik und Poliklinik für Nuklearmedizin
Klinikum rechts der Isar
Ismaninger Str. 22
D-81675 Munich
Germany
phone: +49 89 4140 7722
a.drzezga@lrz.tum.de

Missing information?

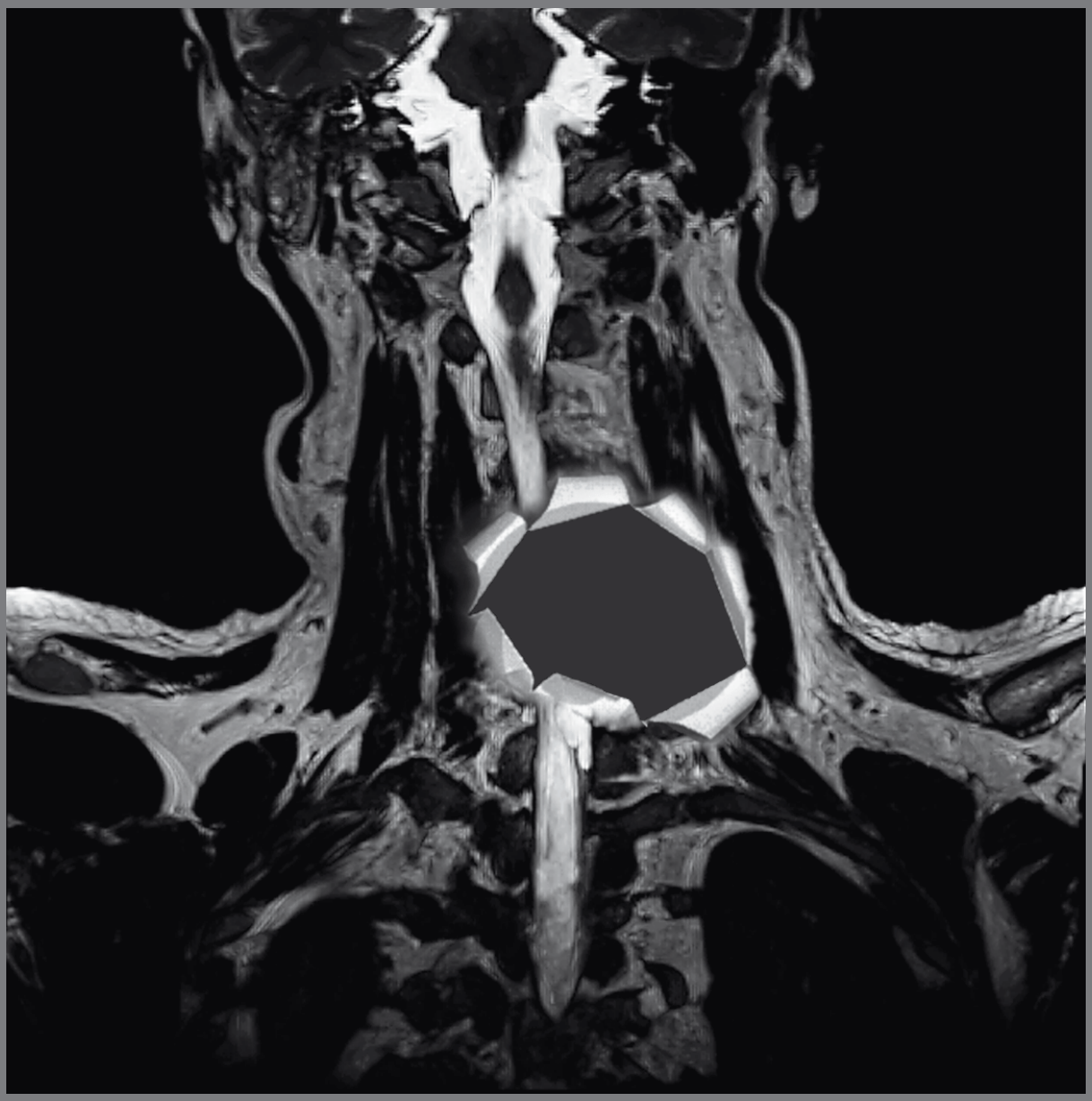

To make sure you have all the information you need, register for our free monthly newsletter on clinical MRI information.
Check out case reports from MAGNETOM users around the world and stay up-to-date with Siemens software applications.

Register at
www.siemens.com/magnetom-world
Go to
Publications > Subscriptions

IMRIS*neuro* 70 cm Bore 3T in Intra-Operative Neurosurgery

Jeanne Elliott

IMRIS, Winnipeg, Manitoba, Canada

1 IMRIS*neuro* 3T system. *(Image courtesy of: the Seaman Family MR Research Centre, Foothills Medical Centre, Calgary, Alberta, Canada.)*

The first IMRIS*neuro* system using a MAGNETOM Verio 3T magnet was installed at the Foothills Medical Centre in Calgary, Canada in early 2009.

Physicians appreciate High Field MR

The Seaman Family MR Research Centre at Foothills Medical Centre, under the leadership of Dr. Garnette Sutherland recently upgraded their 10-year old prototype 1.5T magnet to the latest IMRIS*neuro* with 3T MAGNETOM Verio technology. After successfully treating more than 1,000 neurosurgical patients using the 1.5T technology, the centre was ready to upgrade its capabilities. It became clear that the 3T Verio system including Diffusion Tensor Imaging (*syngo* DTI) and functional MRI would add significant value to surgical planning and intra-operative imaging.

The benefits of applying MR imaging during surgery has been recognized for many years. However, more recently the field has seen major growth in awareness and usage of MR guided imaging for neurosurgery. Many peer reviewed articles report the benefits of MR imaging including one, which concluded that in 41% of cases, the use of intra-operative MRI resulted in extended tumor resection. A different study concluded that in 27.5% of cases the original surgical plan was altered based on the intra-operative MR findings.

Many of the original observations were often based on past generation high field intra-operative MR technologies. They provided good image quality, but lacked the ability to deliver efficient workflow as the patient had to be moved to the MRI. Seeking the best in intra-operative MR technology, leading institutes like Barnes-Jewish Hospital (St. Louis, MO, USA), Johns Hopkins Hospital (Baltimore, ML, USA), Mayo Clinic (Jacksonville, FL, USA), Cleveland Clinic (Cleveland, OH, USA), Seaman Family MR Research Centre (Calgary, Canada), and PLA 301 Army Hospital (Beijing, China) have selected IMRIS*neuro*. These systems include the 1.5T MAGNETOM Espree or the 3T MAGNETOM Verio magnets and provide superior imaging capabilities with a technology workflow that brings MR to the patient. When the MR scanner is not in the operating room, the surgical team has full 360-degree access to the patient, and relocation of the magnetic field enhances operating room safety.

IMRIS*neuro* with the Siemens Verio or Espree magnets provide industry-leading capability and may also be used for diag-

2

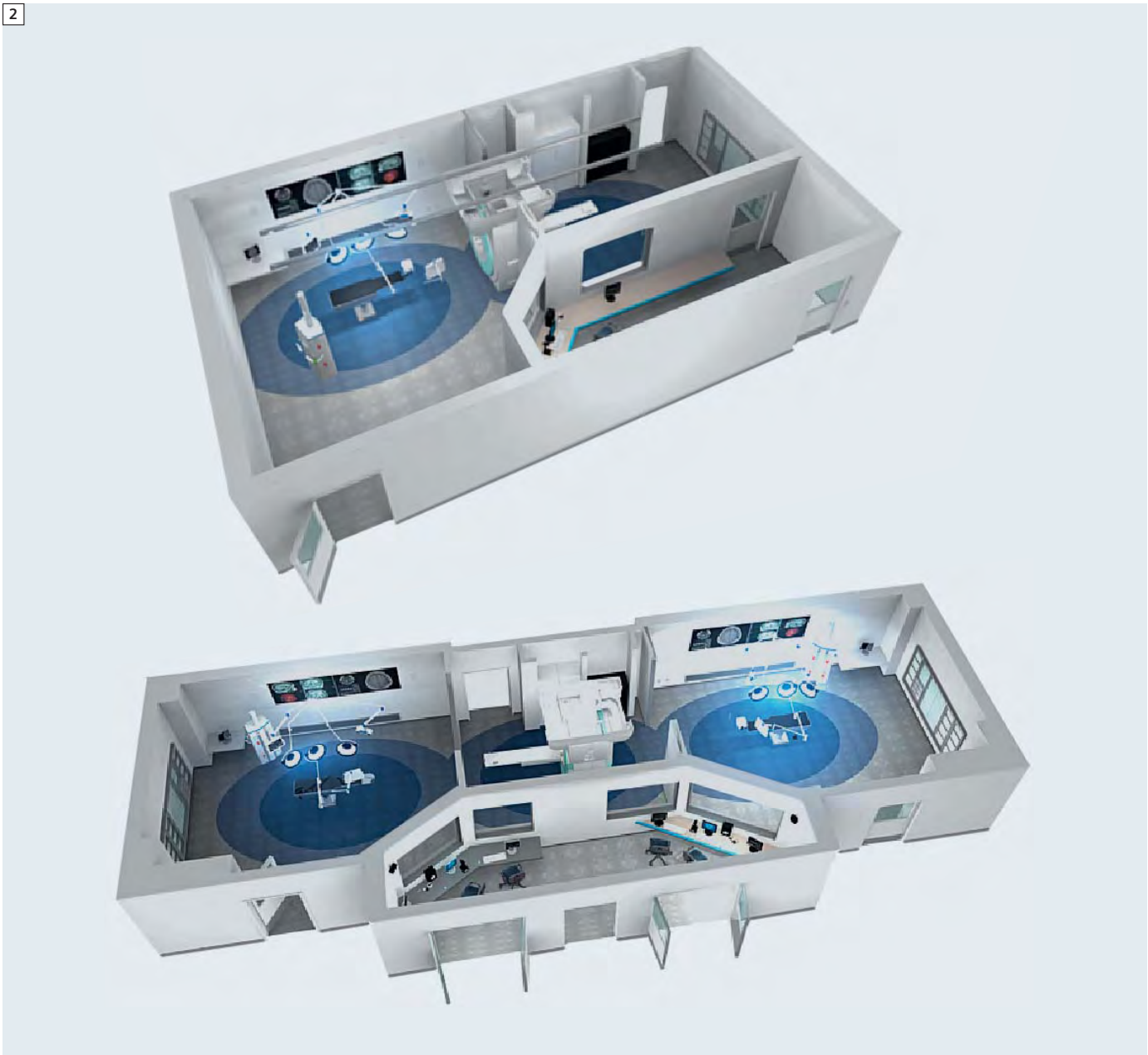

2 IMRIS*neuro* 2-room and 3-room configurations.

nostic examination of non-surgical patients who require the service of anesthesia or critical support. The IMRIS*neuro* solution is available in five configurations that allow the use of the 3T or 1.5T magnets for routine diagnostic imaging procedures while the system is not in use intra-operatively. For centers with significant surgical volumes, the magnet can move between two separate operating rooms further enhancing efficiency and the ability to offer better patient care.

Clinical cases with IMRIS*neuro* 3T MAGNETOM Verio

The moving magnet concept began with Dr. Garnette Sutherland's desire to bring the imaging benefits of an MRI to the neurosurgical operating room environment. His motivation was to preserve the current surgical workflow and to avoid moving the positioned surgical patient. IMRIS translated Dr. Sutherland's concept to pioneer the original 1.5T moving magnet design. More than 10-years later, Dr. Sutherland is also the first in the world to use the advanced IMRIS*neuro* with 3T MAGNETOM Verio: "The images obtained using the upgraded 3T intra-operative MRI system are of remarkable quality. The new system has been used for over 75 surgeries, in surgical planning, assessment during surgical dissection and for quality assurance. We have taken advantage of complex imaging techniques including fibre tracking, MR angiography and the rapid image pro-

cessing software. I am pleased that this innovation has turned into a commercial product that has gone on to benefit close to 3000 patients throughout the world." It is well understood in normal MR diagnostic scans that 3T image quality offers superior resolution and definition of soft tissue structures in the brain versus 1.5T. Initial intra-operative experience with the 3T MAGNETOM Verio shows the same advantages existing in image quality before, during and after surgery. The state-of-the-art imaging techniques and rapid processing times characteristic of the 1.5T are enhanced through the inherent higher signal-to-noise ratio (SNR) of the 3T. Surgical planning intra-operative MR images were obtained from a 61-year-old woman with a left subtentorial meningioma. Diffusion tensor imaging (*syngo* DTI) sequences show well the relationship of fibers to the tumor. Interdissection images (not shown) demonstrated deformation for the fiber tracks as a result of tumor removal. Knowledge of these relationships increased the safety of tumor resection.

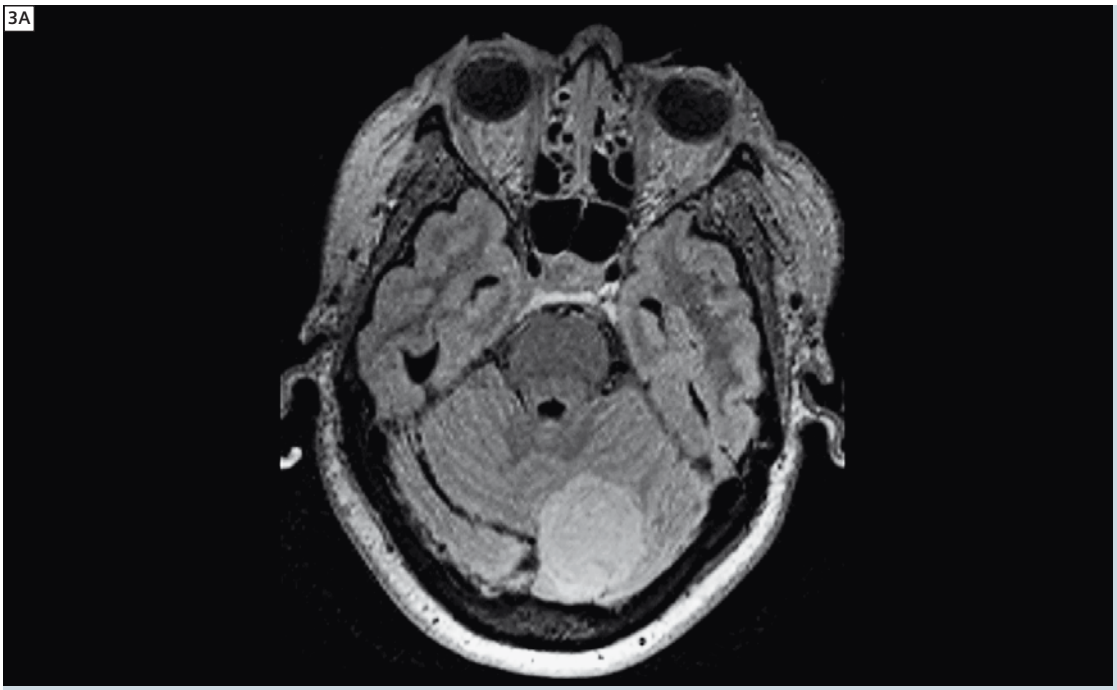

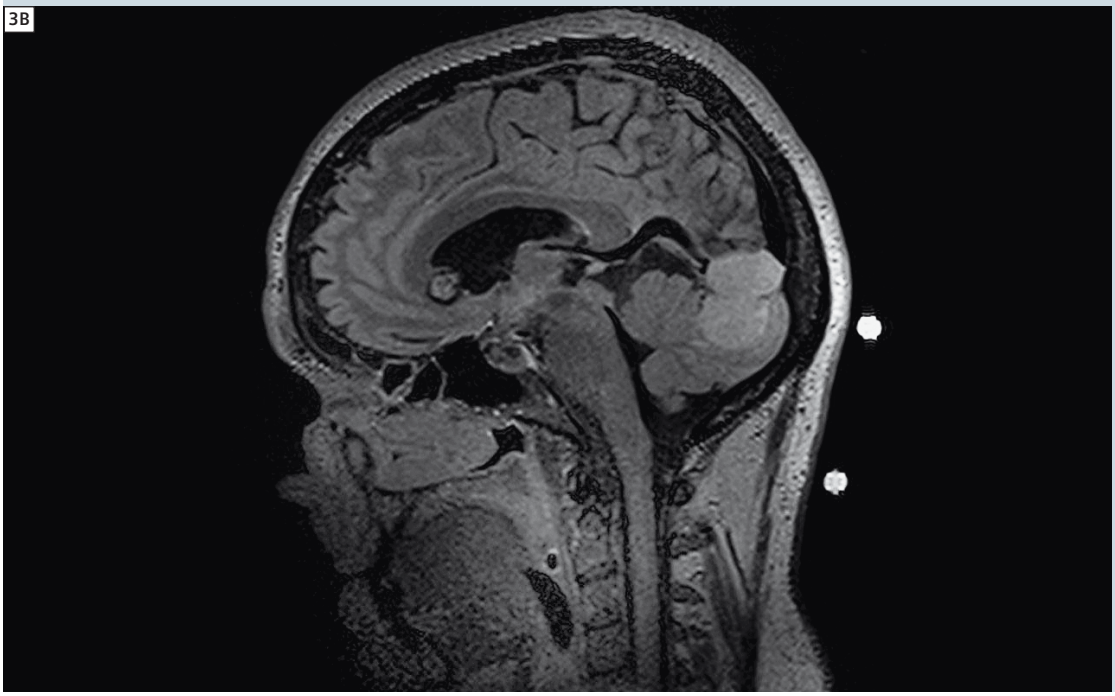

3 3T intra-operative. (*Images courtesy of the Seaman Family MR Research Centre, Foothills Medical Centre, Calgary, Alberta Canada 2009).*

New and additional clinical applications

The unique wide bore 70 cm 3T MAGNETOM Verio system is extremely valuable for intra-operative and interventional procedures. More often than not, interventional procedures require specialized patient positioning that can only be fully achieved with the 70 cm bore MAGNETOM Verio and Espree magnets. Positioning patients in lateral or prone positions is easily achievable with the use of wide bore, moving MR technology from IMRIS.

Excellent patient positioning and imaging capability is further supported by the enhancements made to the IMRIS*neuro* surgical bed. This newly developed surgical table is MR-compatible and X-Ray translucent for spine imaging and applications. The bed allows use of a single plane X-ray system in combination with MR imaging in the operating room (OR).

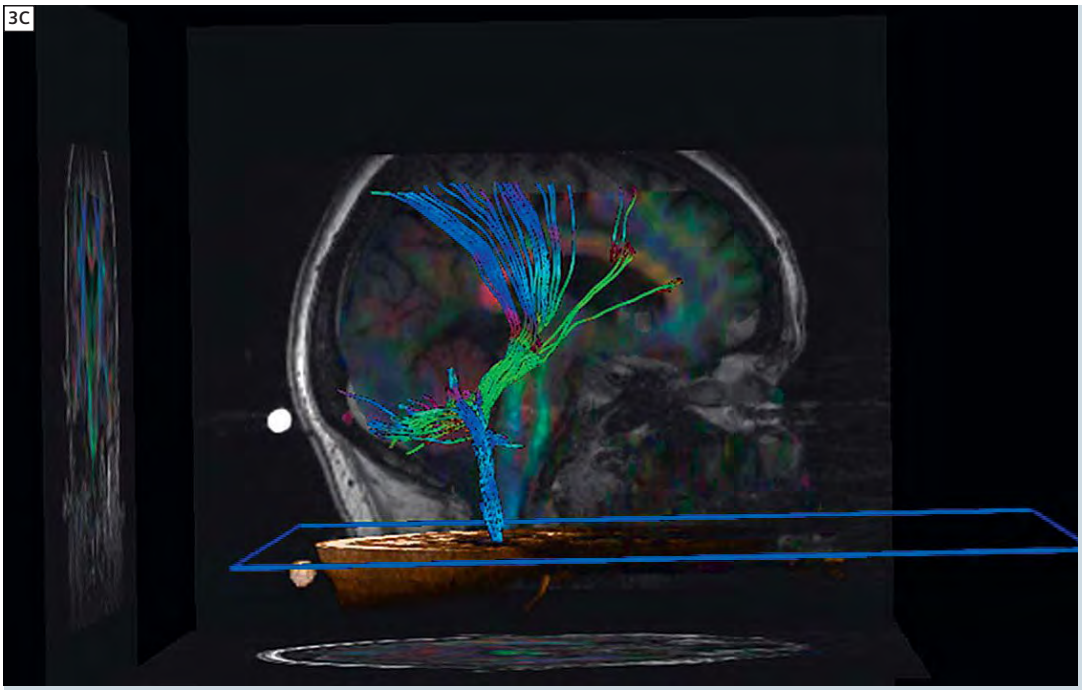

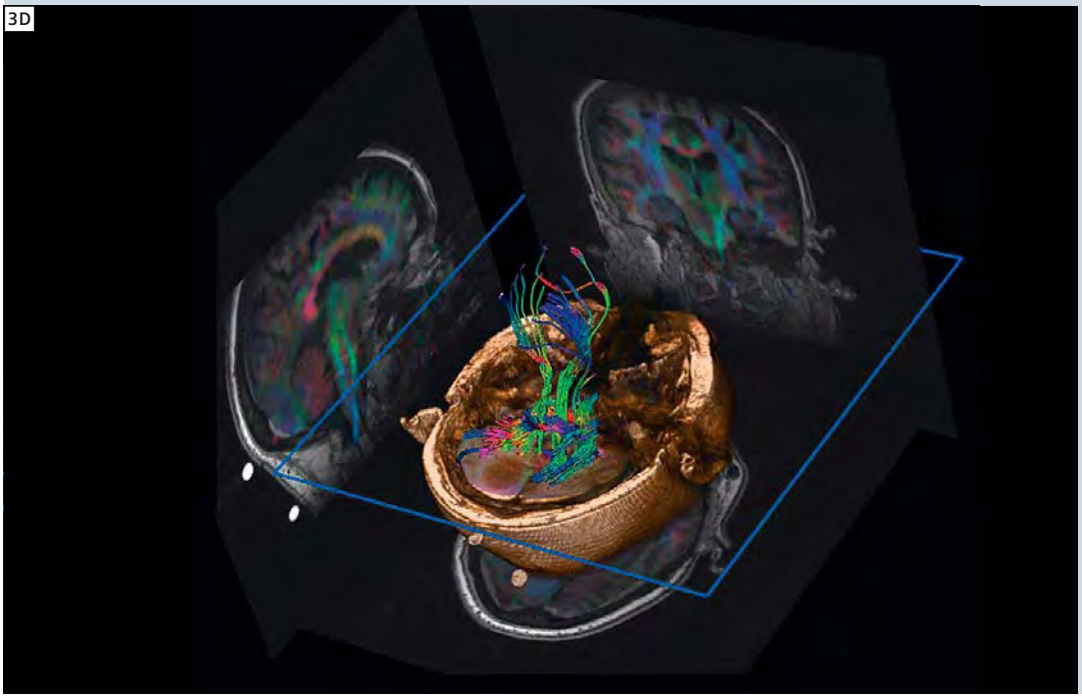

3 3T intra-operative. (*Images courtesy of the Seaman Family MR Research Centre, Foothills Medical Centre, Calgary, Alberta Canada 2009).*

4 IMRIS*neuro* surgical bed and collage images of prone/lateral/supine positioning. *(Images courtesy of IMRIS, Inc., Canada, 2009.)*

5 $IMRIS_{NV}$ and $IMRIS_{cardio}$

Future applications and technologies

IMRIS is widening the use of its image guided therapy solutions by expanding into new applications, combining 3T or 1.5T MR with single and bi-plane X-ray systems. $IMRIS_{NV}$ and $IMRIS_{cardio}$ are unique and advanced interventional suites providing an imaging environment that physicians may apply in providing stroke management and neurovascular care and in performing structural cardiac and minimally invasive procedures.

References

1 Intraoperative Visualization for Resection of Gliomas Nimsky C, Ganslandt O, Buchfelder M, Fahlbusch R. "Intraoperative visualization for resection of gliomas: the role of functional neuronavigation and intraoperative 1.5T MRI". Neurological Research 28(5): 482–7, July 2006.

2 Intraoperative High-Field-Strength MR Imaging: Implementation and Experience in 200 Patients. Nimsky C, Ganslandt O, von Keller B, Romstöck J, Fahlbusch R. 'Intraoperative High-Field Strength MR Imaging: Implementation and Experience in 200 Patients." Radiology 2004; 233:67–78.

Contact
Jeanne Elliott
IMRIS
100 – 1370 Sony Place
Winnipeg, Manitoba
Canada, R3T 1N5
jelliott@imris.com

High-Resolution 3T MR Neurography of the Lumbosacral Plexus

Avneesh Chhabra, M.D.; Aaron Flammang, MBA, BS; John A. Carrino, M.D., M.P.H.

Russell H. Morgan Department of Radiology and Radiological Science, Johns Hopkins Medical Institutions, Baltimore, MD, USA

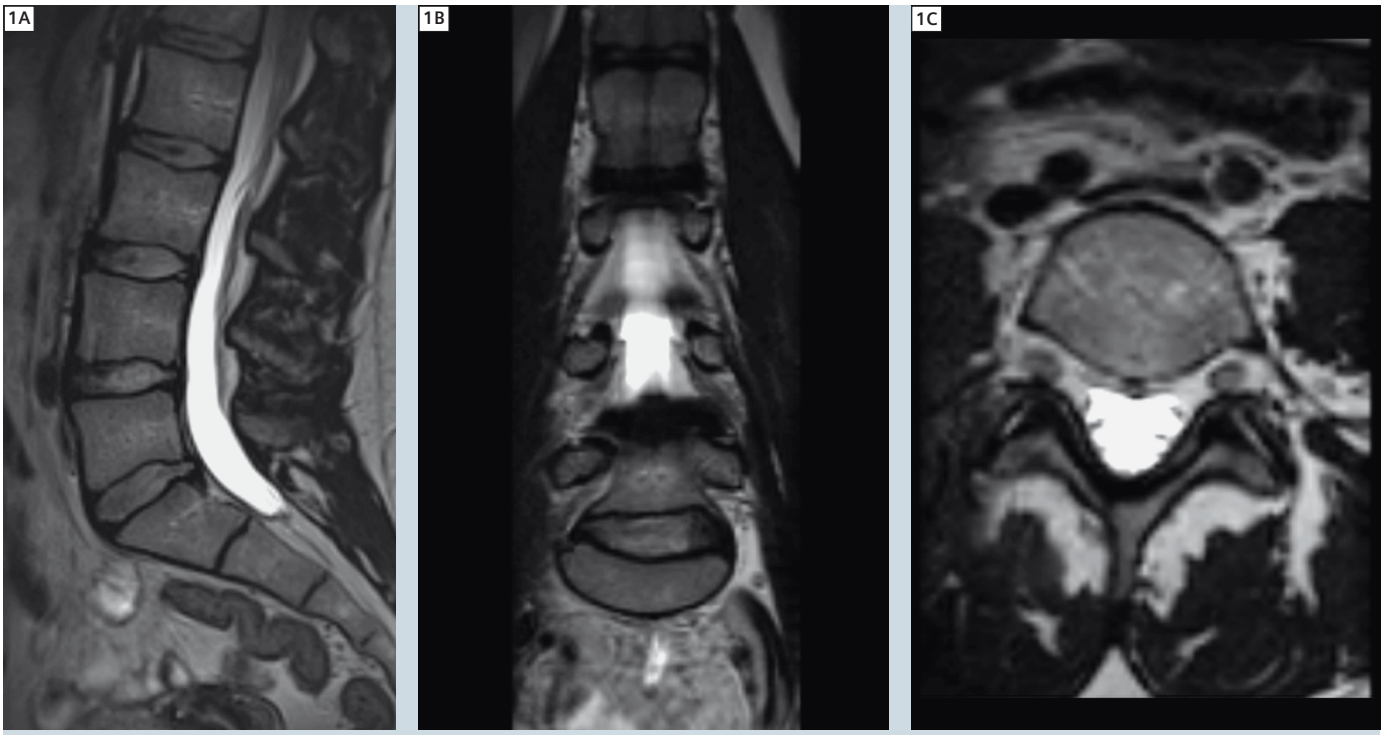

1A–C Lumbosacral Plexus 3T MR Neurography evaluation: Isotropic multiplanar reformats from 3D T2 SPACE **(1A–1C)**.

Abstract

The lumbosacral (LS) plexus is a series of nerve convergences and ramifications that provide motor and sensor innervation to pelvis and lower extremities. LS plexopathy is a serious condition caused by a variety of pathologies. Magnetic Resonance Neurography is an important modality for evaluation of LS plexopathy due to variable clinical presentations and deep location leading to suboptimal accessibility of the plexus to electrodiagnostic studies. This article describes the role of MR Neurography in evaluation of the LS plexus and illustrates the spectrum of pathologies along with their respective imaging findings using 3 Tesla MR Neurography.

Introduction

The lumbosacral (LS) plexus is comprised of an intricate architecture of nerves that supply the pelvis and lower extremity. It can be subject to a variety of pathologies, which may result in LS plexopathy, a clinical syndrome that includes motor and sensory disturbances. The diagnosis of LS plexopathy has traditionally relied on clinical findings and electrodiagnostic study results. However, differentiation of LS plexopathy from spine related abnormality and definition to type, location and extent of pathology often remains a diagnostic challenge due to deep location of the nerves and variable regional muscle innervation [1, 2]. With current high resolution 3 Tesla (T) Magnetic Resonance Neurography (MRN) techniques, diagnostic evaluation of large LS plexus branches, such as sciatic and femoral nerves, as well as smaller segments, such as nerve roots convergences and

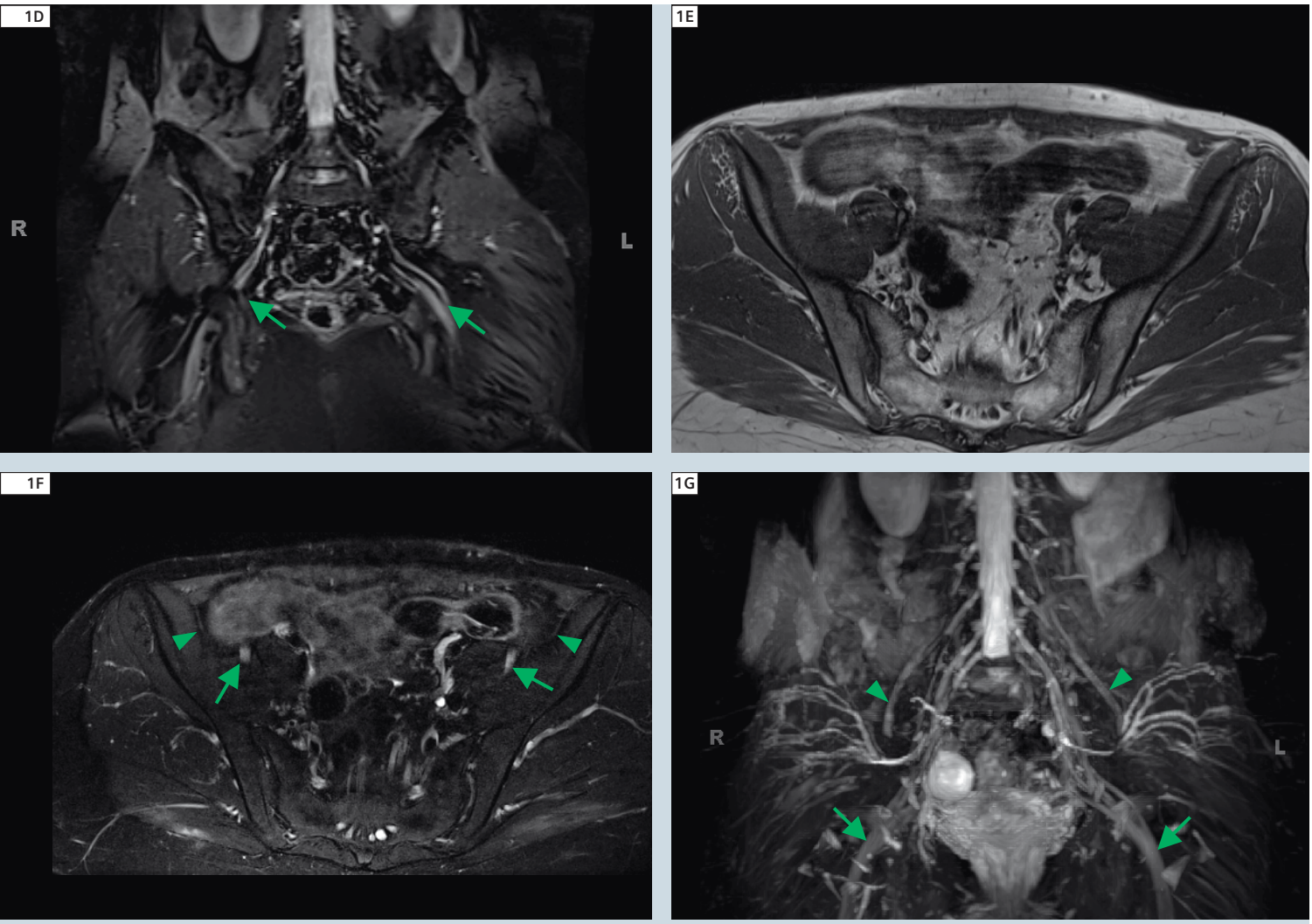

1D–G Coronal reconstructed 3D STIR SPACE **(1D)** showing sciatic nerves (arrows). Axial T1w **(1E)** and T2 SPAIR **(1F)** images showing bilateral femoral nerves (arrows) and lateral femoral cutaneous nerves (arrowheads). MIP coronal 3D STIR SPACE **(1G)** image showing bilateral LS plexus nerve roots, femoral nerves (arrowheads) and sciatic nerves (arrows).

peripheral nerves is feasible, aiding in pre-surgical evaluation and appropriate patient management [3, 4]. This article provides a pertinent discussion of the LS plexus anatomy, current role of MRN in evaluation of plexopathy and describes the respective imaging findings of various pathologies using 3T MR Neurography.

Anatomic considerations

The LS plexus is comprised of lumbar plexus, sacral plexus and the pudendal plexus, with contributions from the ventral rami of lumbar (L1–4 +/– T12), sacral (S1–4 and LS trunk, L4–S1) and the lower sacrococcygeal (S2–4 and C1) nerves, respectively [5]. The plexus is formed lateral to the intervertebral foramina and various branches course through the psoas major muscle. The ventral rami are further split into anterior and posterior divisions. The anterior divisions give rise to the iliohypogastric (L1), ilioinguinal (L1), genitofemoral (L1-L2) and obturator nerves (L2–4). The posterior divisions combine to form the posterior branches [femoral (L2–4) and lateral femoral cutaneous nerves (L2, 3)]. All branches exit lateral to the psoas muscle and course under the inguinal ligament, except the obturator nerve and LS trunk, which exit medial to the psoas muscle. The sacral plexus gives rise to anterior branches, namely the tibial part of the sciatic nerve (L4–S3), pudendal nerve (S1–4) and medial part of the posterior femoral cutaneous nerve (S1–3) and, posterior branches, namely the common peroneal part of the sciatic nerve (L4–S2), superior (L4–S1) and inferior gluteal nerves (L5–S2),

Table 1: S The 3T MR imaging protocol employed in our institution of the evaluation of the lumbosacral plexus.

Sequence	Slice	Field-of-view (cm)	Voxel size (mm³)	TR/TE (ms)	Turbo factor
Axial T1 TSE	BL	33	0.64	800/12	6
Axial T2 SPAIR	BL	33	1.00	4500/80	17
Coronal PD SPAIR	BL	36-38	0.6	4980/38	7
Coronal T1 TSE	BL	36-38	0.5	550/10	3
3D Coronal STIR SPACE	BL	36-38	1.45	1500/103	61
3D Sagittal T2 SPACE	Lumbar spine	28	1.45	1000/99	69
Coronal 3D VIBE *	BL	36-38	0.58	4.39/2.01	–

Abbreviations are: TSE = Turbo Spin Echo, SPAIR = spectral adiabatic inversion recovery, STIR = short tau inversion recovery, 3D SPACE = three-dimensional Sampling Perfection with Application optimized Contrasts using constantly varying flip angle Evolutions, VIBE = Volume Interpolated Breathhold Exam (* optional), BL = bilateral

lateral part of the posterior femoral cutaneous nerve (S1–3) and the nerve to the piriformis muscle (L5, S2). The above two plexuses connect via the LS trunk to form the LS plexus [2, 5].

Pathologic conditions and indications of MRN

The LS plexus is relatively protected by the axial skeleton and entrapment neuropathy is much less common than brachial plexopathy. It is considered as the counterpart of the brachial plexus in the lower body and is affected by similar types of diseases. The LS plexus may be involved by local processes in the viscinity of the plexus, such as extrinsic compression by space occupying lesions, injury or infiltration by tumor / infectious process – which is an indication for MRN; or in systemic conditions, such as metabolic, autoimmune, vasculitis, ischemic or inflammatory disorders – which are usually diagnosed based on clinical and laboratory findings. MRN may be used in the latter case to confirm lumbar plexitis / plexopathy in clinically confusing presentation and underlying known systemic condition. In addition, a primary or idiopathic form of LS plexopathy may occur, possibly due to altered immunological response and is considered analogous to idiopathic brachial plexopathy [6–8]. The entity has a favorable outcome and spontaneous recovery, whereas its diagnosis is based upon exclusion of other etiologies and sometimes may require confirmation with MRN in case of indeterminate electrodiagnostic results. An important indication of MRN is in patients under consideration for surgery for peripheral nerve lesions (piriformis syndrome/meralgia paresthetica), post abdominal surgery entrapment of ilioinguinal/genitofemoral nerves, or after injury to a large branch (sciatic, femoral, obturator). Finally, MRN is increasingly used for guidance during perineural and intramuscular medication injection.

Clinical findings

LS plexopathy most often presents with asymmetric weakness, pain and/or paresthesias in the lower extremities involving multiple contiguous LS nerve root distributions. Generally, unilateral localization of symptoms indicates a local pathology, whereas bilateral symptoms suggest a systemic process. The clinical picture often varies depending upon the location and degree of plexus involvement. In cases of involvement of the upper nerve roots, patients predominantly present with femoral and obturator nerve symptoms. LS trunk and upper sacral plexus lesions result in foot drop depending on the extent of involvement and weakness of knee flexion or hip abduction. Sensory symptoms may vary based on the individual nerves involved, which may include numbness or

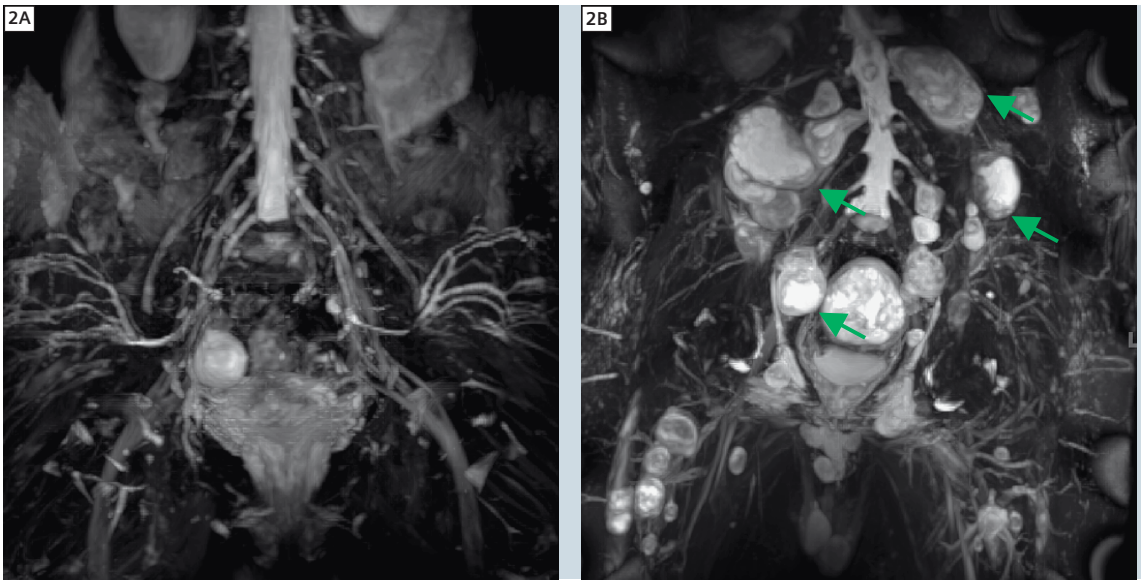

2 Normal vs abnormal LS Plexus. Coronal MIP 3D STIR SPACE images in a normal subject **(2A)** and another subject with schwannomatosis (arrows in **2B**).

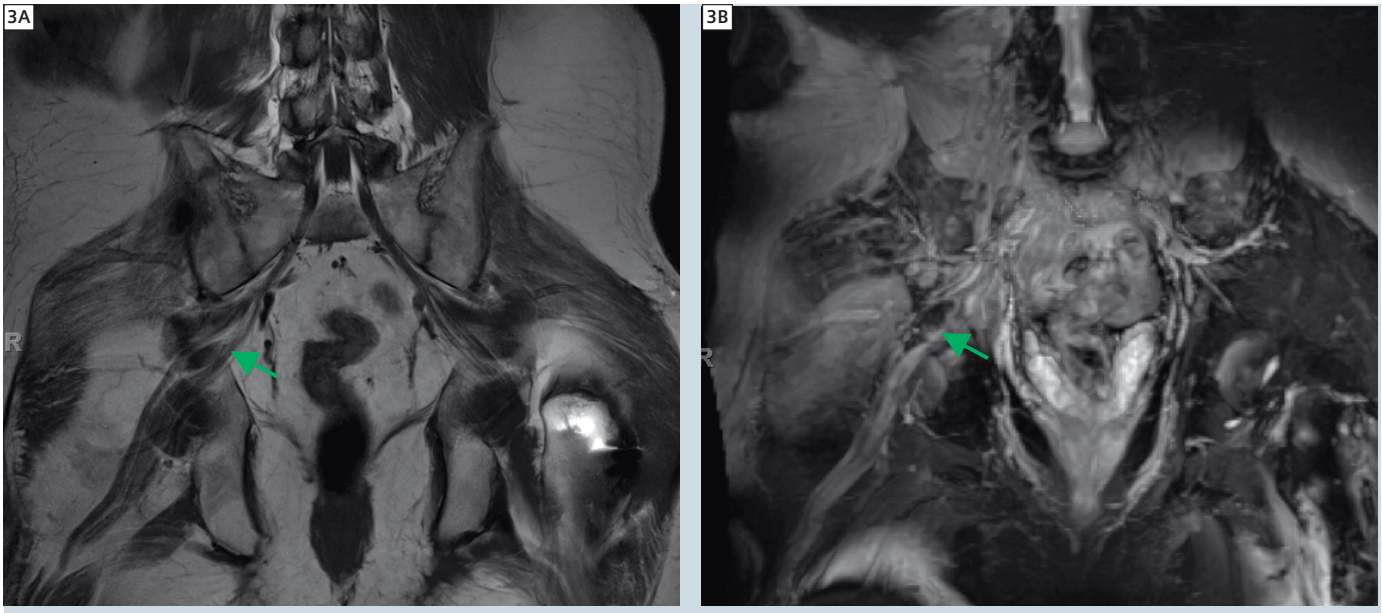

3 Piriformis syndrome – large LS plexus branch nerve abnormality. 33-year-old man with right buttock and pelvic pain, suspected piriformis syndrome. Coronal T1w **(3A)** and coronal MIP 3D STIR SPACE **(3B)** images through the pelvis show split right sciatic nerve by an accessory slip of the right piriformis muscle (arrow). Notice abnormal T2 hyperintensity of the sciatic nerve in keeping with entrapment neuropathy.

dysesthesia in the anterolateral thigh from lateral femoral cutaneous nerve involvement; in the mons and labia majora from genitofemoral nerve involvement and in the lower abdomen and inguinal area, upper medial thigh or pelvis from damage to the ilioinguinal, iliohypogastric, or pudendal nerves, respectively. Rarely, there may be associated bowel and bladder incontinence as well as sexual dysfunction [6–8].

MRN technique and normal appearances

Compared to 1.5T systems 3 Tesla (MAGNETOM Verio and MAGNETOM Trio, Siemens, Erlangen, Germany) imaging is preferred for most MRN examinations by the authors due to high quality scans obtained by these systems due to better signal-to-noise ratio and contrast resolution available in short imaging times. Due to the relatively small nerve structures under interrogation, it is essential to use high resolution imaging with a combination of 2D (dimensional) and 3D isotropic spin echo type imaging for optimal assessment. In the presence of known metal* in the area of imaging, 1.5T imaging is preferred. Table 1 and Fig. 1 show the 3T MRN imaging protocol employed at Johns Hopkins for the evaluation of the LS plexus. For fascicular architecture and subtle signal intensity

changes, high-resolution 2D axial T1w and T2 SPAIR (Spectral Adiabatic Inversion Recovery) images are ideal. Fascicular appearance of nerves is consistently seen with T2 SPAIR images in larger branches, such as femoral nerves and sciatic nerves, as well as in smaller nerves that are affected and enlarged due to neuropathy, such as lateral femoral cutaneous and genitofemoral nerves. 2D imaging is complemented by isotropic 3D images reconstructed in planes perpendicular and longitudinal to the nerves in question. 3D imaging (SPACE – Sampling Perfection with Application optimized Contrasts using constantly varying flip angle Evolutions) allows multiplanar and curved planar reformations. Two types of 3D imaging are performed, focusing in two different locations with two different purposes, 3D STIR SPACE for the LS plexus (from L2-3 level to lesser trochanter of femurs), while T2 SPACE (from L2-S2) is used for the lumbar spine, as spondylosis is a major confounder in the diagnosis of peripheral nerve pathology (Fig. 1). 3D imaging shows the lesions along the long axis of the nerve, course deviations, focal neuroma, nerve gap in cases of injury, etc. for better pre-operative planning and understanding of the referring physicians. Side-side imaging differences of the nerves can also be highlighted on maximum intensity projection (MIP) images. Gadolinium administration is reserved for cases of suspected neoplasm, inflammation, diffuse polyneuropathy, neurocutaneous syndrome, or post-operative complication [9–13]. Additional coronal T1w and STIR/PD SPAIR images aid in detection of lesions along the long axis of the nerves, side-to-side comparison of the nerve morphology and signal intensity (generally symmetrical), as well as for depiction of other incidental findings in relation to hips or spine. SPAIR produces higher SNR and is less prone to pulsation artifacts than STIR imaging, and is also more SAR favorable at 3T imaging [3, 4].

MR Neurography findings of LS plexopathy

MRN assessment of the LS plexus relies on the evaluation of direct morphologic features, such as altered nerve size, abnormal fascicular morphology (disrupted, effaced or enlarged) and focal or diffuse deviations in nerve course. T2 signal intensity (SI) changes (signal alterations approaching the adjacent vascular signal intensity, or asymmetric SI to the other side, given variations due to non-uniform fat saturation); as well as indirect features such as effacement of perineural fat planes due to focal fibrosis/mass lesions (Figs. 2, 3) and regional muscle denervation changes (edema like T2 signal alteration in acute and subacute cases to fatty replacement and atrophy in chronic cases). MRN is useful for detecting the individual segmental nerve abnormalities (enlarged or asymmetrically T2 hyperintense) in cases of plexitis/plexopathy or nerve injury. Similar to brachial plexus imaging, minimal increased nerve T2 signal intensity alone should be perceived with caution, as magic-angle artifact is a well-recognized artifact in LS plexus MR imaging [3, 4]. MRN is also useful in differentiating the plexopathy (nerve abnormality starting distal to the neural foramina, and often involving multiple nerve roots) from lumbar spondylosis (presence of substantial spondylosis, disc herniations, intraspinal mass, and nerve abnormality starting from within and immediately distal to the neural foraminal level in a distribution of the narrowed foramina). It is also worth mentioning that MRN may help exclude LS plexopathy in clinically confusing cases by demonstrating normal symmetrical appearance of bilateral nerve segments. In trauma cases, it is critical to demonstrate whether the injury is merely a stretch injury (merely T2 signal alterations) with nerve continuity; or if there is neuroma formation (focal enlargement of the nerve with effaced fascicular appearance) or nerve root avulsion or nerve discontinuity, which may be indications for surgery (Fig. 4). Peripheral nerve sheath tumors are depicted as focal or fusiform enlargements of the nerves, and may variably demonstrate classic signs, such as the tail, target, fascicular, bag of worms and split-fat signs. Differentiation between benign and malignant peripheral nerve sheath tumors is generally not reliable by imaging, although large size, ill-defined margins, peritumoral edema, significant interval growth and internal heterogeneity,

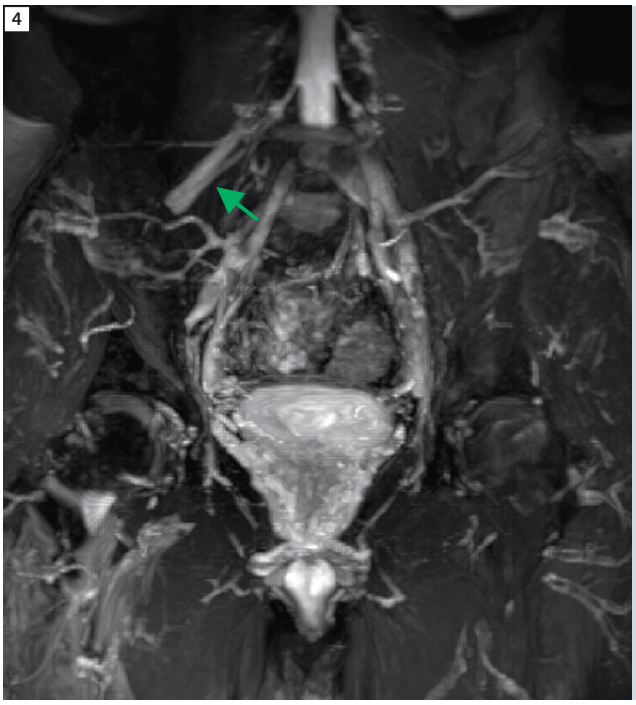

4 Right femoral nerve transection – large LS plexus branch nerve abnormality. 64-year-old man with right leg weakness following recent surgery. Coronal MIP 3D STIR SPACE image through the pelvis shows abrupt termination of the right femoral nerve in keeping with transection (arrow) (Sunderland Grade V injury).

5 Genitofemoral nerve entrapment – small LS plexus branch nerve abnormality. 50-year-old man with right inguinal and scrotal pain, following a prior right inguinal hernia repair. Axial T2 SPAIR **(5A)** and oblique coronal MIP 3D STIR SPACE **(5B)** images through the pelvis show abnormally enlarged and hyperintense right genitofemoral nerve (arrows), with most abnormality at the site of previous hernia repair in keeping with entrapment neuropathy.

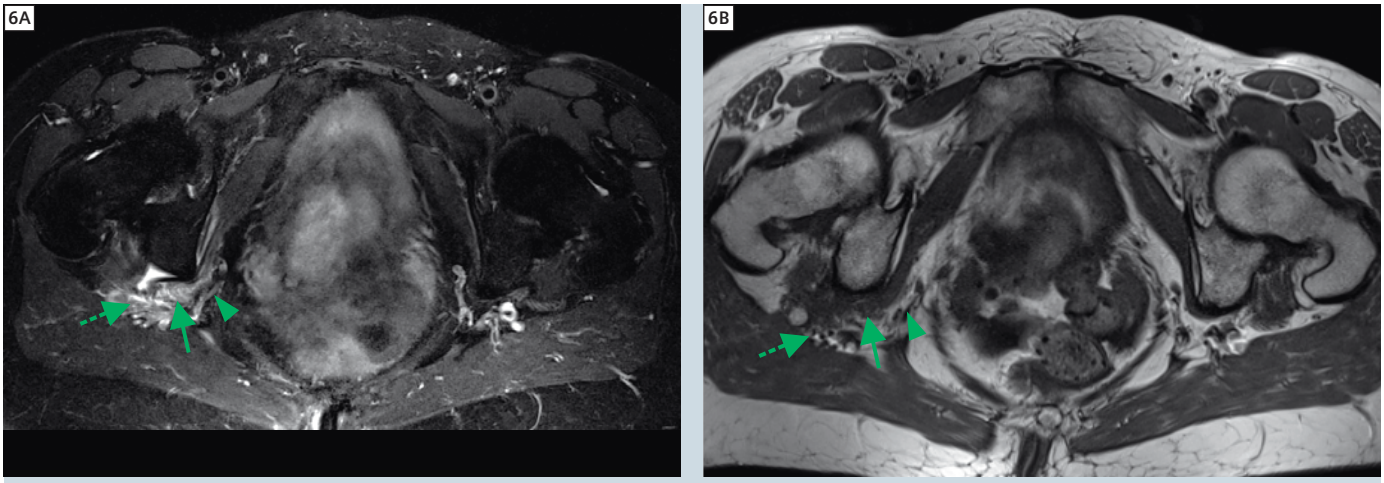

6 Right pudendal and sciatic Neuropathy – small LS plexus branch nerve abnormality. 61-year-old man with right pelvic pain, suspected pudendal neuralgia. Axial T2 SPAIR image through the pelvis shows grade I/II strain of the right obturator internus muscle (large arrow) with mild hyperintensity of the right pudendal nerve (small arrow) and right sciatic nerve (dotted arrows) in keeping with acute neuropathy.

especially in neurofibromas, are suspicious for malignancy. In those cases, a combination of clinical (new onset or increasing pain / neurological deficit), MRN imaging findings (as above), as well as ^{18}F FDG PET uptake (SUV_{max} >3–4 and increased uptake on delayed imaging) are used to make a clinical decision about percutaneous biopsy/surgical biopsy/ resection. Finally, MRN aids in differentiation of radiation neuropathy (diffuse nerve signal intensity alterations and enhancement in a geographic distribution corresponding to the radiation field) from recurrent mass lesion (focal enhancing lesions) [11–14].

Lumbosacral plexus branch anatomy and pathology

Current high-resolution 3T techniques allow depiction of internal nerve pathology of normal sized large branches, such as sciatic (Fig. 3), obturator, femoral (Fig. 4), various lumbosacral nerve roots as well as enlarged smaller branches,

such as ilioinguinal, genitofemoral (Fig. 5) and pudendal (Figs. 6, 7) nerves. Many of the smaller nerves are sensory nerves, and electrodiagnostic studies are usually not useful for their assessment. Nerve blocks have also been variably used, more so for therapeutic effect rather than for diagnosis of pathology. MRN may detect lesions within (diffuse enlargement proximal to entrapment, neuroma, etc.) or surrounding these nerves (focal fibrosis/mass lesion), thereby impacting patient management. Iatrogenic insults, such as during laparotomy, lymph node dissection, difficult parturition, hernia repair, etc are the leading cause of injury to these fine nerves. MRN may be used to detect focal fibrosis along the course of these nerves and their branches, which may be used to guide neurolysis. Such a procedure may give back patients' necessary sensation or provide pain relief. Finally, MRN may be used to provide guidance for perineural (local anesthetic and steroids) and intramuscular medication (e.g. Botulinium Toxin) injections. It is important to know that an appropriately performed image guided negative block / placebo controlled or graded positive nerve block confers more specificity to the diagnosis rather than a single positive block. Few studies have however, shown the therapeutic value of these blocks [15–22].

Conclusion

In the evaluation of LS plexopathy, 3T MRN provides high quality imaging and is a valuable adjunct to clinical examination and electrodiagnostic tests as it can offer anatomic information and lesion assessment otherwise unattainable by other modalities.

Contact
Avneesh Chhabra, M.D., DNB
Assistant Professor Radiology & orthopedic Surgery
Russell H. Morgan Department of Radiology and Radiological Science
Johns Hopkins Medical Institutions
achhabr6@jhmi.edu

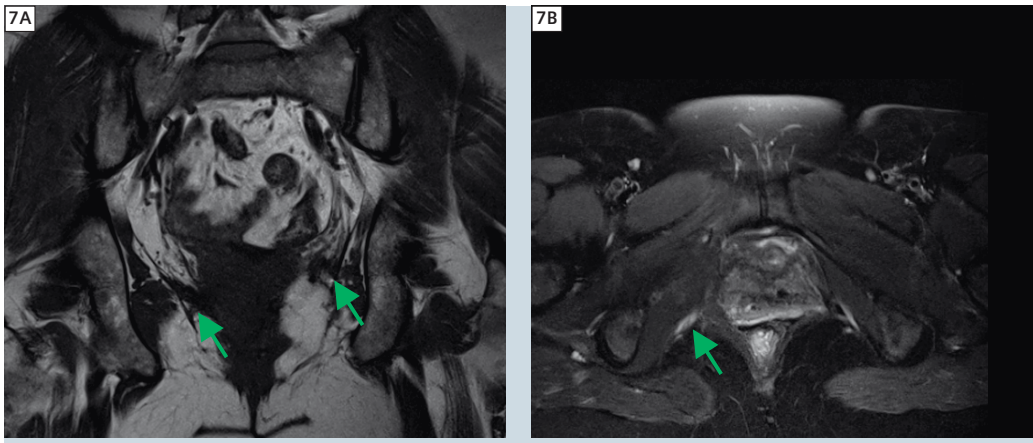

7 Chronic pudendal Neuralgia – small LS plexus branch nerve abnormality. 41-year-old woman with pelvic pain, right > left for many months. Coronal T1w **(7A)** and axial T2 SPAIR **(7B)** images through the pelvis show bilateral pelvic scarring (right > left), along the expected course of the pudendal nerves, causing entrapment (arrows). Notice asymmetrically prominent right pudendal neurovascular bundle (arrow).

*In the US, metal near or in the MR system must be labeled as MR-safe or conditional (with conditions stated).

References

1 Gebarski KS, Gebarski SS, Glazer GM, Samuels BI, Francis IR. The lumbosacral plexus: anatomic-radiologic-pathologic correlation using CT. Radiographics. 1986;6(3):401-25.
2 Petchprapa CN, Rosenberg ZS, Sconfienza LM, Cavalcanti CF, Vieira RL, Zember JS. MR imaging of entrapment neuropathies of the lower extremity. Part 1. The pelvis and hip. Radiographics. 2010;30(4):983-1000.
3 Chhabra A, Lee PP, Bizzell C, Soldatos T. 3 Tesla MR neurography-technique, interpretation, and pitfalls. Skeletal Radiol. 2011 May 6. [Epub ahead of print].
4 Chhabra A, Andreisek G, Soldatos T, Wang KC, Flammang AJ, Belzberg AJ, Carrino JA. MR Neurography: Past, Present, and Future. AJR Am J Roentgenol. 2011 Sep;197(3):583-91.
5 Kirchmair L, Lirk P, Colvin J, Mitterschiffthaler G, Moriggl B. Lumbar plexus and psoas major muscle: not always as expected. Reg Anesth Pain Med. 2008;33(2):109-14.
6 Evans BA, Stevens JC, Dyck PJ. Lumbosacral plexus neuropathy. Neurology. 1981;31(10):1327-30.
7 Sander JE, Sharp FR. Lumbosacral plexus neuritis. Neurology. 1981;31(4):470-3.
8 Hollinger P, Sturzenegger M. Chronic progressive primary lumbosacral plexus neuritis: MRI findings and response to immunoglobulin therapy. J Neurol. 2000;247(2):143-5.
9 Maravilla KR, Bowen BC. Imaging of the peripheral nervous system: evaluation of peripheral neuropathy and plexopathy. AJNR Am J Neuroradiol. 1998;19(6):1011-23.
10 Thawait SK, Chaudhry V, Thawait GK, Wang KC, Belzberg A, Carrino JA, Chhabra A. High-Resolution MR Neurography of Diffuse Peripheral Nerve Lesions. AJNR Am J Neuroradiol. 2010 Nov 24. [Epub ahead of print].
11 Chhabra A, Williams EH, Wang KC, Dellon AL, Carrino JA. MR neurography of neuromas related to nerve injury and entrapment with surgical correlation. AJNR Am J Neuroradiol. 2010 Sep; 31(8):1363-8. Epub 2010 Feb 4.
12 Chhabra A, Soldatos T, Durand D, Carrino JA, McCarthy EF, Belzberg AJ. The role of MRI in the diagnostic evaluation of malignant peripheral nerve sheath tumors. Indian J Cancer. 2011: (in press).
13 Taylor BV, Kimmel DW, Krecke KN, Cascino TL. Magnetic resonance imaging in cancer-related lumbosacral plexopathy. Mayo Clin Proc. 1997;72(9):823-9.
14 Whiteside JL, Barber MD, Walters MD, Falcone T. Anatomy of ilioinguinal and iliohypogastric nerves in relation to trocar placement and low transverse incisions. Am J Obstet Gynecol. 2003;189(6): 1574-8; discussion 8.
15 Klaassen Z, Marshall E, Tubbs RS, Louis RG, Jr., Wartmann CT, Loukas M. Anatomy of the ilioinguinal and iliohypogastric nerves with observations of their spinal nerve contributions. Clin Anat. 2011;24(4):454-61.
16 Hu P, Harmon D, Frizelle H. Ultrasound guidance for ilioinguinal/iliohypogastric nerve block: a pilot study. Ir J Med Sci. 2007;176(2):111-5.
17 Tipton JS. Obturator neuropathy. Curr Rev Musculoskelet Med. 2008;1(3-4):234-7.
18 Beltran LS, Bencardino J, Ghazikhanian V, Beltran J. Entrapment neuropathies III: lower limb. Semin Musculoskelet Radiol. 2010;14(5):501-11.
19 Patijn J, Mekhail N, Hayek S, Lataster A, van Kleef M, Van Zundert J. Meralgia Paresthetica. Pain Pract. 2011;11(3):302-8.
20 Chhabra A, Gustav A, Soldatos T, Wang KC, Belzeberg AJ, Carrino JA. 3T hihg-resolution MR Neurography of sciatic neuropathy. AJR 2011 (in press).

Market your MAGNETOM system

All the tools necessary to market your facility to patients and referring physicians are waiting for you in the **Your MAGNETOM** section on **www.siemens.com/magnetom-world**

Here you will find everything you need from patient pamphlets to advertisements, to trailers and press releases, postcards, posters, event checklists, high-resolution images and much more – ready for immediate use.

MAGNETOM Flash – Imprint

Publisher:
Siemens AG
Medical Solutions
Business Unit Magnetic Resonance,
Karl-Schall-Straße 6, D-91052 Erlangen,
Germany

Editor-in-Chief: Dr. Matthias Lichy, M.D.
(matthias.lichy@siemens.com)

Associate Editor: Antje Hellwich
(antje.hellwich@siemens.com)

Editorial Board: Christiane Bernhardt;
Peter Kreisler, Ph.D.; Wellesley Were;
Milind Dhamankar, M.D.; Michelle Kessler;
Gary McNeal; Sunil Kumar, M.D.

Production: Norbert Moser, Siemens AG,
Medical Solutions

Layout: independent Medien-Design
Widenmayerstrasse 16, D-80538 Munich

Printer: Mediahaus Biering GmbH,
Freisinger Landstr. 21, 80939 Munich, Germany

MAGNETOM Flash is also available on the internet:
www.siemens.com/magnetom-world

Global Siemens Headquarters

Siemens AG
Wittelsbacherplatz 2
80333 Muenchen
Germany

Global Siemens Healthcare Headquarters

Siemens AG
Healthcare Sector
Henkestrasse 127
91052 Erlangen
Germany
Phone: +49 9131 84-0
www.siemens.com/healthcare

www.siemens.com/healthcare-magazine

Order No. A91MR-1100-48X-4A00 | Printed in Germany | CC MR 03120.15 | © 03.12, Siemens AG

Global Business Unit

Siemens AG
Medical Solutions
Magnetic Resonance
Henkestr. 127
DE-91052 Erlangen
Germany
Phone: +49 9131 84-0
www.siemens.com/healthcare

Local Contact Information

In Asia
Siemens Pte Ltd
The Siemens Center
60 MacPherson Road
Singapore 348615
Phone: +65 6490-8096

In Canada
Siemens Canada Limited
Healthcare Sector
6865 Century Avenue, Suite 3001
Mississauga, ON L5N 2E2
Canada
Phone: +1 905 819-5800

Europe/Africa/Middle East
Siemens AG
Medical Solutions
Henkestr. 127
91052 Erlangen
Germany
Phone: +49 9131 84-0

Latin America
Siemens S.A.
Medical Solutions
Avenida de Pte. Julio A. Roca No 516,
Piso 7
C1067ABN Buenos Aires
Argentina
Phone: +54 11 4340-8400

USA:
Siemens Medical Solutions U.S.A., Inc.
51 Valley Stream Parkway
Malvern, PA 19355-1406
USA
Phone: +1-888-826-9702

SIEMENS